# Assessing Impacts of Climate Change on the Hydrology of the Nile River

by

Mohamed S. Siam

B. S. (Civil and Environmental Engineering), Cairo University (2008)

M. S. (Civil and Environmental Engineering), Cairo University (2010)

Submitted to the Department of Civil and Environmental Engineering

in partial fulfillment of the requirements for the degree of

Doctor of Philosophy in the Field of Hydrology

at the

MASSACHUSETTS INSTITUTE OF TECHNOLOGY

June 2016





Signature of Author: Signature redacted

Department of Civil and Environmental Engineering

May 2, 2016

Certified by: Signature redacted

Elfatih A. B. Eltahir

Professor and Associate Department Head of Civil and Environmental Engineering

Thesis Supervisor

Accepted by: Signature redacted

Heidi M. Nepf

Donald and Martha Harleman Professor of Civil and Environmental Engineering

Chair, Graduate Program Committee

# Assessing Impacts of Climate Change on the Hydrology of the Nile River

By

Mohamed S. Siam

Submitted to the Department of Civil and Environmental Engineering

on May 2, 2016, in partial fulfillment of the requirements for the degree of

Doctor of Philosophy in the Field of Hydrology

## Abstract

The human population living in the Nile basin is projected to double by 2050, approaching one billion. The increase in water demand associated with this burgeoning population fuels an ongoing water conflict between the riparian countries. Uncertainty regarding potential future changes in the flow of the Nile River as a result of climate change adds further stress to this critical situation. In this thesis, we investigate the impacts of climate change on hydrology and climate of the Nile basin. In particular, we predict and explain the future changes in interannual variability and long-term mean of the flow in Nile river. We analyze observations on recent change in the flow regime.

First, we examine the role of El Nino Southern Oscillation (ENSO) in shaping the interannual variability of the flow in the Nile river. We document an association between variability of ENSO and interannual variability in the flow of the Nile river. We provide a physically-based explanation of this teleconnection. Then, we build on this teleconnection and future predications regarding the frequency of El Nino and La Nina events to project enhancement in future variability of the flow in the Nile river. Second, an improved version of the MIT-Regional climate model (MRCM) is used to investigate the future changes in the long-term mean flow in the Nile river. The new version of MRCM includes new parameterizations of large scale cloud and rainfall developed as part of this thesis, which significantly improved the simulation of clouds coverage and radiation at the surface under current climate conditions. The updated version of the model is forced with modified lateral boundary

conditions and greenhouse gas concentrations that are assumed to describe future conditions. The impacts on the rainfall over the basin due to local and regional changes in concentration of atmospheric gases are compared to those due to global changes in the humidity and temperature.

The numerical simulations using MRCM suggest that increasing humidity at the lateral boundaries due to global processes would enhance the large scale rainfall, particularly during the rainy season. However, air temperature becomes warmer aloft due to the same global processes, which would tend to stabilize the atmosphere and reduce convective rainfall. On the other hand, increasing the concentration of greenhouse gases at local and regional scales would destabilize the vertical profile of air temperature, by increasing the air temperature in the middle and lower atmospheric layers, and hence would enhance convective rainfall.

Based on the conclusions of this thesis, the long-term mean and standard deviation of the annual flow in the Nile river are projected to increase for the future period (2000-2100) compared to the past period (1900-2000) by approximately 15% and 50%, respectively. Although the increase in long-term mean of the annual flow should slightly reduce the water stress in the Nile basin, additional water storage capacity in the basin would be needed in order to benefit from the expected additional water in the future.

**Thesis Supervisor: Elfatih A. B. Eltahir**
**Title: Professor and Associate Department Head of Civil and Environmental Engineering**

## Acknowledgements

First, I would like to thank my advisor Prof. Elfatih Eltahir for all his guidance and support. I have learned a lot from him during my Phd. He had the capability of keeping track of all the details of my work and also how these details fit in the bigger picture of my project. This work would have been impossible to finish without him. I would like also to thank my committee members Dr. Earle Williams and Prof. Alan Plumb for their valuable feedbacks, comments and helping me to make my thesis as complete as possible. I am also very grateful to my colleagues in the group: Teresa Yamana, Rebecca Giannotti, Marc Marcella, Noriko Endo, Hamed Ibrahim, Osama Mekki, Marie Estelle Demory, Ross Alter, Eun-Soon Im, and Mariam Allam. They have provided a nice environment for our work together and were always available when I needed help or support. Also, I would like to thank Joanne Batziotegos for helping us by taking care of all our administrative work.

During my Phd, I also met a lot of Egyptians at MIT and we tried together to establish connections between MIT and Egyptian researchers. I would like also to thank them for all the efforts they did to achieve this goal. This big team included: Tarek Moselhy, Tarek Rakha, Dina ElZanfaly, Dina ElDamak, Mostafa Bedewy, Perihan AbouZeid, Karim Gad, Islam Hussein, Mariam Allam, and my roommate for one year Amr AbdelZahir.

Last and but not least, I am very grateful for my mother and father who were a great support for me. Finally, I would like to thank my wife Mariam Allam, she had different roles in my life and my partner in everything.

Table of Contents

List of Figures

List of Tables

# Chapter 1: Introduction

## 1.1 Motivation

The Nile river basin is an ecosystem under severe stress. The basin is shared by 400 million people in eleven countries with economies that depend heavily on agriculture, which employs the vast majority of the labor force in most of these countries (World Population Prospects, 2013). Furthermore, almost half of the Nile basin countries are projected to live below the water scarcity level, 1000 $m^3$/person/year, by 2030 (FAO 2000, Baecher et al. 2015). Thus, any future changes in the magnitude of the flow volume of the Nile river can lead to significant impacts on the lives of the people living within the basin and may increase the already high level of water stress.

The climate around the world is changing due to natural and anthropogenic factors. The increase in greenhouse gas concentrations in the atmosphere is the main cause of the global climate change (Forster et al., 2007). This change may have crucial impacts on water resources and hydrology at global and regional scales. For the Nile basin, climate change may alter the distribution of the water resources of the basin. Furthermore, there is no consensus on the findings among Global Climate Models (GCMs), not only on the magnitude of change of the rainfall over the basin, but also on the sign of this change. This disagreement among the GCMs was evident in the fourth assessment report (AR4) of the Intergovernmental Panel on Climate Change (IPCC) and is still persistent in the new fifth assessment report (AR5) as shown in Figure 1.1 (Christensen et al. 2007, 2013).

The uncertainty regarding potential future changes in the flow of the Nile River as a result of climate change may add further stress to this critical situation. In addition, these changes

may affect the demand for, as well as operation and profitability of, the new hydropower projects in the basin. Thus, we need to estimate the magnitude of these changes in the flow and understand the mechanisms behind them in order to prepare the necessary adaptation plans.

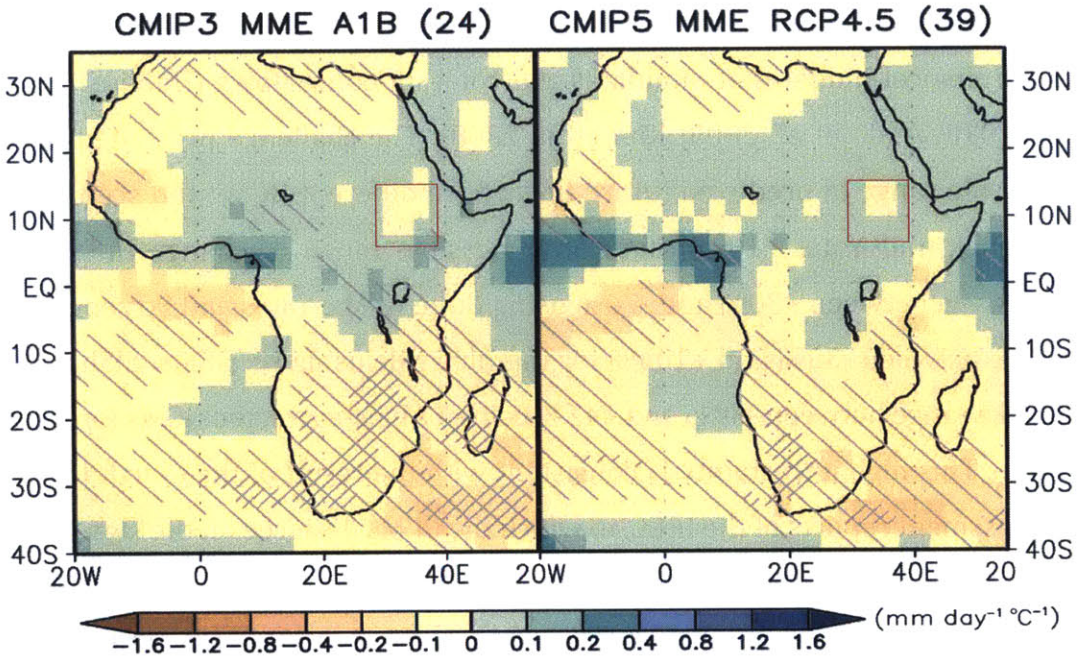


**Figure 1.1:** Maps of rainfall changes for Africa in 2080–2099 with respect to 1986–2005 in June to September in the SRES A1B scenario with 24 CMIP3 models (left), and in the RCP4.5 scenario with 39 CMIP5 models (right). Rainfall changes are normalized by the global annual mean surface air temperature changes in each scenario. Light hatching denotes where more than 66% of models have the same sign with the ensemble mean changes, while dense hatching denotes where more than 90% of models have the same sign with the ensemble mean changes. This figure is adapted from the IPCC-AR5 report, WG1-Chapter 14. The red boxes indicates the Eastern Nile basin region.

## 1.2 Background

Many studies attempted to identify the impacts of climate change on future flows in the Nile river using GCMs projections. The common approach among these studies was the use of statistical downscaling methods applied to rainfall and temperature simulated by the GCMs. These methods produce the same variables at a spatial resolution suitable for use with a calibrated hydrological model that simulates the corresponding flows (Booij et al. 2011; Beyene et al. 2010; Abdo et al. 2009; Kim et al. 2008). The challenge presented by these studies is the wide range of predicted future flows from different GCMs and scenarios. For example, Strzepek and Yates (1996) showed a possible range of change in Nile flows measured at Aswan between +30% and -70% using three GCMs. Yates and Strzepek (1998) showed a range between -35% and +104% for the Blue Nile using six GCMs. ElShamy et al. (2009) showed a range between -60% and +45% using 17 bias-corrected GCMs for the flows of the Blue Nile. This high uncertainty is consistent with the result of the fourth (AR4) and fifth (AR5) assessment reports of the IPCC, in which the GCMs disagree on the sign of change of the rainfall during the rainy season (June to August) as shown in Figure 1.1 (Christensen et al., 2007 and Christensen et al., 2013). Furthermore, these studies did not provide any explanation of the potential mechanisms behind these projected changes in the future flow.

An alternative approach for predicting the future changes in the flow of the Nile river emphasizes understanding of the mechanisms of the observed natural variability of the flow and to use this understanding in guiding predictions of the future flows. Several studies investigated the interannual variability in the flow of the Nile river (Eltahir 1996, Amarasekera et al., 1997, Abtew et al.,2009, Melesse et al., 2011, and ElSanabary et al., 2014). The interannual variability in the flow of the Nile River is strongly correlated with El Nino Southern Oscillation (ENSO). The warm phase of ENSO is associated with a reduced Nile flow. Eltahir (1996) determined that sea surface temperature (SST) anomalies over the tropical Eastern Pacific ocean could explain 25 % of the interannual variability of the Nile flow. This high correlation is the basis for many forecast models that are used to predict the Nile flow (e.g. Wang and Eltahir 1999; Eldaw et al. 2003). However, the mechanism behind this

interannual variability is not yet fully understood. Thus, an understanding of the mechanism of the relation between ENSO and the Nile flow is needed to predict future changes in the interannual variability of the flow in the Nile river.

Finally, the effects of complex topography on the hydrological cycle of the Nile basin are not easily captured by the typically coarse resolution (~200km) of GCMs. Thus, high-spatial-resolution simulations with regional climate model are needed to resolve the effects of topography on the hydrological cycle of this region. Here, several improvements in the large scale clouds and rainfall parametrizations are incorporated in the MIT regional climate model (MRCM), which enhanced simulation of the current climate of the basin. Then, the model was forced with future GCM simulations to predict the impact of climate change on the basin. The GCMs were carefully selected to avoid introducing biases in the regional model simulations.

In this thesis, we focus on the changes in the flow and rainfall over the Eastern Nile basin, which contributes by approximately 85% of the total Nile flow and includes the Upper Blue, the Atabra and Sobat basins. The White Nile is not investigated in this thesis as it has a low contribution to the total flow of the Nile (~15%) and the mechanisms that shape the rainfall and runoff over this region are different from the Eastern Nile basin. In addition, this thesis mainly focuses on the changes in the flow and the mechanisms that shapes these changes, the changes in the evaporation are not investigated as they are not the main focus of this thesis.

## 1.3 Thesis Structure

This thesis investigates the impacts of climate change on the flow of the Nile basin. First, it provides an explanation of the mechanism behind the teleconnection between Nile flow and ENSO. Second, it estimates the future changes in the mean and variability in the future flow of the Nile river using carefully selected GCMs and investigates the mechanisms behind these changes. Finally, an enhanced version of the MIT-Regional climate model (MRCM) is forced

with modified lateral boundary conditions that mimic the expected changes in the future to provide high resolution simulation of the future climate over the basin. The thesis structure is organized as follows:

Chapter 2 investigates the teleconnection between the Nile flow and ENSO and its role in shaping the interannual variability of the flow in the Nile river.

Chapter 3 includes an evaluation of the GCMs and reanalysis data based on atmospheric and soil water balance and investigates the effect of spatial resolution on the simulations of the hydrological cycle over the Upper Blue Nile basin.

Chapter 4 investigates the changes in interannual variability of future Nile flow and the mechanisms behind these changes due to climate change.

Chapter 5 presents the new model developments and modifications in the MIT-Regional Climate Model (MRCM) which were introduced to accurately simulate the climate of the Nile basin.

Chapter 6 analyzes simulations from CMIP5 GCMs and investigates the mechanisms of potential changes in the long-term mean of Nile flow. It also includes future simulations using the modified version of MRCM with modified lateral boundary conditions and greenhouse gas concentrations assumed to describe mimic the future conditions.

Chapter 7 investigates the runoff elasticity to rainfall over the Upper Blue Nile basin using observations of streamflow and rainfall and from GCMs simulations

Chapter 8 summarizes the conclusions of this thesis and provides recommendations for future studies.

# Chapter 2: Mechanism of the Interannual Variability in the Flow of Nile River

The interannual variability in the flow of the Nile river is shaped to a significant degree by El Nino Southern Oscillation (ENSO). However, the mechanism describing the teleconnection between the Nile flow and ENSO is not yet fully understood. Thus, it is important to understand the mechanism behind this teleconnection as it might also shape the interannual variability of the future flow in Nile river. In this chapter, the mechanism of this teleconnection is investigated and in particular the role of Indian ocean in shaping this teleconnection.

## 2.1 Introduction

The interannual variability in the flow of the Nile river is strongly correlated with the El Niño Southern Oscillation (ENSO), its warm phase being associated with a reduced Nile flow. Eltahir (1996) determined that sea surface temperature (SST) anomalies over the tropical Eastern Pacific Ocean could explain 25% of the interannual variability of the Nile flow. This high correlation is the basis for forecast models that are used to predict the Nile flow (e.g. Wang and Eltahir, 1999; Eldaw et al., 2003). However, the mechanism behind the teleconnection between the Nile flow and ENSO is not yet fully understood.

The connection between El Niño events and the rainfall over East Africa was investigated in several studies (e.g. Bertlando and Camberlin, 1993; Black et al., 2003). However, a clear distinction must be made between rainfall over the Upper Blue Nile (UBN) basin shown in Figure 2.1 and rainfall over East Africa, along the East coast and Horn of Africa but away from the Ethiopian highlands. The mechanism that connects rainfall over these regions to ENSO is different from the corresponding mechanism in the UBN basin. The UBN basin has one rainy season period (May to September) during which more than 80% of its rainfall occurs, while

along the East coast of Africa, and depending on the location from the equator, the seasonal cycle of rainfall has two rainy seasons (Black et al., 2003; Hastenrath et al., 2011). This pattern in the seasonal cycle is related to the migration of the Intertropical Convergence Zone (ITCZ) across the equator over these regions. In addition, the warm phase of ENSO is positively correlated to rainfall during the short rainy season (October to December) over East Africa (Mutai and Ward, 2000), while it is not correlated to rainfall during the long rainy season in March to June (Pohl and Camberlin, 2006).

The rainfall over the UBN in (May to September) season is negatively correlated to ENSO. Rainfall over East Africa and the UBN basin are significantly coupled to the intensity of the Indian monsoon (Camberlin, 1995). During El Niño events, the monsoon circulation is weaker due to its modulation of the Walker circulation and the enhanced subsidence over West Pacific and South Asia (Shukla and Wallace, 1983; Ju and Slingo, 1995; Soman and Slingo, 1997 and Kawamura, 1998). Camberlin (1997) suggested that during strong Indian monsoon seasons, sea level pressure over India decreases significantly, which enhances the pressure gradient between East Africa and India, thus increasing the westerly winds that advect moisture from the Congo basin to Ethiopia, Uganda and western Kenya. Amarasekera et al. (1997) hypothesized that the reduced Nile flow during El Niño events is due to the enhanced subsidence that suppresses rainfall as a consequence of the increased upwelling over the Eastern Pacific ocean. In the nearby region of the Sahel, Giannini et al. (2003) suggested that a warming of the Indian and Atlantic Oceans leads to a reduction in rainfall by enhancing convection over ocean and by decreasing convergence of air over land. Zaroug et al., 2014a also investigated the interannual variability in the flow of the Upper Blue Nile flow and its connection with ENSO. They showed that when El Nino event is followed by La Nina event, there is a 67% chance for the occurrence of extreme flood in the Upper Blue Nile basin, although the mechanism behind this phenomenon was not investigated. Zaroug et al., 2014b were able to simulate the connection between the Upper Blue Nile flow and ENSO using tropical-band version of the regional climate model version 4 (Regcm4). Their simulations showed low rainfall over the Upper Nile basin during El Nino, but they did not also investigated the mechanism behind the connection between Nile flow and ENSO.

The main aim of this chapter is to investigate the mechanism of the teleconnection between ENSO and Nile flow and the role of Indian Ocean SSTs in affecting this teleconnection.

## 2.2 Description of Data used

The data used in this study consist of observations of river flow and global SST distribution together with reanalysis products that provide information on the atmospheric circulation. The longest recorded and most accurate hydrological variable that can be considered in this study is the measured stream flow at Dongola (Figure 2.1b), referred hereafter as the Nile flow, which can be used as an index of rainfall over the Upper Blue Nile in Ethiopia. The flow at Dongola peaks during the summer (Figure 2.2), mainly from July to October as a result of the rainfall over the Upper Blue Nile, Atbara and Sobat basins during the summer. The Upper Blue Nile provides almost 60% of the annual mean Nile flow at Dongola, while the Sobat and Atabara rivers (Figure 2.1b) provide each around 10%. Thus, the signature of the Upper Blue Nile flow on the Nile flow is dominant. Moreover, more than 80% of the JJASO (June-October) mean Nile flow at Dongola is a result of the summer rainfall over the Upper Blue Nile. The other 20% of the JJASO (June-October) mean Nile flow is mainly from the Sobat and Atbara basins. More importantly, the flow in the Blue Nile explains almost 80% of the interannual variability in the flow of the Nile river at Dongola (Figure 2.3). The monthly mean flow data at Dongola were extracted from the Global River Discharge Database (RivDIS v1.1) for the period 1871-2000 (Vörösmarty et al., 1998).

The SST data were extracted from the global monthly mean (HadISST V1.1) dataset, available on a 1-degree latitude-longitude grid from 1871 to 2000 (Rayner et al. 2003). Monthly anomalies of the SSTs were averaged over three Eastern Pacific Ocean regions (2°N-6°N, 170°W-90°W; 6°S-2°N, 180°W-90°W; 10°S-6°S, 150°W-110°W) and used as ENSO indices. These regions have the highest correlations with the mean Nile flow and cover the same areas as the Niño 3 and 3.4 indices (Trenberth, 1997). In addition, monthly anomalies of SSTs were averaged over two different regions in the Indian Ocean. These regions are defined hereafter as the North of Equator Indian ocean (0-15°N, 50°E-70°E) and the South of Equator

Indian ocean (10 °S-0, 50°E-70°E). Also, these regions exhibit the highest correlations with the Nile flow, compared to other regions of the Indian ocean.

The variables considered to study the atmospheric circulation in response to changes in SST include zonal and meridional wind speed components on pressure levels. These are obtained from the ERA-Interim (ERAI) reanalysis product for the period 1979-2010 (Dee et al., 2011). ERAI was chosen among other reanalysis products because it has the most accurate representation of the hydrological cycle over the UBN basin (Siam et al., 2013) and wind circulation over Africa compared to other reanalysis products such as ERA40 (Uppala et al., 2005) or NCEP-NCAR (Kalnay et al., 1996).

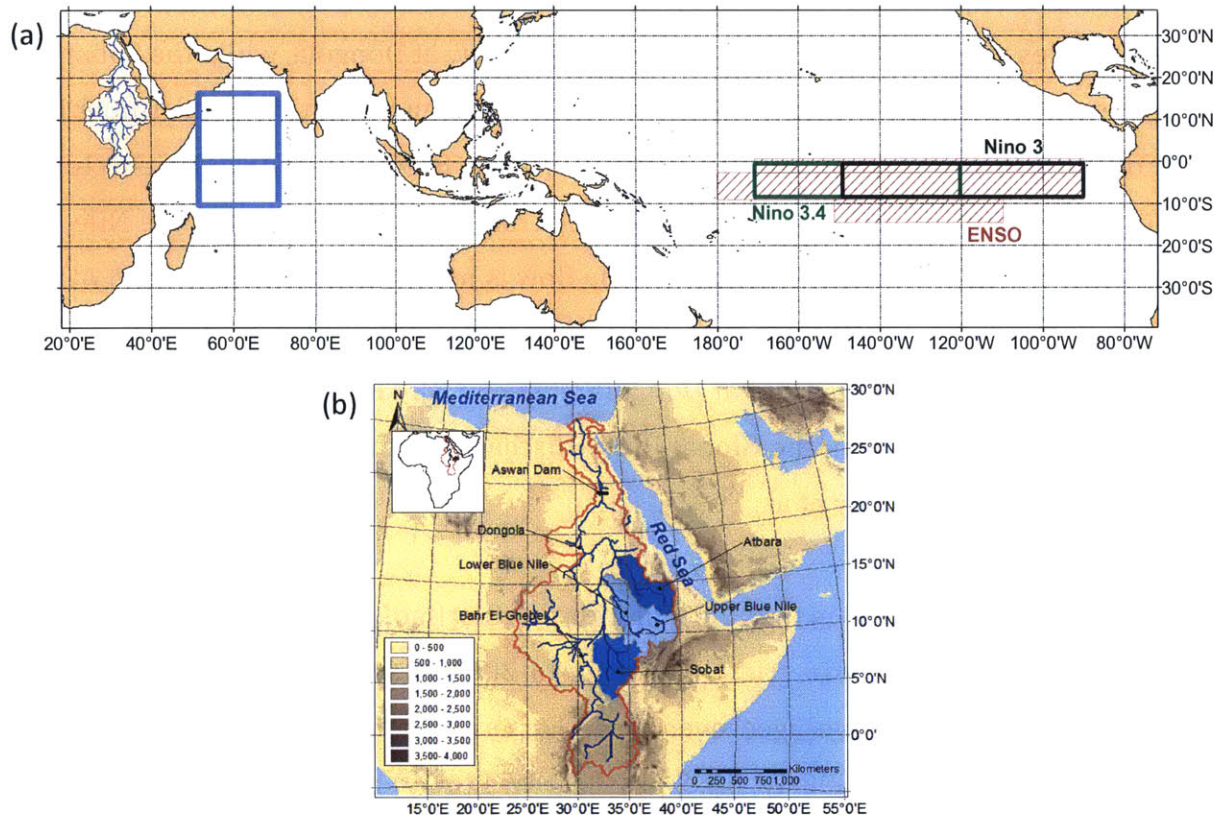


**Figure 2. 1:** (a) Map of the Indian and Pacific oceans showing the region used to define ENSO index (hatched in red) and the North and South of equator regions (blue boxes) over the Indian ocean, (b)Topographic map of the Nile basin showing the main sub-basins of the Nile (i.e. Atbara, Upper Blue Nile (UBN) and Sobat). The Nino 3 are Nino 3.4 regions are enclosed by the black and green boxes respectively.

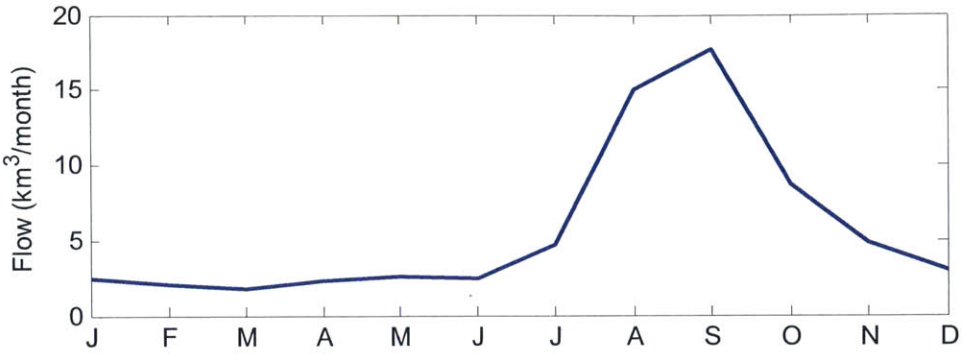


**Figure 2.2:** Average Seasonal cycle of the observed streamflow at Dongola for the period (1900-2000).

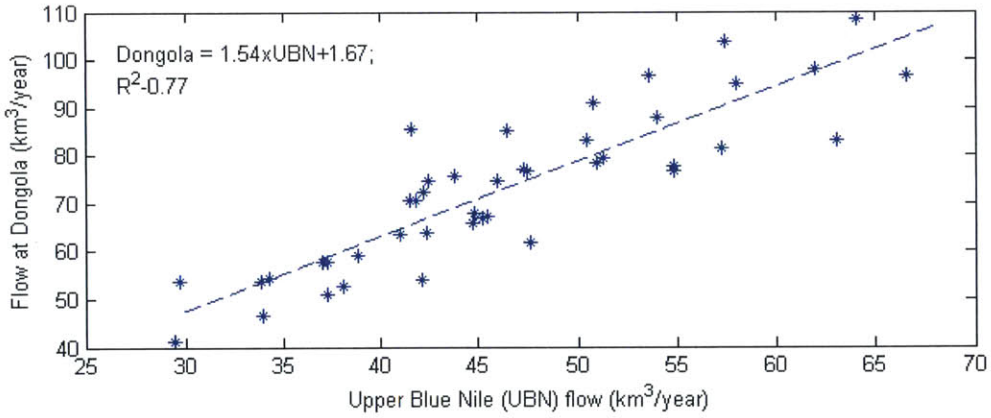


**Figure 2.3:** Relation between the annual average flow of the Upper Blue Nile basin and flow at Dongola for the period (1965-2010).

## 2.3 Observational Analyses of the relationships between Nile flow and SSTs in Indian and Pacific Oceans

### 2.3.1 Cross-correlation analyses

In this section, a detailed analysis of correlations between SSTs over the Indian and Pacific Oceans and the Nile flow is presented to document the connection between ENSO and the Nile flow. In addition, the cross-correlation analysis is used to investigate the connection between the Nile flow and SST over the Indian Ocean. From July to October, tropical Eastern Pacific SSTs show a persistent and significant negative correlation with the JASO (July-October) mean Nile flow for the period (1871-2000) as illustrated in Figures 2.4a to 2.4d. Figures 2.5a to 2.5d show the correlation between SON (September-November) ENSO index and the global SST distributions in July, August September, and October. The comparison between Figures 2.4 and 2.5 reveals that the correlation between the Nile flow and the global SSTs seems to reflect the correlation between ENSO and those SSTs.

In order to estimate the highest correlation between the Nile flow and ENSO, Figure 2.6 shows the correlation between the ENSO index, considered separately for each month of the year, and the mean Nile flow over several months of the rainy season (JJAS: June-September, JASO: July-October, ASON: August-November). The JASO mean Nile flow has the highest negative correlation with ENSO index, especially during the months of September to November. This result may be explained as due to the fact that all the Nile flow from July to October is necessary to consider in order to capture all the variability in the rainfall over Ethiopia during the entire rainy season from June to September and the signal of ENSO is the strongest during September to November (Wang and Eltahir, 1999).

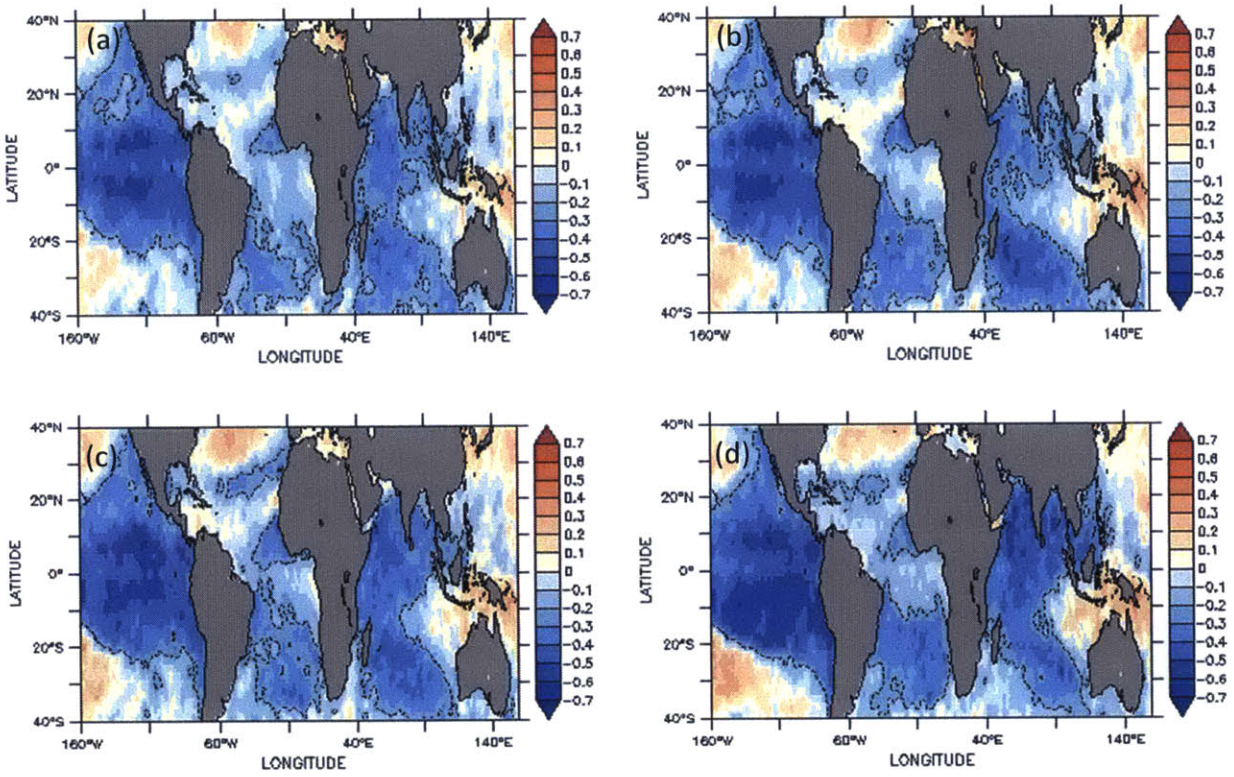


**Figure 2. 4:** Correlations for the period (1871- 2000) between average Nile flow during (July to October) and average monthly SST: a) July, b) August, c) September and d) October. The 1% significance level of the correlation is -0.23 and shown using the black dashed contour line.

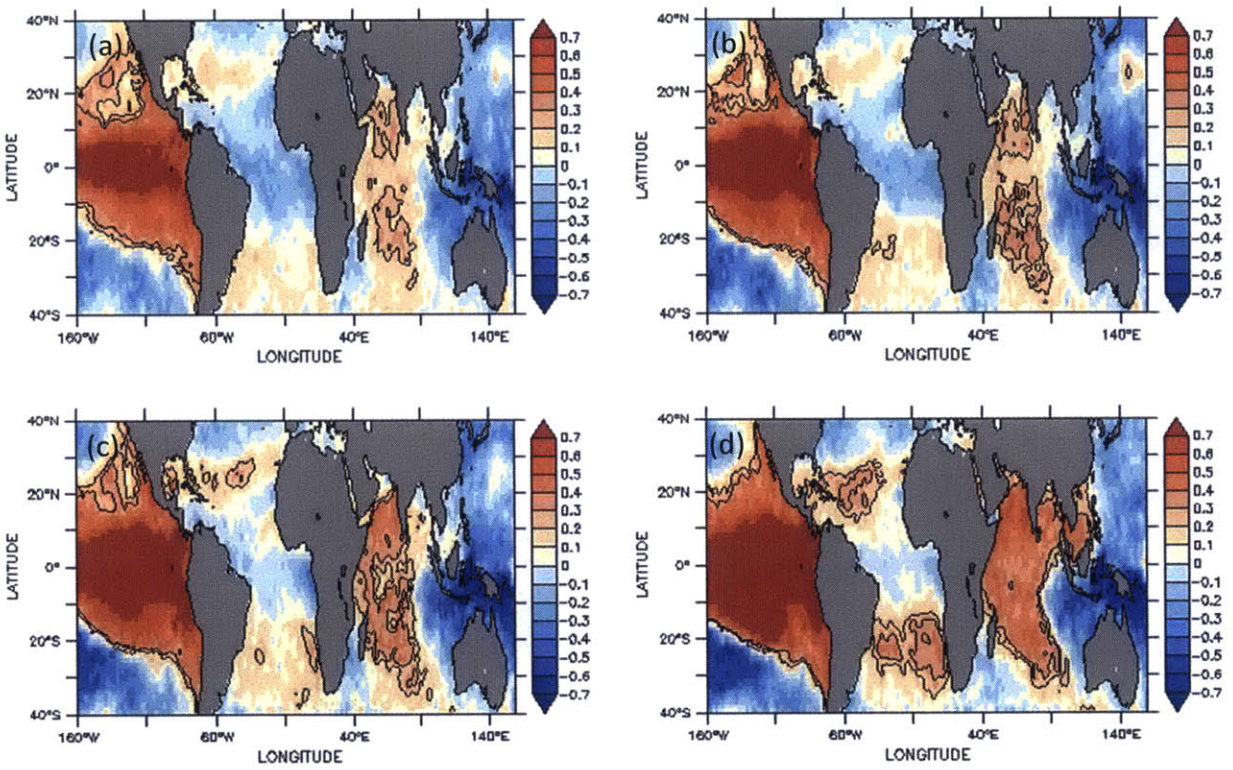


**Figure 2. 5:** Correlations for the period (1871- 2000) between average ENSO index during (September to November) and average monthly SST: a) July, b) August, c) September and d) October. The 1% significance level of the correlation is 0.23 and shown using the black contour line.

The correlation analysis is repeated between the Nile flow averaged for JASO and monthly SSTs averaged over two different regions in the Indian Ocean: North of Equator Indian ocean and South of Equator Indian ocean (defined in section 2.2). The SST is considered separately for each month of the year. The JASO mean Nile flow is negatively correlated with North and South of equator Indian ocean SSTs from September to December (Figure 2.7). This period of high negative correlation lags by approximately one month the high correlation found between the JASO mean Nile flow and monthly ENSO index (blue line of Figure 2.6). This lag is consistent with the lag estimated in the cross correlation analysis between the monthly Nile flow and the monthly SSTs in Indian Ocean where the peak of the correlation occurs at a lag of approximately 2 to 3 months while with a similar lag is estimated with the ENSO index of about 2 months as shown in Figure 2.8a. The lagged anti-correlation between the Nile flow and the Indian Ocean SSTs compared to ENSO is explained by the fact that North and South of Equator Indian ocean SSTs respond to ENSO (Figure 2.8b; Nicholson, 1997; Cole et al, 2013). This lag is consistent with the time required for the warm water to travel from the Pacific to the Indian Ocean through the "Indonesian through flow" and advection by the Indian Equatorial Current (Tomczak and Godfrey, 1995). Measurements of the surface current velocity gave an estimate along this region of the magnitude of 50 cm/s (Fieux, et al. 1994). Thus, considering a rough length scale from the western Pacific Ocean to the northern region of the Indian Ocean along the path of the "Indonesian Throughflow" and dividing this length scale by the surface current velocity of 50 cm/s, this will yield a time scale of 2 to 3 months.

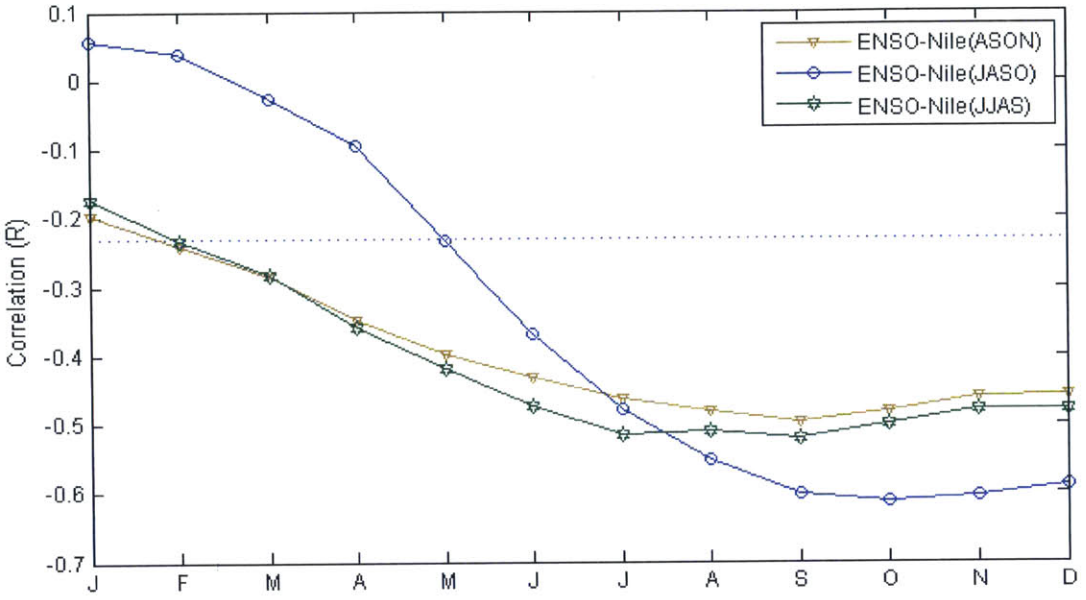


**Figure 2. 6:** Correlation between the monthly ENSO index and the average Nile flows during July to October (JASO), June to September (JJAS) and August to November (ASON) for 1871 to 2000. The dashed line represents the 1% significance level of the correlation.

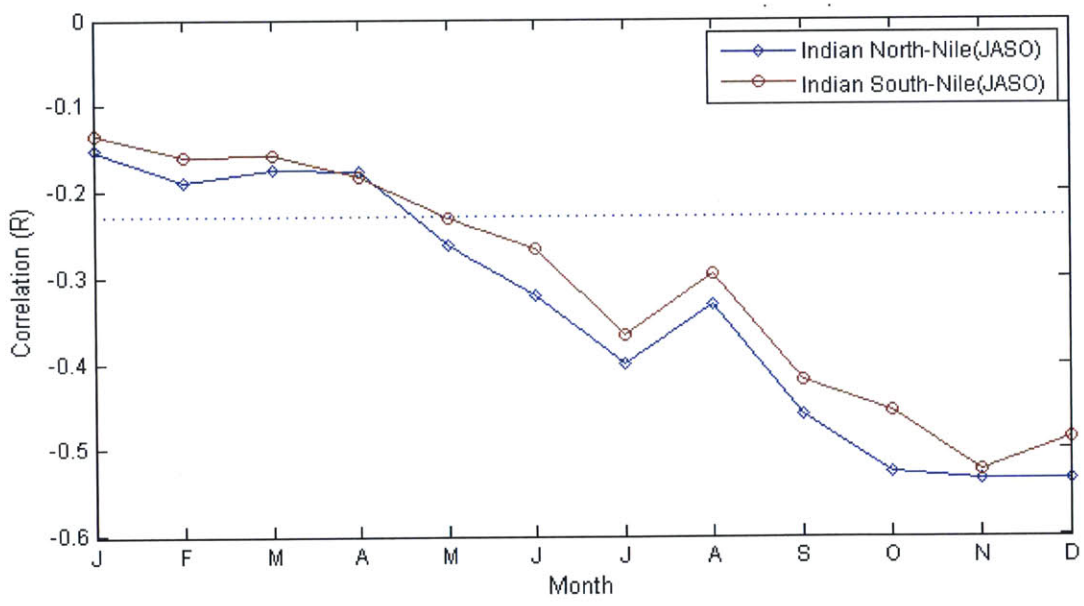


**Figure 2. 7:** Correlation between the monthly Indian Ocean North and South of equator SSTs and the average Nile flows during July to October (JASO) for 1871 to 2000. The dashed line represents the 1% significance level of the correlation.

The cross-correlation in Figure 2.8a should be interpreted with caution. The cross-correlation analysis needs continuous time series, while most of the annual flow in the Nile occurs during the rainy season from June to October. It is unavoidable that the use of the whole monthly flow time series (including the winter season) suppresses the magnitude of the cross-correlation, and results in an apparently lower cross-correlation coefficient. However, these results can still be used to support qualitative reasoning. Figure 2.8a shows the peak of the cross-correlation between Nile flow and Indian Ocean SSTs occurs one month later than the corresponding peak between the Nile flow and ENSO. This result indicates that the North and South of equator Indian ocean SSTs are strongly linked to ENSO, which reveals that any indices based on the North and South of equator Indian ocean SST cannot be used independently from the ENSO index to predict the Nile flow, which will be illustrated further in the next section.

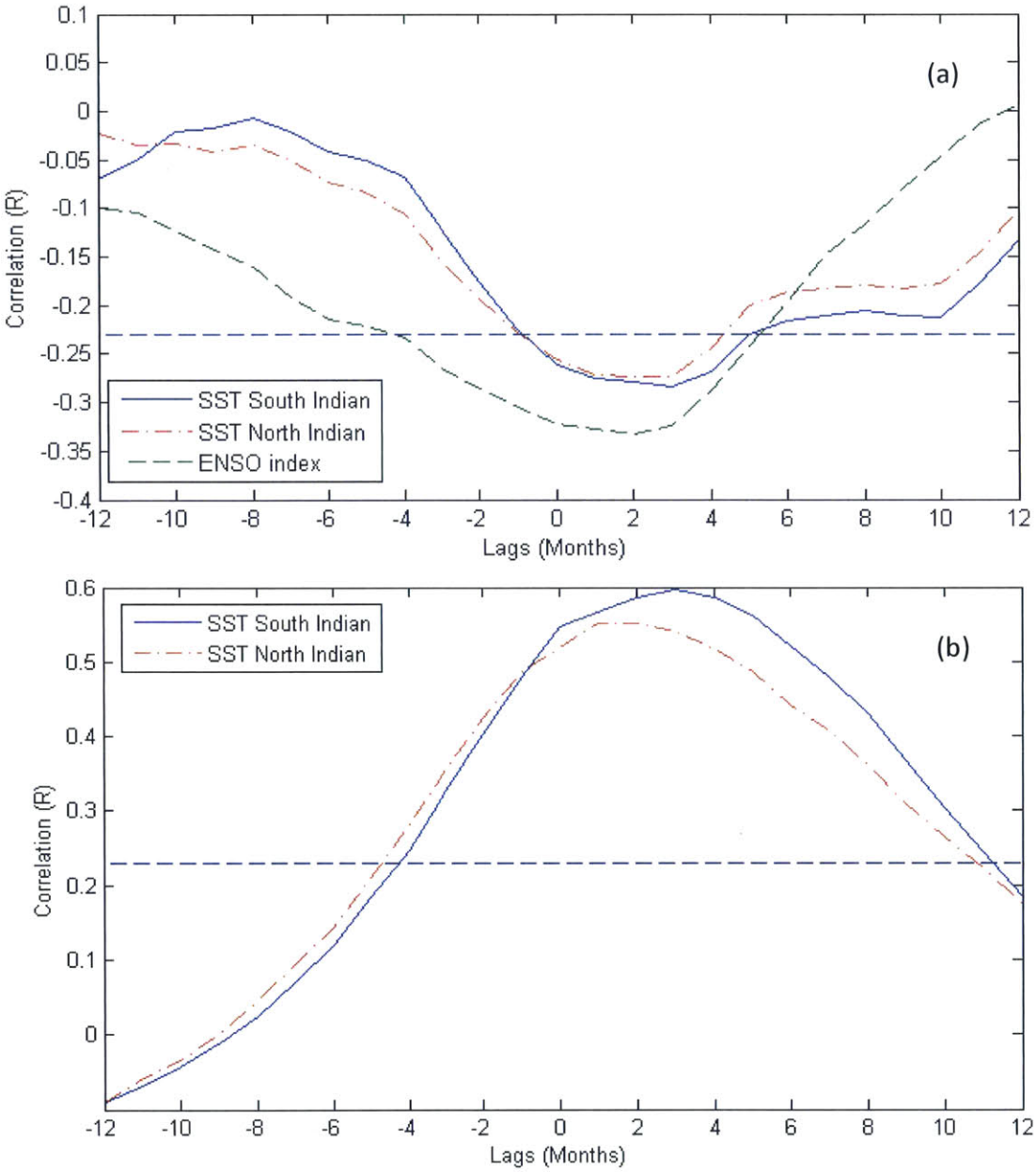


**Figure 2. 8:** a) Cross Correlation between the monthly SSTs in the North and South of the equator Indian Ocean and ENSO index with the monthly Nile flows. b) Cross Correlation between the monthly SSTs in the North and South of the equator Indian Ocean and the monthly ENSO index for 1871 to 2000. The dashed straight lines represent the 1% significance level of the correlation.

### 2.3.2 Partial Coherency analysis

The dependence of the Nile flow on SSTs in the Indian and Pacific Oceans is analysed in this section using partial coherency analysis. "Partial coherency" represents a generalization of the concept of partial correlation coefficient. Partial correlation analysis focuses on the relationship between two variables in the presence of a third variable (Jobson, 1991). It quantifies the correlation between these two variables after evaluating the impact of the third variable. In this study, the two variables are the Nile flow and Indian ocean SSTs, and the third variable is the ENSO index. The partial correlation coefficient quantifies how much of the Nile flow variability, which cannot be explained by ENSO, is explained by Indian ocean SSTs. However, the partial correlation coefficient does not show how this correlation is distributed over different frequencies. Here, we apply the partial coherency analysis, which describes how the partial correlation is distributed among different frequencies. By "partial coherency", we mean the cross-coherency between Indian ocean SSTs and the portion of the Nile flow variability that cannot be explained by ENSO.

The ENSO spectrum, calculated from monthly anomalies, depicts a peak at a time scale of almost 50 months (about 4 years; Figure 2.9a). The squared coherency spectrum, also calculated from monthly anomalies, shows a high coherency between ENSO and North and South of equator Indian ocean SSTs at the same time scale of 50 months (Figure 2.9b).

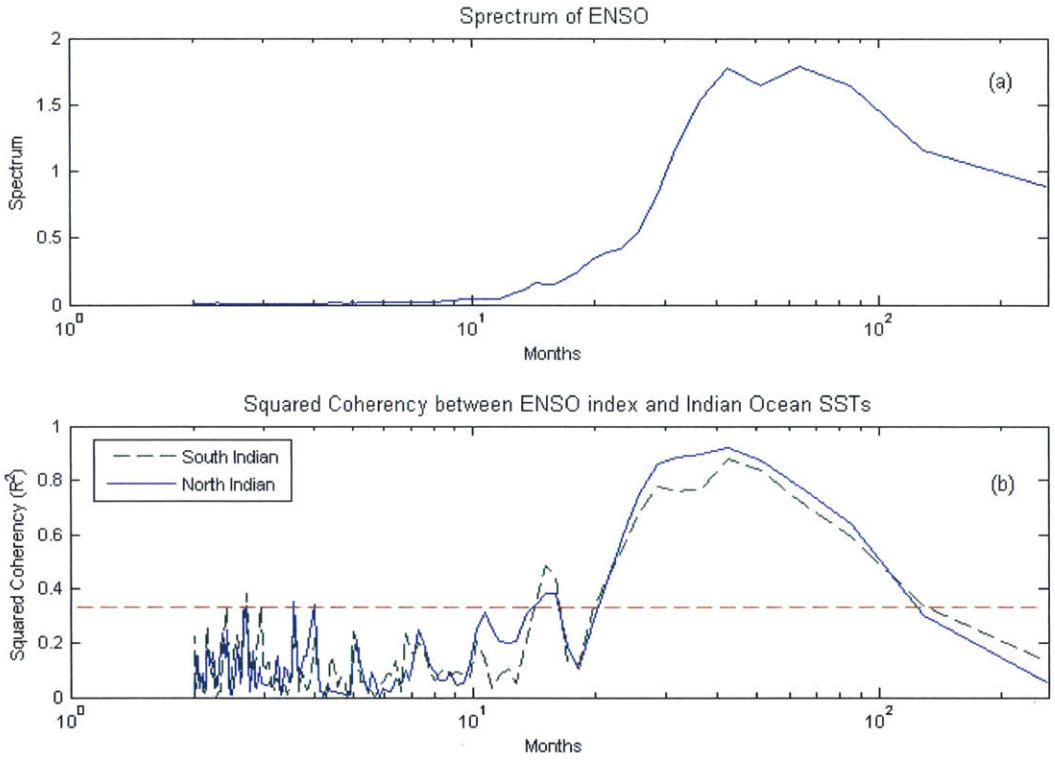


**Figure 2. 9:** a) Spectrum of ENSO, b) squared coherency between ENSO and SSTS in the North and South of the equator Indian Ocean for 1871 to 2000. The straight dashed line represents the 1% significance level of the coherency that is estimated using Equation (4.101) in Shumway and Stoffer (2010), where the significant coherency (C) at a particular significance level ($\alpha$) is equal to: $C = \frac{F_{df-2}(\alpha)}{\frac{df}{2}-1+F_{df-2}(\alpha)}$, and df is the degree of freedom of the F-distribution.

To verify that Indian Ocean SSTs cannot explain any additional variability of the Nile flow, we use the partial coherency analysis as described above but this time between the Nile flow and ENSO and Indian ocean SSTs. First, we perform 12 linear regressions from January to December between the monthly-mean Nile flow and the monthly-mean ENSO index (u) months earlier, where (u) denotes the possible lag between ENSO and the Nile flow. The linear regressions depend on the time lag (u) according to:

$$R_{new}(i) = a(i) \times E(i-u) + b(i) \qquad (2.1)$$

$R_{new}$ (i) is the predicted Nile flow for a specific month (i) where i=1 to 12, and E(i-u) is the ENSO index (u) months earlier than month (i). Accordingly, a(i) and b(i) are also functions of (u).

The Nile flow residuals that are not explained by ENSO are estimated by:

$$R(i, j)=R_{obs}(i, j) - R_{new}(i, j) \qquad (2.2)$$

$R_{obs}$ (i, j) is the observed Nile flow index in month (i) of year (j), $R_{new}$ (i, j) is the predicted flow in year (j). The new time series describing the flow residual R(i, j) contains the part of the Nile flow variability that cannot be explained by ENSO. The partial coherency is the squared coherency between the time series of the residual flow and the Indian Ocean SSTs. Because of the dependence of the flow residual on time lag (u) between the Nile flow and ENSO, the partial coherency also depends on (u), but the results indicate that the partial coherency estimates are not sensitive to the change of the time lag. Therefore, the difference between the partial coherences for u=-2, -1, 0, 1, 2 is negligible.

Figure 2.10 shows the normal and partial coherency spectrum between the Nile flow and Indian Ocean SSTs. The normal coherency between North and South of equator Indian ocean SSTs and the Nile flow peaks at the time scale of 50 months (solid lines; bottom panels of Figure 2.10), which is similar to the squared coherency between ENSO and the Nile flow (top left panel). However, the partial coherency is almost zero at the position of this peak (dashed lines).

These results are consistent with the conclusion that at the 4-year time scale, North and South of equator Indian ocean SSTs cannot explain variability in the Nile river flow that is not already explained by ENSO. Furthermore, the peak of the normal coherency at the time scale of 4 years can indeed only be explained by a response of North and South of equator Indian ocean SSTs to ENSO that leads to a response in the Nile flow.

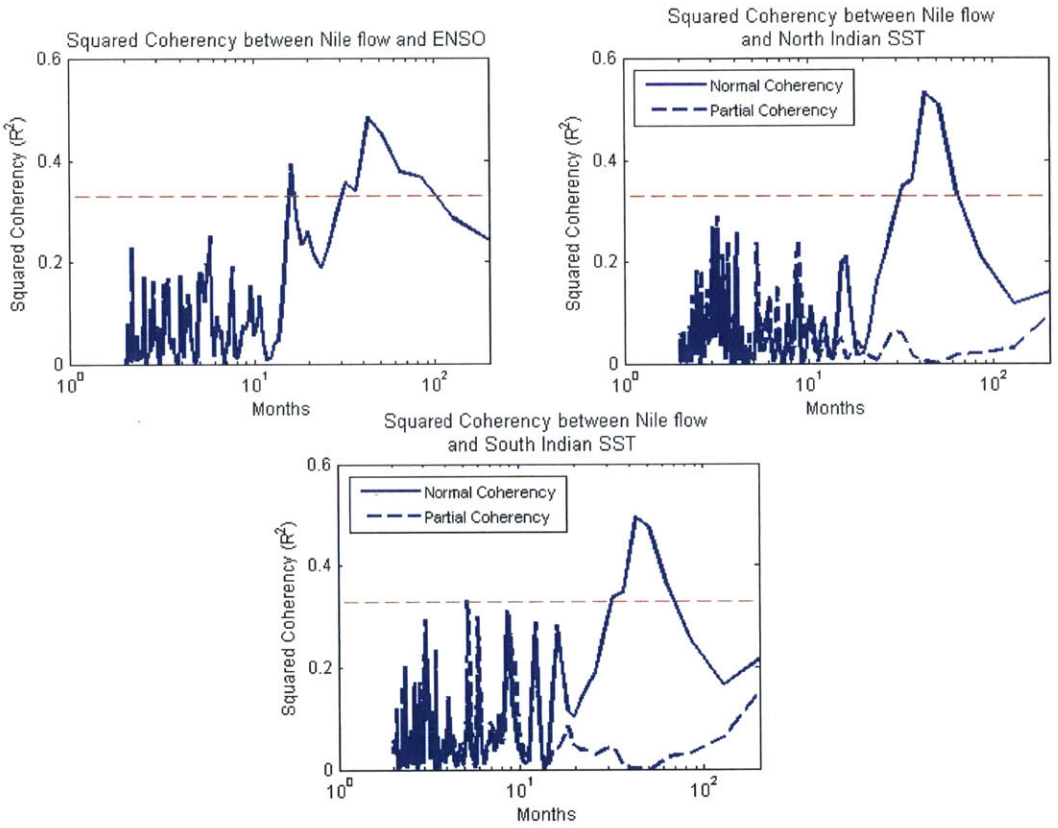


**Figure 2.10:** Squared Coherency between the Nile flows and SSTs in the Pacific (ENSO index) and North and South of equator Indian Ocean for 1871 to 2000. The straight dashed lines represent the 1% significance level of the coherency that is estimated using Equation (4.101) in Shumway and Stoffer (2010), where the significant coherency (C) at a particular significance level ($\alpha$) **is equal to**: $C = \frac{F_{df-2}(\alpha)}{\frac{df}{2}-1+F_{df-2}(\alpha)}$, and df is the degree of freedom of the F-distribution.

## 2.4 Mechanism relating the Indian Ocean SSTs and UBN flow

It is shown in the previous section that the Nile river flow is moderately correlated with the SSTs in the Indian Ocean. Furthermore, it is shown that the SSTs in the North and South of equator Indian Ocean respond to the warming in the Pacific. In this section, a mechanism that explains these teleconnections between ENSO, Indian Ocean SSTs and Nile flow is proposed.

Figure 2.11 shows the ERAI averaged wind at 800 mb during August 1979-2011. The wind circulation is mainly composed of a main anticyclonic circulation around the equator, which is associated with low level westerly winds that forces divergence of air away from the UBN.

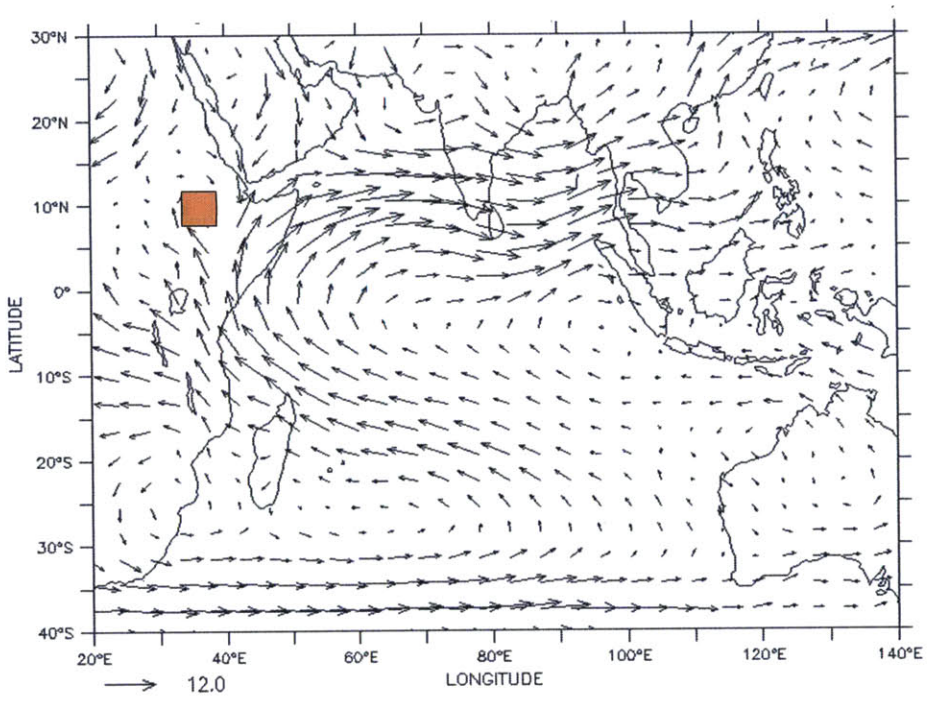


**Figure 2. 11:** Average wind circulation during August (1979-2011) at 800 mb using ERA-Interim reanalysis product. The UBN basin (shaded in brown).

The intensity of the anticyclonic circulation is reflected in the magnitude of the relative vorticity: strong westerly low-level flows correspond to high values of relative vorticity over the North Indian Ocean. It is important to notice that the sign of vorticity in the North of Indian Ocean is negative (clockwise) (Figure 2.11). The correlation between relative vorticity at 700 mb and convergence of air in the lowest 300 mb over the UBN basin in July is shown on Figure 2.12a, and that for August is shown on Figure 2.13a. The highest correlation exists over the North and South of equator Indian Ocean; the positive sign of the correlation indicates that an increase in convergence of air over the UBN is associated with weaker vorticity over North Indian Ocean (i.e. the westerly winds have a smaller magnitude).

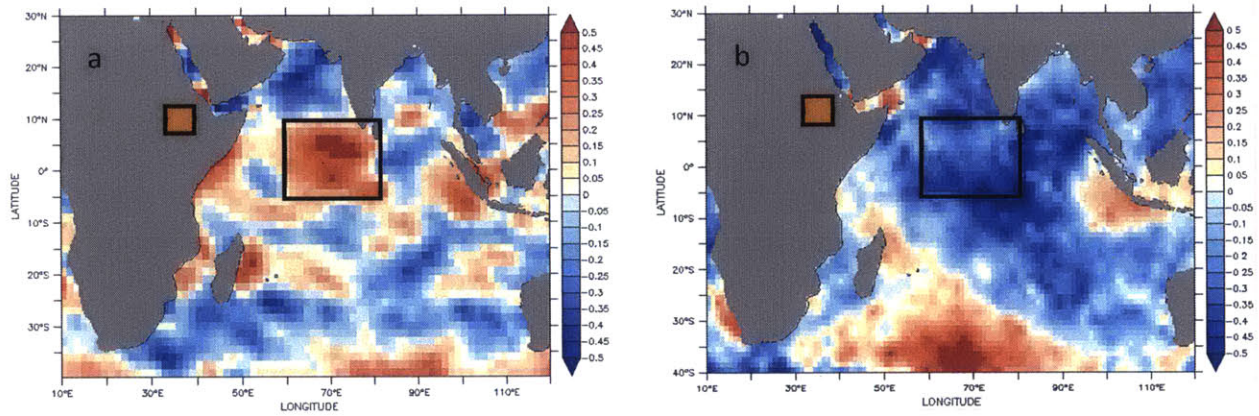


**Figure 2. 12:** (a) Correlation between the relative vorticity at 700 mb over the Indian Ocean and averaged convergence of air in the lowest 300 mb over the UBN basin (shaded in brown) during July, and b) Correlation between average relative vorticity over (60°E-80°E and 5°S-10°N) and SSTs in the Indian Ocean during July.

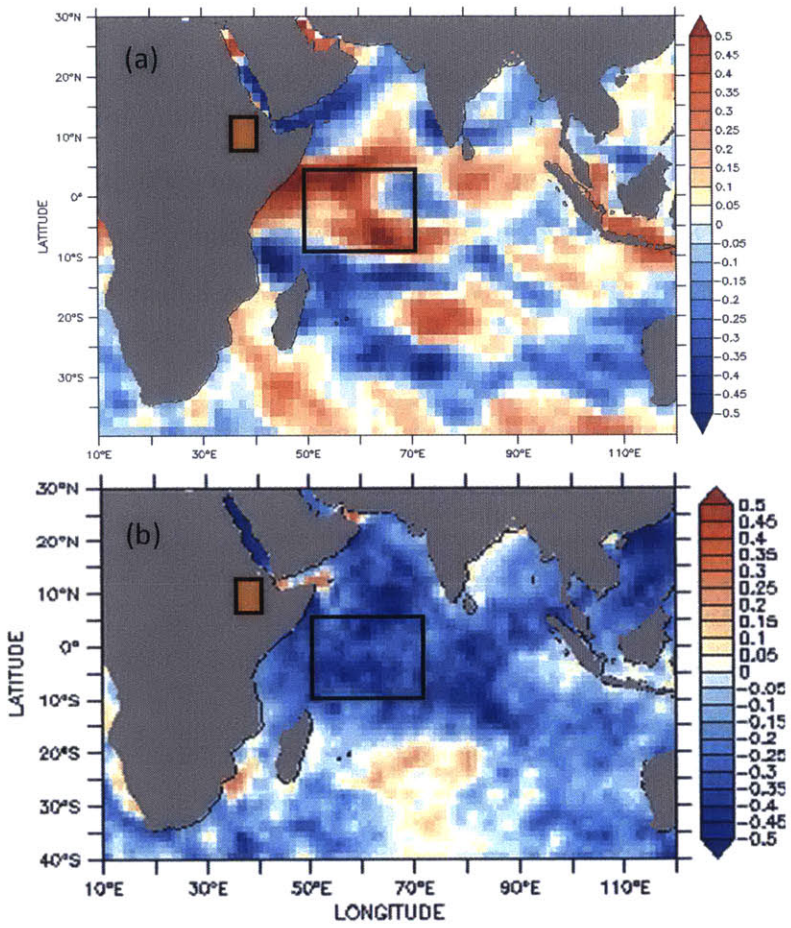


**Figure 2. 13**: (a) Correlation between the relative vorticity at 700 mb over the Indian Ocean and averaged convergence of air in the lowest 300 mb over the UBN basin (shaded in brown) during August and b) Correlation between average relative vorticity over (50°E-70°E a and 5°N-10°S) and SSTs in the Indian Ocean during August.

The magnitude of the relative vorticity is negatively correlated with SSTs in both July (Figure 2.12b) and August (Figure 2.13b). Thus, warming around the equator of the Indian Ocean enhances the anticyclonic circulation by inducing westerly winds over the North Indian Ocean. The anomalous westerlies are induced following a Matsuno-Gill circulation forced by an increase in SSTs around the equator, particularly during El Niño years. The Matsuno-Gill circulation pattern responds to an increase in the Indian ocean SSTs in July and August. Vizy and Cook (2003) and Yang et al. (2007) also showed the same response of the increased low level westerly winds over the Western Indian Ocean due to warming over the Indian Ocean.

Figure 2.14 shows the same results but using composite analysis of the difference in circulation between the four warmest minus the four coldest SSTs over the North Indian Ocean during August. Four events are chosen because they almost represent 10% of the available events (35 events), which makes each analysis include almost 20% of the available data (i.e. 10% warmest and 10% coldest events). Figure 2.14 shows the increased westerly winds over the North Indian Ocean due to the warming, which reduces the convergence of air of the UBN basin and hence the rainfall as will be shown in the following analysis.

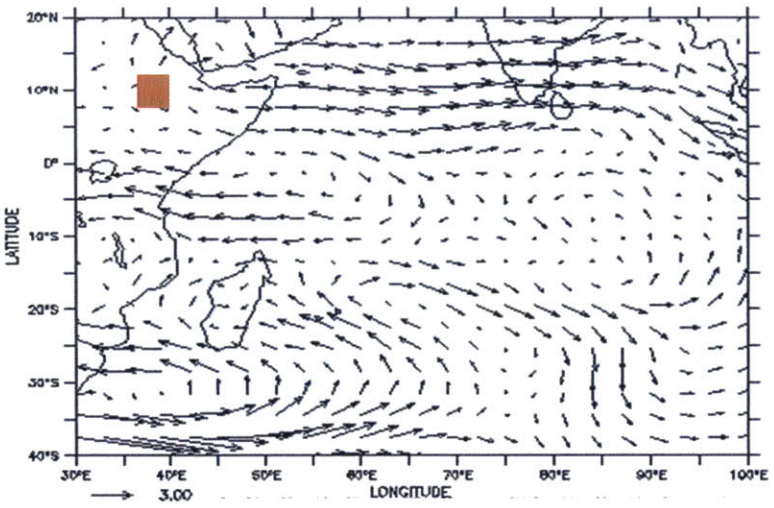


**Figure 2. 14:** Average wind circulation using ERA-Interim reanalysis for the lowest 300 mb from the surface during August for: a) warm years minus cold years over the North Indian Ocean. The UBN basin is shaded in brown.

Figure 2.15 shows the long-term averages of rainfall and SST over the Indian Ocean during July and August. The comparison between SSTs and rainfall figures shows that the 2 mm/day threshold of rainfall almost coincides with the 26°C contour lines of the SSTs. It also shows that the western tropical Indian Ocean has low SSTs and rainfall rates (i.e. lower than the above mentioned thresholds). Thus, the changes of SSTs over this region may induce changes in the rainfall in the surrounding regions including the UBN as will be in the next part.

The relation between the SSTs and rainfall over the Indian Ocean is presented in Figure 2.16. The SSTs from HadISST and rainfall from the GPCP are both interpolated to a common grid of $2^{o}x2^{o}$ degrees. Each point in figure 2.16 represents the relation between the long-term averages of the SST and rainfall over the same grid. This relation is very well fitted with power equations between the two variables, which indicated that the increase of the SSTs is associated with an increase in rainfall. This can be explained as the increase of the SSTs leads to an increase in the moist static energy over the lower layers of the atmosphere, which favours convection and hence increase the rainfall (Roxy and Tanimoto, 2007).

Figures 2.15c and 2.15d show the difference between the four warmest and four coldest SSTs events over the North Indian Ocean. The figures show that the warming is spread over most of the Indian Ocean and is slightly higher along the East coast of Africa and the Arabian Sea region. However, most of the anomalous increase in the rainfall is seen over the tropical Indian Ocean. This can be explained as the SSTs over the tropical Indian Ocean are originally higher than the Western part of the Ocean and above the $27^{o}C$ threshold needed to have significant rainfall rates (i.e. greater than 2 mm/day) as shown in Figure 2.16. The $27^{o}C$ limit is close to the observations of Williams and Renno (1993) who found that the SST over the ocean should be greater than $26^{o}C$ to enhance the Convective Available Potential Energy (CAPE) and substantially increases the rainfall. The rainfall during July and August also show a decrease in the rainfall to west of the increase and including parts of the Eastern Nile basin. However, the moisture content in the air is higher during warm events (Figure 2.17b). Thus, the reduction of the rainfall west of the increase can be attributed to the subsidence by the downward motion of air, which follows the enhanced westerly low flow, as shown in Figure 2.17b. This figure also shows an increase of vertical upward motion over the region of increased rainfall and SSTs in the Indian Ocean. These results are consistent with the previous analysis focusing on the relative vorticity and the results in the next section using climate model simulations.

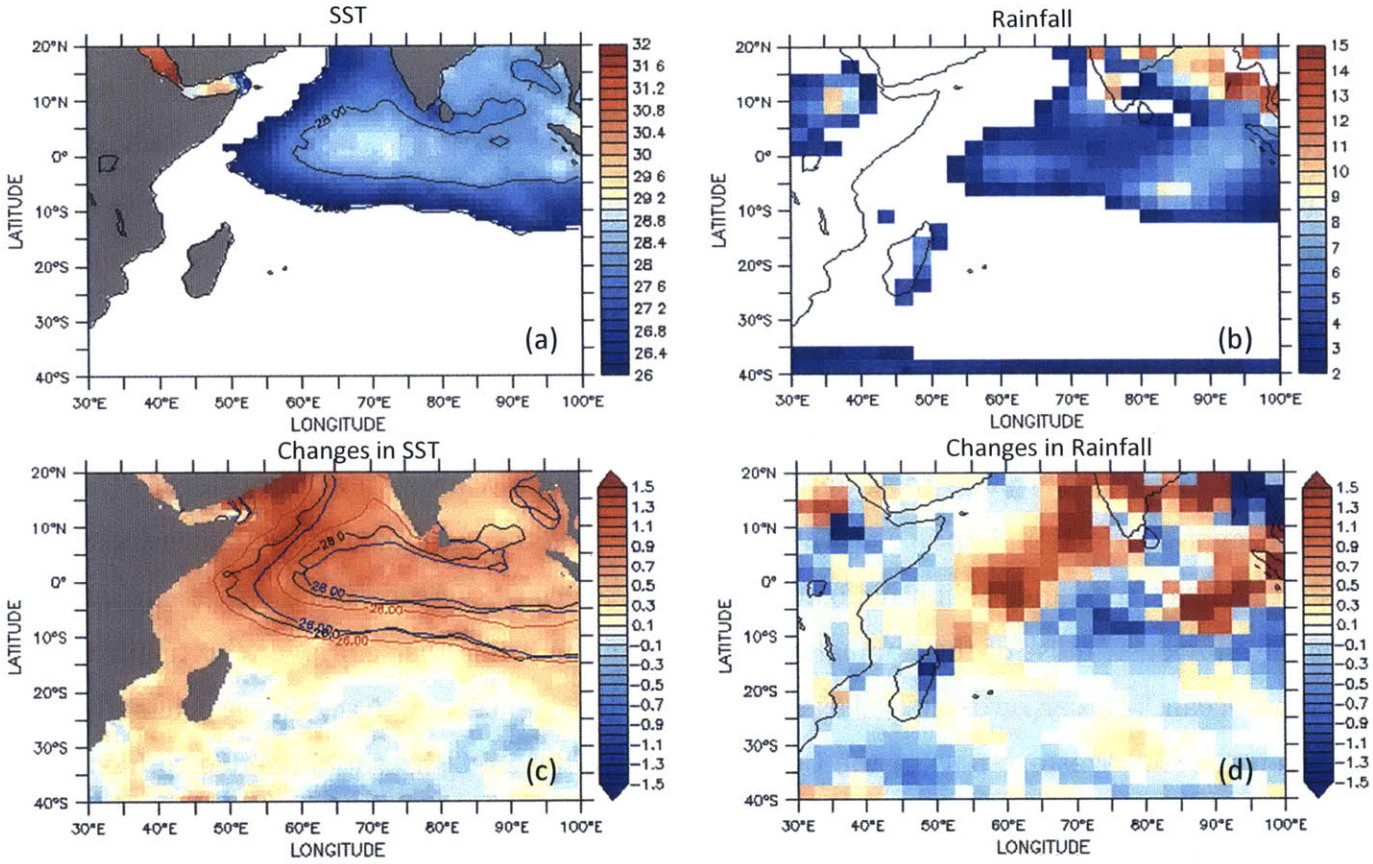


**Figure 2. 15:** Monthly average of July and August for the period (1979-2012) for: a) Sea Surface Temperature (SST) using HadISST dataset and b) rainfall in (mm/day) using GPCP dataset. c) The difference of SST in (°C)between the average four warmest events (1987, 1997, 2002 and 2003 and four coldest events (1979, 1981, 1985 and 1996) over the North Indian Ocean defined as (55°E-70°E and 0-15°N) during July and August. The red lines represent the isotherms of the 28°C and 26°C during the four warmest July and August events, the blue lines represent the isotherms of the 28°C and 26°C during the four coldest July and August events, the back lines represent the isotherms of the 28°C and 26°C for the average of SST during July and August of the period (1979-2012). d) The same as in c) but for the difference in rainfall.

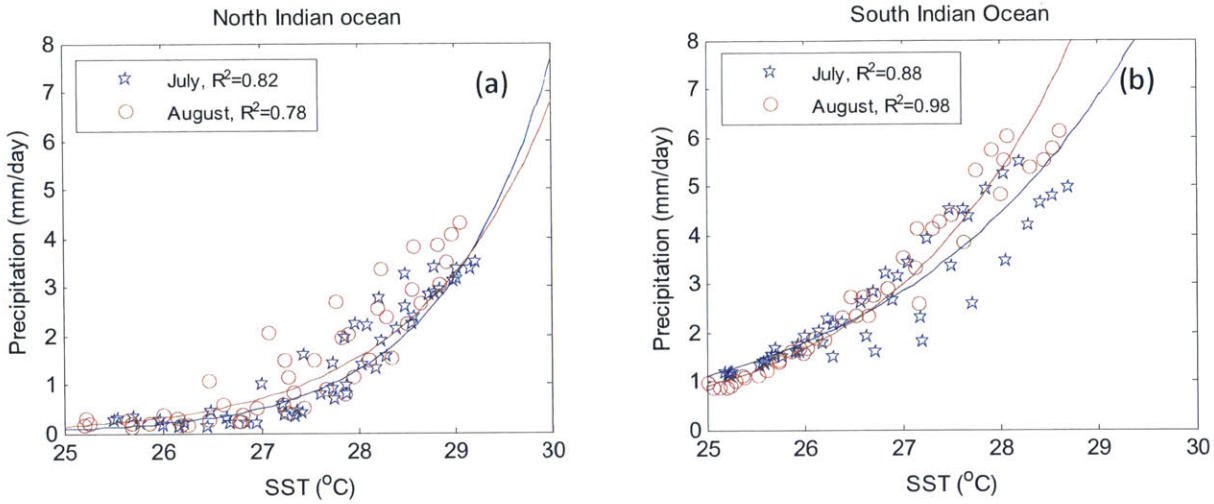


**Figure 2. 16:** Relation between SSTs and rainfall over North Indian ocean (55°E-70°E, 0-15°N) and South Indian ocean (55°E-70°E, 0-15°S) during July and August. The relations are fitted using powers equations (i.e. Rainfall = Constant1x $SST^{Constant2}$). The coefficients of determination are for the fitted lines using powers equations. Each point represents the long-term averages of the SST and rainfall over the same grid.

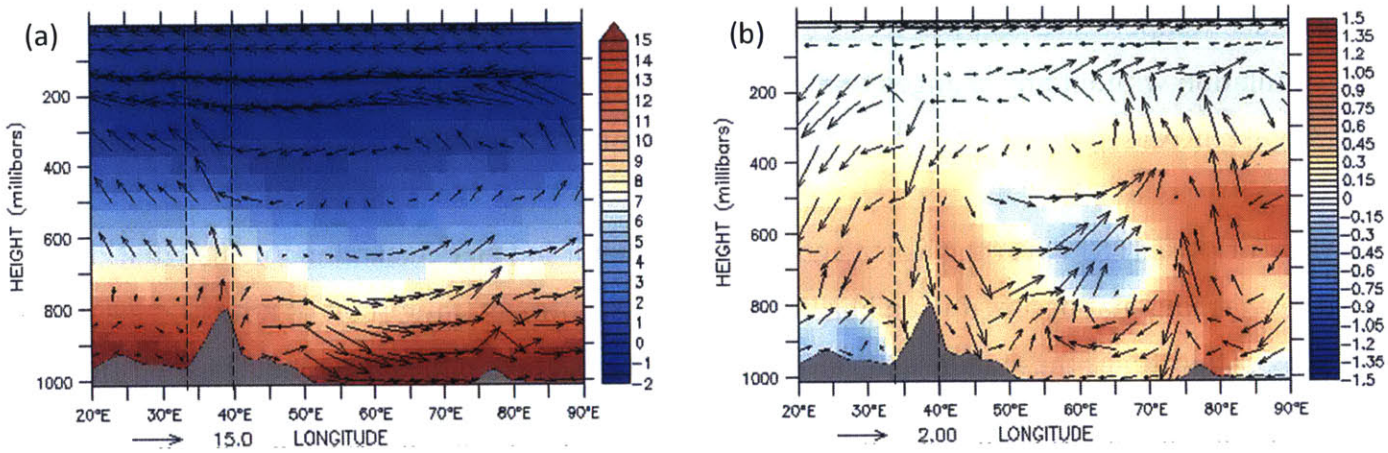


**Figure 2.17:** Monthly average of July and August for the period (1979-2012) for: a) winds averaged between 5°N and 15°N and the specific humidity (g/kg) shown in the background. b) Same as in a) but for the difference between the average four warmest July and August events and the average four coldest July and August events as in Figure 2.15. The vertical lines are the longitudinal boundaries of the UBN basin.

## 2.5 Sensitivity experiments on the response of the UBN flow to Indian Ocean SSTs

In order to analyse the mechanism suggested above as well as the connection between the UBN flow and the Indian Ocean SSTs, several sensitivity simulations were performed using the UK Met Office Hadley Centre General Environmental Model version 1 (HadGEM1). Complete description of the model can be found in Johns et al., 2006, Martin et al., 2006 and Ringer et al., 2006. HadGEM1 and its atmospheric version, HadGAM, took part in the Intergovernmental Panel on Climate Change (IPCC) Fourth Assessment Report (AR4) (Solomon et al. 2007). This model uses hybrid vertical coordinates in height with 38 vertical levels extending to over 39 km and uses a regular longitude-latitude grid at N96 resolution (approximately 135 km at 50N).

Two different simulations, in which the SSTs were prescribed for 24 years for the period 1979-2002 using the monthly Atmospheric Model Intercomparison Project II (AMIP-II) sea surface temperature and sea ice (Taylor et al., 2000). The simulations include a control simulation without any changes to the SSTs and one experiment with SSTs during July and August increased by 2°C over the North and South of equator Indian Ocean.

The increased SSTs over the North and South of equator Indian Ocean mimic, in distribution, the warming that occurs during El Niño events. It is, however, important to note that 2°C is almost four times the standard deviation of the SST variation in these regions. The intention for applying such a large SST warming is to force the model to respond strongly, which makes it easier to analyse the results than with a weak warming. The monthly mean runoff of the two simulations is shown in Figure 2.17. The model was able to simulate the hydrological cycle of the UBN basin by capturing the seasonal cycle of the runoff (Figure 2.18). In the control simulation, the magnitude of the annual mean rainfall is 3.53 mm/day, which is close to observations (3.3 mm/day) estimated by the CRU TS3 rainfall dataset (Mitchell and Jones, 2005). Also, the simulated annual mean runoff for the control simulation (0.48 mm/day) represents ~65% of the observed value for the UBN basin (0.76 mm/day). The decrease of the runoff is relatively large (i.e. 20 %), relative the coefficient of variation in the observed

flow ~22%, which indicates that the UBN flow is sensitive to the warming over selected regions and that SSTs are negatively correlated with the UBN flow. In addition, it is important to notice that these experiments are made with one model; it is possible that other models may have stronger/weaker response on the Nile flow for the warming of the Indian Ocean.

The corresponding anomalous wind circulation for the simulation in which the SSTs are increased over the North and South of equator Indian Ocean is shown in Figure 2.19. The anomalous westerlies are seen for August along the coast of Africa and over the North and South of equator Indian Ocean following the Matsuno-Gill circulations. This anomalous circulation reduces convergence of air in the boundary layer over the UBN basin and thus the rainfall and the runoff over the basin. The mechanism of the teleconnection between the Nile flow and the ENSO and Indian Ocean SSTs is summarized in Figure 2.20.

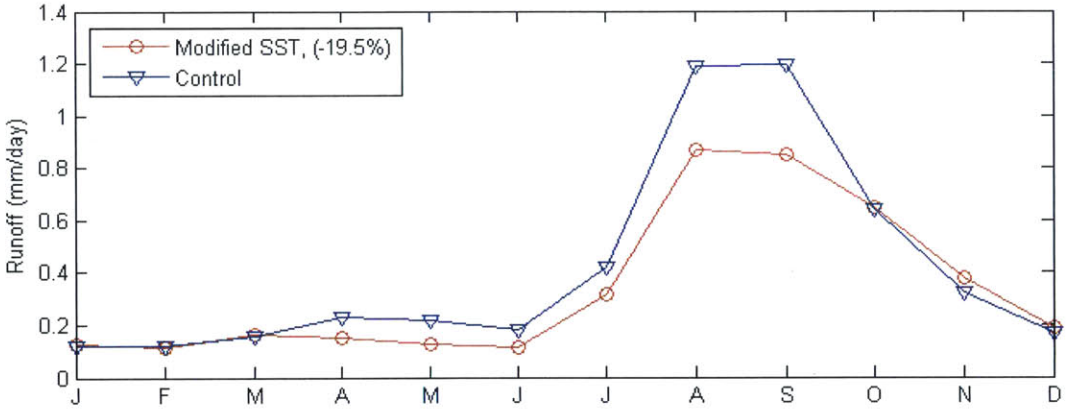


**Figure 2.18:** Average monthly runoff of the UBN basin (1979-2002) for control simulation compared to the simulation where the SSTs are increased by 2 °C over North and South of Equator Indian Ocean. The values between brackets are the percentage reduction relative to the mean annual runoff of the control simulation (0.48 mm/day).

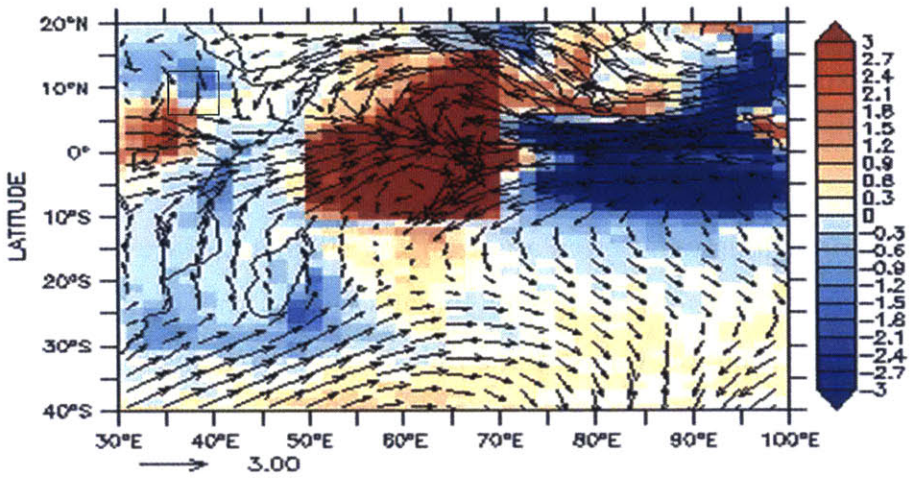


**Figure 2.19:** Average wind circulation of August for the lowest 300 mb from the surface and rainfall (1979-2002) for perturbed simulation, where SSTs are increased by 2 °C over North and South of Equator the Indian Ocean, minus the control simulation. The small box encloses the UBN basin.

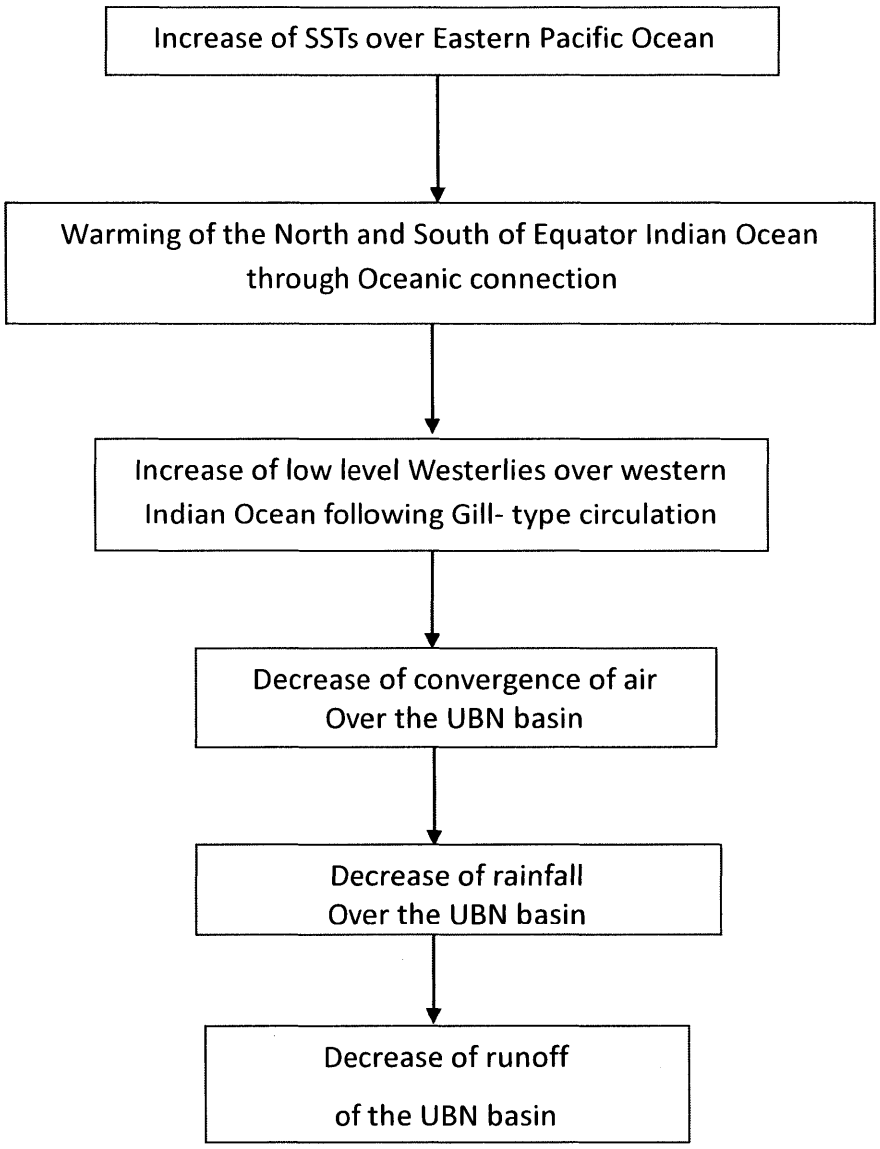


**Figure 2.20:** Schematic diagram showing the mechanism of the teleconnection between ENSO, Indian ocean SST and Nile flow.

## 2.6 Conclusions

In this chapter, the connections between the Nile flow, Indian ocean SSTs and ENSO is investigated. It is shown using cross-correlation analysis and partial coherency analysis that the SSTs over North and South of equator Indian ocean are responding to the warming of the Pacific ocean. Moreover, they do not force any independent significant variability of the Nile river flow different from ENSO.

A mechanism that connects the Nile flow to SSTs in Indian Ocean and the Pacific ocean is investigated in this chapter using observations of SST, rainfall, streamflow and winds from reanalysis data. The increase of the SSTs over the North and South of equator Indian ocean, during El Niño events, forces a Matsuno-Gill circulation over these regions, which enhances low-level westerly winds that induce subsidence and reduces the convergence of air over the UBN basin. This reduction in convergence of air is translated to a reduction of rainfall and runoff over the UBN basin. This mechanism was simulated using an AGCM forced with observed SSTs that were modified to simulate a warming over the Indian Ocean. It is shown that increasing SSTs over Indian Ocean reduces the Nile flow, which highlights some of the potential mechanisms shaping the impact of climate change on the Nile river flow, through warming of the Pacific and Indian Oceans.

# Chapter 3: Evaluation of the Hydrological Cycle over the Upper Blue Nile Basin in Global Climate Models Simulations and Reanalysis Products

Global Climate Models (GCMs) are currently used to predict the changes in future climate due to the increased concentration of greenhouse gases. However, these models should be carefully evaluated before using them in climate change studies as using poor modelling tools can introduce biases in the projections of future climate. On the other hand, using GCMs that are able to accurately simulate the current climate increases our confidence in their projections of future climate. Furthermore, as reanalysis data are used to validate GCMs simulations and to force regional climate models, it is also important to evaluate them before using them in climate studies. Thus, this chapter aims to: (i) evaluate GCMs and reanalysis products in representing the hydrological cycle under present-day climate conditions over the Upper Blue Nile basin using the atmospheric and soil water balance approaches, and (ii) identify the best GCM candidates for use in studying climate change impacts on water resources over the Upper Blue Nile basin.

## 3.1 Introduction

Global Climate Models are the best available tools to predict changes in climate due to the increased concentrations of greenhouse gas in the future. However, an analysis of their outputs reveals that these models do not accurately reproduce the past and current climates. This is particularly the case for hydrological variables (e.g. rainfall) that show large inconsistency, especially over Africa (Figure 1.1) (Christensen et al., 2007). Over large basins, such as African basins, model outputs are often statistically or dynamically downscaled for impact studies on water resources, floods and droughts, and agriculture. However, many

uncertainties lie behind the choice of a downscaling method, which may amplify inherent errors in GCM outputs and increase uncertainties associated with climate change predictions of the hydrological cycle at smaller scale, such as over river basins (Boe et al., 2009). These errors are reflected in the disagreement between GCM predictions on the sign and magnitude of changes in river runoff over major African basins (Strzepek and Yates, 1996; Conway and Hulme, 1996; Yates and Strzepek, 1998; Nohara et al., 2006; Kim et al., 2008). Furthermore, reanalysis products such as ERA-Interim (Dee et al., 2011, Berrisford et al., 2011) and NCEP-NCAR (Kalnay et al., 1996) are often used to validate GCMs or to drive Regional Climate Models (RCM), so that a use of biased reanalysis products may lead to errors in assessing model performances. The choice of reanalyses and GCMs is therefore crucial and can have large consequences on the decision-making process related to climate change. Thus, by evaluating GCMs and reanalyses products and by only choosing the models that can accurately reproduce the observed hydrological cycle we may increase our confidence in GCM predictions of future changes in the hydrological cycle over any basin.

Several methods are used to evaluate the performance of climate models in simulating climate features at different spatial scales (Schaller et al., 2011). The methods depend on the variables or phenomena that are evaluated. The most common evaluation methods can be grouped into three categories (Raisanen, 2006; Randall et al., 2007): 1) statistical measures or 'performance metrics' (e.g. mean errors, correlations, root-mean square errors, performance indices, etc.) that compare model outputs with observations and provide information on the performance of the model without detailing the cause of biases (e.g. Glecker et al., 2008; Reichler et al., 2008; Perkins et al., 2007; Lambert et al., 2001); 2) diagnostics that provide information on the sources of model discrepancies and include a detailed analysis to identify processes connected to the errors (e.g. analysis of energy and water budgets, analysis of atmospheric and land processes, etc.) and 3) the evaluation of climate models based on the representation of specific events (e.g. monsoons, ENSO teleconnections, etc.). These approaches are widely used to validate climate models and reanalysis products (Dee et al., 2011; Johns et al., 2006; Uppala et al., 2005; Kalnay et al., 1996).

In this study, the second approach is considered to assess GCMs and reanalyses performance in representing the hydrological cycle over the Upper Blue Nile (UBN) basin. The atmospheric and soil water balance constraints are used to evaluate GCMs and reanalyses. Those constraints state that the long-term mean of river flow should approximately balance rainfall minus evaporation (Eq. 3.3) and should equal atmospheric moisture convergence (Eq. 3.7). This method allows an evaluation based on the ability of GCMs and reanalyses to accurately represent the observed stream flow of the UBN basin. These approaches are commonly used to estimate components of the hydrological cycle (e.g. evaporation, soil moisture, atmospheric moisture convergence) that are not or insufficiently available from observations (Karam and Bras, 2008; Seneviratne et al., 2004; Yeh et al., 1998; Oki et al., 1995; Calanca and Ohmura, 1994; Rasmusson, 1967, 1968). This method emphasizes the ability of GCMs to simulate processes that control the hydrological cycle, which provides a good indicator of the general performance of the model. The hydrological cycle depends on several variables, such as wind, specific humidity, rainfall, soil water storage, evaporation, radiation and clouds. An inaccurate representation of any of these variables would therefore be reflected in the simulation of rainfall, evaporation and runoff, which highlights the necessity to thoroughly validate each component of the hydrological cycle and understand how they are connected. A detailed analysis of the different components of hydrological cycle is also important, as GCMs or reanalyses can accurately represent one variable of the hydrological cycle but show large errors in other variables (Trenberth et al., 2007)

## 3.2 Study Area

The evaluation of the hydrological cycle in reanalyses and GCMs is applied over the Upper Blue Nile basin. The Upper Blue Nile basin is the main source of water for the Nile River. It contributes approximately 60% of the main flow of the Nile (based on analyses of the period 1945-1984, Conway and Hulme, 1993) and almost 80% of the total Nile flow during the rainy season between July and October. It extends from 7° N to 12°5' N and from 34°5' E to 40° E. The basin is characterized by its spatial topographic variability. The eastern part of the basin

has the highest elevation reaching 4,000 m above sea level and decreasing gradually toward the western outlet of the basin where the elevation is approximately 500 m above sea level (Figure 3.1). The mean annual rainfall is 1224 mm (i.e. 215 $km^3$) and stream flow of the basin is 257 mm (i.e. 46 $km^3$) and the total area of the basin is 176,000 $km^2$ (Conway and Hulme, 1993 and ElShamy et. al., 2009).

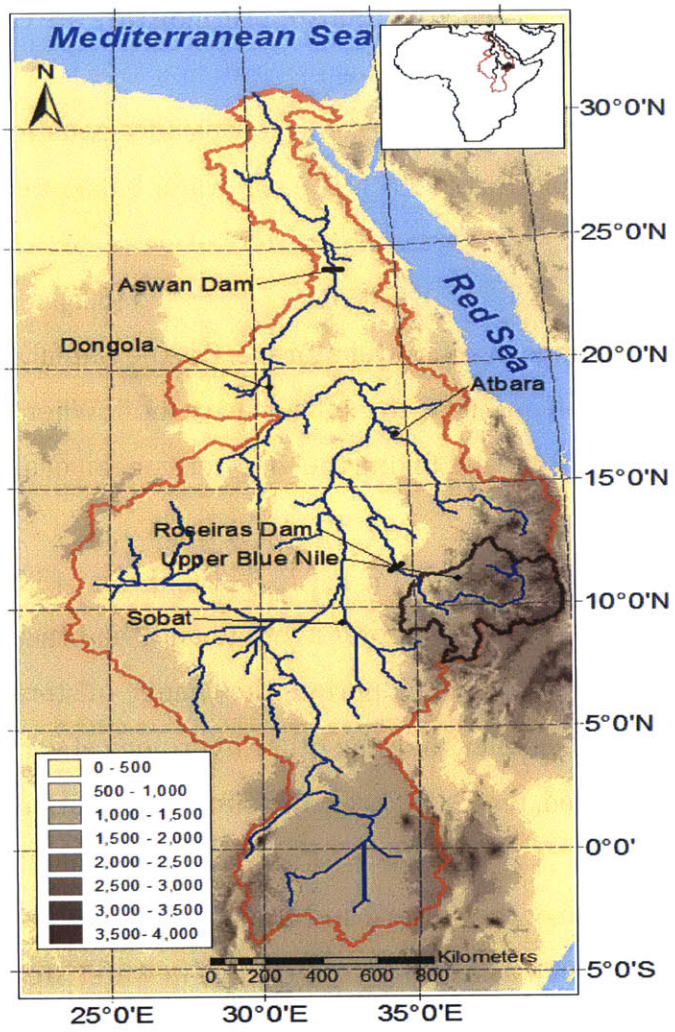


**Figure 3. 1:** Topographic map of Eastern Africa (scale in meters) overlaid by the Nile basin (red) and the Upper Blue Nile basin (black).

## 3.3 Methodology and Datasets

### 3.3.1 Methodology

The water balance is analysed for soil and the atmosphere, as the long-term averages of the convergence of horizontal atmospheric moisture fluxes and the excess of rainfall over evaporation must be in balance with each other and with the observed stream flow. The moisture fluxes and the convergence of atmospheric moisture are calculated using the winds and specific humidity fields from the atmospheric data.

The formulations of the atmospheric and soil water balance equations used in this study, are similar to that of Peixoto and Oort (1992). The soil water balance equation is described by:

$$\Delta S = P - E - R_o - R_u \qquad (3.1)$$

where $\Delta S$ is the rate of change in soil water storage, P is the rainfall rate, E is the evaporation rate, $R_o$ is the surface runoff and $R_u$ is the subsurface runoff. When this equation is spatially averaged over a specified basin and taking the long-term mean of all its components, it takes the form;

$$\{\Delta\bar{S}\} = \{\bar{P}\} - \{\bar{E}\} - \{\overline{R_o}\} - \{\overline{R_u}\} \qquad (3.2)$$

where the over bar indicates the temporal average and the brackets indicates the spatial average over a large basin. Over a long period, the change in storage is found to be two to three orders of magnitude smaller than the other hydrological variables (Siam et al. 2013). It can therefore be neglected, which leads to the following equation:

$$\{\bar{P}\} - \{\bar{E}\} = \{\bar{R}\} \qquad (3.3)$$

where R is the combination of the surface and subsurface runoff rates.

Over shorter timescales, such as a month, the change in water storage cannot be neglected and the stream flow can be estimated using the equation;

$$\{R\} = \{P\} - \{E\} - \{\Delta S\} \quad (3.4)$$

The atmospheric water balance is satisfied when the excess of rainfall minus evaporation is in balance with the column integrated atmospheric moisture fluxes. The moisture fluxes Q(u) and Q(v) are calculated by vertically integrating the product of specific humidity (q) and wind components in the zonal (u) and meridional (v) directions from the surface to the top of the atmosphere as follows:

$$Q(v) = \int_0^{P_o} qv\frac{dp}{g} \qquad Q(u) = \int_0^{P_o} qu\frac{dp}{g} \qquad W(\lambda,\phi,t) = \int_0^{P_o} q\frac{dp}{g} \qquad (3.5)$$

where W is the mass of water vapor contained in an air column per unit area; $W_c$ is the mass of condensed water in an air column of unit area and $P_o$ is the surface pressure.

The atmospheric water balance equation can be written as:

$$\frac{\partial W}{\partial t} + \nabla.Q + \frac{\partial W_c}{\partial t} + \nabla.Q_c = E - P \qquad (3.6)$$

This equation can be represented as a control volume where the divergence terms ($\nabla$. Q) and ($\nabla$. $Q_c$) account for the exchange of moisture across the boundaries of the control volume and the terms $\frac{dW}{dt}$ and $\frac{dW_c}{dt}$ are the changes in atmospheric water storage inside the control volume (the subscript (c) indicates the condensed mass of water vapor).

The amount of condensed water is compared to the total amount of water vapor in an air column and it was found that at least two to three orders of magnitude separate the water vapor content and the condensed water content in form of liquid or ice (Figure 3.2). The change in storage of the water vapor term is usually small compared to the other terms in Eq. (3.4) when considering relatively long time interval (e.g., monthly or longer) (Yeh et al., 1998, and Senevirante et al., 2004), thus after taking the temporal and spatial averages, Eq. (3.6) simplifies to:

$$\{\ \overline{\nabla.Q}\ \} = \{\ \overline{P}\ \} - \{\ \overline{E}\ \} \qquad (3.7)$$

and using Eq. (3.4) with (3.6) and rearranging, we can write:

$$\{\ \overline{R}\ \} = -\{\ \overline{\nabla.Q}\ \} - \{\ \overline{S}\ \} \qquad (3.8)$$

where the divergence term is calculated using a central finite difference scheme.

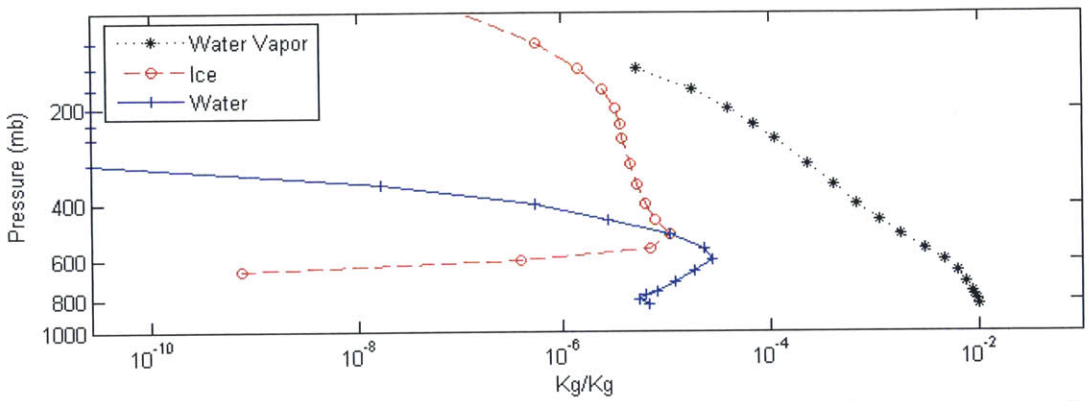


**Figure 3.2:** Vertical profiles of the average annual content of water vapor, cloud ice and liquid water content over the Upper Blue Nile basin using ERA-Interim data.

### 3.3.2 Datasets

The methodology detailed above makes use of rain and flow gauge observations and can be systematically applied to several GCM outputs as well as reanalysis products. The rainfall observations are based on the CRU TS 3.1 data product, which is the successor of the CRU TS 2.1 (Mitchell and Jones, 2005). In addition, we use the estimates of Allam et al., 2016 of the rainfall and evaporation over the Upper Blue Nile basin. These estimates are based on an optimization model that is constrained with soil water balance equation to calculate the long-term mean of rainfall and evaporation over the basin. The stream flow at the outlet of the UBN basin is available as monthly values from the Global River Discharge Database (RivDIS v1.1) (Vörösmarty et al., 1998) and personal communications respectively.

The European Centre for Medium-Range Weather Forecast (ECMWF) ERA-Interim reanalysis product (Dee et al., 2011) is used in this study. The atmospheric variables, which include the zonal and meridional wind components and specific humidity at 37 pressure levels starting from the surface to the top of the stratosphere at 1 mb and at 6-hourly time steps, are used to calculate the atmospheric moisture convergence. Rainfall, evaporation, runoff and soil moisture over four layers are based on the 12-hourly accumulated fields (Table 3.1). In addition, the ECMWF reanalysis product (ERA40: Uppala et al., 2005) and the National Center for Environmental Prediction-National Center for Atmospheric Research reanalysis product (NCEP-NCAR: Kalnay et al., 1996) are also analyzed in this study.

The simulation outputs from 17 GCMs of the World Climate Research Programme's (WCRP's) Coupled Model Intercomparison Project phase 3 (CMIP3) multi-model dataset (Meehl et al., 2007), as well as 11 GCMs of the CMIP5 multi-model dataset (Taylor et al., 2012) (Table 3.2) are used.

**Table 3.1:** Summary of reanalysis products and observations data used.

| Data | Variables | Coverage Period | Horizontal Resolution | Number of Atmospheric layers |
|---|---|---|---|---|
| ERA-INTERIM | zonal wind(U), Meridional wind(V), Specific humidity(q) Runoff(R ), Rainfall (P), Evaporation(ET), Soil moisture(SM) | 1989-2010 | 1.5°x1.5° | 37 pressure levels (1000mb-1mb) |
| ERA-40 | U, V, q, R, P, ET, SM | 1979-2002 | 2.5°x2.5° | 23 pressure levels (1000mb-1mb) |
| NCEP-NCAR | U, V, q, R, P, ET, SM | 1979-2002 | 2.5°x2.5° | 8 pressure levels (1000mb-300mb) |
| CRU TS 3.1 | P | 1901-2009 | 0.5°x0.5° | -- |
| Allam et al. 2016 | P, ET | 2002-2012 | 0.25°x0.25° | -- |

**Table 3.2:** Summary of GCMs used in this study

| Project | Model | Outputs Resolution | Agency |
|---|---|---|---|
| CMIP3 | 1- HADGEM1 | 1.875°x1.25° | Hadley Center for Climate Prediction and Research, Met Office, UK |
| | 2- MPI-ECHAM5 | 1.875°x1.87° | Max Planck Institute for Meteorology, Germany |
| | 3 -CSIRO-MK3.5 | 1.875°x1.86° | CSIRO Atmospheric Research, Australia |
| | 4- CSIRO-MK3 | 1.875°x1.86° | CSIRO Atmospheric Research, Australia |
| | 5- GFDL-CM2 | 2.5°x2° | Geophysical Fluid Dynamics Laboratory, USA |
| | 6- BCCR-CM2 | 2.8°x2.8° | Bjerknes Center for Climate Research, Norway |
| | 7- MRI-CGCM2.3.2 | 2.8°x2.8° | Meteorological Research Institute, Japan |
| | 8- NCAR-PCM1 | 2.8°x2.8° | National Center for Atmospheric Research (NCAR), NSF, DOE, NASA, and NOAA |
| | 9- CNRM-CM3 | 2.8°x2.8° | National Center of Meteorological Research, France |
| | 10- IAP-FGOALS | 2.8°x2.8° | Institute of Atmospheric Physics, Chinese Academy of Sciences, China |
| | 11- CCMA-GCM3.1(T63) | 2.8°x2.7° | Canadian Center for Climate Modeling and Analysis, Canada |
| | 12- HADCM3 | 3.75°x2.5° | Hadley Center for Climate Prediction and Research, Met Office, UK |
| | 13- IPSL-CM4 | 3.75°x2.5° | Institute of Pierre Simon Laplace, France |
| | 14- MIUB-ECHO | 3.75°x2.7° | Meteorological Institute University of Bon, Germany |
| | 15- CCMA-GCM3.1(T47) | 3.75°x3.7° | Canadian Center for Climate Modeling and Analysis, Canada |
| | 16- GISS-AOM3.1 | 4°x3° | Goddard Institute for Space Studies, USA |
| | 17- INMCM3 | 5°x4° | Institute for Numerical Mathematics, Russia |
| CMIP5 | 1- MRI-CGCM3 | 1.12°x1.12° | Meteorological Research Institute |
| | 2- CNRM-CM5 | 1.4°x1.4° | National Center of Meteorological Research, France |
| | 3- INMCM4 | 2°x1.5° | Institute for Numerical Mathematics, Russia |
| | 4- HadGEM2-CC | 1.875°x1.25° | Hadley Center for Climate Prediction and Research, Met Office, UK |
| | 5- CSIRO | 1.85°x1.85° | CSIRO Atmospheric Research, Australia |
| | 6- IPSL-CM5-MR | 2.5°x1.26° | Institute Pierre Simon Laplace, France |
| | 7- NORM-ESM-ME | 2.5°x1.9° | Norwegian Climate Centre, Norway |
| | 8- GISS-E2-H | 2.5°x2° | Goddard Institute for Space Studies, USA |
| | 9- GFDL-CM3 | 2.5°x2° | Geophysical Fluid Dynamics Laboratory, USA |
| | 10- BCC-CSM1 | 2.8°x2.8° | Beijing Climate Center, China |
| | 11- CAN-ESM2 | 2.8°x2.8° | Canadian Center for Climate Modeling and Analysis, Canada |

## 3.4 Results and Discussion

### 3.4.1 The hydrological cycle in reanalysis products

The hydrological cycle of reanalysis products is analyzed in this section for two reasons: i) reanalysis fields have the advantage of including assimilated observations and potentially represent the hydrological cycle more realistically than GCMs; ii) the same fields provide the lateral boundary conditions for Regional Climate Models simulations, hence biases in these products can result in misleading interpretations of Regional Climate Models results, so that it is important to choose carefully the reanalysis products used to drive Regional Climate Models. In this section, the analysis investigates the representation of the hydrological cycle in ERAI, ERA40 and NCEP-NCAR over the UBN basin

The area of the UBN basin is approximately $2 \times 10^5$ km$^2$, which is close to the smallest area ($1 \times 10^5$ km$^2$) necessary for applying the atmospheric water balance approach to obtain reasonable and accurate results. The small areas are more sensitive to variations in the moisture fluxes, which can vary across the boundaries of the studied area. On the other hand, the variation of the moisture fluxes across the boundaries of larger domain are less, hence, the errors from applying the atmospheric water balance approach are less (Rasmusson, 1971 and Yeh et al., 1998). This can be a problem when analysing models and reanalyses that have very low resolutions. However, with the availability of higher resolution climate models and reanalysis data, the atmospheric water balance approach can be applied for smaller areas.

The seasonal cycle of rainfall over the UBN basin is close to observations as shown in Figures 3.3a. However the long-term mean is overestimated as shown in table (3.3). In Figures 3.3b, the atmospheric water balance is tested. It is shown that the seasonal cycle of atmospheric moisture convergence, and rainfall minus evaporation in ERAI are overestimated compared to observations of difference between rainfall and evaporation from the estimates of the rainfall and evaporation of Allam et al., 2016 over the UBN basin as shown in Table 3.3. The difference between the long-term averages of ERAI moisture fluxes and the net rainfall is

approximately 0.2 mm/day over the UBN basin (Table 3.3). This small imbalance can be related to the errors that arise from the finite difference scheme used in the calculations or the fact that the rainfall and evaporation values are based on 12-hourly accumulated fields of the forecast model, while the fluxes fields are based on reanalysis fields that are based on direct observations (Dee et al., 2011, Berrisford et al., 2011).

**Table 3.3:** Summary of results using the reanalysis products over the Upper Blue Nile basin.

| Data | P | ET | P-ET | Runoff | $-\nabla . Q$ | ds/dt |
|---|---|---|---|---|---|---|
| ERAI | 4.09 | 2.27 | 1.82 | 1.93 | 1.61 | 0.004 |
| ERA40 | 1.56 | 0.55 | 1.06 | 0.82 | 1.76 | -0.003 |
| NCEP-NCAR | 5.1 | 2.95 | 2.15 | 1.36 | 1.61 | -0.012 |
| Obs. | 3.3 (CRU)<br>3.36 (Allam) | 2.6 (Allam) | 0.7<br>0.76 | 0.72 | -- | -- |

* All values are in mm/day.

In order to validate the soil water balance, the different estimates of runoff are compared in Figures 3.3c. The calculated runoff from ERAI model is compared to estimates from Eqs. (3.4 and 3.8). The overestimation in rainfall values without a similar overestimation in evaporation enhanced the estimates of runoff, which is approximately equal to more than double the observed stream flows (Table 3.3).

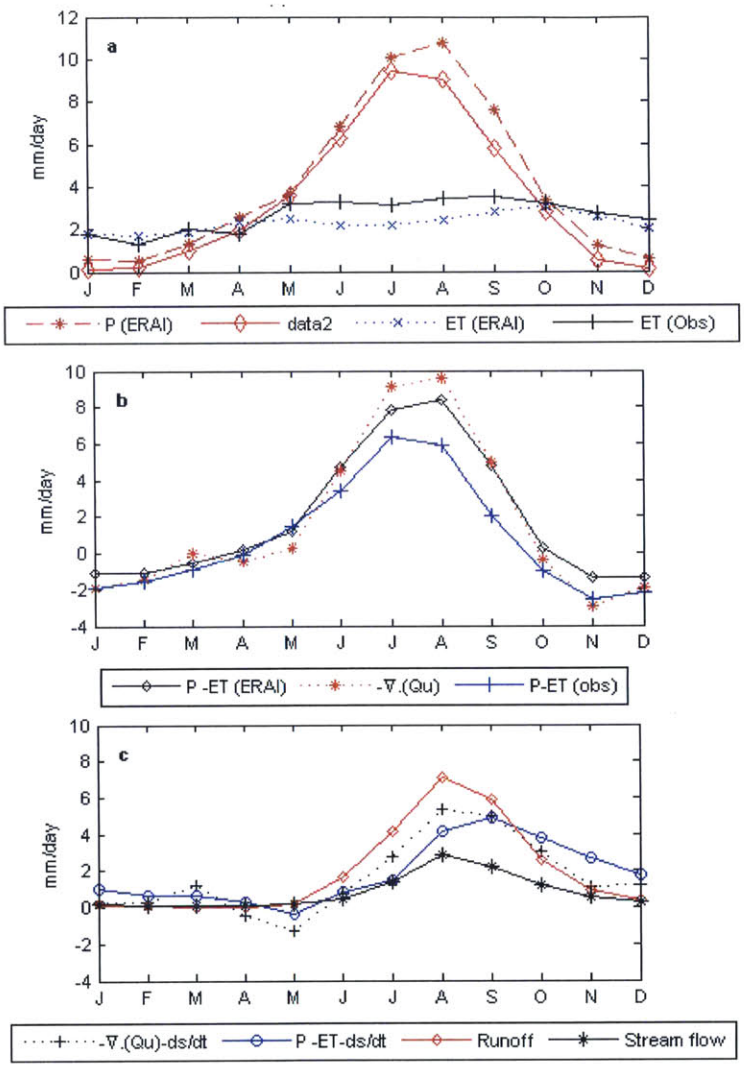


**Figure 3. 3:** Monthly average values for twenty two years (1989-2010) using the ERAI data for the rainfall and evaporation compared with the rainfall and evaporation data of Allam et al., 2016 as observed values (a), convergence of moisture and difference between rainfall and evaporation of ERAI and observed rainfall and evaporation (b) and Observed stream flow, runoff and estimated runoff from the atmospheric and soil water balance approaches (c).

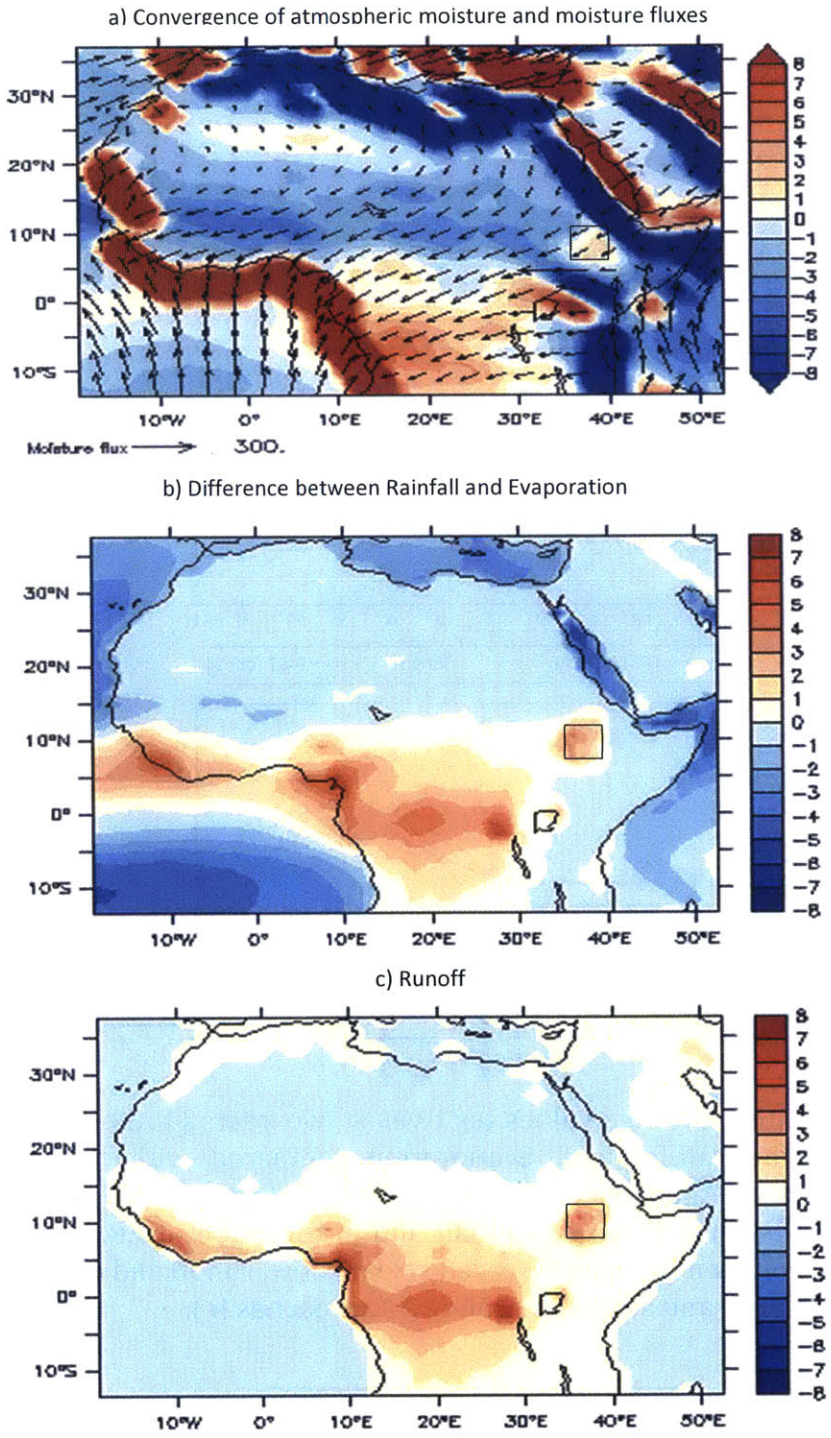


**Figure 3. 4:** Spatial distribution of the average of twenty two years (1989-2010) using the ERAI data for a) Convergence of atmospheric moisture (mm/day) overlaid by the vertically integrated moisture fluxes field (Kg/ms), b) difference between rainfall and evaporation (mm/day) and c) runoff (mm/day). The small boxes encloses the UBN basin.

A comparison between the spatial distribution of the net rainfall, runoff and convergence of atmospheric moisture is illustrated in Figure 3.4. Their long-term spatial distribution is nearly the same, as expected, except for the convergence of atmospheric moisture near the coastlines. An analysis of the moisture fluxes along the land/Ocean boundaries has shown that this significant bias over these regions is induced by the sudden change in magnitude of moisture fluxes between land and ocean. This change is amplified when the derivative of moisture fluxes is calculated. This can explain the strong convergence and divergence regions that are located beside each other along the Red Sea, Mediterranean Sea and Gulf Area. Another reason for this bias is the strong convergence of moisture fluxes simulated by the ERAI data along western coast of Africa (Figure 3.4).

Although the ERAI product overestimates the hydrological variables compared to observations, it is considered better than the ERA40 and the NCEP-NCAR products for the studied regions. The ERA40 and the NCEP-NCAR do not satisfy the atmospheric and soil water balances as shown in Table (3.3) and the simulated seasonal cycle of the hydrological variables did not match the observation as the ERAI. This imbalance problem between the long-term averages of the convergence of moisture calculated using the reanalysis products and the stream flow was highlighted by Seneviratne et al., (2004) assigning the potential sources of these errors the insufficient spatial and temporal sampling of the radiosondes measurements or errors related to the data assimilation process. For the ERA40, the water imbalance of the ERA40 data was noticed by Berrisford et al., 2011 and was adjusted in the ERAI product. However, the results of the ERAI and ERA40 were better than the NCEP-NCAR for the studied region. A similar observation was made by Karam and Bras (2008) for the amazon basin where they found that the ERA40 moisture fluxes were more accurate than the NCEP-NCAR but still both of them are significantly biased. The bias of the NCEP-NCAR fluxes data was shown in similar studies (Ruprecht and Kahl, 2003; Maurer et al., 2001; Lenters et al., 2000; Roads and Betts et al., 1999).

### 3.4.2 The hydrological cycle in CMIP3 and CMIP5 GCMs

In this section, the hydrological cycles of 17 GCMs of the CMIP3 project and 11 GCMs of the CMIP5 project are analysed. The analysis of convergence of atmospheric moisture is not repeated for these GCMs as the required outputs for this calculation are not available at suitable time interval (i.e., less than a day) for some of the GCMs. However, as land surface schemes and the dynamical cores of these models are coupled without any assimilation of observations, as for the reanalysis products, the potential inconsistency between the atmosphere and land water balance should not exist for these models. Furthermore, the analysis discussed in this section is exactly repeated but for the Eastern Nile basin (i.e. Upper Blue Nile, Sobat and Atbara basins) using 18 GCMs of the CMIP5 project as presented in Appendix D.

Figures 3.5 and 3.6 illustrate the biases present in the analysed GCMs for simulating the rainfall and runoff for the UBN basin. A general pattern seen in these models is that most of the models, particularly among the CMIP3 models, show a wetter climate by overestimating rainfall and runoff, as reflected by their high model ensemble averages compared to observations. As the UBN basin is a very small region with complex topography, it is possible that such a bias is the result of the coarse resolution used by some models, rather than due to model formulation. In order to verify this hypothesis, the CMIP3 and CMIP5 models are sorted in Figures 3.5 and 3.6 respectively, according to their horizontal resolution. In the CMIP3 models, some of the highest and lowest resolution models tend to have values of rainfall and runoff close to observations over the UBN basin. These variables are mainly overestimated for the medium resolution models. This finding tends to show that the water budget does not depend on model resolution. However, the simulated seasonal cycle of runoff and rainfall in the high-resolution (~1.8°x1.8°) CMIP3 models (Figure 3.7a) is usually better simulated than in the medium (~2.8°x2.8° (Figure 3.7b) and low (~4°x3°) (Figure 3.7c) resolution models. Similarly, the high-resolution CMIP5 models (Figure 3.8a) generally show a better simulation of the seasonal cycle compared to the medium resolution models (Figure 3.8b).

It can be concluded that the increase in resolution of climate models may improve the representation of the seasonal cycle of hydrological variables. However, increasing horizontal resolution does not remove all the biases in simulating the hydrological cycle and improvements in the simulation of other processes (e.g. energy cycle) are required to accurately simulate the hydrological cycle as discussed in the next section. Roeckner et al., 2006, found that the GCMs must have at least medium resolutions to be able to simulate the climate realistically. The transition between resolutions was described by Williamson et al., 1995: they showed that the transition from low to medium resolution is required to capture the climate statistics and the movement to higher resolution is required to solve the nonlinear processes in the models that forces the medium scale processes in the atmosphere.

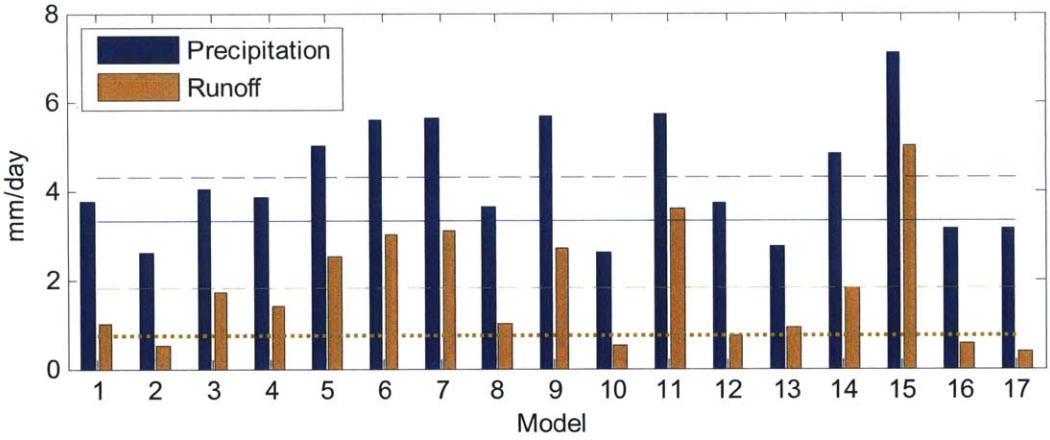


**Figure 3. 5:** Analysis of rainfall and runoff of 22 years (1979-2000) for 17 GCMs of the CMIP3 project for the Upper Blue Nile basin. The long-term average of the CRU TS 3.1 rainfall (Blue Solid line) and the observed streamflow (Brown dotted line). The dash dashed lines are for the ensemble average. The model number is as listed in Table 3.

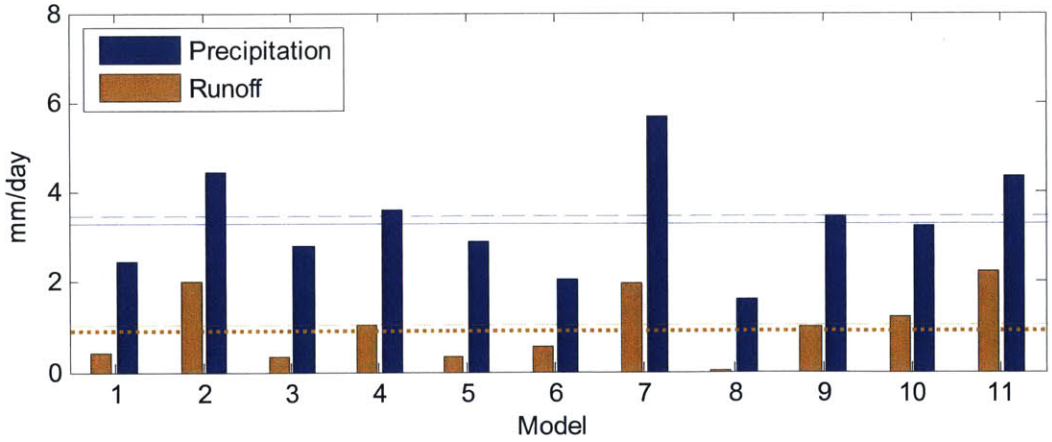


**Figure 3. 6:** Same as 3.5, but for GCMs of the CMIP5 project

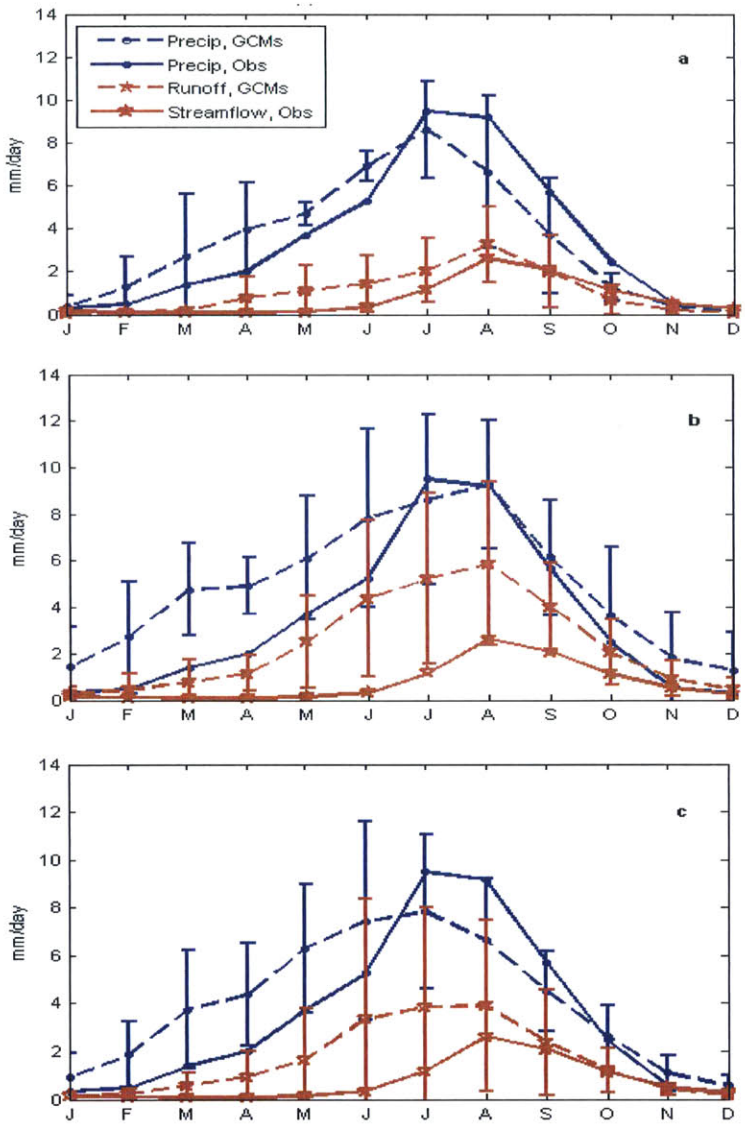


**Figure 3. 7:** Seasonal cycle of rainfall and runoff of 22 years (1979-2000) for 17 GCMs of the CMPI3 project for the Upper Blue Nile basin. The figures are sorted according to the spatial resolution of the GCMs; (a) is for the highest resolution GCMs (models 1 to 4) of approximately (1.8°x1.8°), (b) is for medium resolution models (models 5 to 11) of approximately (2.8°x1.8°) and (c) for low resolution models (models 12 to 17) of approximately (4°x3°). The error bars indicates a variation around the ensemble mean of the models of equivalent resolution by one standard deviation. The solid lines with circles and stars are for the long-term averages of observations of rainfall using CRU TS 3.1 and the observed streamflow respectively, while the dotted lines are for corresponding values from the GCMs.

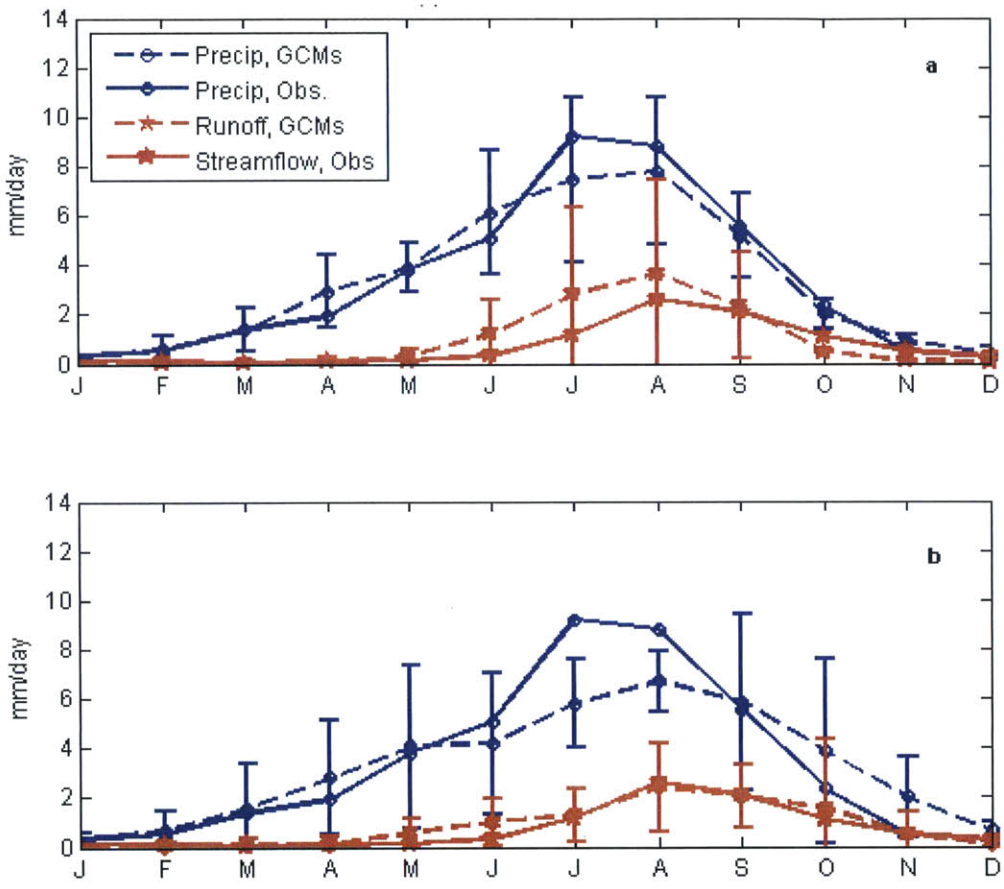


**Figure 3. 8:** Same as 3.7, but for GCMs of the CMIP5 project

### 3.4.3. The hydrological cycle in Hadley climate model simulations

In this section, we further investigate the effect of spatial resolution on the simulation of hydrological cycle over the Upper Blue Nile basin. For this purpose, simulations of the UK Met Office Atmospheric Hadley Centre General Environmental Model version 1 (HadGEM1) at four different spatial resolutions are investigated (described in Johns et al., 2006, Martin et al., 2006 and Ringer et al., 2006). These models use hybrid vertical coordinates in height with 38 vertical levels extending to over 39 km and uses a regular longitude-latitude grid (N48: 3.75°x2.5°; N96: 1.88°x1.25° ; N144: 1.25°x0.83° ; N216: 0.83°x0.56°). The SSTs are prescribed for 24 years for the period 1979-2002 using the monthly Atmospheric Model Intercomparison Project II (AMIP-II) sea surface temperature and sea ice (Taylor et al., 2000).

Figure 3.9a shows the effect of the spatial resolution on the rainfall over the Upper Blue Nile basin. The increase of the spatial resolution of the simulation systematically increases the magnitude of the simulated rainfall (Table 3.4) and also the shape of the seasonal cycle of the rainfall becomes closer to observations (Figure 3.9a). This pattern is similar for the different hydrological variables. For example, the difference between the rainfall and evaporation (Figure 3.9c), the convergence of moisture (Figure 3.9d) and finally the runoff (Figure 3.9j). This increase in the magnitude of the rainfall over the basin with increasing the spatial resolution of the simulation is primarily because of the increase of the convergence of moisture with the resolution as shown in Figure 3.9d and Table 3.4. Demory et al. 2013 showed similar results, however on global scale, that increasing the spatial resolution of the simulations increases the rainfall over land because of the increased transport of moisture.

**Table 3.4:** Summary of the results for different HadGEM1 simulations.

| Data | P | ET | R | P-ET | $-\nabla.Q$ |
|---|---|---|---|---|---|
| N216 | 4.5 | 3.04 | 1.48 | 1.46 | 1.66 |
| N144 | 3.53 | 3.05 | 0.47 | 0.48 | 0.49 |
| N96 | 3.36 | 2.89 | 0.49 | 0.48 | 0.53 |
| N48 | 2.75 | 2.76 | 0.02 | 0 | 0.04 |

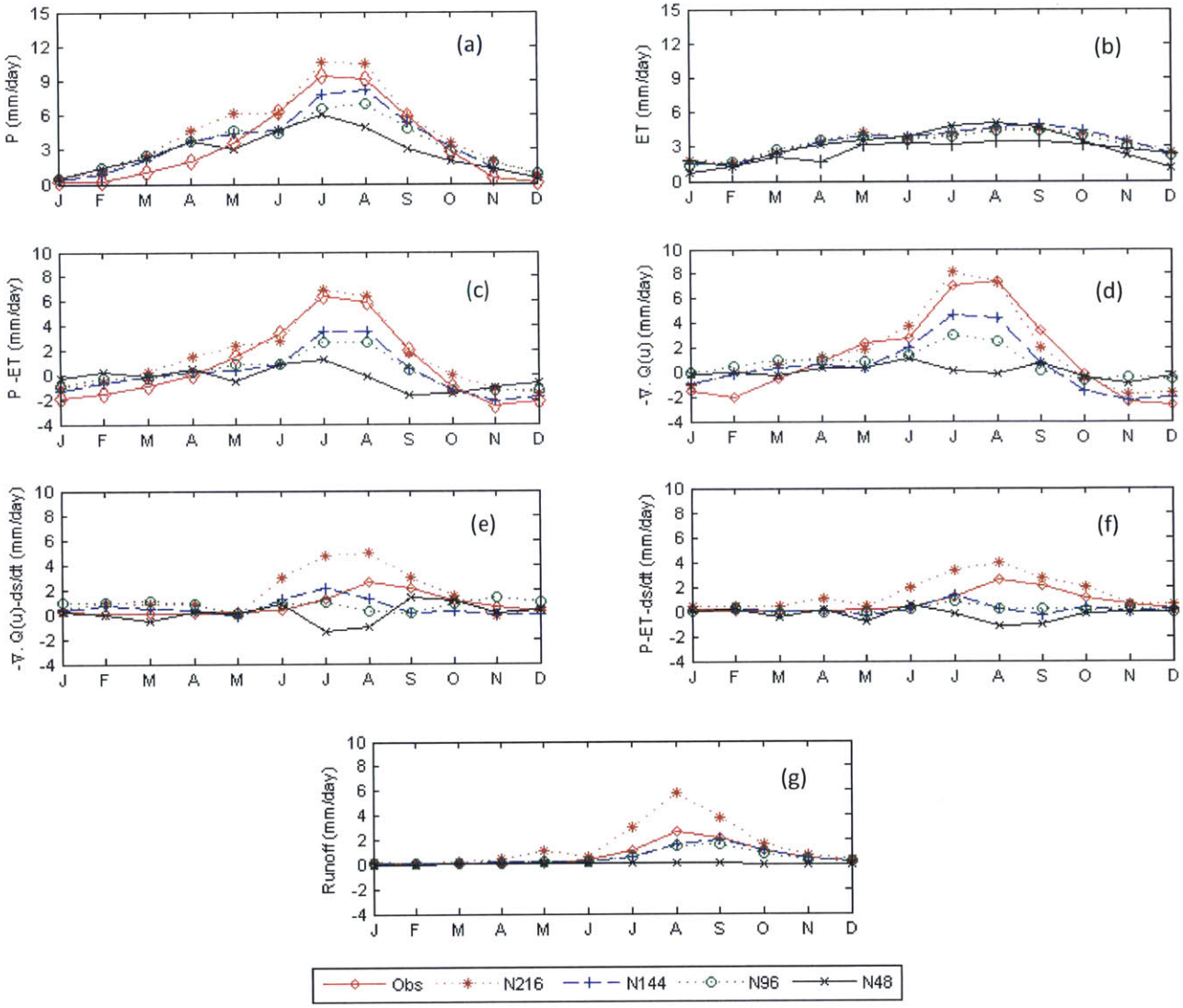


**Figure 3.9:** Average seasonal cycle over 24 years for different hydrological variables using HadGEM1 simulations data at different spatial resolutions over the Upper Blue Nile basin. The observations of rainfall and evaporation are from Allam et al., 2016, convergence of moisture is based on ERA-Interim reanalysis product and finally the runoff based on the stream flow of the Upper Blue Nile.

## 3.5 Conclusions

In this chapter, an evaluation method is introduced to analyse the hydrological cycle represented by GCMs and reanalysis products over the UBN basin. The method uses the approaches of atmospheric and soil water balance evaluate the ability of GCMs and reanalyses products to reproduce the observed river flow. River flow is one of the best observed and most accurate variable of the hydrological cycle. The use of the observed stream flow as a reference instead of the commonly used variables (e.g. rainfall) therefore allows a reduction in the uncertainties related to observations, which can be of the same order of magnitude as biases in GCMs or reanalyses products.

The evaluation method is first applied for three reanalyses products (ERAI, ERA40 and NCEP-NCAR). Among them ERAI shows the best performance. It satisfies the atmospheric and soil water balances, represents accurately the seasonal cycle of the hydrological variables, and shows a realistic spatial distribution of the moisture fluxes over Africa and the Middle East. This result has important implications for regional climate modeling studies, which often use reanalysis products as boundary conditions and therefore strongly depend on the ability of these products to represent the moisture fluxes at the boundary of the region of study.

Most of the 28 GCMs of the CMIP3 and CMIP5 projects selected for this study simulate a strong-bias in the hydrological cycle over the UBN basins by overestimating rainfall and runoff compared to observations. The relationship between GCM horizontal resolutions and their ability to simulate the hydrological cycle over the UBN basin is studied. It was shown that most of the models with the highest resolution (200 km) are able to simulate more accurately the seasonal cycle the hydrological variables compared to the medium (300 km) and low-resolution (400 km) models over both basins. Several reasons could be responsible for improving the hydrological cycle simulation associated with increasing horizontal resolution. For example, increasing model resolution can enhance the simulation of moisture transport particularly over small-scale basins. In addition, the high-resolution GCMs considered in this study better represent topography, which directly affects the

amount and distribution of rainfall, particularly over the UBN basin. The presented analysis gives some guidance for selecting the suitable GCMs to use for climate change studies over the UBN basin as using only the models that are able to simulate correctly the water cycle can increase the confidence on their future projection of changes in the hydrological cycle.

# Chapter 4: Future Changes in the Mean and Interannual Variability of the Flow in the Nile River

The interannual variability in the flow of the Nile river is shaped by El Nino Southern Oscillation (ENSO) as described in Chapter 2. It is projected that the frequency of El Nino and La Nina events will increase due to climate change (Cai et al., 2014 and Cai et al., 2015). Therefore, it can be expected that the interannual variability in the flow of the Nile river will also increase in the future. In this chapter, the changes in the mean and interannual variability in the flow of the Nile river are investigated. Furthermore, the mechanisms behind these changes in interannual variability will be discussed in this chapter.

## 4.1 Introduction

The population of the Nile basin countries is expected to double by 2050 (World Population Prospects, 2012). This huge increase in the population without a similar increase in the water resources increases the water stress in the basin and could potentially lead to a lot of water conflicts between the Nile basin countries. Furthermore, the uncertainty of the potential future changes in the flow of the Nile river due to climate changes may add further stress to the already high level water stress.

In order to fully utilize the water resources of the basin, several dams were built in the last century to control the seasonal and interannual variability of the Nile flow. The recent conflict over the Nile water has received significant attention in the last few years after the decision by Ethiopia to build a large dam on the Blue Nile (the Grand Ethiopian Renaissance Dam, or GERD) to produce electricity, mostly for export to neighbouring countries. The dam, currently under construction, is relatively large compared to previous designs for the same location, which raised serious concerns regarding its effect on the water shares of the

downstream countries (i.e. Egypt and Sudan). If variability of the Nile flow changes in the future, then the need to build dams and adjust the storage capacity in the basin will change as well.

Until recently, attempts to project the future of the Nile flow yielded inconsistent results. While several studies examined the impacts of climate change on the Nile basin using different approaches (Yates and Strzepek, 1998; Kim and Kaluarachi, 2000; ElShamy et al., 2009; Beyene et al., 2009; Taye et al., 2011; Gebre and Ludwig, 2015), the uncertainty surrounding conclusions from these studies was high for several reasons. First, none of the previous studies presented observational evidence to support their hypotheses. Second, no consistent physical mechanism was advanced to explain the future changes. Third, wide disagreement persists between the results of simulations using different global climate models (GCMs), not only in magnitude but also in the sign of projected changes in rainfall over the basin (Christensen et al., 2007; Christensen et al., 2013). These combined factors made it difficult to reach a consensus on the impact of climate change on the Nile river flow. In this chapter, consistent evidence from observations and climate models simulations are presented to support the hypothesis that the interannual variability of the Nile river flow will increase due to climate change.

## 4.2 Recent changes in the flow of the Nile basin tributaries

The Nile river basin has four main tributaries: the Upper Blue Nile, Atbara, Sobat and Bahr el-Ghebel (Figure 4.1). The Upper Blue Nile is responsible for almost 56% of the total Nile flow, and each of Sobat and Atbara adds about 12% of the total flow at Dongola (Conway and Hulme, 1993). Here, the focus is on the Upper Blue Nile, Sobat and Atbara, hereinafter referred to as the Eastern Nile (ENB) basin, as they represent almost 80% of the total Nile flow at Dongola (Figure 4.1).

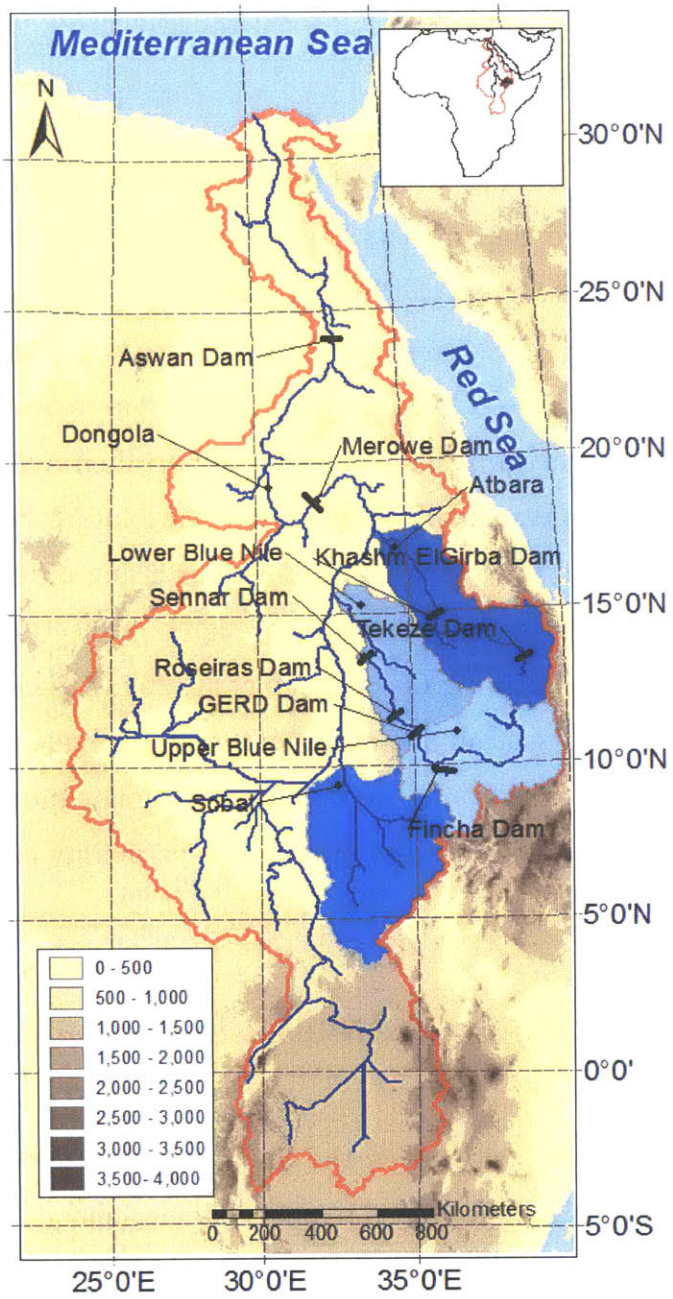


**Figure 4. 1:** Topographic map of Eastern Africa showing the main Eastern Nile basins (Upper Blue Nile, Sobat and Atabara) and different dams in these basins.

Several rainfall and stream flow stations are used to estimate trends in rainfall and stream flow over the Eastern Nile basin. The observed flow data for the Upper Blue Nile and Atbara basins was available through personal communications with the ministries of water in the countries of the Nile basin. Similar flow data for Sobat basin was not accessible. In addition, however, only a few stations were available over the Upper Blue Nile basin with sufficient data that overlaps with the flow data. These stations are (Addis Ababa: 9°01'N, 38°44'E; Debre Markos: 10°19'N, 37°44'E, Dessie Zuria: 11°07'N, 39°38'E, Gondar: 12°31'N, 37°25'E and Nekemet: 9°05'N, 36°27'E). The rainfall data were available through personal communications with the National Meteorological Agency in Ethiopia, and using the Global Historical Climatology Network (GHCN-V2). The data of the different rainfall stations were averaged by using a multiple linear regression of the different rainfall data for each station as the predictors and the observed flow of the Upper Blue Nile basin as predictand. The analysis was repeated using the Thiessen polygons approach and the same patterns in mean and variability were found.

The flows and rainfall patterns of the Upper Blue Nile and Atbara have been increasing over the last 50 years (Figures 4.2a, 4.2b, and 4.2c). These changes are reflected in the 30-year moving averages of the mean and standard deviation of annual river flow and annual rainfall, as they both persistently increase with time (Figures 4.2d, 4.2e, and 4.2f).

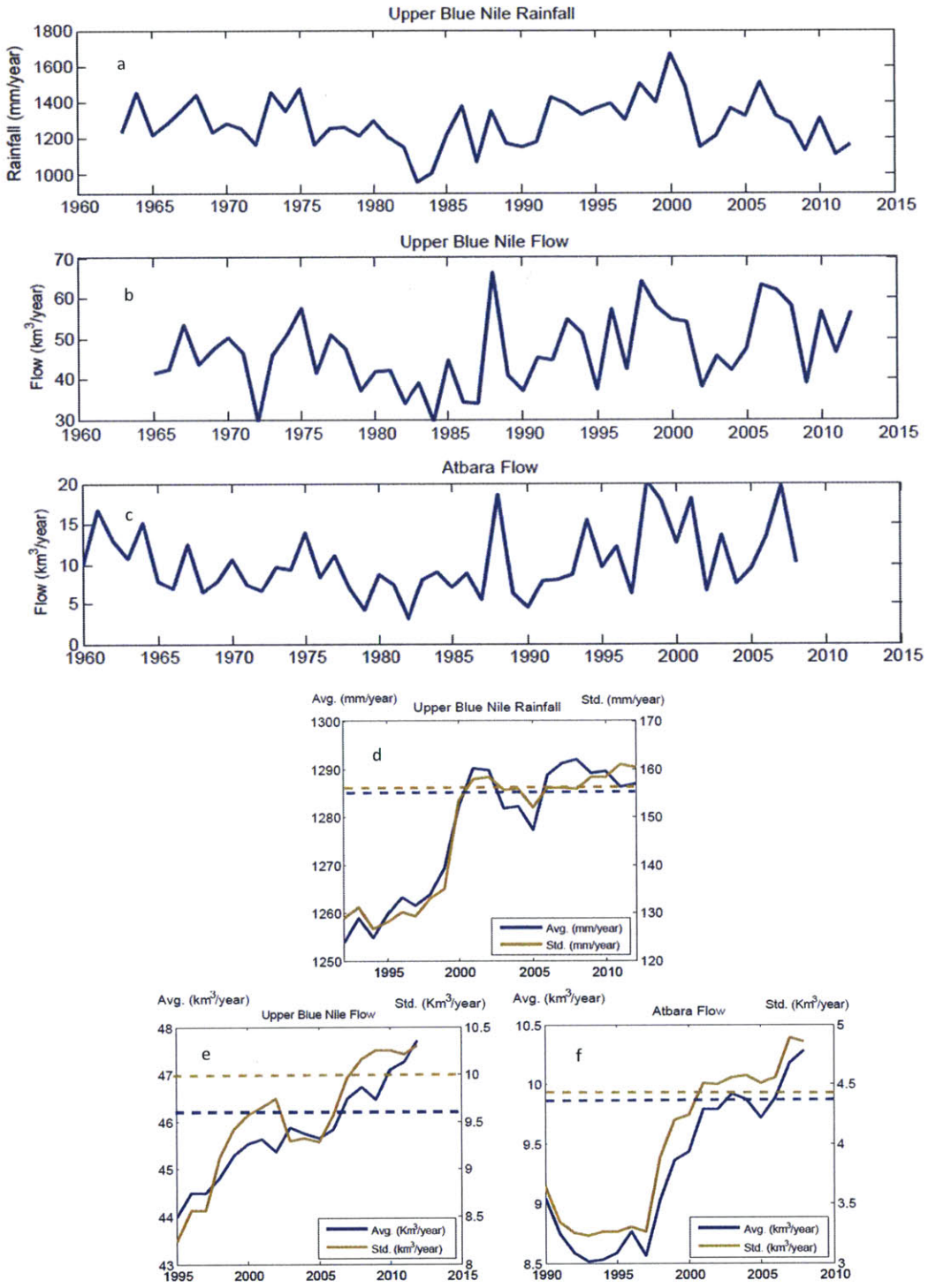


**Figure 4. 2:** Observed stream flows and rainfall, and moving averages for the mean and standard deviation for the Upper Blue Nile and Atbara basins. (a) time series of the annual rainfall based on the weighted average of rainfall stations over the Upper Blue Nile basin. (b, c) time series of the annual stream flow averaged between June and May for the Upper Blue Nile and Atbara basins, respectively. (d) 30-years moving averages for the rainfall mean and standard deviation of the Upper Blue Nile. (e, f) 30-years moving averages for the stream flow mean and standard deviation of the Upper Blue Nile and Atbara basins respectively. In (d, e, f) the dashed lines in blue and brown are the 90% confidence levels of the mean and standard deviation using the t-test and Chi-square distributions, respectively, based on the mean and standard deviation of the periods (1965-1995) and (1960-1990) for the Upper Blue Nile and Atbara, respectively.

## 4.3 Future Changes in the flow of the Nile basin

### 4.3.1 Analysis of changes in mean and variability using simulated runoff by GCMs

Several GCMs are used to predict the future trends in the flow of the Nile basin. 18 GCMs that participated in the Coupled Model Inter-comparison Project Phase 5 (CMIP5) with the Representative Concentration Pathway (RCP 8.5) for future projected emissions of greenhouse gases were selected for use in this study (Table 4.1) (Taylor et al., 2015). The selected models were identified in previous studies by other research groups to be the best in simulating the frequency of El Niño and La Niña events as they have a skewness of rainfall over the Nino3 region greater than 1 and were able to simulate at least one event of extreme El Niño (Details of these studies are discussed in Appendix A) (Cai et al., 2014, Cai et al., 2015). ENSO is one of the most important phenomena shaping tropical climate. Hence, models used to predict the future climate in any tropical region should have credibility in simulating this phenomenon.

The increase in the mean and standard deviation shown in the previous section for the past are predicted to persist during the twenty-first century, as evident in the runoff simulated by the GCMs (indicated by the multi-model ensemble average, thick red line, Figures 4.3, Figure 4.4 and Figure 4.5). The long-term mean and standard deviation of annual river flow are expected to increase by almost 15% and 50% respectively for the 21$^{st}$ century (2000-2100) compared the 20$^{th}$ century (1900-2000). Hence, it is concluded that the projected relative changes in interannual variability are significantly larger than the corresponding change in long-term mean flow. This conclusion is consistent with the magnitudes of the changes that has already been observed in the Nile river flow (See Figure 4.2).

**Table 4.1:** Summary of Global Climate Models (GCMs) used in this study

| Models | AGCM (Lon. x Lat.) | Agency |
|---|---|---|
| 1- BCC-CSM1-1M | 1.12° × 1.12° | Beijing Climate Center, China Meteorological Administration |
| 2- BCC-CSM1-1 | 2.8° × 2.8° | Beijing Climate Center, China Meteorological Administration |
| 3- CCSM4 | 1.25° × 0.94° | National Center of Atmospheric Research, USA |
| 4- CMCC-CMs | 1.88° × 1.87° | Centro Euro-Mediterraneo per I Cambiamenti Climatici |
| 5- CMCC-CM | 0.75° × 0.75° | Centro Euro-Mediterraneo per I Cambiamenti Climatici |
| 6-CNRM-CM5 | 1.4° × 1.4° | National Centre of Meteorological Research, France |
| 7- GFDL-CM3 | 2.5° × 2.0° | NOAA Geophysical Fluid Dynamics Laboratory, USA |
| 8- GFDL-ESM2G | 2.5° × 2.0° | NOAA Geophysical Fluid Dynamics Laboratory, USA |
| 9- GFDL-ESM2M | 2.5° × 2.0° | NOAA Geophysical Fluid Dynamics Laboratory, USA |
| 10- MPI-ESM-MR | 1.88° × 1.87° | Max Planck Institute for Meteorology, Germany |
| 11- MRI-CGCM3 | 1.1° × 1.1° | Meteorological Research Institute, Japan |
| 12- NORESM1-ME | 2.5° × 1.9° | Norwegian Climate Center, Norway |
| 13- NORESM1-M | 2.5° × 1.9° | Norwegian Climate Center, Norway |
| 14- CMCC-CESM | 3.75° × 3.71° | Centro Euro-Mediterraneo per I Cambiamenti Climatici |
| 15- CESM1-BGC | 1.2 5° × 0.94° | Community Earth System Model Contributors |
| 16- CESM1-CAM5 | 1.25° × 0.94° | Community Earth System Model Contributors |
| 17- ACCESS1 | 1.25° x1.87° | Commonwealth Scientific and Industrial Research Organization/ Bureau of Meteorology (CSIRO-BOM) |
| 18-FGOALS | 2.8 ° × 2.8° | LASG, Institute of Atmospheric Physics, Chinese Academy of Sciences |

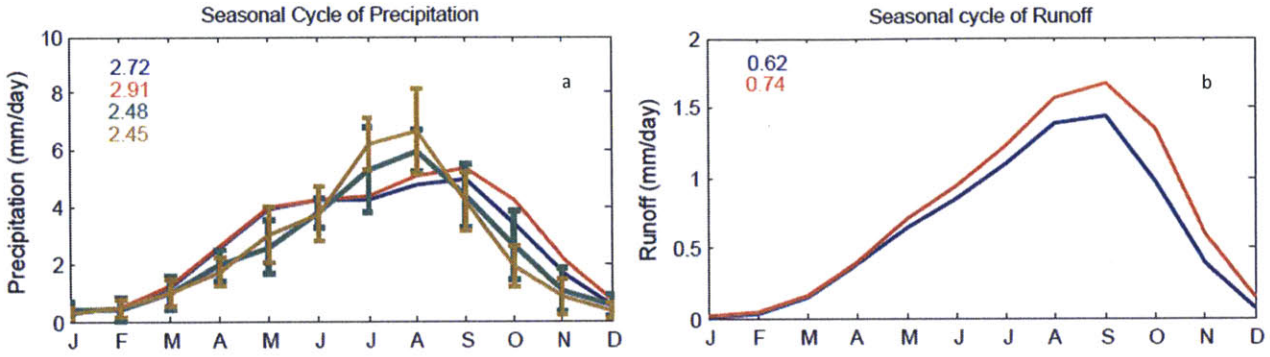


**Figure 4. 3:** Seasonal cycles of rainfall and runoff. (a, b) Seasonal cycle of rainfall and runoff over the Eastern Nile basin, where the blue and red lines are the averages of the periods (1900-2000) and (2000-2100), respectively. The error bars are for the standard deviation of the rainfall for each month. In (a, b) the numbers in blue and red are the annual averages for the periods (1900-2000) and (2000-2100), respectively, and the green and brown numbers are the annual average of rainfall for the observation from TRMM V7-3B43 and CRU TS 3.1, respectively.

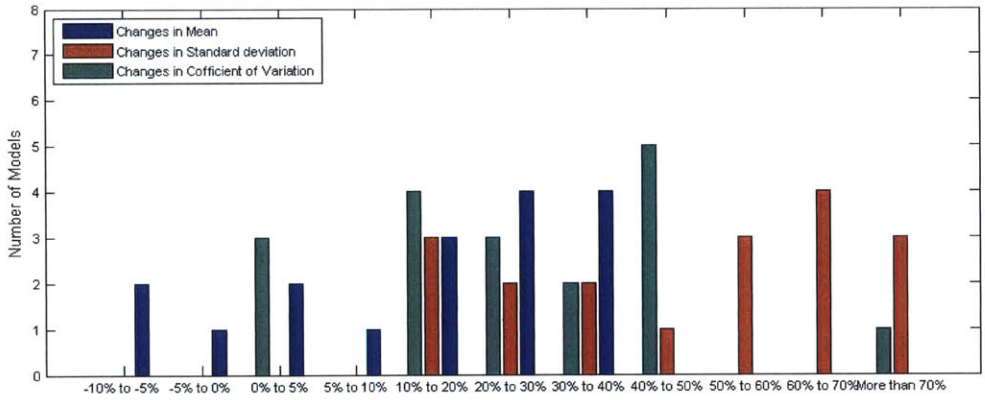


**Figure 4. 4:** The mean, standard deviation and coefficient of variation for the runoff simulated by 18 CMIP5 GCMs over the Eastern Nile basin. Percent changes in the mean, standard deviation and coefficient of variation for the period (2000-2100) relative to the period (1900-2000) showing the number of models that fall in each group of these percent changes.

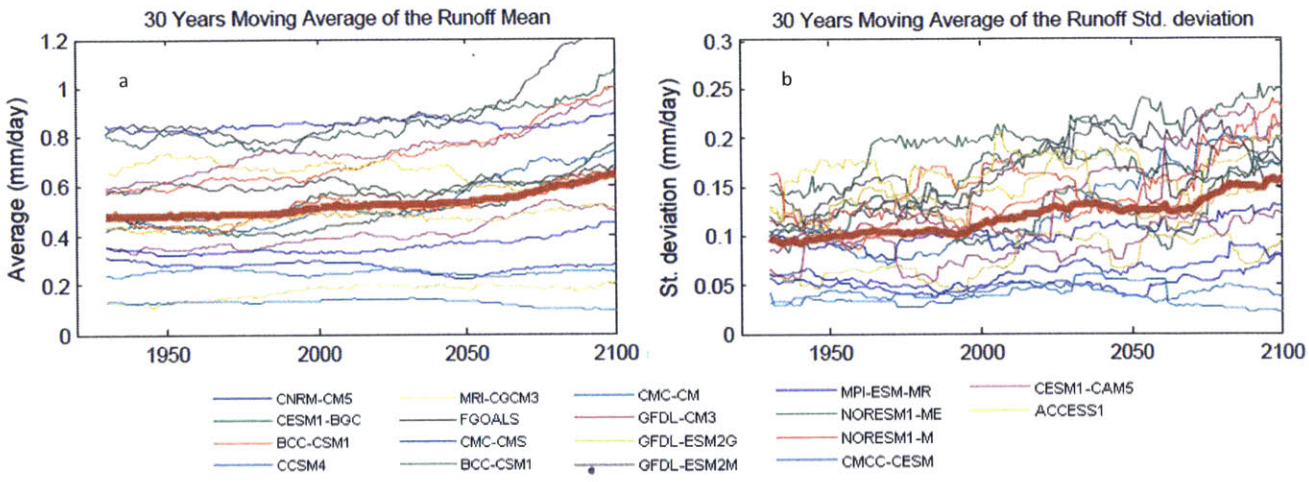


**Figure 4. 5:** The moving averages for the mean and standard deviation and frequency distribution of flow over Eastern Nile basin using 18 CMIP5 GCMs. (a, b) 30-year moving averages of the mean and standard deviation of the runoff simulated by the models from 1900 to 2100, the 95% confidence levels of the mean and standard deviation using Student t and Chi-square tests are 0.54 (mm/day) and 0.11 (mm/day), respectively, based on the mean and standard deviation of the period (1900-1930).

In the following sections, a standard bias correction and sampling approaches are used to project the future Nile flows. The main difference between the two approaches is that the sampling approach relies on the frequencies of different El Niño and La Niña events to predict the Nile flows, regardless of the simulated flow by the models. On the other hand, the bias correction approach relies completely on the simulated runoff by the models. The two approaches yield the same conclusions and show similar distributions of the past and future Nile flows

### 4.3.2 Prediction of Nile flow using Bias correction using probability matching method

The bias correction approach was used to correct for bias in hydrological variables in several previous studies (Elshamy et al., 2009; Yamana, 2015; Beyene et al. 2009; Ahmed et al. 2013). In this study, the cumulative distribution function is calculated for the observed annual

average Nile flow at Dongola for the past period (1900-2000). In the following step, the cumulative distribution function is calculated for the annual average simulated runoff by each GCM for the past period (1900-2000). Then, a set of bias correction factors are estimated by the ratio of the observed Nile flow at each cumulative probability to the corresponding Nile flow simulated by the GCM at that same cumulative probability. In other words, for each range of simulated Nile flow values produced by a GCM, a correction factor is estimated that would effectively match the observed and simulated probability distributions of past flows. For the period (2000-2100), the simulated runoff by each GCM is bias corrected by multiplying the GCM simulated value by the corresponding correction factor (Factors for each GCM is shown in Appendix B).

These changes in the mean and variability in the annual flow of Nile river, presented in the previous section, are also evident in the projected change of frequency distribution of the annual Nile flow. The distribution of the flow in the twentieth century is closely clustered around the mean with few extreme events (i.e., below 70 $km^3$/year and higher than 100 $km^3$/year), while the future flows have fewer normal events (i.e., between 70 $km^3$/year and 100 $km^3$/year) and more high flow events (i.e., greater than 100 $km^3$/year) (Figure 4.6).

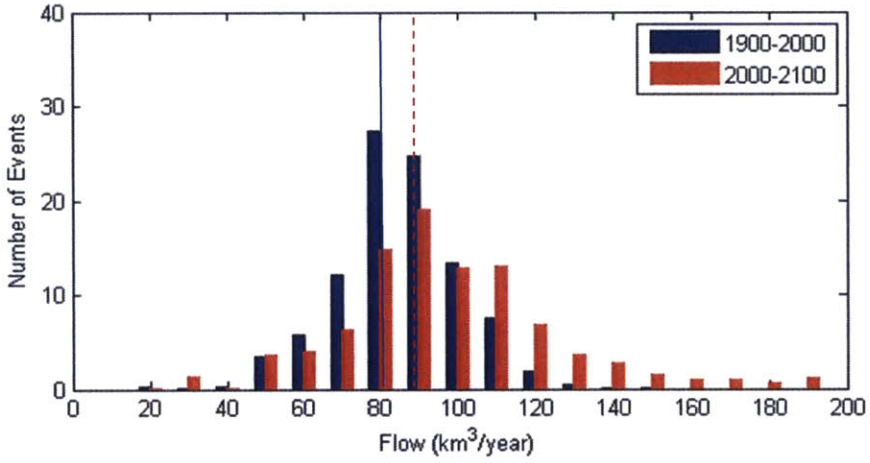


**Figure 4. 6:** The frequency distribution of flow over Eastern Nile basin using 18 CMIP5 GCMs for the past period (1900-2000) and future period (2000-2100). The change in the long-term mean of annual Nile flow for the future period (2000-2100; red dashed lines) is statically significant above the 95% confidence level using Student t-test compared the past period (1900-2000; blue solid lines).

### 4.3.3 Prediction of Nile flow using sampling analysis

The projected increase in the interannual variability of the flow of the Nile river, as shown in the observed stream flows of the major tributaries (Figure 4.2 d, 4.2e and 4.2f) and simulated runoff of the GCMs (Figure 4.4 and Figure 4.5b), is consistent with the increase in the frequencies of El Niño and La Niña events projected by recent studies (Figure 4.7a) (Cai et al., 2014; Cai et al., 2015). Cai et al., 2014 attributed the increase in the frequency of future El Nino events to the faster warming of SST over the eastern Pacific in the future compared to the surrounding ocean waters, which facilitates the occurrence of weak east-west and meridional SST gradients and thus reduces the easterly winds over the equatorial and suppresses the upwelling cold water in the eastern equatorial Pacific and further increases the SST of the eastern equatorial Pacific. Then the center of convection is moved to the equator and extends eastward leading to extreme rainfall over this region and forming extreme El Nino event. On the other hand, the increase of El Nino events provides favourable conditions for the increase of La Nina events. After the discharge of heat associated with El Nino event, the thermocline across the equatorial Pacific shoals and the greenhouse gases forcing continues to warm the ocean surface, which increases the vertical temperature gradient and enhances the Ekman pumping that cools the equatorial central Pacific and enhances the east-west temperature gradient and thus the easterly surface winds, which further enhances the gradient. In addition, the warming over the maritime continent is faster than the central Pacific, which also enhances the east-west temperature gradient leading to the formation of exceptionally cold conditions over the central equatorial Pacific and La Nina event (Cai et al., 2015). More details these studies in presented in Appendix A. Furthermore, the increase of the frequency of El Nino and La Nina events is evident from observations by repeating the spectrum analysis, presented in Chapter 2. Figure 4.8 shows that the magnitude of the spectrum of ENSO is the highest for the period (1965-2012) compared to the other previous periods and the mean of the distribution is around 80 months for the same period, while it is around 95 months for the period (1918-1965) and 89 months for the period (1871-1918). In addition, Table 4.2 shows that the mean of the SST averaged over the ENSO index region, defined in Chapter 2, is continuously increasing and the variability is the

highest for the (1965-2012) compared to the other two periods as shown by the coefficient of variation.

These changes in the frequencies of El Niño and La Niña events would change the Nile flow patterns following the observed tele-connection between ENSO and the Nile, in which El Niño and La Niña events induce low and high flows in the river, respectively (Figure 4.7b) (Eltahir, 1996; Amerasekera et al., 1997; Wang and Eltahir, 1999; Siam et al., 2014; Siam and Eltahir, 2015). This connection between the variability in the flow of Nile river and frequency of El Nino and La Nina events is also evident in Figure 4.9 where the 30-years moving average of the coefficient of variation of stream flow and number of non-neutral years (i.e. years of El Nino and La Nina events) follow each other using observations and GCMs data.

In a different approach to the same problem, the ENSO-Nile tele-connection is used to predict the future Nile flow based on the changes in the frequency of El Niño and La Niña events projected by an ensemble of GCMs.

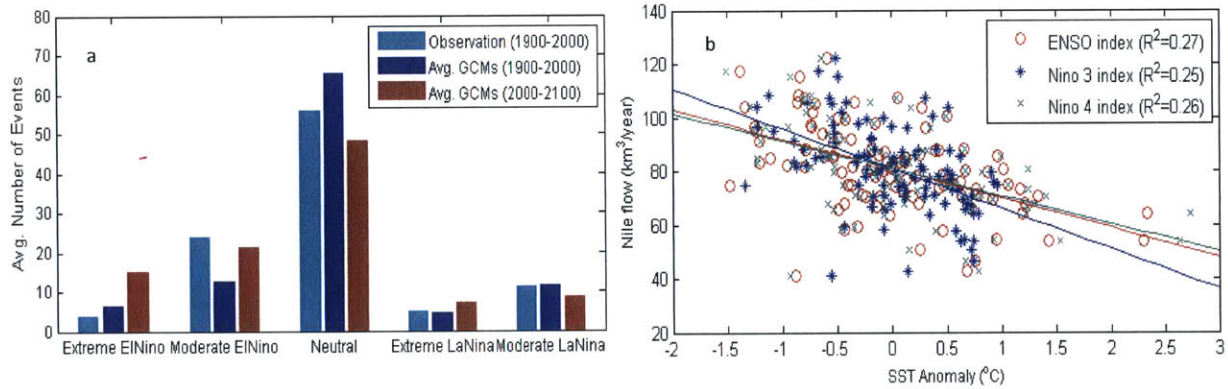


**Figure 4. 7:** Changes in the future Nile flows and their association with changes in the frequencies of El Nino and La Nina through the teleconnection between the Nile and ENSO. (a) Multi-model average changes in the future frequencies of El Nino and La Nina events using 18 CMIP5 GCMs and their comparisons to the observed number of events. (b) Relation between annual Nile flow averaged between June and May and the sea surface temperature over Nino 3 (5◦N-5◦S, 150◦W-90◦W), Nino 4 (5◦N-5◦S, 160◦E-150◦W) and ENSO index (6N–2◦ N, 170– 90◦ W; 2◦ N–6◦ S, 180◦W–90◦ W; and 6◦S–10◦ S, 150◦W–110◦ W).

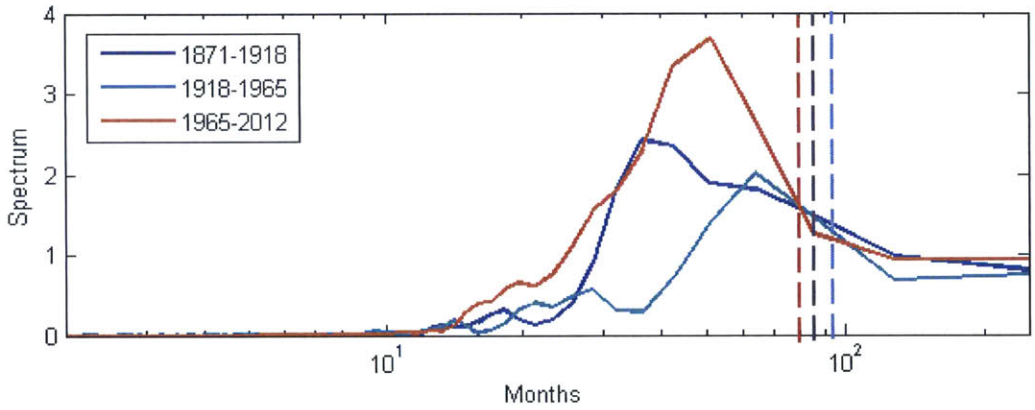


**Figure 4.8:** Spectrum of ENSO for three different periods, 1871-1918 (dark blue line), 1918-1965 (light blue line) and 1965-2012 (red line). The vertical lines are the mean of the distribution.

**Table 4.2:** Summary of the mean, standard deviation and coefficient of variation of ENSO index for three different periods, 1871-1918, 1918-1965, and 1965-2012

| Period | Mean (°C) | Standard deviation (°C) | Coefficient of Variation |
|---|---|---|---|
| **1871-1918** | 26.4 | 0.92 | 0.035 |
| **1918-1965** | 26.5 | 0.87 | 0.032 |
| **1965-2012** | 26.65 | 0.97 | 0.036 |

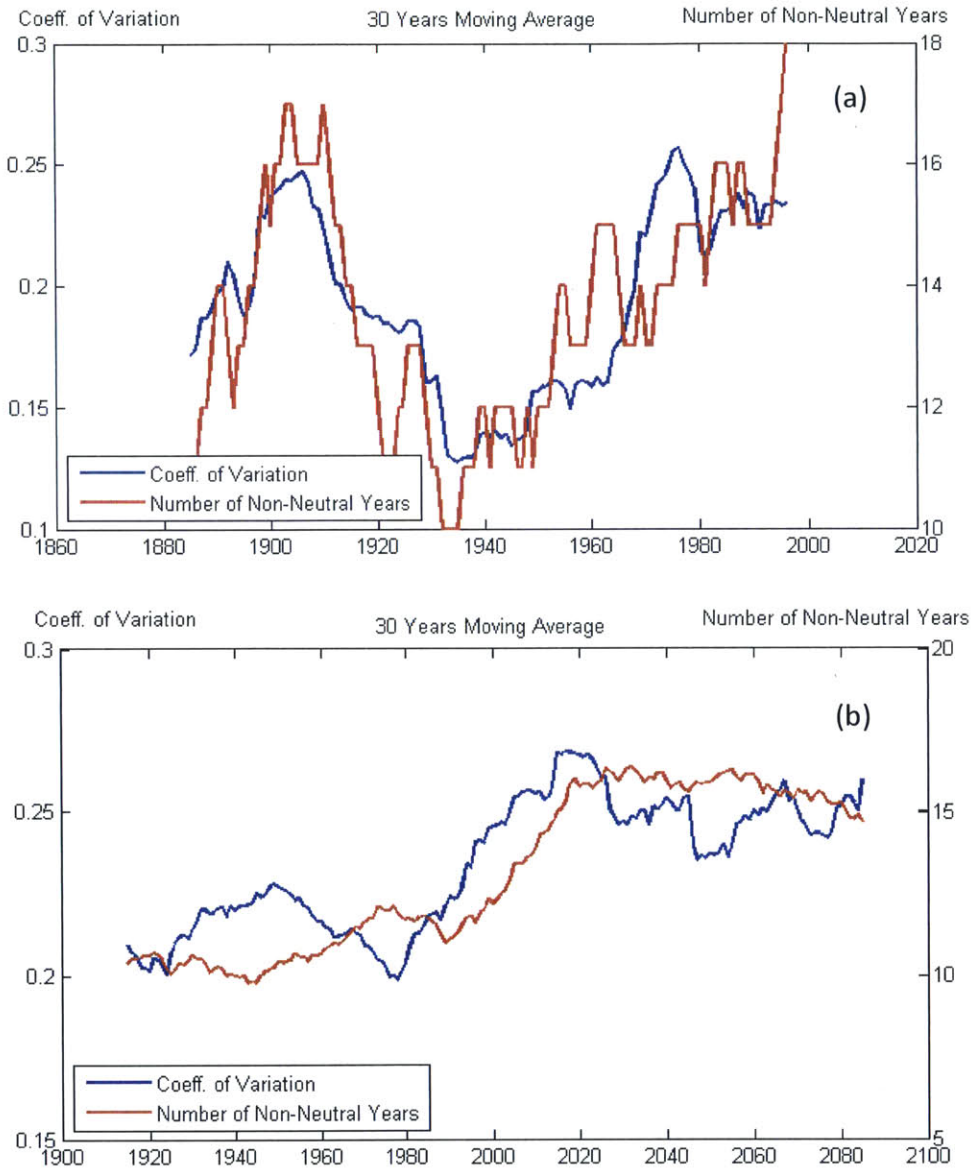


**Figure 4. 9:** 30-years moving averages of the coefficient of variation of the runoff (blue lines) and the number of non-neutral years (red lines). (a) 30-years moving average of the coefficient of variation of the stream flow at Dongola with the number of non-neutral years (red lines). (a) 30-years moving average of the coefficient of variation of the stream flow at Dongola with the number of non-neutral years (i.e. moderate and extreme ElNino and LaNina years). (b) 30-year moving average of ensemble average of the coefficient of variation of 18 GCMs of the runoff of the Eastern Nile basin with the number of non-neutral years (i.e. moderate and extreme ElNino and LaNina years). The 30-years moving average is calculated and displayed at the middle of the 30-years period.

In the sampling approach, the Nile flow is estimated based on the frequency of occurrence of different types of El Niño and La Niña events (i.e., extreme El Niño, moderate El Niño, neutral, extreme La Niña and moderate La Niña). First, we compute the frequency of different events based on sea surface temperature (SST) observations using HadISST for the period (1900-2000) (Rayner et al., 2003). The identification process of the different types of events follows the methodology of previous studies that were investigating the changes in the frequencies of El Niño and La Niña events (Cai et al., 2014, Cai et al., 2015). In these studies, the extreme El Niño events are identified when the average (December-February) rainfall over Nino 3 region is greater than 5 mm/day. However, this condition is replaced by satisfying a SST condition over the Nino 3 region as there is no observed rainfall data available over the oceans for the whole period (1900-2000). It is estimated based on Figure 1d in Cai et al., 2014 that when the rainfall over Nino 3 exceeds 5 mm/day, the average SST anomalies during December to February over Nino 3 are greater than 1.75 times the standard deviation. Thus, extreme ElNiño events are identified when the (December-February) SST anomalies over Nino 3 are greater than 1.75 times the standard deviation. On the other hand, the extreme LaNiña events are identified when the average (December-February) SST anomalies over Nino 4 are less than 1.75 times the standard deviation. The moderate El Niño events are identified when the average (December-February) SST anomalies over Nino 3 are greater than 0.5 times the standard deviation and less than 1.75 times the standard deviation. The moderate La Niña events are identified when the average (December-February) SST anomalies over Nino 4 are less than 0.5 and greater than 1.75 times the standard deviation. The remainder events are considered as neutral events.

Second, for each type of event (i.e. extreme El Niño, moderate La Niña, neutral, extreme La Niña and moderate La Niña) within the past period (1900-2000), the corresponding observed total Nile flows at Dongola are identified and grouped together for each type. The same identification process of the different types is repeated for GCMs simulations for the periods (1900-2000) and (2000-2100). The different types of events are identified for each model and for the past period (1900-2000). Table 4.3 summarizes the number of different El Nino and La Nina events simulated by the GCMs and the corresponding runoff simulated over the ENB for each GCM. Each time the model simulates any event, a value is picked

randomly from the group of the observed Nile flow values for this type of event and is assigned to be the corresponding Nile flow. This step is repeated for the future period (2000-2100), however, the magnitude of assigned flow is modified by the ratio of the simulated future runoff over ENB for that type of event in the period (2000-2100) to the past simulated runoff over ENB for the same type of event in the period (1900-2000).

The future Nile flows estimated based on future El Niño and La Niña events exhibit the same changes in the mean, interannual variability and frequency distribution as the simulated runoff by the GCMs (Figure 4.10). The agreement between the changes in the future flows predicted using these two different approaches (i.e. simulated flow by the GCMs and based on projected changes in El Niño and La Niña events) increase our confidence in the predicted changes and support the mechanism proposed to explain the future changes in the Nile flows.

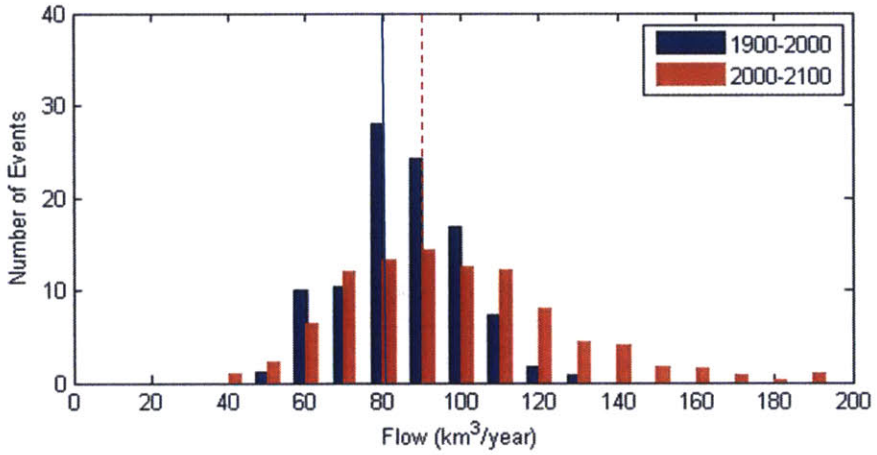


**Figure 4. 10:** The frequency distribution of flow over Eastern Nile basin using 18 CMIP5 GCMs. The change in the long-term average of annual Nile flow for the future period (2000-2100; red dashed lines) is statically significant above the 95% confidence level using Student t-test compared the past period (1900-2000; blue solid lines).

**Table 4.3:** Number of different El Nino and La Nina events simulated by the GCMs and the corresponding runoff simulated over the Eastern Nile basin (ENB).

| | | Moderate El Nino | | Extreme El Nino | | Moderate La Nina | | Extreme La Nina | | Neutral Years | |
|---|---|---|---|---|---|---|---|---|---|---|---|
| | | 1900-2000 | 2000-2100 | 1900-2000 | 2000-2100 | 1900-2000 | 2000-2100 | 1900-2000 | 2000-2100 | 1900-2000 | 2000-2100 |
| BCC-CSM1-1M | # of Events | 29 | 26 | 3 | 4 | 13 | 9 | 6 | 7 | 50 | 53 |
| | ENB Runoff | 0.58 | 0.82 | 0.59 | 0.94 | 0.62 | 0.72 | 0.66 | 1.01 | 0.62 | 0.84 |
| BCC-CSM1-1 | # of Events | 29 | 25 | 0 | 1 | 14 | 9 | 5 | 4 | 53 | 59 |
| | ENB Runoff | 0.76 | 0.82 | 0.00 | 0.99 | 0.71 | 1.08 | 0.87 | 0.94 | 0.80 | 0.79 |
| CCSM4 | # of Events | 9 | 6 | 15 | 23 | 14 | 0 | 5 | 3 | 58 | 65 |
| | ENB Runoff | 0.37 | 0.54 | 0.41 | 0.63 | 0.50 | 0.00 | 0.52 | 0.52 | 0.46 | 0.63 |
| CMCC-CMs | # of Events | 9 | 29 | 1 | 9 | 6 | 8 | 7 | 12 | 76 | 39 |
| | ENB Runoff | 0.27 | 0.26 | 0.24 | 0.23 | 0.32 | 0.30 | 0.29 | 0.27 | 0.29 | 0.27 |
| CMCC-CM | # of Events | 13 | 29 | 0 | 3 | 9 | 11 | 7 | 5 | 72 | 48 |
| | ENB Runoff | 0.30 | 0.24 | 0.00 | 0.22 | 0.31 | 0.25 | 0.26 | 0.24 | 0.24 | 0.25 |
| CNRM-CM5 | # of Events | 5 | 5 | 15 | 25 | 15 | 8 | 4 | 3 | 62 | 51 |
| | ENB Runoff | 0.74 | 0.79 | 0.80 | 0.83 | 0.83 | 0.94 | 0.94 | 0.66 | 0.84 | 0.86 |

**Table 4.3 (Continued)**: Number of different El Nino and La Nina events simulated by the GCMs and the corresponding runoff simulated over the Eastern Nile basin (ENB).

| | | Moderate El Nino | | Extreme El Nino | | Moderate La Nina | | Extreme La Nina | | Neutral Years | |
|---|---|---|---|---|---|---|---|---|---|---|---|
| | | 1900 - 2000 | 2000 - 2100 | 1900-2000 | 2000 - 2100 | 1900 - 2000 | 1900 - 2000 | 2000 - 2100 | 1900 - 2000 | 2000 - 2100 | 1900 - 2000 |
| GFDL-CM3 | # of Events | 2 | 5 | 15 | 33 | 13 | 6 | 4 | 11 | 65 | 38 |
| | ENB Runoff | 0.38 | 0.35 | 0.39 | 0.47 | 0.35 | 0.47 | 0.35 | 0.45 | 0.35 | 0.43 |
| GFDL-ESM2G | # of Events | 11 | 43 | 0 | 2 | 17 | 10 | 2 | 8 | 69 | 26 |
| | ENB Runoff | 0.68 | 0.59 | 0.00 | 0.82 | 0.65 | 0.67 | 0.61 | 0.56 | 0.69 | 0.67 |
| GFDL-ESM2M | # of Events | 5 | 39 | 11 | 10 | 13 | 9 | 4 | 4 | 66 | 26 |
| | ENB Runoff | 0.67 | 0.66 | 0.62 | 0.45 | 0.59 | 0.64 | 0.66 | 0.46 | 0.57 | 0.57 |
| MPI-ESM-MR | # of Events | 16 | 38 | 0 | 2 | 14 | 10 | 4 | 8 | 67 | 40 |
| | ENB Runoff | 0.34 | 0.34 | 0.00 | 0.38 | 0.33 | 0.83 | 0.33 | 0.46 | 0.33 | 0.39 |
| MRI-CGCM3 | # of Events | 18 | 28 | 0 | 5 | 14 | 9 | 3 | 11 | 66 | 43 |
| | ENB Runoff | 0.14 | 0.21 | 0.00 | 0.19 | 0.17 | 0.18 | 0.14 | 0.21 | 0.15 | 0.18 |
| NORESM1-ME | # of Events | 8 | 11 | 11 | 13 | 10 | 9 | 3 | 1 | 69 | 63 |
| | ENB Runoff | 0.48 | 0.54 | 0.44 | 0.44 | 0.48 | 0.73 | 0.73 | 0.87 | 0.50 | 0.62 |

**Table 4.3 (Continued)**: Number of different El Nino and La Nina events simulated by the GCMs and the corresponding runoff simulated over the Eastern Nile basin (ENB).

| | | Moderate El Nino | | Extreme El Nino | | Moderate La Nina | | Extreme La Nina | | Neutral Years | |
|---|---|---|---|---|---|---|---|---|---|---|---|
| | | 1900-2000 | 2000-2100 | 1900-2000 | 2000-2100 | 1900-2000 | 1900-2000 | 2000-2100 | 1900-2000 | 2000-2100 | 1900-2000 |
| NORESM 1-M | # of Events | 1 | 14 | 17 | 11 | 9 | 10 | 7 | 2 | 67 | 53 |
| | ENB Runoff | 0.50 | 0.46 | 0.40 | 0.53 | 0.54 | 0.71 | 0.60 | 0.55 | 0.47 | 0.57 |
| CMCC-CESM | # of Events | 11 | 22 | 4 | 17 | 13 | 21 | 3 | 4 | 68 | 32 |
| | ENB Runoff | 0.13 | 0.13 | 0.12 | 0.10 | 0.14 | 0.12 | 0.14 | 0.17 | 0.13 | 0.11 |
| CESM1-BGC | # of Events | 6 | 6 | 10 | 23 | 13 | 9 | 4 | 3 | 67 | 55 |
| | ENB Runoff | 0.45 | 0.49 | 0.37 | 0.58 | 0.49 | 0.57 | 0.41 | 0.75 | 0.41 | 0.60 |
| CESM1-CAM5 | # of Events | 9 | 17 | 5 | 18 | 14 | 21 | 3 | 7 | 69 | 33 |
| | ENB Runoff | 0.59 | 0.75 | 0.82 | 0.80 | 0.69 | 0.90 | 0.75 | 1.18 | 0.65 | 0.77 |
| ACCES1 | # of Events | 1 | 0 | 34 | 59 | 13 | 8 | 5 | 5 | 47 | 26 |
| | ENB Runoff | 0.47 | 0.00 | 0.46 | 0.48 | 0.40 | 0.50 | 0.49 | 0.43 | 0.44 | 0.49 |
| FGOALS | # of Events | 2 | 6 | 21 | 18 | 14 | 9 | 4 | 6 | 59 | 58 |
| | ENB Runoff | 0.71 | 0.89 | 0.72 | 0.67 | 0.93 | 1.07 | 0.99 | 1.10 | 0.81 | 1.07 |

- **All the runoff values are in (mm/day).**

### 4.3.4 Sensitivity of the results to changing the GCMs selection

In the following analysis, the robustness of the projected changes in the future Nile flow is tested using different combination of GCMs to show that these changes are independent of the choice of GCMs. The GCMs are divided to five different groups according the different criteria.

Group 1 includes the GCMs that simulate correctly the teleconnection between Nile flow and ENSO. Each GCM is evaluated based on its ability to simulate the teleconnection between Nile flow and ENSO for four different criteria (i.e., the Nile flow simulated during extreme El Nino years is less than that of extreme La Nina years; the Nile flow simulated during moderate El Nino years is less than that of moderate La Nina years; the Nile flow simulated during moderate El Nino years is less than that of neutral years; and the Nile flow simulated during moderate La Nina years is greater than that of neutral years).

Group 2 includes the GCMs that are able to simulate at least three out of four teleconnection between ENSO and the Nile flow as previously described, and the coefficient of determination between the average annual seasonal cycle of the simulated rainfall over the ENB compared to observation from TRMM-V73B43 is at least 50% and the simulated rainfall is within ±20% of the observations.

Group 3 combines the GCMs that meet all four teleconnection criteria, and the coefficient of determination between the average annual seasonal cycle of the simulated rainfall over the ENB compared to observations from TRMM-V73B43 is at least 50% and the simulated rainfall is within ±20% of the observations.

Group 4 includes the GCMs that are the best in simulating the different ENSO feedbacks depicted by Bjerknes index (Kim et al., 2014). These GCMs are able to simulate the different air-sea feedback processes that includes weakening of the deep cold water upwelling because of increased anomalous westerly winds during El Nino event, which flattens the thermocline and enhances the warming over the central Pacific, which further enhances the westerly winds.

Group 5 includes the GCMs that have the highest spatial resolution as the models with the highest resolution tend to better represent the rainfall seasonal cycle over the basin (Siam et al., 2013) (i.e., higher than $1.5^{o}$ x $1.5^{o}$), and the coefficient of determination between the average annual seasonal cycle of the simulated rainfall over the ENB compared to observations from TRMM-V73B43 is at least 50% and the simulated rainfall is within ±20% of the observations. In addition, the analysis presented in chapter 3 on the effect of the resolution on the simulation of the hydrological cycle over the ENB is repeated for the 18 GCMs discussed in this chapter. These results are presented in Appendix .It is important to note that the GCMs of Group 3 are also high resolution GCMs, and satisfy the tele-connection criteria.

Figures 4.11 and 4.12 show the changes in the future Nile flows for the different groups of GCMs based on sampling and bias correction approaches respectively. For the two approaches and using any combination of models, the changes are almost the same in the distribution of the Nile flows (i.e. the number of average flow events decreases, while the extreme wet events increases). The changes are also reflected in the changes of the mean, standard deviation and $10^{th}$ and $90^{th}$ percentile of future flows compared to the past as shown in table 4.5 where the mean and standard deviation increase by almost 15% and 50% respectively in the future compared to the past.

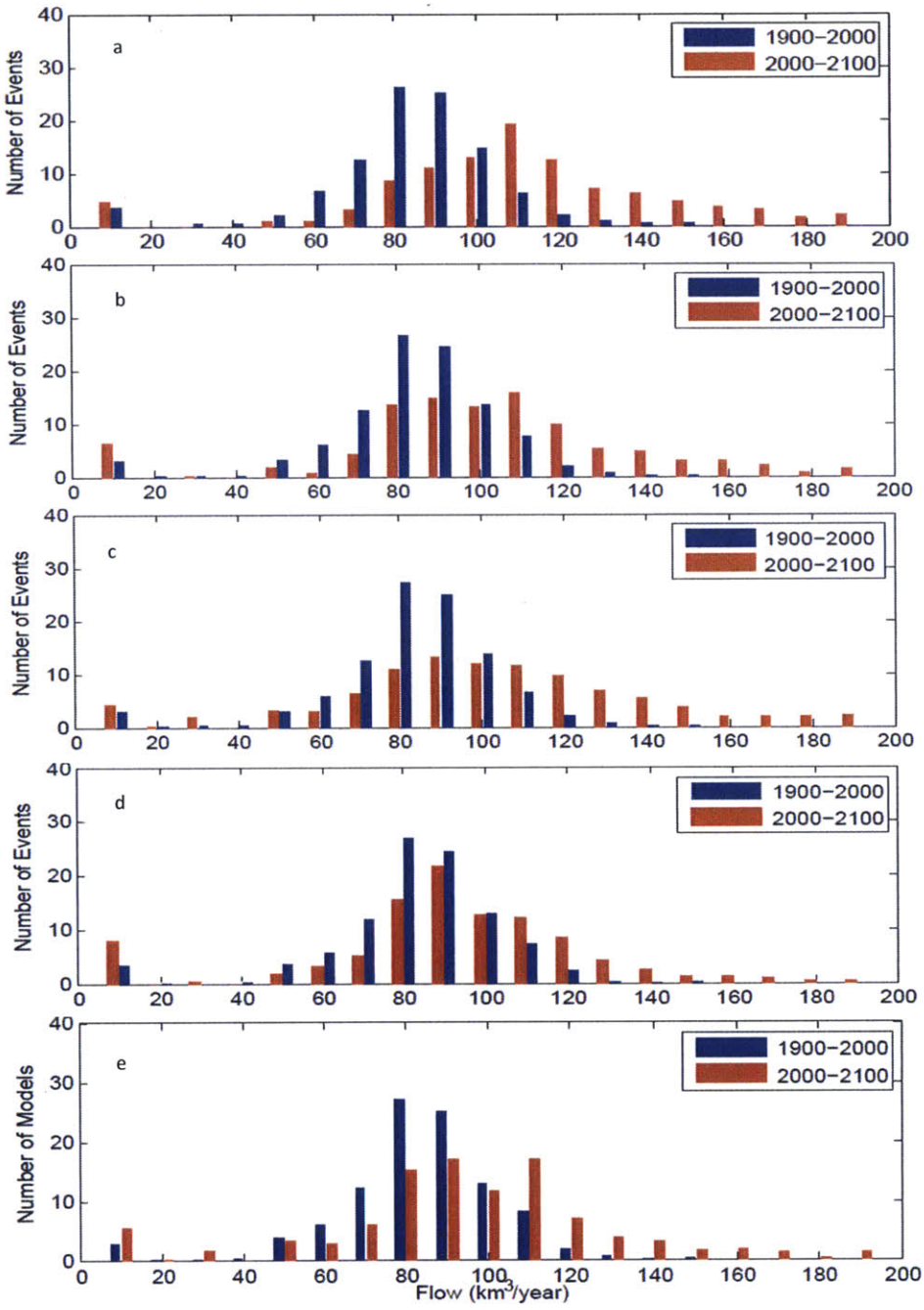


**Figure 4. 11:** The future Nile flows using different combinations of GCMs based on bias correction approach. (a, b, c, d, e) are the flow distributions for the different combinations of GCMs, which represent Group 1, 2, 3, 4 and 5, respectively. The future flows for the period (2000-2100) are in red and the past flows for period (1900-2000) are in blue.

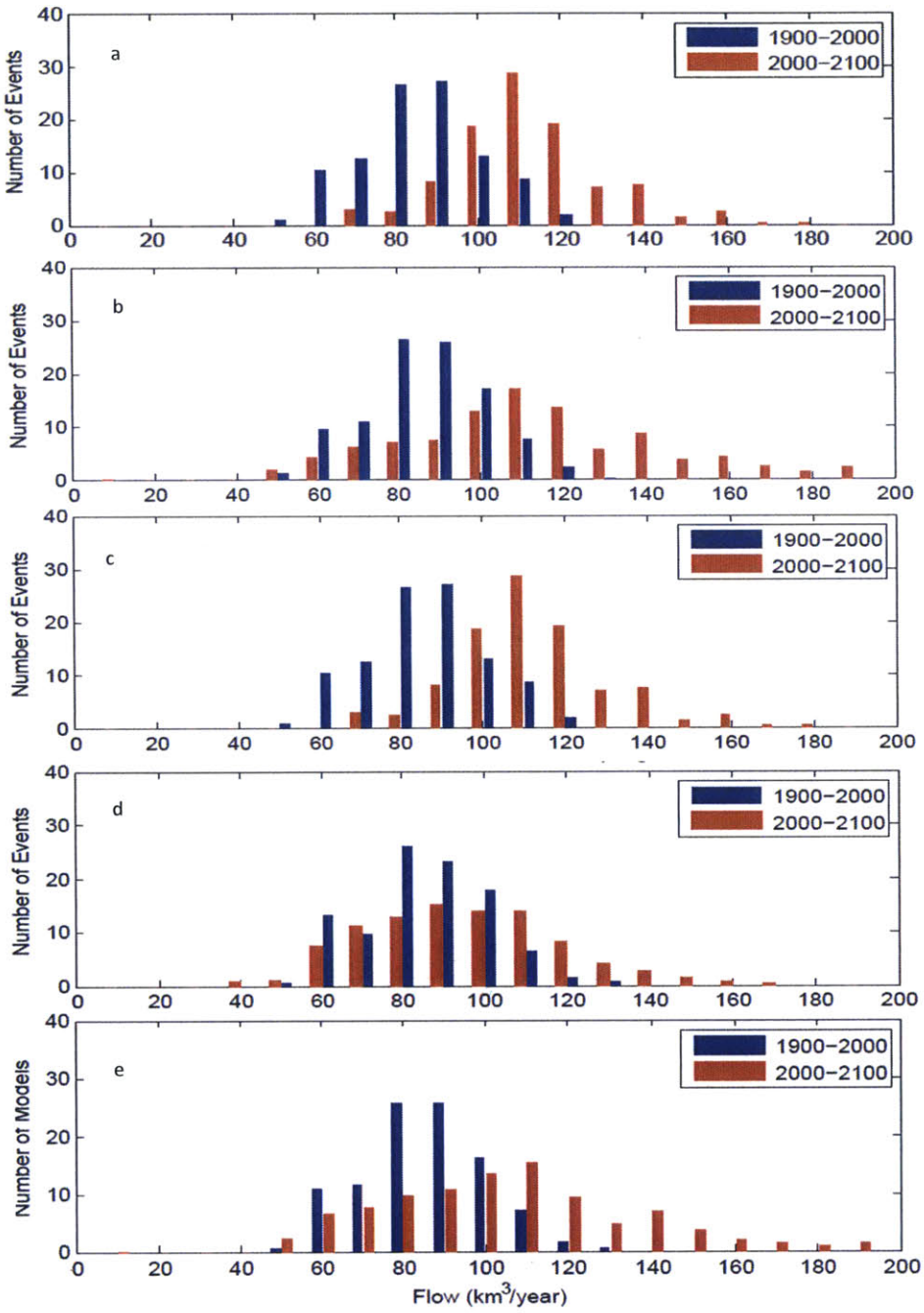


**Figure 4. 12:** The future Nile flows using different combinations of GCMs based on a sampling approach. (a, b, c, d, e) are the flow distributions for the different combinations of GCMs, which represent Group 1, 2, 3, 4 and 5, respectively. The future flows for the period (2000-2100) are in red and the past flows for period (1900-2000) are in blue.

**Table 4.4:** Summary of the runoff simulated over the Eastern Nile basin during different El Nino and La Nina types for different combinations of GCMs.

| Runoff | Extreme El Nino | Moderate El Nino | Neutral | Extreme La Nina | Moderate La Nina |
|---|---|---|---|---|---|
| **All GCMs (1900-2000)** | 0.58/0.21 | 0.54/0.21 | 0.56/0.24 | 0.61/0.29 | 0.58/0.25 |
| **Group 1 (1900-2000): BCC-CSM1-1M, CCSM4, CMCC-CMS, MRI-CGCM3, FGOALS** | 0.55/0.22 | 0.49/0.27 | 0.54/0.3 | 0.62/0.39 | 0.61/0.36 |
| **Group 2 (1900-2000): BCC-CSM1-1M, CCSM4, CNRM-CM5, CESM1-BGC** | 0.54/0.19 | 0.54/0.16 | 0.58/0.19 | 0.64/0.23 | 0.61/0.16 |
| **Group 3 (1900-2000): BCC-CSM1-1M, CCSM4** | 0.5/0.13 | 0.48/0.15 | 0.54/0.12 | 0.59/0.1 | 0.56/0.09 |
| **Group 4 (1900-2000): CCSM4, GFDL-CM3, GFDL-ESM2M, NOREMS1-ME, NORESM1-1M, ACCESS1** | 0.76/0.08 | 0.75/0.11 | 0.76/0.79 | 0.84/0.13 | 0.77/0.09 |
| **Group 5 (1900-2000): BCC-CSM1-1M, CCSM4, CMCC-CMS, CNRM-CM5, MPI-ESM-MR, CESM1-BGC, CESM1-CAM5, ACCESS1** | 0.53/0.22 | 0.48/0.15 | 0.5/0.18 | 0.55/0.22 | 0.52/0.18 |
| **All GCMs (2000-2100)** | 0.65/0.36 | 0.64/0.29 | 0.66/0.39 | 0.73/0.5 | 0.71/0.34 |
| **Group 1 (2000-2100): BCC-CSM1-1M, CCSM4, CMCC-CMS, MRI-CGCM3, FGOALS** | 0.71/0.53 | 0.66/0.41 | 0.77/0.54 | 0.91/0.80 | 0.73/0.51 |
| **Group 2 (2000-2100): BCC-CSM1-1M, CCSM4, CNRM-CM5, CESM1-BGC** | 0.74/0.17 | 0.66/0.17 | 0.73/0.14 | 0.73/0.21 | 0.74/0.18 |
| **Group 3 (2000-2100): BCC-CSM1-1M, CCSM4** | 0.79/0.2 | 0.68/0.21 | 0.73/0.15 | 0.76/0.35 | 0.72/NA |
| **Group 4 (2000-2100): CCSM4, GFDL-CM3, GFDL-ESM2M, NOREMS1-ME, NORESM1-1M, ACCESS1** | 0.83/0.07 | 0.77/0.23 | 0.87/0.84 | 0.87/0.17 | 0.99/0.12 |
| **Group 5 (2000-2100): BCC-CSM1-1M, CCSM4, CMCC-CMS, CNRM-CM5, MPI-ESM-MR, CESM1-BGC, CESM1-CAM5, ACCESS1** | 0.61/0.24 | 0.57/0.23 | 0.61/0.21 | 0.66/0.31 | 0.68/0.23 |
| **Observed corresponding Nile Flow ($km^3$/year)** | 60.4 | 72.6 | 83.2 | 95.8 | 87.1 |

Notes: All the values are in (mm/day).The first number is the multi-model average runoff simulated over the Eastern Nile basin by the different GCMs for each type of event and the second number is the multi-model standard deviation of the simulated runoff by these GCMs.

**Table 4.5:** Statistics of the change in the Nile flow for the different combinations of GCMs estimated using the bias correction and sampling approaches. The statistics include changes in the mean, standard deviation and 10th and 90th percentile of the flows.

| Model | Period | Bias Correction | | | | Flow Sampling | | | |
|---|---|---|---|---|---|---|---|---|---|
| | | Mean | Standard deviation | 10 Percentile | 90 Percentile | Mean | Standard deviation | 10 Percentile | 90 Percentile |
| Group 1 | 1900-2000 | 80.70 | 16.64 | 63.05 | 101.70 | 79.65 | 15.90 | 63.90 | 103.70 |
| | 2000-2100 | 109.84 | 29.03 | 76.10 | 145.75 | 108.58 | 17.91 | 80.00 | 134.10 |
| Group 2 | 1900-2000 | 80.37 | 16.48 | 61.00 | 101.08 | 79.46 | 16.35 | 60.78 | 102.98 |
| | 2000-2100 | 102.24 | 26.09 | 73.90 | 137.00 | 101.01 | 20.19 | 74.70 | 128.98 |
| Group 3 | 1900-2000 | 79.96 | 16.14 | 61.87 | 100.00 | 80.50 | 15.75 | 61.07 | 100.58 |
| | 2000-2100 | 101.44 | 28.91 | 65.58 | 136.03 | 109.61 | 27.85 | 73.18 | 140.80 |
| Group 4 | 1900-2000 | 80.25 | 16.15 | 61.34 | 100.60 | 78.99 | 16.59 | 59.24 | 101.61 |
| | 2000-2100 | 93.30 | 21.72 | 68.11 | 120.90 | 89.10 | 21.87 | 64.14 | 117.67 |
| Group 5 | 1900-2000 | 80.32 | 16.1 | 61.1 | 100.7 | 79.95 | 15.28 | 59.7 | 101.9 |
| | 2000-2100 | 94.03 | 24.84 | 66 | 124.3 | 94.57 | 24.53 | 65.4 | 123.8 |
| All GMCs | 1900-2000 | 79.98 | 15.99 | 60.9 | 100.7 | 80.12 | 16.2 | 60.4 | 100.9 |
| | 2000-2100 | 92.16 | 23.8 | 64.7 | 120.7 | 93.38 | 25.28 | 64.1 | 122.7 |

Table 4.6 shows the results Mann-Kendall test of the trends in the time series of the Nile flow for the sampling, bias correction and simulated runoff by the GCMs. Most of the GCMs show a positive trend in the flow with time and only three models show a significant negative trend. The number of GCMs with statistically significant and positive trends are 12, 10, and 12 out of 18 GCMs for the bias correction, sampling and raw data respectively. The corresponding number of GCMs with statistically significant and negative trends are 2, 3, and 3 out of 18 GCMs. Furthermore, table 4.7 shows the results of Kolmogorov–Smirnov test of the changes in the distribution of the future Nile flow for the sampling, bias correction and simulated runoff by the GCMs. At least 14 out 18 GCMs show significant change in the distribution of the future Nile flow compared to the past using three approaches.

**Table 4.6:** Mann-Kendall coefficients (tau) for the trends in the time series of the Nile flow (1900-2100) for the different GCMs, calculated for the simulated runoff (raw data), and using the flows estimated with the bias correction, and sampling approaches.

| | Bias Correction | Sampling | Raw Data |
|---|---|---|---|
| **CNRM-CM5** | 0.07 | -0.07 | 0.07 |
| **CESM1-BGC** | 0.42* | 0.15* | 0.41* |
| **BCC-CSM1-1M** | 0.48* | 0.44* | 0.49* |
| **CCSM4** | 0.42* | 0.27* | 0.42* |
| **MRI-CGCM3** | 0.26* | 0.2* | 0.23* |
| **FGOALS** | 0.36* | 0.34* | 0.36* |
| **CMC-CMS** | -0.14* | -0.18* | -0.17* |
| **BCC-CSM1-1** | 0.21* | 0.04 | 0.22* |
| **CMC-CM** | -0.03 | -0.09 | -0.04 |
| **GFDL-CM3** | 0.35* | 0.19* | 0.35* |
| **GFDL-ESM2G** | -0.07 | -0.18* | -0.13* |
| **GFDL-ESM2M** | 0.06 | -0.07 | 0.08 |
| **MPI-ESM-MR** | 0.21* | 0.19* | 0.24* |
| **NORESM1-ME** | 0.26* | 0.27* | 0.27* |
| **NORESM1-M** | 0.25* | 0.16* | 0.19* |
| **CMCC-CESM** | -0.21* | -0.06 | -0.22* |
| **CESM1-CAM5** | 0.4* | 0.14* | 0.41* |
| **ACCESS1** | 0.09 | -0.05 | 0.12* |

*Indicates values that are significant at 5% significance level

**Table 4.7:** The test statistic of the Kolmogorov–Smirnov test for the change in the distribution of the future Nile flow (2000-2100) relative the past (1900-2000) calculated for the runoff simulated by the GCMs (raw data) and using the flows estimated with the bias correction and sampling approaches.

| | Bias Correction | Sampling | Raw Data |
|---|---|---|---|
| **CNRM-CM5** | 0.14 | 0.18 | 0.14 |
| **CESM1-BGC** | 0.47* | 0.38* | 0.45* |
| **BCC-CSM1-1M** | 0.62* | 0.72* | 0.62* |
| **CCSM4** | 0.51* | 0.45* | 0.49* |
| **MRI-CGCM3** | 0.28* | 0.41* | 0.27* |
| **FGOALS** | 0.46* | 0.68* | 0.44* |
| **CMC-CMS** | 0.33* | 0.31* | 0.33* |
| **BCC-CSM1-1** | 0.29* | 0.11 | 0.28* |
| **CMC-CM** | 0.09 | 0.22* | 0.09 |
| **GFDL-CM3** | 0.42* | 0.37* | 0.41* |
| **GFDL-ESM2G** | 0.21* | 0.33* | 0.28* |
| **GFDL-ESM2M** | 0.11 | 0.2* | 0.16 |
| **MPI-ESM-MR** | 0.31* | 0.33* | 0.34* |
| **NORESM1-ME** | 0.37* | 0.42* | 0.36* |
| **NORESM1-M** | 0.28* | 0.31 | 0.24* |
| **CMCC-CESM** | 0.25* | 0.09 | 0.27* |
| **CESM1-CAM5** | 0.41* | 0.38* | 0.42* |
| **ACCESS1** | 0.14 | 0.23* | 0.16 |

*Indicates values that are significant at 5% significance level

## 4.4 Implications of the changes in the mean and variability of the Nile flow on the water storage capacity

Several previous studies investigated the water storage capacity required to control the variability in the flow of a certain river over certain periods (Hurst, 1951; Hurst et al., 1965). The storage capacity required to accommodate the variability in any river flow and to supply an equal flow each year (i.e., the long term average) over a certain period of time (N) can be calculated by taking the departures of the flow from the mean and summing these departures. Thus, the difference between the maximum and minimum of these continued sums is the required storage capacity. Several phenomenon, including the Nile flow, which have long time series follow a certain relation between the range (R) defined as the difference of maximum and minimum continued sum, the standard deviation ($\sigma$), and N (Hurst, 1951). The relation has the form $R/\sigma = (N/2)^k$, where k is the Hurst coefficient (Hurst, 1951). The Hurst coefficient can be estimated by fitting the relation between ($R/\sigma$) and (N/2) for different lengths of the time series of length (N).

For the Nile basin, the required storage capacity to provide a yield each year equal to the mean of the flow for N years, is proportional to $N^{0.72}$ where 0.72 is the Hurst coefficient that depends on the sequence and variability in the time series of the flow. For N = 100 years, the corresponding storage capacity in the Nile flow at Dongola is approximately 345 $Km^3$. In this study, the Hurst coefficient (k) is calculated for each GCMs simulations for the past (1900-2000) and future (2000-2100) periods and estimated the changes in the required storage capacity to accommodate the future Nile flows with the enhanced variability. The summary of the changes in the 100 year-storage and Hurst coefficients for the different GCMs is presented in Table 4.8.

**Table 4.8:** Changes in the Hurst coefficients and corresponding changes in the 100-year storage (R100) required to accommodate the change in the future Nile flows using the bias correction and sampling approaches.

| | Hurst coefficient | | | | R100 | | | |
|---|---|---|---|---|---|---|---|---|
| | Bias Correction | | Sampling | | Bias Correction | | Sampling | |
| Model | 1900-2000 | 2000-2100 | 1900-2000 | 2000-2100 | 1900-2000 | 2000-2100 | 1900-2000 | 2000-2100 |
| BCC-CM1-M | 0.72 | 0.75 | 0.62 | 0.72 | 258.8 | 403.9 | 197.1 | 349.5 |
| BCC-CSM | 0.81 | 0.74 | 0.74 | 0.55 | 359.8 | 502.1 | 270.1 | 196.6 |
| CCSM4 | 0.86 | 0.74 | 0.72 | 0.67 | 514.4 | 661.4 | 240.1 | 205.2 |
| CMCC-CMS | 0.81 | 0.82 | 0.67 | 0.69 | 366.2 | 749.9 | 174.5 | 239.7 |
| CMCC-CM | 0.9 | 0.72 | 0.69 | 0.74 | 566.7 | 310.0 | 221.4 | 294.2 |
| CNRM-CM5 | 0.68 | 0.73 | 0.65 | 0.74 | 237.9 | 317.3 | 203.4 | 287.5 |
| GFDL-CM3 | 0.9 | 0.8 | 0.7 | 0.65 | 543.7 | 456.6 | 250.6 | 314.2 |
| GFDL-ESM2G | 0.78 | 0.77 | 0.81 | 0.67 | 355.0 | 443.9 | 288.4 | 221.9 |
| GFDL-ESM2M | 0.75 | 0.8 | 0.76 | 0.68 | 316.8 | 583.5 | 389.5 | 266.8 |
| MPI-ESM | 0.78 | 0.75 | 0.69 | 0.58 | 314.6 | 368.5 | 239.2 | 412.5 |
| MRI-CGCM3 | 0.8 | 0.7 | 0.69 | 0.7 | 394.9 | 351.0 | 250.0 | 445.6 |
| NORESM1-ME | 0.65 | 0.79 | 0.77 | 0.66 | 193.9 | 403.5 | 333.1 | 368.1 |
| NORESM1-M | 0.86 | 0.76 | 0.7 | 0.57 | 437.5 | 335.3 | 263.8 | 208.7 |
| CMCC-CESM | 0.76 | 0.7 | 0.78 | 0.72 | 309.9 | 406.5 | 432.6 | 410.2 |
| CESM-BGC | 0.75 | 0.82 | 0.72 | 0.72 | 300.8 | 693.1 | 294.1 | 485.6 |
| CESM-CAM5 | 0.73 | 0.76 | 0.63 | 0.7 | 273.3 | 526.4 | 184.5 | 509.2 |
| ACCESS | 0.61 | 0.66 | 0.73 | 0.68 | 183.8 | 231.9 | 290.6 | 340.5 |
| FGOALS | 0.76 | 0.78 | 0.75 | 0.64 | 308.0 | 534.5 | 334.7 | 538.5 |
| Average All GCMs | 0.78 | 0.76 | 0.71 | 0.68 | 346.4 | 460.1 | 269.6 | 338.6 |
| Standard deviation All GCMs | 0.08 | 0.04 | 0.05 | 0.06 | 110.7 | 147.7 | 69.2 | 109.1 |

The relatively large increase in interannual variability in the flow of Nile river dictates an increase of almost 33% in the total storage capacity (from 340 to 460 $Km^3$) that is needed in order to maintain a flow in each year, for over 100 years, equivalent to the long-term mean flow (Figure 4.13a). It is also important to note that the long-term mean flow for the past (1900-2000) was about 80 $km^3$/year, while the mean flow for the future (2000-2100) is projected to be about 92 $km^3$/year. The current total storage capacity in the Eastern Nile river basin is about 155 $km^3$ and is expected to increase to 230 $km^3$ if the GERD is built (Figure 4.13a). Based on the analysis presented in Figure 4.12a, applying the Hurst equation, the current storage in the basin is sufficient for securing a yield equivalent to the observed mean annual flow, for about 40 years. In order to secure a yield equivalent to the projected mean annual flow for a similar 40 years into the future, the storage will have to be expanded by about 55%. However, after GERD is built, the new storage in the basin will be sufficient for securing a yield equivalent to the observed flow, for about 60 years (Figure 4.13a). In order to secure a yield equivalent to the projected mean flow for a similar 60 years into the future, the storage will have to be expanded by about 45%. Thus, it is projected that in the future significant expansion of the current storage capacity will be needed in order to control the enhanced interannual variability in the flow and to capture the additional flow due to climate change. However, this increase in storage capacity may or may not be feasible depending on several factors including the availability of suitable sites for dams, economic considerations, and agreement between the Nile basin countries.

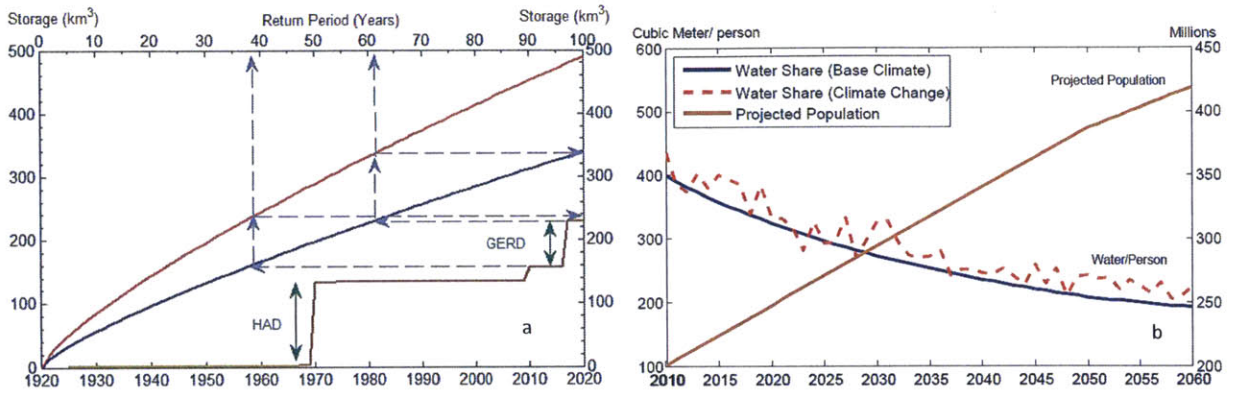


**Figure 4. 13:** Increase in the population with time, total current water storage in the Eastern Nile basin and required changes in future storage to accommodate the effects of climate change. (A) The estimated water storage as function of the return period based on Hurst equation, the blue and red lines are for the base climate (1900-2000) and climate change (2000-2100) periods respectively (See Supplementary materials) and the increase in water storage capacity of the dams in the Eastern Nile basin with time including (Sennar, Khashm El Girba, Roseiras, High Aswan Dam (HAD), Fincha, Meroewe, Tekeze and Grand Ethiopian Renaissance Dam (GERD) to be completed by 2017). (b) Increase in the population (solid brown line) versus the decrease of the water share per person assuming no changes in the flow (i.e., 80 $km^3$/year, which is the long-term average between 1900 and 2000, blue solid line), and the water share per person using the multi-model average time series of the Nile flow predicted using the bias correction (dashed red line).

## 4.5 Conclusions

The lack of consensus between the past studies that investigated the impacts of climate change on the Nile river flow hinders the development of effective climate change adaptation plans. The first implication of our projections regarding the impact of climate change on the Nile flow concerns the availability of water resources. Climate change is likely to increase the mean flow in the basin. This increase in the flow is a welcome change, and can slightly enhance the water share per person and thus reduce the water stress in the basin (Figure 4.12b), but this positive impact will persist for only few years before being overwhelmed by the large decrease in the water share per capita due to the projected population growth. Population growth poses a serious challenge to availability of water in the Nile. Knowledge about the future flow of the Nile river is needed to guide water resources planning including proposals for dams and hydropower projects (e.g. Grand Ethiopian Renaissance dam). Based on our analysis using two different approaches and several different combinations of GCMs results, we project that the mean and variance of the annual flow in the Nile river basin will increase due to climate change. This projected increase may limit the benefits of the projected increase in mean flow and hence motivate a significant increase in the water storage capacity in order to fully utilize the additional water resource. The impacts of climate change are likely to increase the need for building more dams in the Nile basin. All the future projections discussed in this chapter assume a business-as-usual scenario of greenhouse gas emissions. Any effective mitigation efforts are likely to impact these projections and hence reduce the intensity of the projected impacts.

# Chapter 5: Development of New Large-Scale Cloud and Rainfall Parameterizations

## 5.1 Introduction

There is a consensus that climate is changing and that most of the observed warming over the last 50 years is likely to have been due to the increase in greenhouse gas concentrations resulting from anthropogenic activities (Forster et al., 2007). Global Climate Models (GCMs) are commonly used to investigate the impacts of climate change. However, GCMs have resolutions of hundreds of kilometers while studying the impacts of climate change, particularly for regional scale, requires information at much higher spatial resolution. Several downscaling methods are used to bridge this gap in spatial resolution between the GCMs and the required resolution for a climate change study. In general, these methods can be divided in two groups: (i) statistical downscaling and, (ii) dynamical downscaling. The statistical downscaling method is based on establishing a statistical relation for a variable (e.g. rainfall) between the GCMs at low resolution and observation of the same variable at higher resolution for the past. Then, the same relation is applied to statistically downscale this variable for the future using the coarse resolution information from the GCMs. On the other hand, the dynamical downscaling method involves nesting a higher resolution Regional Climate Model (RCM) within a coarser resolution GCM. The RCM uses the GCM to define time-varying atmospheric boundary conditions around a finite domain, within which the physical dynamics of the atmosphere is modelled using horizontal grid spacing of 20-50 km. Furthermore, the main advantage of RCMs is that they can resolve smaller-scale atmospheric features such as orographic rainfall or low-level jets better than the host GCM. In addition, the dynamical downscaling method downscales all the climate variables with a physically based approach, which is not possible to achieve with the statistical downscaling approach. Thus, the dynamical downscaling method is used in this study for the Nile basin as it is more appropriate to resolve the complex topography of the basin.

The first step is using a RCM for climate change study is to verify the model ability to accurately simulate the past climate. In this step, several variables should be verified, not only the variables of interest in the climate change study as it is possible that the model simulates correctly one of the variables because of biases in other variables. In this study, the main purpose is identifying the impacts of climate change on the hydrology of the Nile basin. However, several other processes have direct impact on the water budget of the basin. For example, biases in the cloud coverage may induce biases in the radiation budget at the surface, which may induce biases in the water budget. Several studies have shown that the biases in cloud cover may increase the uncertainty in the climate change predictions because of different feedbacks between the cloud cover, rainfall formation and radiation (Christensen et al., 2007; Soden and Held, 2006; Bony et al., 2006). Thus, an assessment of the accuracy of the Regional climate model is required and the source of biases in the simulation should be identified before using the model to study climate change.

In the second step, modifications and development of new parameterizations for the processes that introduce biases in the simulation should be incorporated to improve the model simulations. In this study, the performance of new parameterizations of large-scale cloud and rainfall are investigated for use within climate models. The performance of the new parameterizations is evaluated within the MIT-Regional Climate Model (MRCM), a modified version of Regional Climate Model, version 3 (RegCM3) including the land surface scheme Integrated Biosphere Simulator (IBIS) and recently developed parameterizations for the convective cloud cover and convective rainfall. The simulations domain cover East Africa and the focus of the simulation is over the Upper Blue Nile basin as it is the main source of water for the Nile basin. The new parameterizations improved the simulations of the water budget, cloud cover, downward shortwave and net radiation at the surface as shown in the following sections.

## 5.2 Model description

### 5.2.1 General Model description

The MIT Regional Climate Model (MRCM) is a modified version of the Regional Climate Model, version 3 (Regcm3) (Pal et al., 2007). It is a three-dimensional, hydrostatic, compressible, primitive equation, sigma-coordinate regional climate model. Regcm3 maintains much of the dynamical core of the fifth-generation Pennsylvania State University-NCAR Mesoscale Model (MM5) and employs NCAR's Community Climate Model version 3 (CCM3) scheme for atmospheric radiative transfer. Planetary boundary layer dynamics follow the formulation of Holtslag et al. (1993). Ocean surface fluxes are handled by Zeng's scheme for bulk aerodynamic ocean flux parameterization (Zeng et al. 1998), where sea surface temperatures are prescribed. It is also coupled to a new land surface scheme with name Integrated Biosphere Simulator (IBIS) by Winter et al., (2009).

The cloud fraction within a grid cell can be created using both convective and large-scale (i.e. resolvable, non-convective) processes. Each type of cloud fraction is calculated independently of the other. Similarly, the rainfall is calculated independently in the form of large scale or convective rainfall and then the two values are added to form the total rainfall. The Subgrid Explicit Moisture Scheme (SUBEX) is used to handle large-scale, resolvable, non-convective clouds and rainfall (Pal et al. 2000). On the other hand, the recently developed parameterizations for the convective cloud and rainfall (Gianotti, and Eltahir, 2014a, 2014b) are used to handle these two variables. In the following sections, we develop new parametrizations for large scale cloud fraction and rainfall that can be implemented within climate models and easily tuned by the user. The new parameterizations depend mainly on the cloud liquid water simulated by the large scale model of MRCM and the climatological value of cloud liquid water, which can be specified by the user within a range of observations as presented in the following sections.

### 5.2.2 Existing parameterizations of Large-Scale cloud fraction and Rainfall

The Subgrid Explicit Moisture Scheme (SUBEX) is the existing parameterizations of the large-scale cloud fraction and rainfall that follow the work of Pal et al. 2000. The scheme uses the average grid relative humidity simulated by the model to calculate the large scale cloud fraction ($FC_{LS}$) as follows:

$$FC_{LS} = \sqrt{\frac{\mathrm{RH} - \mathrm{RH_{min}}}{\mathrm{RH_{max}} - \mathrm{RH_{min}}}} \qquad (5.1)$$

where RHmin is the threshold relative humidity required for cloud formation and RHmax is maximum value that relative humidity can take. In MRCM, the default values are RHmax = 1.01, RHmin = 0.8 over land and RHmin = 0.9 over ocean. This formula is applied to each model grid cell in the horizontal and vertical directions.

The large scale rainfall is calculated using the average cloud liquid water (CLW) in the grid cell simulated by the model. The cloud liquid water is formed when the average grid cell relative humidity exceeds saturation. The water vapor in excess of saturation is converted to cloud liquid water. Then, the rainfall forms at each model level when the CLW exceed the autoconversion threshold that depends on the temperature as follows:

$$P_{LS} = \mathrm{Cppt}\,(\frac{\mathrm{Q}_c^{LS}}{FC_{LS}} - \mathrm{Q}_c^{th})FC_{LS} \qquad (5.2)$$

where, $C_{ppt}$ is the autoconversion rate, $1/C_{ppt}$ can be thought of as the characteristic time required for cloud droplets to convert into rain droplets, $FC_{LS}$ is the large scale cloud cover, $\mathrm{Q}_c^{LS}$ is the simulated CLW from the model, and $\mathrm{Q}_c^{th}$ is empirically derived from:

$$\mathrm{Q}_c^{th} = C_{acs}\, 10^{-0.49+0.013T} \qquad (5.3)$$

with, T, temperature in degrees Celsius and $C_{acs}$ is the autoconversion scale factor, which accounts for the land or ocean based threshold that results from differences in density between land and ocean-based clouds due to differences in cloud condensation nuclei's over land and ocean. For the simulation using SUBEX, presented in section 5.3, the following values are used for the different parameters of SUBEX (Rhmax=1.01, Rhmin (land)= 0.8,

Rhmin (ocean)=0.9, Cppt (land)= 5x10-4, Cppt (ocean)=5x10-4, Cacs (land)= 0.65, Cacs (ocean)= 0.3).

### 5.2.3 New parameterizations of Large-Scale cloud fraction and Rainfall

The new parametrizations of large scale cloud and rainfall follows the same exact equations of Gianotti and Eltahir (2014a and 2014b) for the convective cloud and rainfall using the cloud liquid water (CLW) simulated by the convection model within the convective clouds. However, for the large scale cloud and rainfall, the CLW simulated by the large scale model, as described in the previous section, is used to calculate the large scale cloud fraction and rainfall.

**New Large scale parameterization of cloud**

The relation between the cloud cover and CLW relies on the work of Eltahir and Bras (1993), which showed that the relationship between rainfall volume and storm area is close to being linear. Similarly, a relationship can be derived that uses the CLW simulated by a climate model to infer the fractional area covered by cloud. The distribution of CLW over a grid cell can be described as the average of clear and cloudy portions of the grid cell using the following distribution:

$$g_{CLW} = FC f_{CLW} + (1 - FC)\delta(CLW - 0) \qquad (5.4)$$

where $g_{CLW}$ = is the probability density function (PDF) of CLW over the total area, $FC$ = fractional area of the grid cell covered with cloud, $\delta$ = Dirac delta function, and $f_{CLW}$ = conditional probability density function (PDF) of the CLW within the cloud, given that CLW is greater than zero. Thus, the expected value of CLW, *E(CLW)*, over a model grid cell can be calculated as follows:

$$E(CLW) = \int_{CLW=0}^{\infty} CLW\, g_{CLW}\, dCLW$$

$$= (1 - FC)0 + FC \int_{CLW=0^+}^{\infty} CLW\, f_{CLW}\, dCLW = CLW_{clim} FC$$

which implies that:

$$FC = \frac{E(CLW)}{CLW_{clim}} \qquad (5.5)$$

Where $CLW_{clim}$ is the mean of the conditional PDF $f_{CLW}$. It is important to note that for calculating the expected value of the CLW, *E(CLW)*, no assumptions are made about the distribution of the PDF $f_{CLW}$. Thus, this formulation is general and does not depend on the distribution of probability density function of the CLW. Furthermore, this formulation provides a flexibility for tuning the cloud cover simulated by the model by changing the $CLW_{clim}$, which can vary geographically and take different values over land and Ocean. Giannotti et al, 2014a defined a range of values that $CLW_{clim}$ can have based on observations of CLW. These values for $CLW_{clim}$ fall within (0.1-3) g $m^{-3}$ and (0.25-1.3) g $m^{-3}$ over land and ocean respectively. It is also important to note that the FC is constrained to be less than 1 in the model simulations.

**New Large scale parameterization of rainfall**

As discussed in the previous section, the fractional coverage of the grid cell that contains rainfall can be estimated using the relationship derived by Eltahir and Bras (1993) as following:

$$\mu = \bar{R}/R_{clim} \qquad (5.6)$$

where $\mu$ = fractional coverage of rainfall, $\bar{R}$ = grid-average simulated rainfall and $R_{clim}$ = climatological rainfall intensity. Furthermore, the fractional coverage of rainfall, $\mu$, within a raining model grid cell may also be expressed as the portion of the cloudy area within the grid cell that produces rainfall as following:

$$\mu = f_r FC \qquad (5.7)$$

where $f_r$ = fraction of total cloudy area that is raining, and *FC*= fractional coverage of cloud

$$\mu = f_r \frac{E(CLW)}{CLW_{clim}} \qquad (5.8)$$

Equations (5.6) and (5.8) can be combined to form:

$$\frac{\bar{R}}{R_{clim}} = f_r \frac{E(CLW)}{CLW_{clim}} \qquad (5.9)$$

The simulated grid-average rainfall, $\bar{R}$, can be represented as some fraction, $f_e$, of the simulated CLW as follows:

$$\bar{R} = f_e E(CLW) \qquad (5.10)$$

where $\bar{R}$ = grid-mean rainfall, $E(CLW)$ = simulated grid-mean CLW, and $f_e$ = autoconversion efficiency. The previous two equations (5.9) and (5.10) can be combined and rearranged to be written as following:

$$f_e = f_r \frac{R_{clim}}{CLW_{clim}} \qquad (5.11)$$

The fractional coverage of rainfall $f_r$ can estimated by using the previous distribution of the PDF of the CLW assuming that rainfall occurs when the CLW exceeds some autoconversion threshold $CLW_T$, as following:

$$f_r = \int_{CLW_T}^{\infty} f_{CLW} dCLW \qquad (5.12)$$

In the derivation to this point the PDF of the CLW ($f_{CLW}$) has not been specified. For simplicity and in the absence of a well-defined PDF for CLW, an exponential distribution for CLW is assumed as follows:

$$f_{CLW} = \frac{1}{CLW_{clim}} exp\left(-\frac{CLW}{CLW_{clim}}\right) \qquad (5.13)$$

Thus, the fractional coverage of rainfall $f_r$ can be written as follows:

$$f_r = \int_{CLW_T}^{\infty} \frac{1}{CLW_{clim}} exp\left(-\frac{CLW}{CLW_{clim}}\right) dCLW$$

$$f_r = exp\left(-\frac{CLW_T}{CLW_{clim}}\right)$$

$$f_e = exp\left(-\frac{CLW_T}{CLW_{clim}}\right)\frac{R_{clim}}{CLW_{clim}} \qquad (5.14)$$

This previous relationship represents the long-term climatological rainfall production efficiency, i.e. the autoconversion rate. It could be evaluated using mean observed values of convective CLW and rainfall intensity and then used within a large-scale climate model to represent the average autoconversion rate. However, a point-scale for the autoconversion rate is desirable to capture this temporal and spatial variability within the model. At the point-scale, i.e. the scale of a small parcel, the amount of rainfall that is produced will be a function of the cloud droplets that are large enough to coalesce to form rainfall in the cloud parcel. This volume can be represented as:

$$R = \alpha(CLW - CLW_T)^n \qquad (5.15)$$

where $R$ = point-scale rainfall, $CLW$ = amount of cloud liquid water within the cloud parcel, $CLW_T$ = point-scale threshold volume of CLW that must be exceeded to produce rainfall and $n$ = parameter that represents the degree of linearity of the autoconversion process. The parameter $\alpha$ (it is assumed that $\alpha$ = 1) ensures that the units remain dimensionally proportional for cases when $n \neq 1$. Then, as described before that the CLW has certain PDF $f_{CLW}$, the simulated large scale rainfall can be written as following:

$$\bar{R} = \alpha \int_{CLW_T}^{\infty} (CLW - CLW_T)^n f_{CLW} dCLW \qquad (5.16)$$

And using the exponential distribution of the CLW

$$f_{CLW} = \frac{1}{E(CLW)} exp\left(-\frac{CLW}{E(CLW)}\right) \qquad (5.17)$$

The grid-scale simulated large scale rainfall can be expressed as:

$$\bar{R} = \alpha \int_{CLW_T}^{\infty} (CLW - CLW_T)^n \frac{1}{CLW} exp\left(-\frac{CLW}{E(CLW)}\right) dCLW$$

$$\bar{R} = \alpha\, E(CLW)^n \Gamma(n+1) exp\left(-\frac{CLW_T}{E(CLW)}\right) \qquad (5.18)$$

where $\Gamma$ = gamma function, which can be evaluated via look-up tables.

This expression can be used with (5.10) to derive a dynamic, grid-scale measure of the autoconversion efficiency, $f_e$:

$$f_e = \alpha\, E(CLW)^{n-1}\Gamma(n+1)exp\left(-\frac{CLW_T}{E(CLW)}\right) \qquad (5.19)$$

This function now permits calculation of the grid-mean large scale rainfall using the simulated grid-scale value of large scale CLW, with specification of two parameter values: $CLW_T$ and $n$ (remembering that the assumption $\alpha = 1$ has already been made). Several studies investigated the critical droplet concentration ($N_d$) and critical droplet radius ($r_{cri}$) required to convert cloud droplets into precipitating raindrops (Reid et al., 1999; Kubar et al., 2009; Rango and Hobbs et al., 2005). Thus, an approximate value of the $CLW_T$ can be estimated based on the critical droplet radius and concentration as the following equation:

$$CLW_T = \frac{4}{3}\pi\rho N_d r_{crit}{}^3 \qquad (5.20)$$

where $CLW_T$ = threshold of cloud water content in g m$^{-3}$, $\rho$ = liquid water density in g m$^{-3}$, $N_d$ = droplet concentration in m$^{-3}$ and $r_{crit}$ = radius of cloud droplets in m. Giannotti and Eltahir 2014b estimated the range in which the $CLW_T$ can fall based on observation of the critical droplet radius, droplet concentration. These values fall within (0.1-3) g m-$^3$ and (0.25-1.3) g m-$^3$ over land and ocean respectively. The difference between land and ocean is mainly because of the different cloud condensation nuclei available over land and ocean and the droplet concentration tend to be higher over land than ocean (Squires, 1958; Rangno and Hobbs, 2005; Kubar, 2009). Finally, the dynamic autoconversion given by equation (5.19) is matched with the long-term mean autoconversion given by (5.14) and values of $n$ = 0.9 over land and $n$ = 0.94 over ocean are estimated.

Therefore the following expressions can be used to calculate the grid-mean convective rainfall:

$$\bar{R} = E(CLW)^{0.9}0.96exp\left(-\frac{CLW_T}{E(CLW)}\right) \qquad \text{for land} \qquad (5.21)$$

$$\bar{R} = E(CLW)^{0.94}0.97exp\left(-\frac{CLW_T}{E(CLW)}\right) \qquad \text{for ocean} \qquad (5.22)$$

where $E(CLW)$ is the simulated grid-scale CLW in kg kg$^{-1}$.

These new parameterizations of large scale cloud fraction and rainfall will be tested by their ability to improve the simulation of radiation budget at the surface and top of atmosphere. Furthermore, by the improvements in the simulation of clouds properties over the Upper Blue Nile basin as presented in the following sections.

## 5.3 Design of Numerical Experiments and datasets used

### 5.3.1 Design of Numerical Experiments

In this study, two numerical experiments are presented to investigate the performance of the new large scale cloud and rainfall parametrizations. The first simulation uses large scale cloud and rainfall parametrizations (SUBEX), while the second simulation uses the new large scale cloud and rainfall parametrizations. Thus, the comparison between the two simulations only shows the impact of the new large scale cloud and rainfall parametrizations on the performance of the model. It is also important to mention that the two simulations include two minor modifications in values of Leaf Area index and ground water recharge parameters. These two values are tuned using several short simulations to match the observations. The original values of the Leaf Area index were overestimated compared to observations from the Moderate resolution Imaging Spectroradiometer (MODIS) Leaf Area index product (MOD15A2) (Knyazikhin et al., 1998; Myneni et al., 2002; Yang et al., 2006b). The land surface model (IBIS) specifies the land cover of each grid cell in the domain. Then, based on climate variables that are available from the input datasets to the model (e.g. growing degree days, maximum and minimum temperature of the grid cell), the model assigns different Plant Functional Types (PFTs) that can grow in each grid cell of the model. Each PFT has four different Leaf Area index values (i.e. evergreen tree and deciduous tree for the upper canopy and shrub and grass for the lower canopy). The original Leaf Area index values of the model were 0.5, 1, 0.5 and 2 for the evergreen tree, deciduous tree, shrub and grass respectively. However, the land cover of the Upper Blue basin is mainly Savannah as shown in Figure 5.1, which mainly consists of grasses and shrubs. Thus, the Leaf Area index for evergreen tree, deciduous are reduced to 0.01 and 0.01 to make the Leaf Area index simulated by the model

match the observations. For the groundwater recharge parameter, the total runoff simulated by the model was also overestimated compared to observation, thus, the groundwater recharge parameter was decreased to match the observations. The land surface model (IBIS) has a parameter, "bperm", that can control the groundwater recharge at the bottom of the soil layer. This parameter can make the bottom layer of the model completely impermeable (i.e. the groundwater recharge is equal to zero), when this parameter is equal to zero or fully permeable when this parameter is equal to one. The original value of this parameter was equal to 0.1. In the new simulations, this value was reduced to 0.03.

The domain of the simulations is centered around the Nile basin and consists of 160 and 180 grid cells of 30 Km resolution in the zonal and meridional directions respectively (Figure 5.1). The time steps used in the simulations are 30 and 300 seconds for the atmospheric and land surface model (IBIS) respectively. The simulations period is 1989 to 2010 and the first year results (i.e. 1989) are removed for spin-up considerations. These simulations period is chosen because it has the longest overlap with many of the observational datasets that are used to verify the model performance.

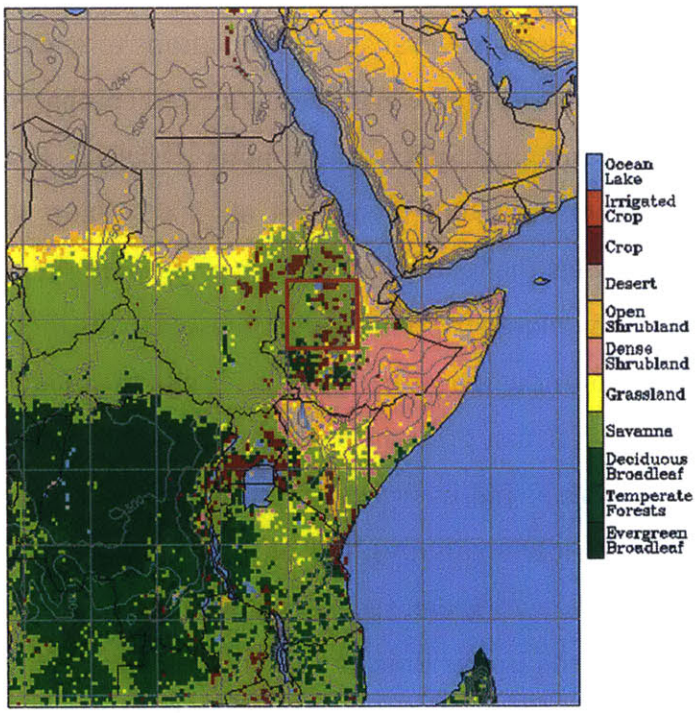


**Figure 5. 1:** Domain of simulation with the different groups of land cover. The red box encloses the UBN basin.

The lateral boundary conditions for the model are provided by the European Center for Medium-Range Weather Forecasts (ECMWF) Interim reanalysis dataset (ERA-Interim) (Dee et al. 2011; Berrisford et al. 2011). They include zonal and meridional wind, relative humidity, air temperature and geopotential heights fields. The ERA-Interim reanalysis dataset provides these fields every 6 hours with $1.5^{o}$x$1.5^{o}$ degrees spatial resolution. The ERA-Interim dataset is chosen in this study as it has the most accurate representation of the hydrological cycle of the Nile basin compared to other reanalysis dataset (e.g. 40-yr ECMWF Re-Analysis (ERA-40) product; Uppala et al. 2005 and the NCEP–NCAR reanalysis product; Kalnay et al. 1996) as estimated from the soil and atmospheric water balances by Siam et al. 2013.

The sea surface temperatures (SSTs) are prescribed by the National Oceanic and Atmospheric Administration (NOAA) Optimum Interpolation (OISST) data set with a horizontal resolution of $1^{o}$x$1^{o}$ and weekly temporal resolution. Topographic information was taken from the United States Geological Survey's Global elevation dataset (GTOPO30), (United States Geological Survey 1996). Vegetation biomes are based on the potential global vegetation dataset of Ramankutty (1999). Then each grid cell is populated with plant functional types (PFTs) based on the biome and two datasets: monthly mean climatology of temperature (New et al. 1999) and minimum temperature ever recorded at a location minus the average temperature of the coldest month (Bartlein 2000). Soil properties, such as albedo and porosity, are determined based on the relative proportions of clay and sand in each grid cell. Sand and clay percentages are taken from the Global Soil Dataset (Global Soil Data Task, IGDP-DIS 2000), which has a spatial resolution of 5 min. Soil moisture and temperature are initialized using the output from a global $0.5^{o}$x$0.5^{o}$ resolution 20-years offline simulation of IBIS as described in Winter et al. (2009).

### 5.3.2 Model Evaluation Datasets

The model performance is evaluated using several observational datasets. These datasets include observations of solar radiation components, cloud properties, rainfall, stream flow

and 2 meters air temperature in order to assure that it is able to correctly simulate the water and energy budgets over the Nile basin. These datasets include:

a. NASA-SRB Data

The shortwave and longwave radiations at the surface and the top of atmosphere are available from the National Aeronautics and Space Administration (NASA)/Global Energy and Water Cycle Experiment (GEWEX) Surface Radiation Budget (SRB) dataset release 3.0 (Stackhouse et al. 2011), obtained from the Langley Research Center Surface Radiation Budget. The NASA-SRB dataset provides both shortwave and longwave radiation at the surface and the top of atmosphere on a monthly averaged $1^{o}x1^{o}$ global grid from January 1984 to December 2007.

b. TRMM Rainfall Data

The total rainfall data is available from Tropical Rainfall Measuring Mission (TRMM) (Huffman et al. 2007). In this study, the 3B43 version is used, which has $0.25^{o}x0.25^{o}$ resolution on a monthly scale and available from 1998 till present day.

c. Stream flow Data

The stream flow is obtained at Diem station that measure the flow of the Upper Blue Nile Basin. The stream flow data are available on a monthly scale for the period of simulation using personal communications.

d. Rainfall and Evaporation Data from Water budget optimization model

The rainfall and evaporation data are available from an optimization model of the water budget components of the Upper Nile basin described in Allam et al. 2016. The data is available as monthly climatology of each calendar month on a $0.25^{o}x0.25^{o}$.

e. Rainfall and 2 meters air temperature from CRU TS3.1 Data

The rainfall and 2 meters air temperature data are available from the CRU TS3.1 data on a monthly averaged $0.5^{o}x0.5^{o}$ global grid from 1900 to 2009.

## 5.4 Results

In this section, the impacts of new parametrizations on the performance of different processes simulated by the model are presented. The performance of the model is evaluated based on the improvements in simulating the hydrological cycle, surface radiation and cloud properties. Several short simulations were conducted to adjust the $CLW_{clim}$ parameter required by the new parameterizations and a value of 0.1 g $m^{-3}$ and 0.75 g $m^{-3}$ are used over land and ocean respectively.

### 5.4.1 Simulation of the hydrological cycle, temperature and surface radiation over the basin

The average seasonal cycle of rainfall over the basin is compared to three different observational datasets that are described in model evaluation datasets section (5.3.2). The annual average rainfall increased from 3 mm/day to 3.2 mm/day, which is closer to observations compared to the simulation using the old parameterizations of large scale clouds and rainfall (Figure 5.2a). This increase is followed by an increase in the annual average evaporation over the basin of almost the same magnitude (i.e. ~ 0.2 mm/day) as shown in Figure 5.2b. The change in the annual average runoff over the basin is small as the increase of rainfall is accompanied by a similar increase of evaporation (Figure 5.2b).

The increase of evaporation is due to the increase of net radiation at the surface, in other words, the energy available to release in the form of latent heat flux, particularly during July and August, as shown in Figure 5.3a. This increase in net radiation is mainly due of the large increase in downward shortwave radiation (~+46 W/$m^2$) at the surface as shown in Figure 5.4a, although downward longwave radiation at the surface has decreased (~-12 W/$m^2$) as shown in Figure 5.4b. It is also important to show that surface albedo of the model is close to observation (i.e. the error is less than 1%) as biases in surface albedo may induce a series of biases in the simulation of radiation and hydrological cycle of the basin (Figure 5.3b). Furthermore, the 2 meters air temperature simulated by the model is compared to observations (Figure 5.5) to verify that the increase of net radiation at the surface did not induce any errors in the simulated temperature close to surface. The model captures the

seasonal cycle of the temperature close the surface and the errors between the model and observed temperature is relatively small and less than 1°C.

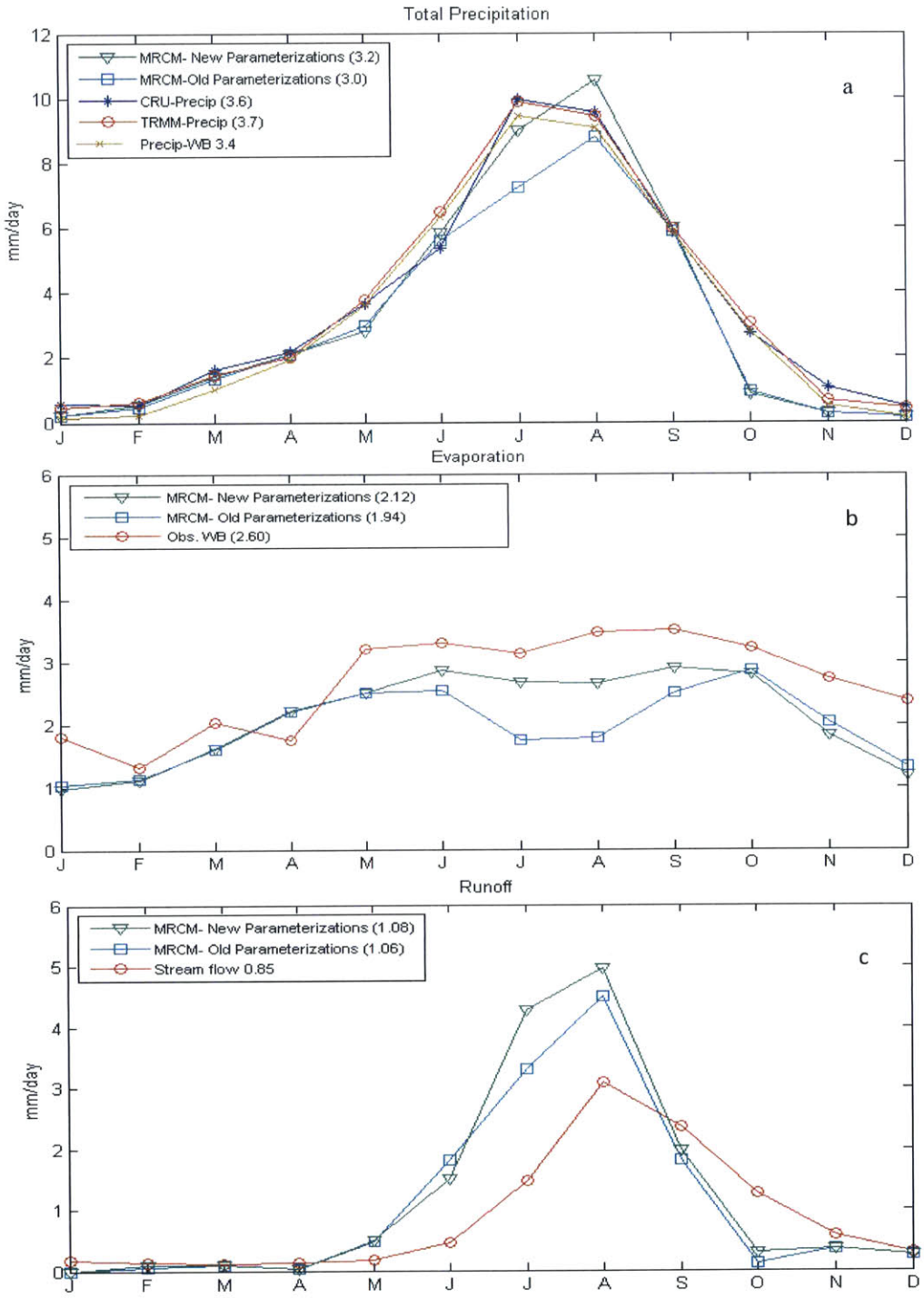


**Figure 5. 2:** Monthly 21-years (1990-2010) averages values for: (a) rainfall, (b) evaporation and, (c) runoff simulated by the old and new parameterizations of large scale cloud and rainfall over the Upper Blue Nile basin.

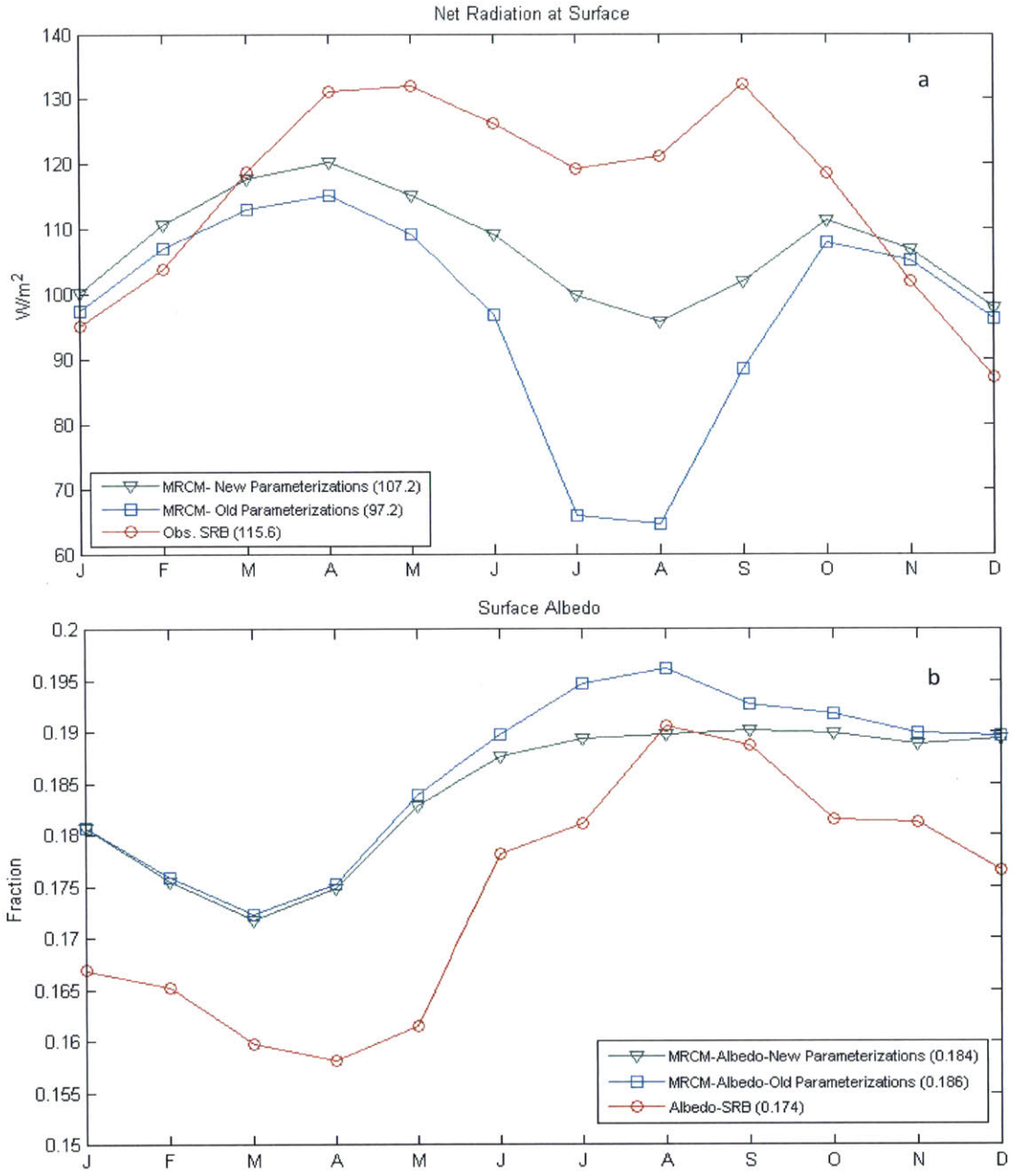


**Figure 5. 3:** Monthly 21-years (1990-2010) averages values for: (a) net radiation at the surface, and (b) surface albedo simulated by the old and new parameterizations of large scale cloud and rainfall over the Upper Blue Nile basin compared to observations from NASA-SRB dataset.

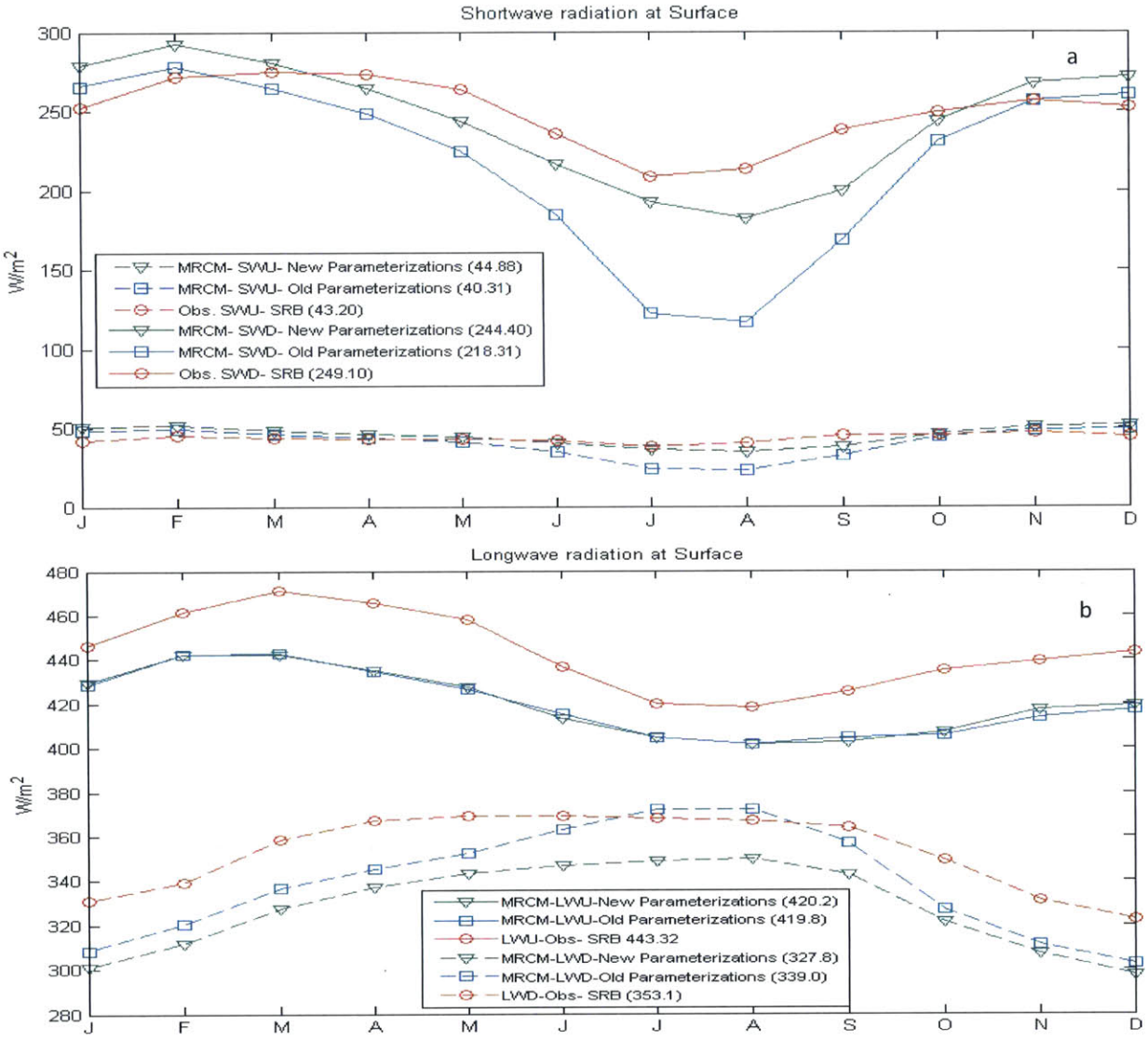


**Figure 5. 4:** Monthly 21-years (1990-2010) averages values for: (a) downward (SWD) and upward (SWU) shortwave radiation, and (b) downward (LWD) and upward (LWU) longwave radiation at the surface simulated by the old and new parameterizations of large scale cloud and rainfall over the Upper Blue Nile basin compared to observations from NASA-SRB dataset.

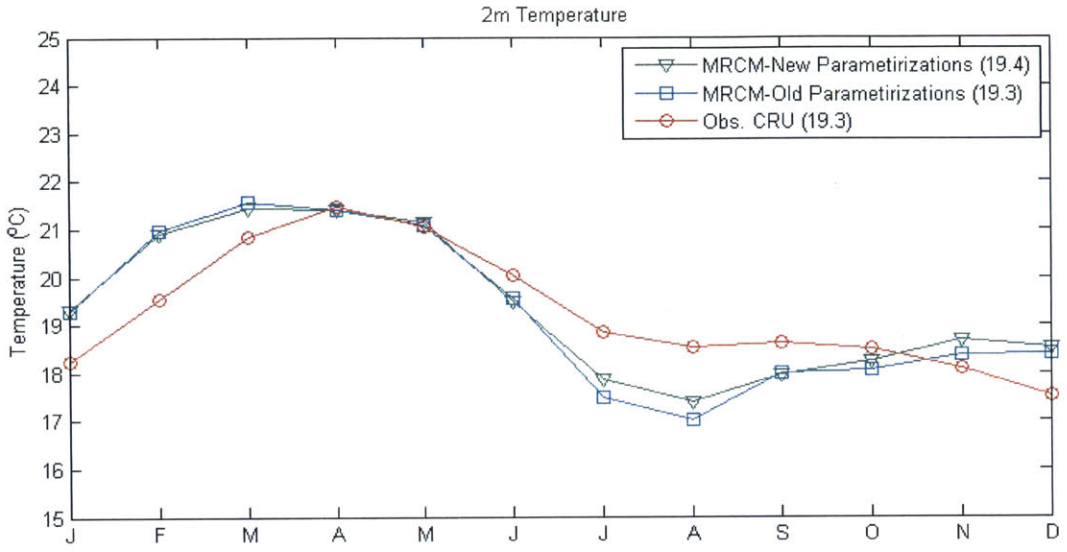


**Figure 5. 5:** Monthly 21-years (1990-2010) averages values of the 2 meters temperature over the Upper Blue Nile basin using the old and new parameterizations compared to observation from CRU TS3.1.

The results of the simulation using the new parameterizations of large scale cloud and rainfall are also compared with the observation spatially. Figure 5.6 shows the simulated rainfall and 2 meters air temperature averaged from June to September and compared to observations. The model is able to capture the spatial pattern of the rainfall and temperature. For example, the region of maximum rainfall simulated by the model almost coincides with the region of maximum rainfall from the observations. Furthermore, the model is able to simulate the region of low 2 meters air temperature centred around the Upper Blue Nile basin as shown in Figure 5.6b and 5.6d.

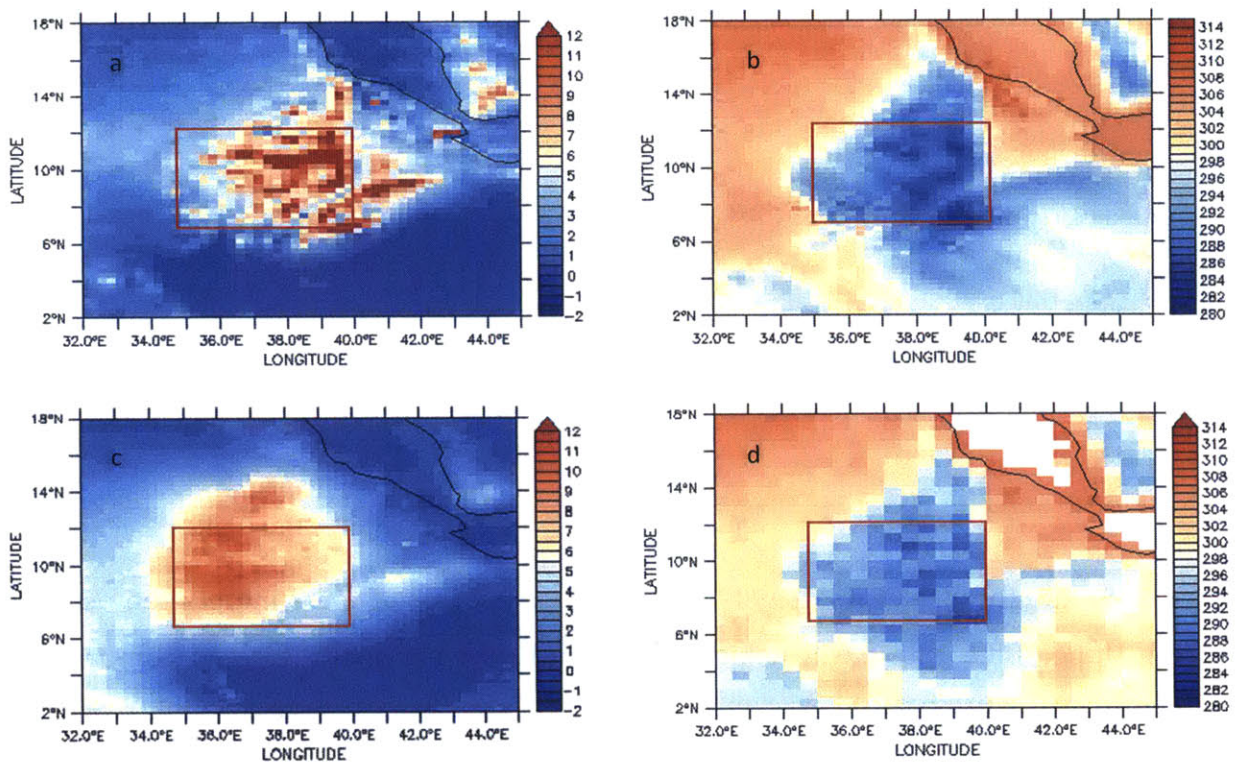


**Figure 5. 6:** Monthly average from June to September of: (a) the rainfall, and (b) the 2 meters air temperature simulated by the new parameterizations of large scale clouds and rainfall for the period (1990-2010), (c) the rainfall from TRMM-V7 3B43 for the period (1998-2015), and (d) the 2 meters air temperature from CRU TS3.1 for the period (1990-2010). The red boxes encloses the boundaries of the Upper Blue Nile basin.

## 5.4.2 Simulation of cloud properties over the basin

The series of increases in the downward shortwave radiation, net radiation at the surface and their impacts on the evaporation and runoff, discussed in the previous section, is mainly because of the adjustments in the simulation of cloud cover using the new parametrizations. The new parameterizations decreased the simulated cloud coverage of the model (Figure 5.7a and 5.7b). The planetary albedo is now closer to observations, particularly during the rainy season as shown in Figure 5.6a. In addition, the values of outgoing longwave radiation are higher during the rainy season, which indicates a reduction of the simulated cloud

coverage. It is also important to note the seasonal cycle of the planetary albedo (Figure 5.6a), which show high values during the summer rainy season and low values between November to May. This is mainly because of the increased cloudiness during the rainy season, which increases the planetary albedo.

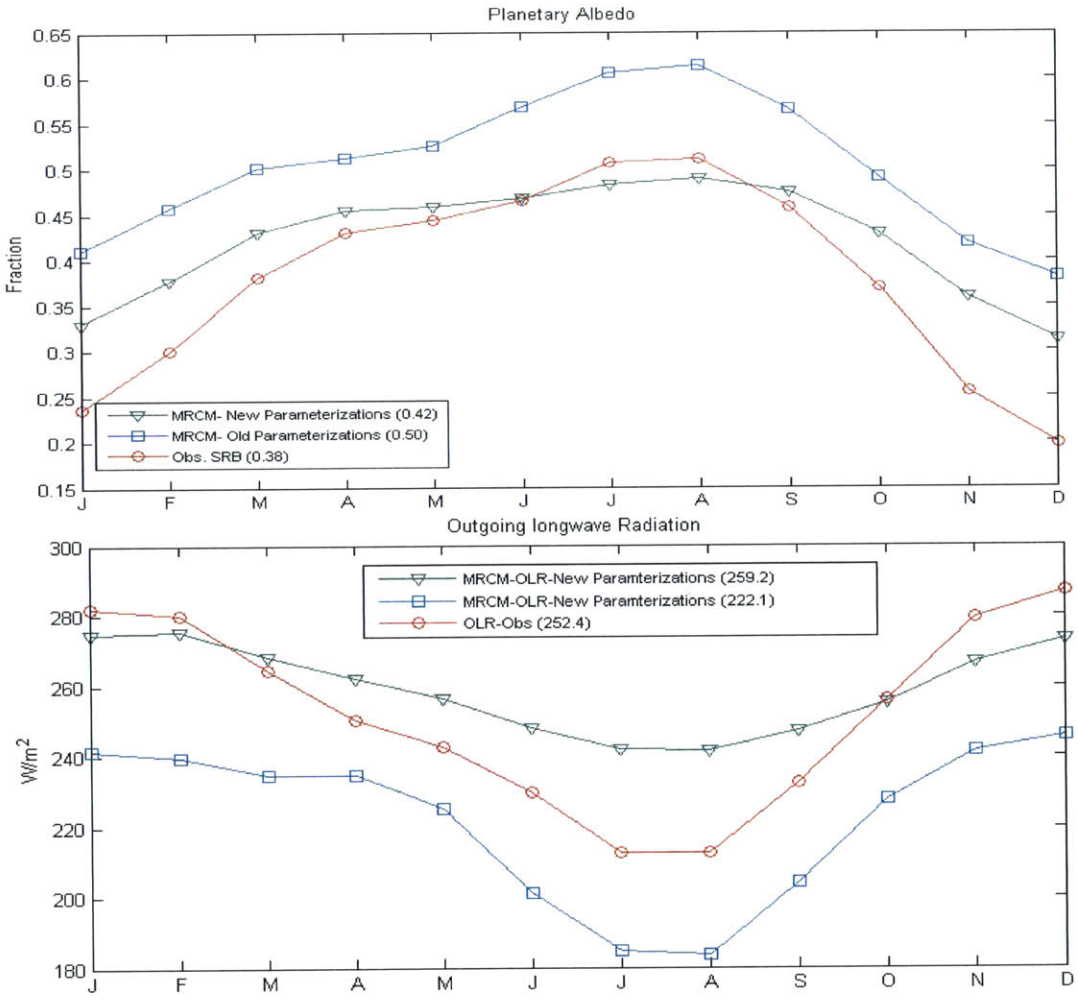


**Figure 5. 7:** Monthly 21-years (1990-2010) averages values for: (a) Planetary albedo, and (b) Outgoing longwave radiation simulated by the old and new parameterizations of large scale cloud and rainfall over the Upper Blue Nile basin compared to observations from NASA-SRB dataset.

## 5.5 Conclusions

In this chapter, new parametrizations of large scale cloud and rainfall are developed and investigated for use within climate models. The new parametrizations mainly depend on two variables. First, the cloud liquid water content is simulated by the large scale model in MRCM. Second, the climatological value of the cloud liquid water, which the user has the flexibility to tune based on a range of observed values of the cloud liquid water. This flexibility allows the user to adjust the simulation of cloud cover and rainfall to match the observations using a physically based approach that is constrained with observational values.

The new parametrizations are tested over the Upper Blue Nile basin within the MIT-Regional climate model (MRCM), which is a modified version of the Regional Climate Model, version 3 (RegCM3) with the land surface scheme Integrated Biosphere Simulator (IBIS) and modified parameterizations for the convective cloud cover and rainfall. The performance of the new parameterizations with MRCM is evaluated using a 21-year simulations. The new parameterizations resulted in consistent and significant improvements of the simulated cloud cover and radiation over the basin. The decrease of the cloud cover, as reflected in the increase of outgoing longwave radiation and decrease of the planetary albedo, resulted in increase of the downward shortwave and net radiation at the surface. These new parametrizations provide us with a new version of MRCM that has credible simulation not only of the hydrology of the Upper Blue Nile basin, but also credible simulation of the cloud cover and radiation budget at the surface and the top of atmosphere.

# Chapter 6: Future changes in the long-term mean of the flow in the Nile river

In chapter 4, it was shown that the variability in the future flow of Nile river will increase due to the increased frequency of future El Nino and La Nina events and the observed teleconnection between the Nile flow and ENSO. In this chapter, the mechanisms shaping changes in the long-term mean of flow in the Nile river are investigated. The analyses in this chapter include two main parts. First, an analysis of the GCMs to discern the common changes between the different GCMs in the future wind pattern, rainfall, sea surface temperature and humidity. Second, applying these changes to the modified version of the regional climate model, developed in chapter 5 to investigate the mechanism of changes in the long-term mean of the flow. The model is used to conduct several simulations that investigate the individual impact of changing the boundary conditions and greenhouses gases concentrations to match the future on the flow of the Nile, which is not possible to achieve without a regional climate model.

## 6.1 Introduction

Several studies examined the impacts of climate change on the long-term mean of the flow in the Nile river (Booij et al., 2011, Kim and Kaluarachi, 2009, ElShamy et al., 2009, Beyene et al., 2009 and Yates and Strzepek, 1998). The main approach of these studies consisted of calibrating a hydrological model of the basin for a control period usually (1960-1990) and adding the predicted signal of climate change by the GCMs on the historical values of the hydrological inputs to this model. For example, Strzepek and Yales (1996) developed a one dimensional water balance model to investigate the possible impacts of climate change over the Nile basin. Then, three GCMs are used to assess impact of climate change on the Nile flow. The differences in temperature between the future climate change scenarios and the past for each grid cell were added to the historic value of the grid cell to produce a new future temperature value for each calendar month. Then, the rainfall changes were added by

multiplying the historical values by the ratio between the future climate change scenarios and the past for each grid cell to produce a new future rainfall value for each calendar month. Catchments' weighted-average climate parameters were calculated from the new temperature and rainfall values. Two of the GCMs show a decrease in the flow at Aswan by 22% and 77%, the third model shows an increase by 30% relative to the average of the historic values from 1900 to 1972.

Conway and Hulme (1996) used three climate scenarios in a study of the sensitivity of Blue Nile river flows to potential climate change. One dry and one wet scenario were selected, and a third scenario was constructed from a weighted average of seven models. Each GCM was given a weighting based on its ability to simulate current rainfall. The temperature changes were given equal weights in the weighted average scenario. For measuring the corresponding flows, a hydrological model for the Blue Nile catchment is divided into 10-minute latitude by 10-minute longitude grid cells. Estimates of mean monthly rainfall and evapotranspiration are calculated for all grid cells and fed into a simple monthly water balance model. The runoff obtained for each cell is then summed to produce an overall estimate of catchment runoff. Simulated changes in runoff ranged from -8.7 to +15.3% for the Blue Nile.

Another study conducted by Yates and Strzepek (1998) to assess the impacts of climate change on the Nile used a lumped hydrologic model. The model was developed and calibrated on a monthly basis. Six different GCMs simulations were used in the assessment. GCM temperature and rainfall changes were interpolated to a 0.5° x 0.5° grid for use with the hydrologic model. The simulated GCMs projections for the Blue Nile ranged from from -32 to +133%.

El.Shamy et al., (2009) used the output of 17 GCMs with the SRES A1B emission scenario to investigate the impacts of climate change on the Upper Blue Nile catchment flows for the period (2081 to 2098) relative to (1961-1990). The temperature and the rainfall are spatially downscaled using a bias-correction approach to use with the NFS (Nile Forecast System) and get the corresponding flow of each GCM. The simulated changes in the flow of the Upper Blue Nile basin ranged from -60% to +45%.

The approach used in the previous studies did not provide any explanation of the estimated changes in the future flows. In addition, the ranges of the estimated changes in the future flow were high. Thus, these studies did not provide any conclusive predictions of the impact of climate change on the future flow in the Nile river or clear explanations of the wide disagreement between the GCMs results.

In this chapter, the GCMs are first analysed to discern the common changes of future key factors that influence the rainfall over the Nile basin. For example, the changes of the sea surface temperature (SST) over the Indian Ocean, humidity and wind pattern. This step is very important as identifying the future changes in these factors and how these changes may impact the rainfall over the Nile basin may increase our confidence of the future predications due to climate change. The second step is applying the estimated changes of these variables to the regional climate model, discussed in the chapter 5, to examine the mechanism by which these factors may impact the rainfall over the basin.

## 6.2 Analysis of the GCMs

### 6.2.1 Selection of the GCMs

The assessment of GCMs before using them is an important step to reduce the uncertainty introduced due to the use of biased models to predict the changes in future climate. In this chapter, 18 GCMs that participated in the Coupled Model Inter-comparison Project Phase 5 (CMIP5) with the Representative Concentration Pathway (RCP 8.5) for future greenhouse gases projected emissions are selected (Table 4.1). These are the same 18 GCMs that are used to predict the changes in the interannual variability of the flow in the Nile river in chapter 4. The selected models were identified in previous studies by other research groups to be the best in simulating the frequency of El Niño and La Niña events (Cai et al., 2014 and Cai et al., 2015). ENSO is one of the most important phenomena shaping tropical climate. Hence, models used to predict the future climate in any tropical region should have credibility in simulating this phenomenon.

### 6.2.2 Identifying future changes in the rainfall, wind, SST and humidity

In this section, the future changes in the rainfall, wind, SST and humidity are investigated for the period of (2070-2100) using the RCP8.5 scenario compared to (1970-2000). Figure 6.1 summarizes the multi-model ensemble averages of rainfall, SST and vertical profiles of wind and specific humidity during July and August for the past period (1970-2000) and the predicted changes in future period (2070-2100). Figure 6.1b shows an increase of SST over the Indian Ocean. A detailed analysis of each GCM (shown in Appendix C) shows that not all of the GCMs have the same magnitude of increase of SSTs or spatial pattern of warming over the Indian Ocean. Most of them show the highest increase of SST north of the equator and over the Arabian sea region. On the other hand, the changes in future rainfall are almost the same as the SST and most of the increase of rainfall is also north of the equator and over the Arabian sea region.

In chapter 2, it is shown that the increase of SST around the equator over the Indian ocean is followed by an increase of rainfall over the same region and induces subsidence over the Eastern Nile (ENB) basin, which reduces rainfall. However, the predictions from the GCMs do not show a similar pattern. Although the SST and rainfall increase over the Indian ocean as shown in Figures 6.1b and 6.1d, there is no consensus between the GCMs that subsidence would occur over the ENB (Shown in Appendix C). This can be explained as the warming pattern shown in chapter 2 (Figure 2.13) is different than the warming pattern projected in the future due to climate change. The warming during El Nino events is centered around the equator over the Indian Ocean, which induces a Gill-type circulation that increases the westerly low level air flow and reduces convergence of air and thus the rainfall over the basin. However, the warming pattern in the Indian ocean due to climate change is mainly over the North of the Indian ocean and the Arabian sea and does not induce similar changes in the wind circulation that may affect the convergence of air and thus the rainfall over the ENB. On the other hand, all the GCMs show an increase of the specific humidity over the basin, which favors the increase of rainfall (Figure 6.1f). In other words, the increase of rainfall shown by the GCMs in the future can be potentially explained as due to the increase

of specific humidity and absence of subsidence over the basin. This hypothesis will be discussed further.

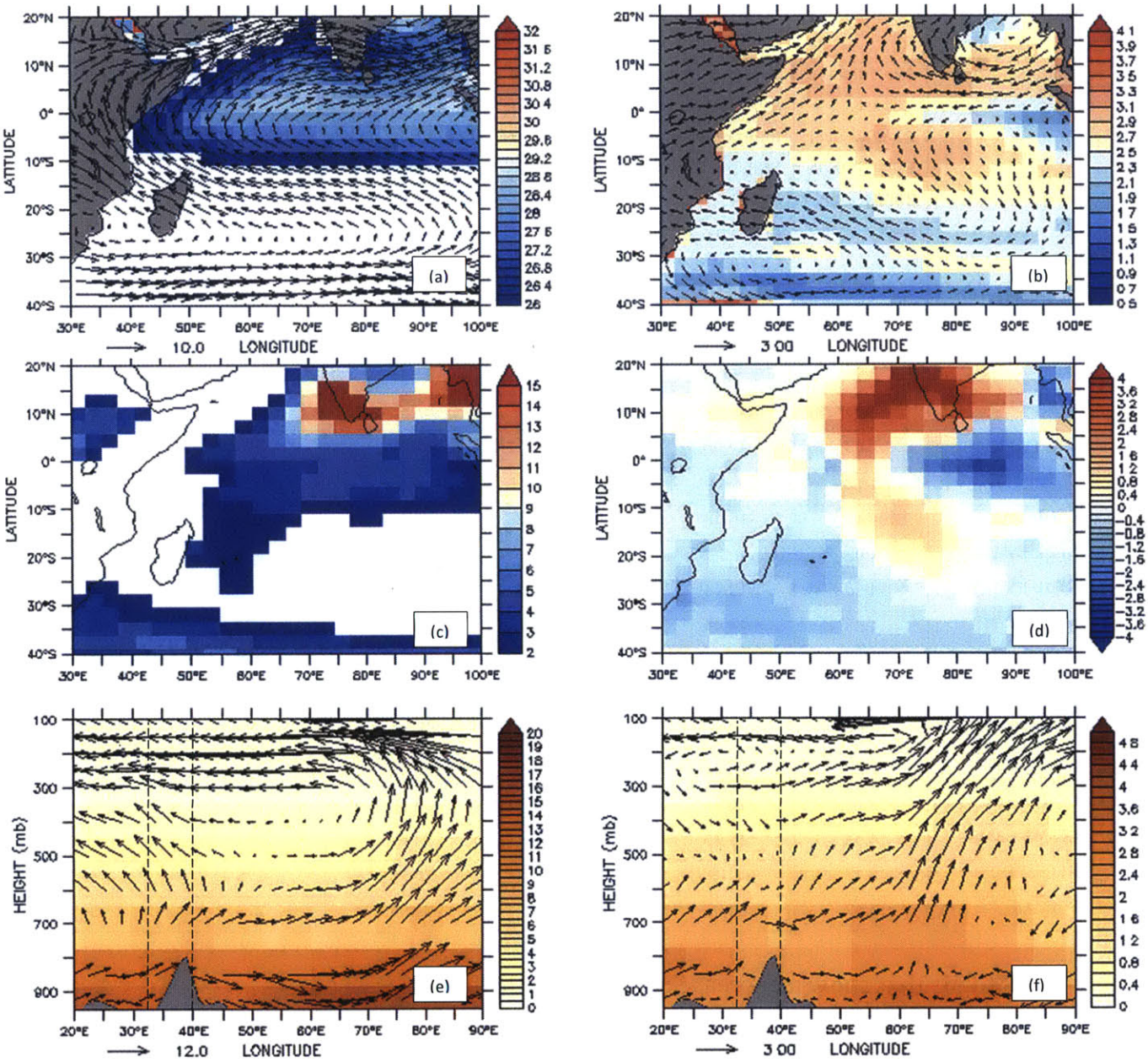


**Figure 6. 1:** Multi-model ensemble average for the period (1970-2000) for July and August for: (a) Sea Surface Temperature (°C) overlaid by the wind (m/s) at 800 mb, (c) rainfall (mm/day), and (e) vertical profiles of specific humidity (g/kg) with wind (m/s) averaged between 5°N to 15°N. Multi-model ensemble average of the changes for the period (2070-2100) compared to the period (1970-2000) for July and August for: (b) Sea Surface Temperature (°C) overlaid by the wind (m/s) at 800 mb, (d) rainfall (mm/day), and (f) vertical profiles of specific humidity (g/kg) with wind (m/s) averaged between 5°N to 15°N. The vertical lines represent the longitudinal the boundaries of the Eastern Nile basin.

**Table 6.1:** Summary of changes in the rainfall, air temperature and specific humidity over the lowest 300 mb from the surface for July and August for (2070-2100) compared to (1970-2000).

| Model | Avg. July and August Rainfall over ENB (1970-2000)(mm/ day) | Avg. July and August Rainfall over ENB (2070-2100) (Percent Change) | Avg. July and August Specific Humidity over ENB (1970-2000)(kg/kg) | Avg. July and August Specific Humidity over ENB (2070-2100)(Percent Change) | Avg. July and August air temperature over ENB (1970-2000)(kelvin) | Avg. July and August air temperature over ENB (2070-2100)(changes in kelvin) |
|---|---|---|---|---|---|---|
| **BCC-CSM1-1M** | 3.81 | 28.40 | 0.0070 | 22.39 | 279 | 3 |
| **BCC-CSM1-1** | 2.85 | 7.81 | 0.0064 | 20.98 | 277 | 4 |
| **CCSM4** | 3.90 | 9.36 | 0.0045 | 23.45 | 277 | 5 |
| **CMCC-CMS** | 3.63 | 10.37 | 0.0074 | 28.33 | 278 | 5 |
| **CMCC-CM** | 2.83 | 17.06 | 0.0072 | 28.66 | 278 | 5 |
| **CNRM-CM5** | 1.12 | 6.04 | 0.0041 | 24.41 | 278 | 3 |
| **GFDL-CM3** | 4.40 | -10.88* | 0.0058 | 33.06 | 277 | 6 |
| **GFDL-ESM2G** | 4.82 | -9.20* | 0.0037 | 26.24 | 274 | 5 |
| **GFDL-ESM2M** | 4.50 | -12.43* | 0.0037 | 23.82 | 275 | 4 |
| **MPI-ESM-MR** | 4.83 | 14.04 | 0.0072 | 24.21 | 277 | 5 |
| **MRI-CGCM3** | 2.56 | -9.18* | 0.0037 | 22.14 | 275 | 4 |
| **NOREMS1-ME** | 3.72 | 9.90 | 0.0066 | 21.21 | 275 | 4 |
| **NORESM1-M** | 3.79 | 7.99 | 0.0066 | 21.02 | 275 | 4 |
| **CMCC-CESM** | 2.39 | -24.26* | 0.0068 | 22.40 | 276 | 5 |
| **CESM1-BGC** | 3.77 | 16.10 | 0.0045 | 23.38 | 275 | 4 |
| **CESM1-CAM5** | 4.63 | 11.16 | 0.0046 | 24.53 | 274 | 5 |
| **ACCESS1-0** | 5.47 | 2.19 | 0.0038 | 28.38 | 275 | 4 |
| **FGOALS** | 4.47 | 34.05 | 0.0040 | 23.68 | 274 | 3 |

*GCMs that show a decrease of rainfall in the future

Table 6.1 shows a summary of the changes in the rainfall, air temperature and specific humidity over the lowest 300 mb from the surface using the 18 GCMs. Most of the GCMs (i.e. 13 out of 18 GCMs) show an increase of the rainfall over the Eastern Nile basin during July and August. The average increase of the rainfall for all the models is 7%. On the other hand, all the models show an increase of specific humidity over the lowest 300 mb from the surface by almost 25% and almost 4 kelvin for the air temperature. The increase of the specific agrees with the increase of air temperature based on Clausis-Clyperon relation and the work of Collins et al., 2010, which showed that the humidity increases with the temperature at a rate of 7%/kelvin.

It is also important to note that 4 of the 5 GCMs (i.e. GFDL-CM3, GFDL-ESM2M, GFDL-ESM2G, CMCC-CESM) that show a decrease of rainfall over the ENB have low spatial resolution ($2.5^{o}\times2.0^{o}$ for GFDL-CM3, GFDL-ESM2M, GFDL-ESM2G and $3.75^{o}$ x$3.71^{o}$ for CMCC-CESM). Figure 6.2 shows the average convergence of moisture, estimated as the difference between the rainfall and evaporation, during July and August for the period (1970-2000) and the change of the convergence of moisture in the future period (2070-2100). The convergence of moisture is calculated as the difference between the rainfall and evaporation as shown in Equation (3.7). These 4 GCMs (i.e. GFDL-CM3, GFDL-ESM2M, GFDL-ESM2G, CMCC-CESM) also show a decrease of the convergence of moisture over the basin for the future period (2070-2100) compared to the past period (1970-2000). Siam et al. 2013 showed that high resolution GCMs have better performance in simulating the hydrological cycle of the Upper Blue Nile basin compared to the low resolution models. This improvement can be primarily because high resolution models better represent the complex topography of the basin, which directly affects the amount of rainfall. Furthermore, the low resolution models do not accurately simulate the convergence of moisture, as discussed in Chapter 2. This might explain the future decrease in the convergence of moisture (Figure 6.2), as it can be expected that these models might not be sensitive to future changes in the humidity. Thus, the magnitude of moisture fluxes to the basin may not increase significantly in the future, while the evaporation over the basin will probably increase because of the increased temperature, then the net effect is a decrease in the future convergence of moisture and the rainfall over the basin.

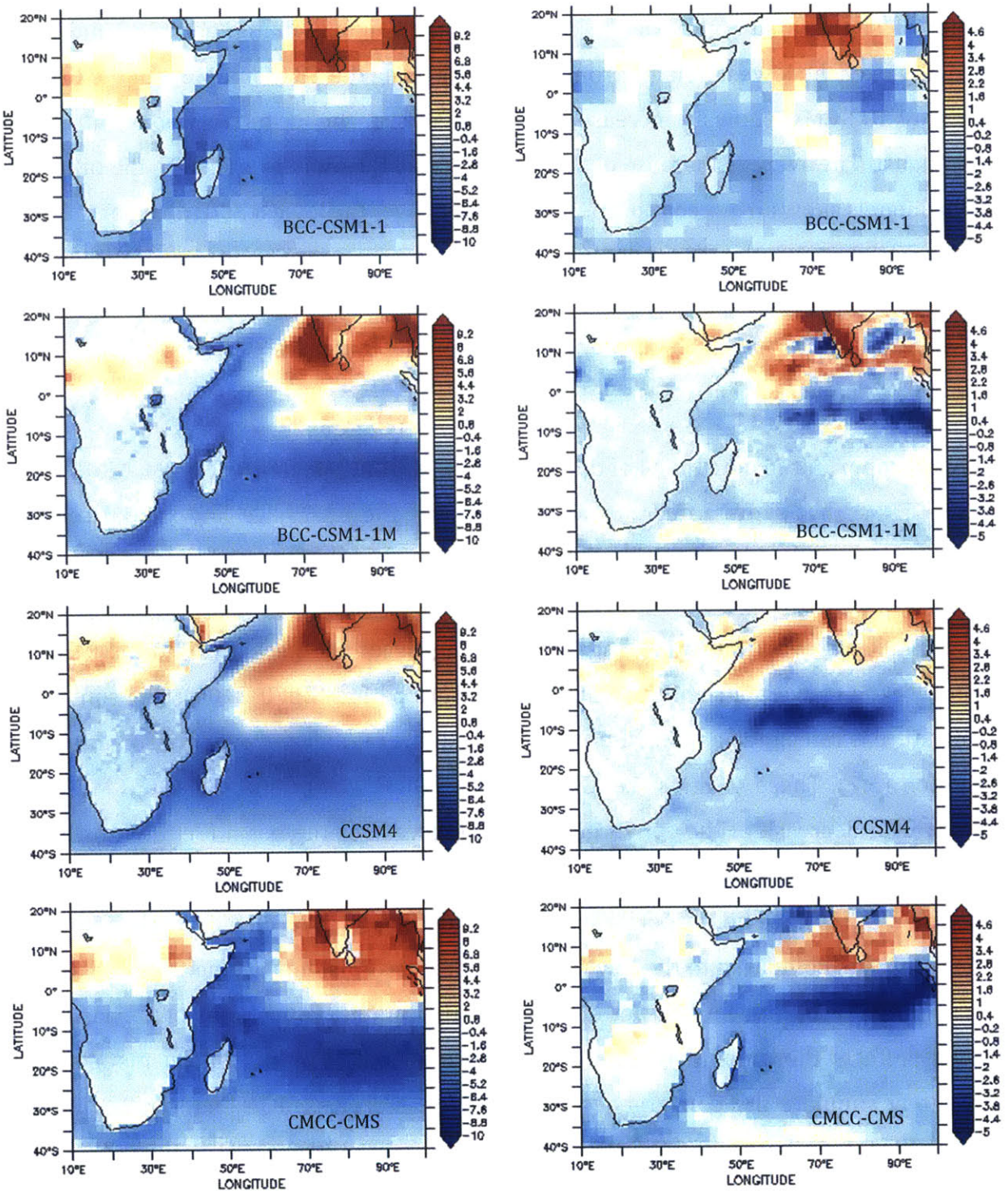


**Figure 6.2:** Average convergence of moisture (Left column in mm/day) estimated using Equation (6.2) during July and August for the period (1970-2000) and the future changes (Right Column in mm/day) for the period (2070-2100) for the different GCMs.

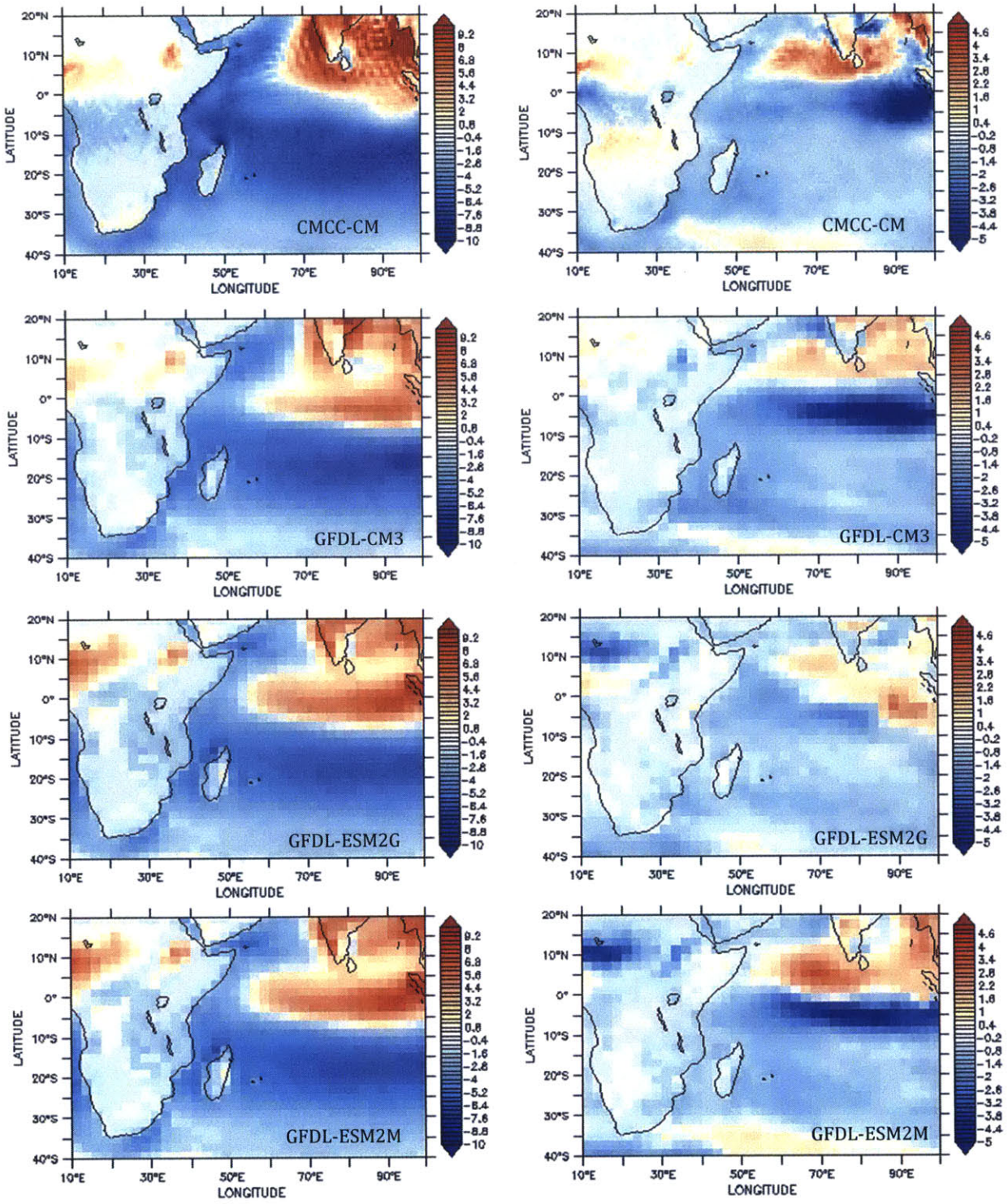


**Figure 6.2 (Continued):** Average convergence of moisture (left column in mm/day) estimated using Equation (6.2) during July and August for the period (1970-2000) and the future changes (right column in mm/day) for the period (2070-2100) for the different GCMs.

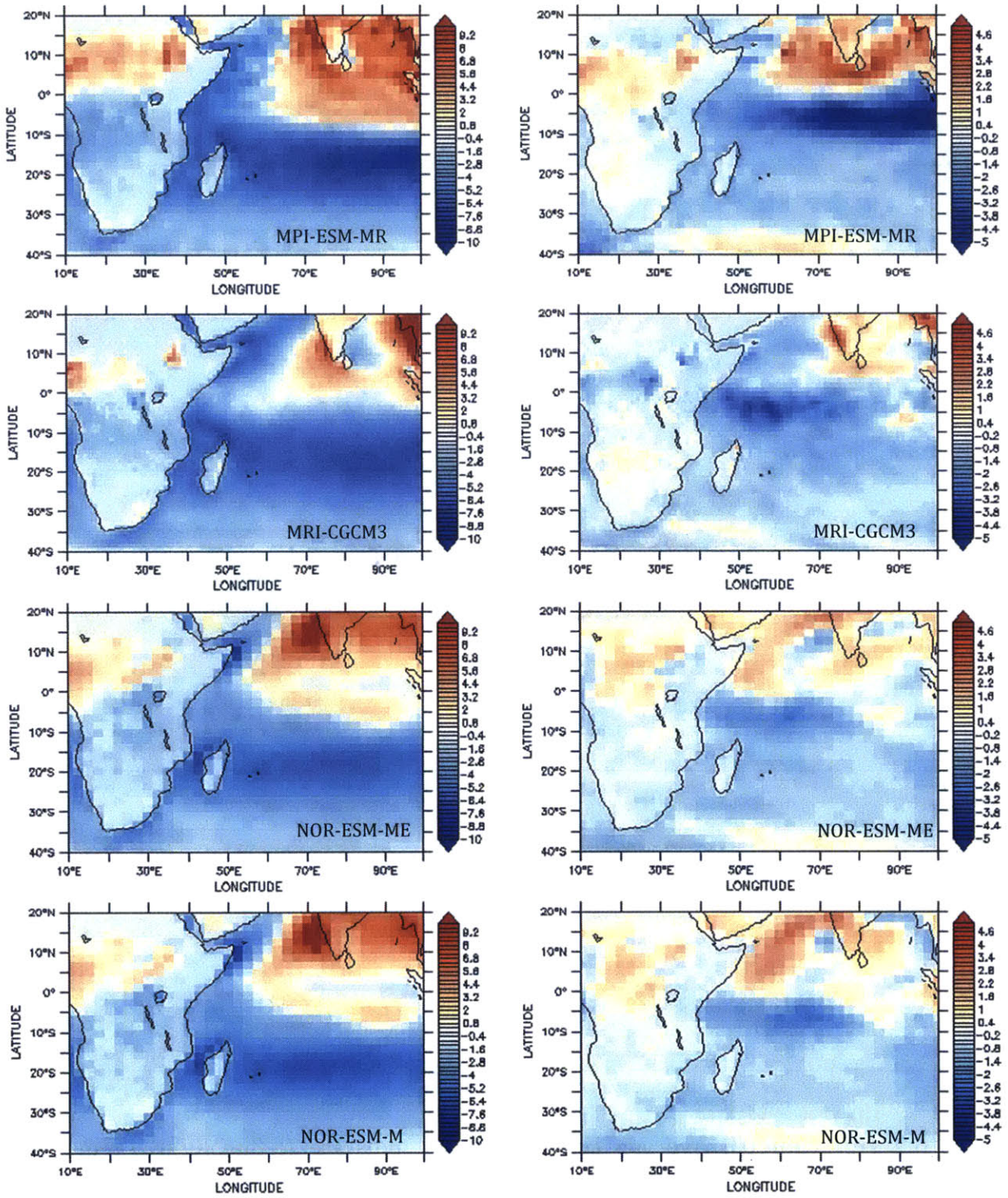


**Figure 6.2 (Continued):** Average convergence of moisture (left column in mm/day) estimated using Equation (6.2) during July and August for the period (1970-2000) and the future changes (right column in mm/day) for the period (2070-2100) for the different GCMs.

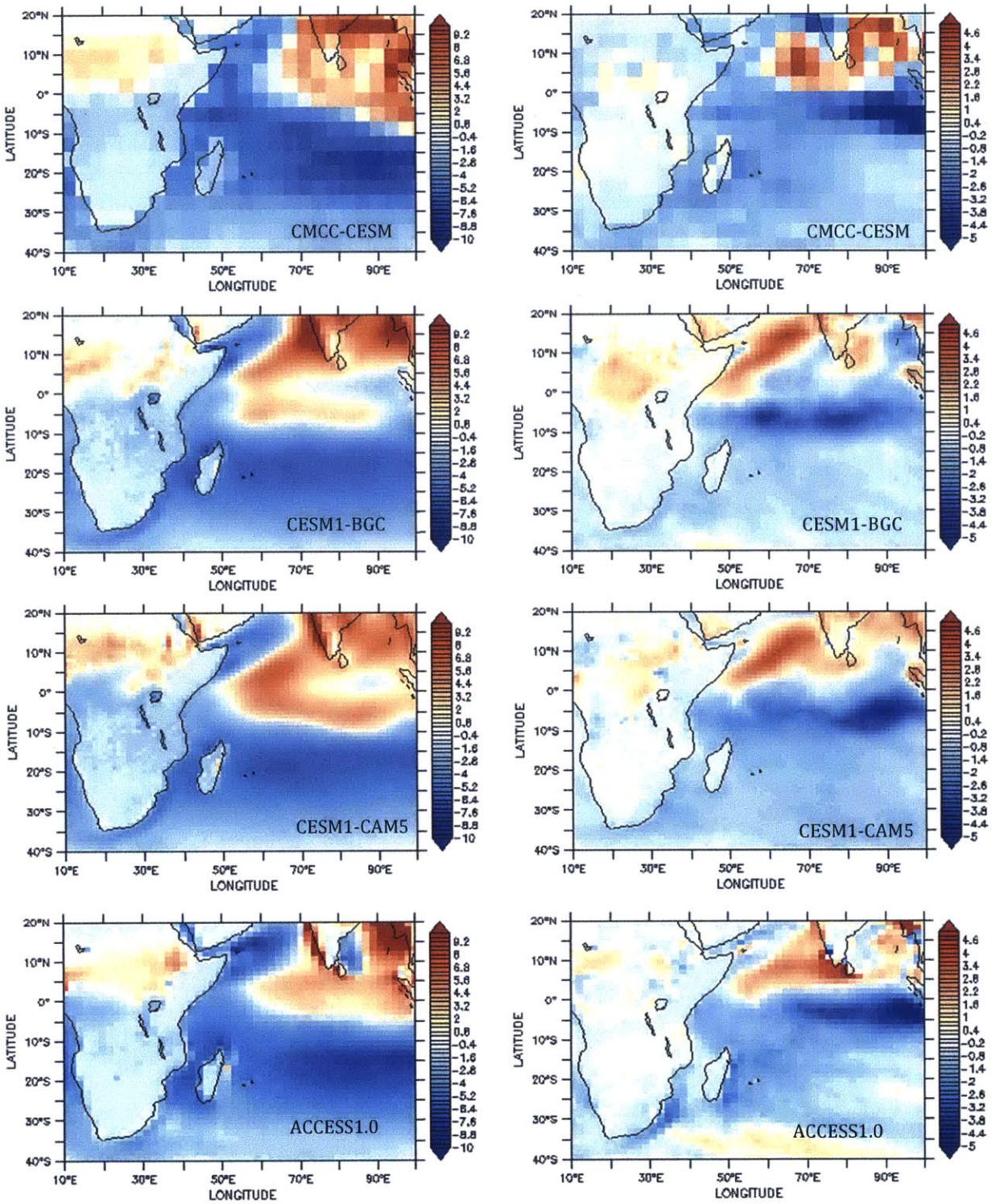


**Figure 6.2 (Continued):** Average convergence of moisture (left column in mm/day) estimated using Equation (6.2) during July and August for the period (1970-2000) and the future changes (right column in mm/day) for the period (2070-2100) for the different GCMs.

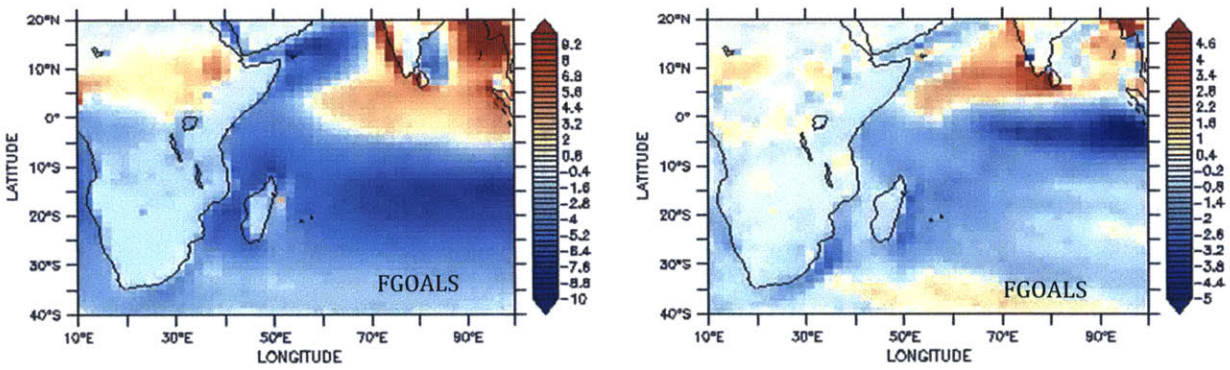


**Figure 6.2 (Continued):** Average convergence of moisture (left column in mm/day) estimated using Equation (6.2) during July and August for the period (1970-2000) and the future changes (right column in mm/day) for the period (2070-2100) for the different GCMs.

## 6.3 Future simulations

In the previous section, it is shown that GCMs agree on the increase of future air temperature, SST and humidity. However, the future changes of wind pattern are not consistent between the different GCMs (as shown in Appendix C). Therefore, in this section, the modified version of the regional climate model, described in section 4, is forced with modified lateral boundary conditions of humidity, SSTs and air temperature that mimics the future conditions. Furthermore, simulations using only increased future concentration of greenhouse gases are conducted to investigate the effects of greenhouse gases on the rainfall over the Upper Blue Nile basin.

### 6.3.1 Description of future simulations

Four different simulations are conducted in this section (Table 6.2). The main purpose of these four simulations is to investigate the individual impact of changing the boundary conditions (i.e. humidity, air temperature and SST) and the greenhouse gases on the rainfall and runoff of the Upper Blue Nile basin.

The (Past) simulation uses the ERA-interim reanalysis data for the lateral boundary conditions and sea surface temperatures (SSTs) are prescribed by the National Oceanic and Atmospheric Administration (NOAA) Optimum Interpolation (OISST). The simulation extends for 23 years period from 1989 to 2010 to be able to represent the mean climate of the basin.

The (BC) simulation is similar to the past simulation, except the lateral boundary conditions for the humidity, air temperature and the SST are modified to present future conditions. In chapter 4, it is shown that group 3 of the GCMs, which includes (CCSM4 and BCC-CSM1-1M) is the best GCMs for this study as they can simulate the teleconnection between the Nile and ENSO, have the best simulation of the seasonal cycle of rainfall over the Eastern Nile basin and have the highest spatial resolution. Therefore, the changes in the future relative humidity, air temperature and SST are estimated using these two GCMs and added to the

lateral boundary conditions from ERA-interim reanalysis data as follows. First, the long-term averages of temperature and relative humidity at each vertical level for each calendar month are calculated for the period (1970-2000) and (2070-2100) using RCP8.5 for each GCM (CCSM4 and BCC-CSM1-1M). Then, the long-term mean changes in the relative humidity and temperature fields in the future are estimated by subtracting the fields of (2070-2100) from the fields of (1970-2000) for each calendar month. Then, the changes from the two GCMs are averaged and applied to the temperature and relative humidity fields of ERA-Interim at all time steps of each calendar month. The same process is applied with the SST, however, the changes in the SST are applied to the observed SST of the National Oceanic and Atmospheric Administration (NOAA) Optimum Interpolation (OISST).

The (GHG) simulation, is similar to the past simulation, except the values of the concentration of greenhouse gases are modified to mimic the greenhouse gas concentrations of the future period (2070-2100) using RCP8.5.

The (BC+GHG) simulation includes both the modified lateral boundary conditions and future greenhouse gas concentrations s. Hereinafter, it will referred to this simulation as (BC+GHG) simulation.

**Table 6.2:** Summary of the four simulations used in this study.

| | **Past Boundary Conditions** | **Future Boundary Conditions** |
|---|---|---|
| **Past GHG** | Past simulation | BC simulation |
| **Future GHG** | GHG simulation | BC+GHG simulation |

### 6.3.2 Results of future simulation

The changes in the rainfall over the Upper Blue Nile basin are shown in Figure 6.3a. In general, all future simulations show an increase of rainfall over the basin. The rainfall increases by 3.4%, 11.8% and 8% for the BC, GHG and BC+GHG simulations respectively. Similarly, the runoff over the Upper Blue Nile basin increases by almost two times the percent increase of the rainfall (i.e. 6.5%, 25% and 17% for the BC, GHG and BC+GHG simulations respectively) as shown in Figure 6.3b. The difference between the rate of increase of the rainfall and runoff can be explained by the runoff elasticity of the Upper Blue Nile basin, which is approximately ~1.5 (i.e. 1% increase in the rainfall will induce 1.5% increase of the runoff in the basin) as discussed in Chapter 7. Furthermore, the 2 meters air temperature increases by almost 4.6$^{o}$C over the basin for the BC and BC+GHG simulations and does not change with the GHG simulation (Figure 6.4).

Figure 6.5a and 6.5b show the seasonal cycle of the large scale and convective rainfall respectively for the four simulations. The changes of the lateral boundary conditions and SSTs increase the large scale rainfall mainly during July to September period. The effect of modifying the boundary conditions on large scale rainfall can be shown by comparing the results of BC simulation with the Past simulation and BC+GHG simulation with the GHG simulation respectively (Figure 6.5a). On the other hand, the changes of greenhouse gas concentrations increase the convective rainfall mainly during January to June period. This effect on the convective rainfall can be shown by comparing the results of GHG simulation with the Past simulation and BC+GHG simulation with the BC simulation respectively (Figure 6.5b). Thus, the mechanisms by which the modified lateral boundary conditions and increased concentration of greenhouse gases increase the rainfall are different.

First, modifying the lateral boundary conditions mainly increases the humidity in the domain of simulation, which tends to increase the moisture fluxes and thus the rainfall over the basin. Figure 6.7c and 6.7d shows the change in average monthly vertical profiles of specific humidity averaged over the Upper Blue Nile basin because of changing the lateral boundary conditions and SSTs. Figure 6.7c and 6.7d show the effect of the boundary conditions on

humidity by subtracting the results of BC simulation from the Past simulation and BC+GHG simulation from the GHG simulation respectively. The specific humidity increases mainly during July to October close to the surface by approximately 2 g/kg as shown in Figure 6.7c and 6.7d. On the other hand, the effect of greenhouse gases on humidity is shown by subtracting the results of the GHG simulation from the Past simulation and BC+GHG simulation from the BC simulation. The increase of the greenhouse gases does not increase the humidity as much as the increase from changing the lateral boundary conditions and SSTs. The specific humidity increases only by approximately 0.5 g/kg close to the surface as shown in Figure 6.7a and 6.7b. Although the increase of the specific humidity is much higher because of the modified boundary conditions, the increase of rainfall is less compared to the effect of modified greenhouse gases. Thus, the increase of greenhouse gas concentrations should be affecting the rainfall through a different mechanism as will be discussed in the next part.

Second, modifying the greenhouse gas concentrations mainly increases the convective rainfall as shown in Figure 6.5b during the January to June period. This increase can be explained as follows: increasing the greenhouse gas concentrations changes the vertical profile of the virtual temperature as shown in Figure 6.9a and 6.9b. The virtual temperature increases between approximately 600 mb and 450 mb, which increases the Convective Available Potential Energy (CAPE) as shown in figure 6.10 and thus increases the vertical upward velocity (Figure 6.12a and 6.12b), which increases the convective rainfall over the basin. The Convective available Potential Energy is calculated by following an air parcel from the surface using dry adiabat till the Level of Free Convection (LFC) and then saturation adiabat till the Level of Neutral bouncy (LNB). Then, the difference in temperature between the air parcel and the surrounding air temperature is used to calculate CAPE from the Level of Free Convection (LFC) to the Level Neutral Buoyancy (LNB) as follows:

$$\text{CAPE} = R.\int_{LFC}^{LNB}(T - T').dP \qquad (6.1)$$

Where: R: is the specific gas constant (287 J $kg^{-1}$ $k^{-1}$), T: is the temperature of the lifted parcel, T': is the temperature of the surrounding air at each pressure level (P). These results are consistent with Romps et al., 2014 results, which showed that CAPE will increase in the

future over the United States of America, although it is not clear if this increase is due to the increased greenhouse gas concentrations or any other factors.

On the other hand, the changes in the lateral boundary conditions increase the virtual temperature close to the surface, however, the increase in temperature is higher aloft, which tends to stabilize the atmosphere (Figure 6.9c and 6.9d) and reduce CAPE and the convection (Figure 6.10). This effect is also illustrated in Figure 6.13a and 6.13b by comparing the distribution of CAPE for March to April and July to September periods. In Figure 6.13a, it is shown that changing the lateral boundary conditions reduces CAPE by increasing the probability of occurrence of low CAPE values (i.e. lower than 100 J/kg) and reducing the probability of occurrence of high CAPE values (i.e. greater than 300 J/KG). This conclusion can be drawn by comparing the BC simulation (red bars) with the Past simulation (blue bars) and also between the BC+GHG (brown bars) with the GHG simulation (green bars). The effect of changing the lateral boundary is similar for July to September period, however, the impact of the lateral boundary is more clear. Figure 6.13b shows that almost 50% of the CAPE values fall below 50 (J/kg) for the BC and BC+GHG simulations, while for the Past and GHG simulations only ~8% of CAPE values fall below 50 (J/kg).

Several studies have shown similar results for the changes in the rainfall due to global warming. Collins et al. (2010) summarized the impact of global warming on the rainfall based on the work of Vecchi and Soden (2007). They showed that with global warming the amount of global water vapor in the atmosphere will increase at a rate of approximately 7% per degree Kelvin of warming averaged globally. This result is consistent with the Clausius-Clapeyron relation that governs the relation between the water vapor pressure and temperature. Furthermore, they found the rainfall only increases at a rate of 1.2% per degree Kelvin of warming averaged globally. They attributed the difference between the rate of increase of water vapor in the atmosphere and rainfall to the reduction of the convection activity. In order to test the hypothesis of the reduction of convection, they used two approaches. First, they used a simple parametrization that relates the humidity, temperature, rainfall and convective mass flux as follows:

$$P=Mq \quad (6.2)$$

Where: P is the rainfall, M is the convective mass flux, q: is the boundary layer mixing ratio and can be related to temperature using the Clausis-Clapyeron relation. In this parametrization it is assumed that the rainfall is formed by the water vapor in the boundary layer that is carried upward by the convective mass flux and condenses and falls out as rainfall.

The analysis of the different GCMs using this parametrization showed that the convective mass flux is decreasing with global warming. A second approach to test the same hypothesis of decreased convection was investigating the vertical velocity at 500 mb using the different GCMs. It also showed that the vertical velocity has decreased with global warming indicating a weakening of the global convection activity.

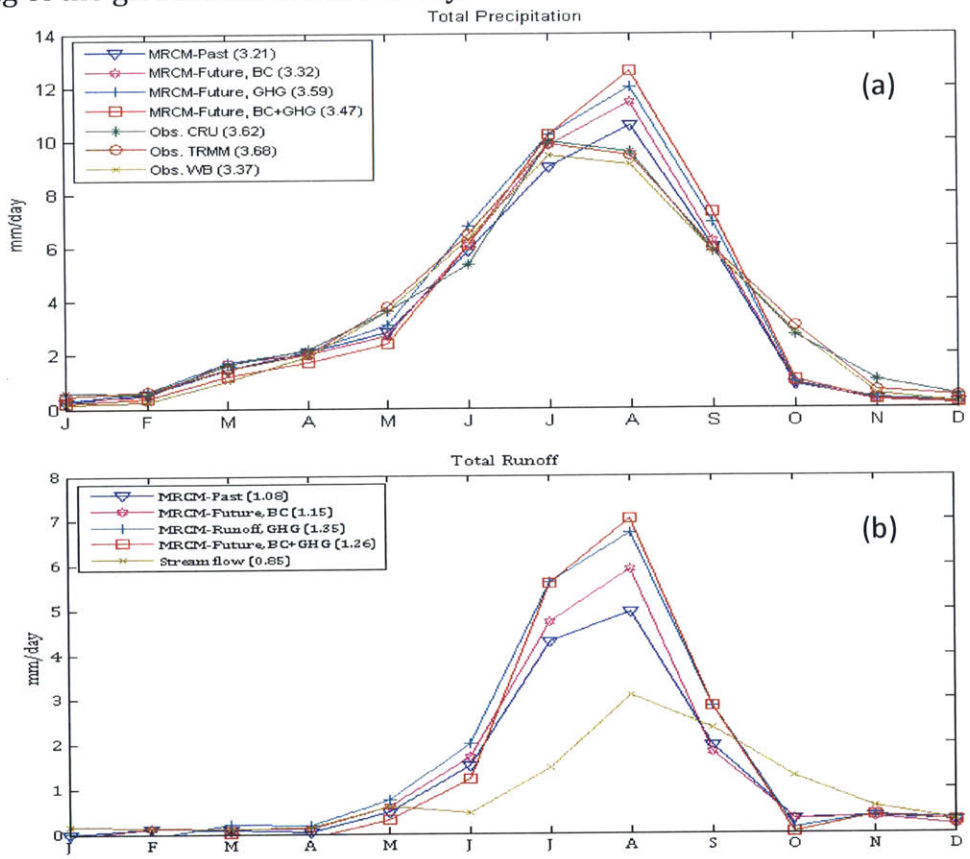


**Figure 6.3:** Monthly 21-years averages values for: (a) Total rainfall (mm/day) compared to observations from TRMM-V7 3B43, CRU and water balance model (WB) of Allam et al., 2016, and (b) Runoff (mm/day) compared to the observed streamflow of the Upper Blue Nile basin for the four simulations.

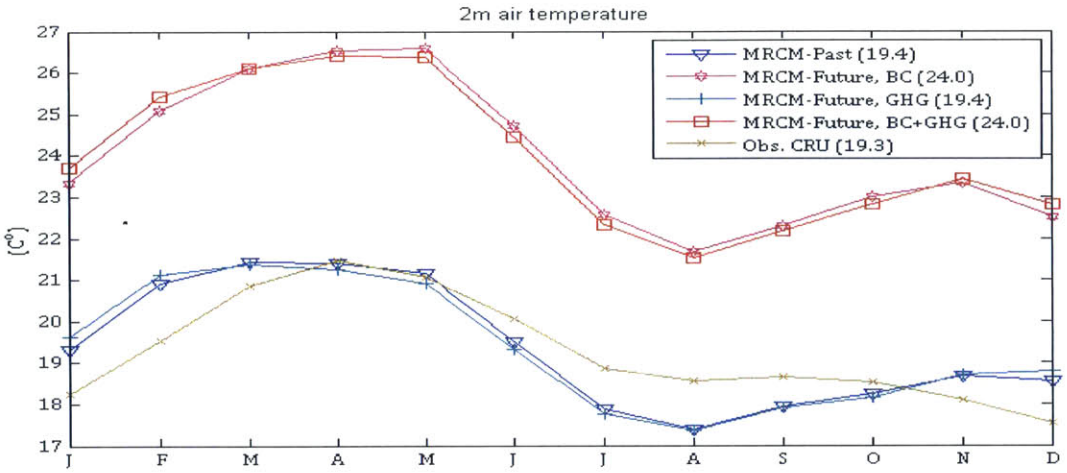


**Figure 6.4:** Monthly 21-years averages values for the 2 meters air temperature for the different simulations and compared to observations from CRUTS3.1 over the Upper Blue Nile basin.

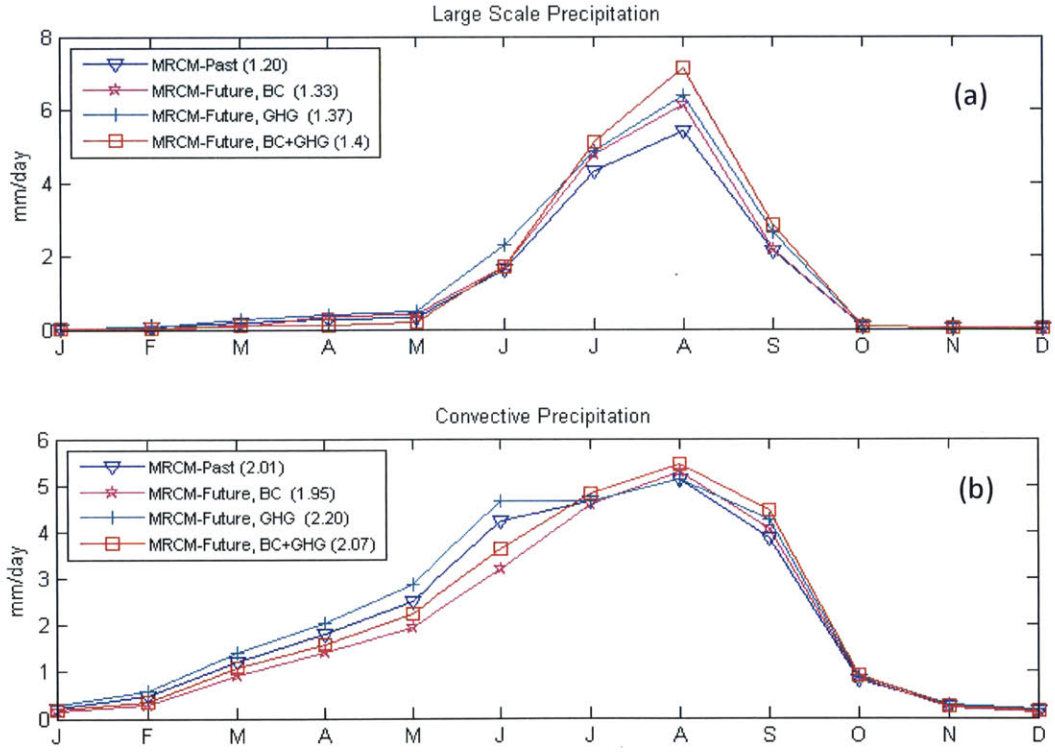


**Figure 6.5:** Monthly 21-years averages values for: (a) Large scale rainfall (mm/day), and (b) Convective rainfall (mm/day) over the Upper Blue Nile basin for the four simulations.

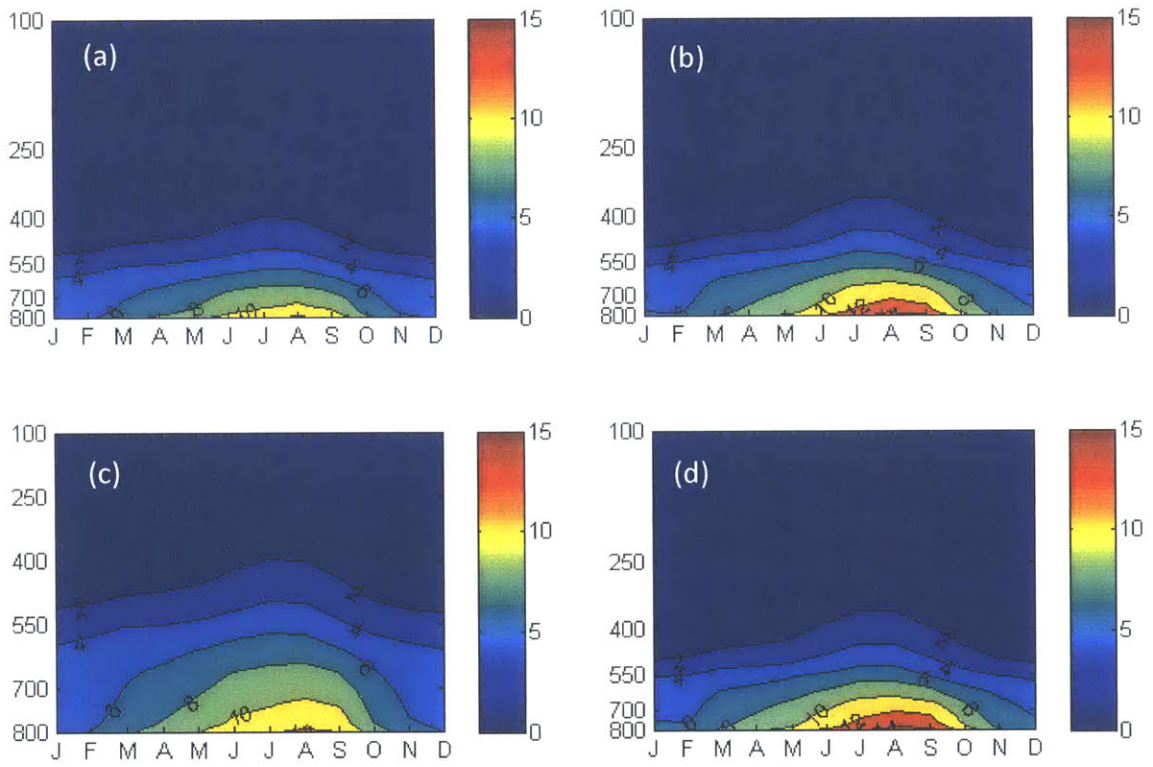


**Figure 6.6:** Monthly 21-years (1990-2010) averages values of the vertical profile in pressure coordinates (mb) of specific humidity (g/kg): (a) Past simulation, (b) BC simulation, (c) GHG simulation, and (d) BC+GHG simulation over the Upper Blue Nile basin.

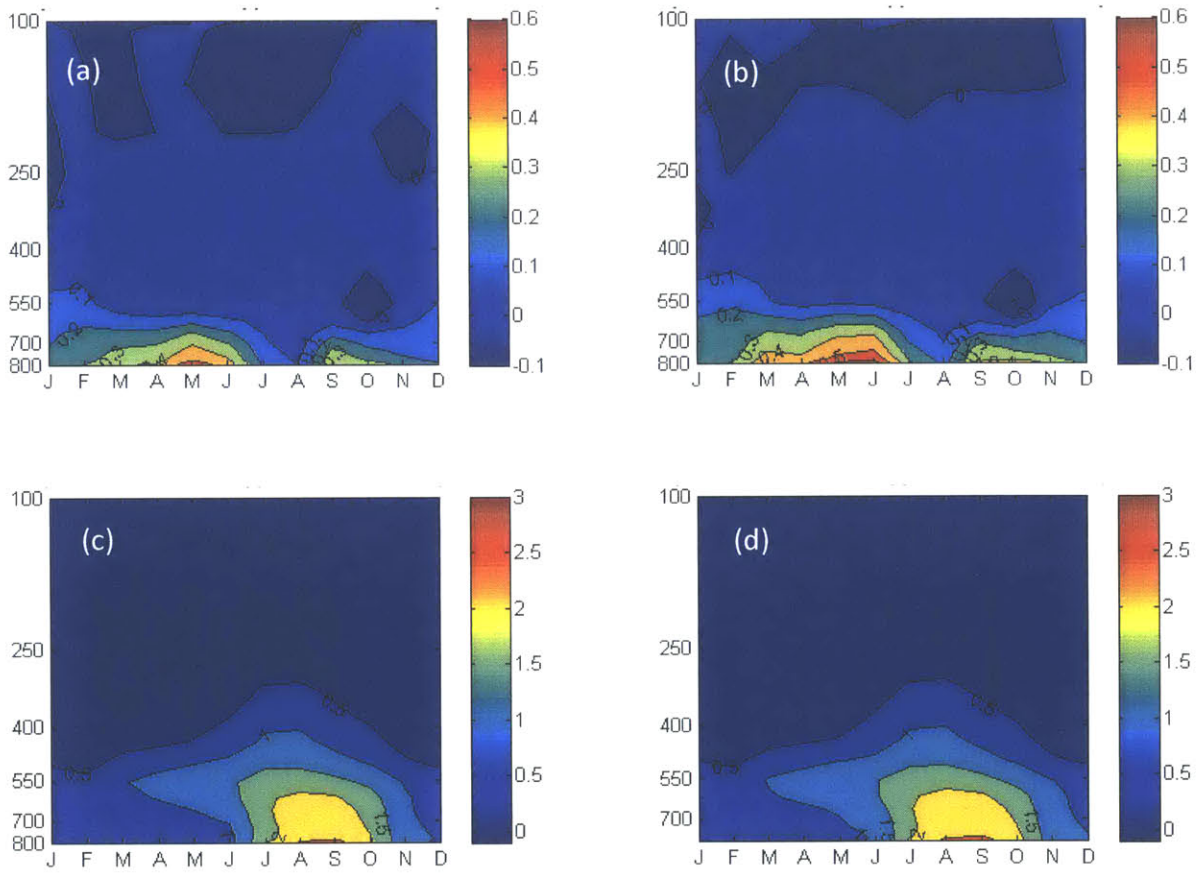


**Figure 6.7:** Monthly 21-years (1990-2010) averages values of the vertical profile in pressure coordinates (mb) of specific humidity (g/kg) over the Upper Blue Nile basin for: (a) Difference between GHG simulation and Past simulation, (b) Difference between BC+GHG simulation and BC simulation, (c) Difference between BC simulation and Past simulation, and (d) Difference between BC+GHG simulation and GHG simulation.

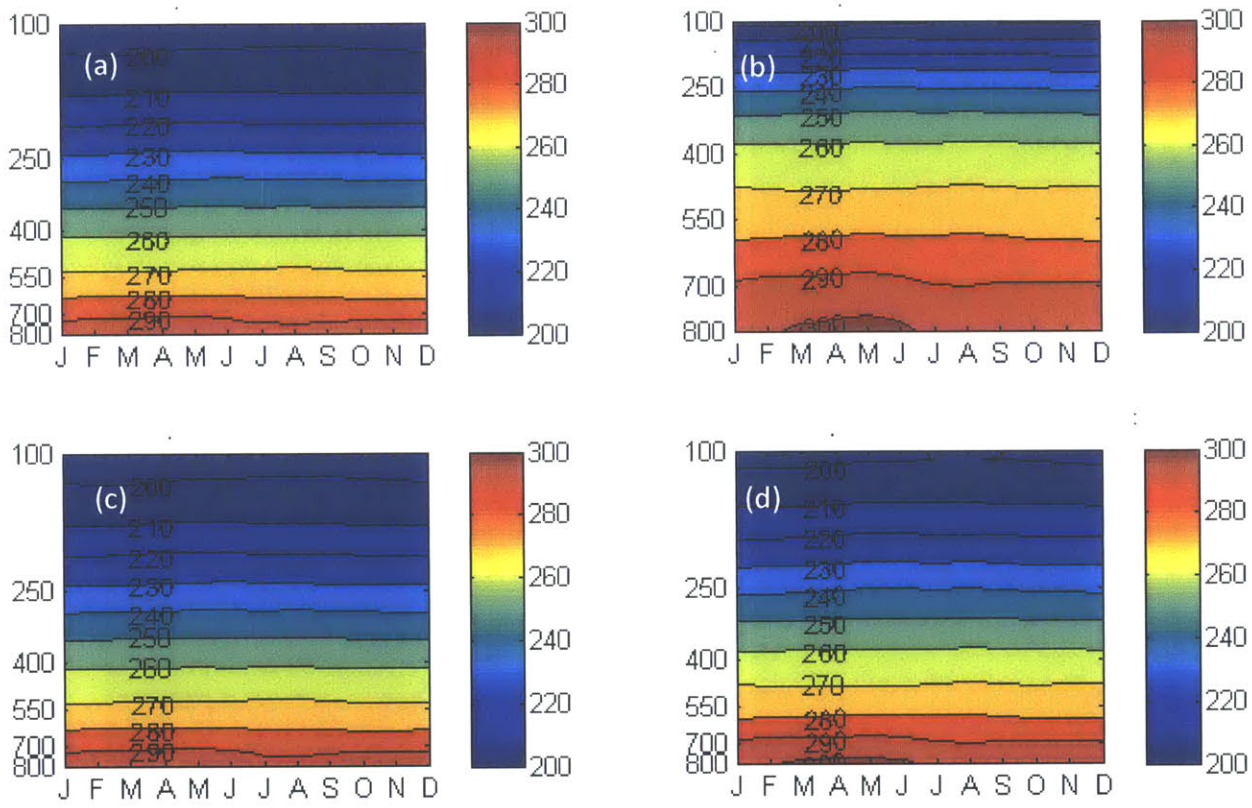


**Figure 6.8:** Monthly 21-years (1990-2010) averages values of the vertical profile in pressure coordinates (mb) of virtual temperature (Kelvin): (a) Past simulation, (b) BC simulation, (c) GHG simulation, and (d) BC+GHG simulation over the Upper Blue Nile basin.

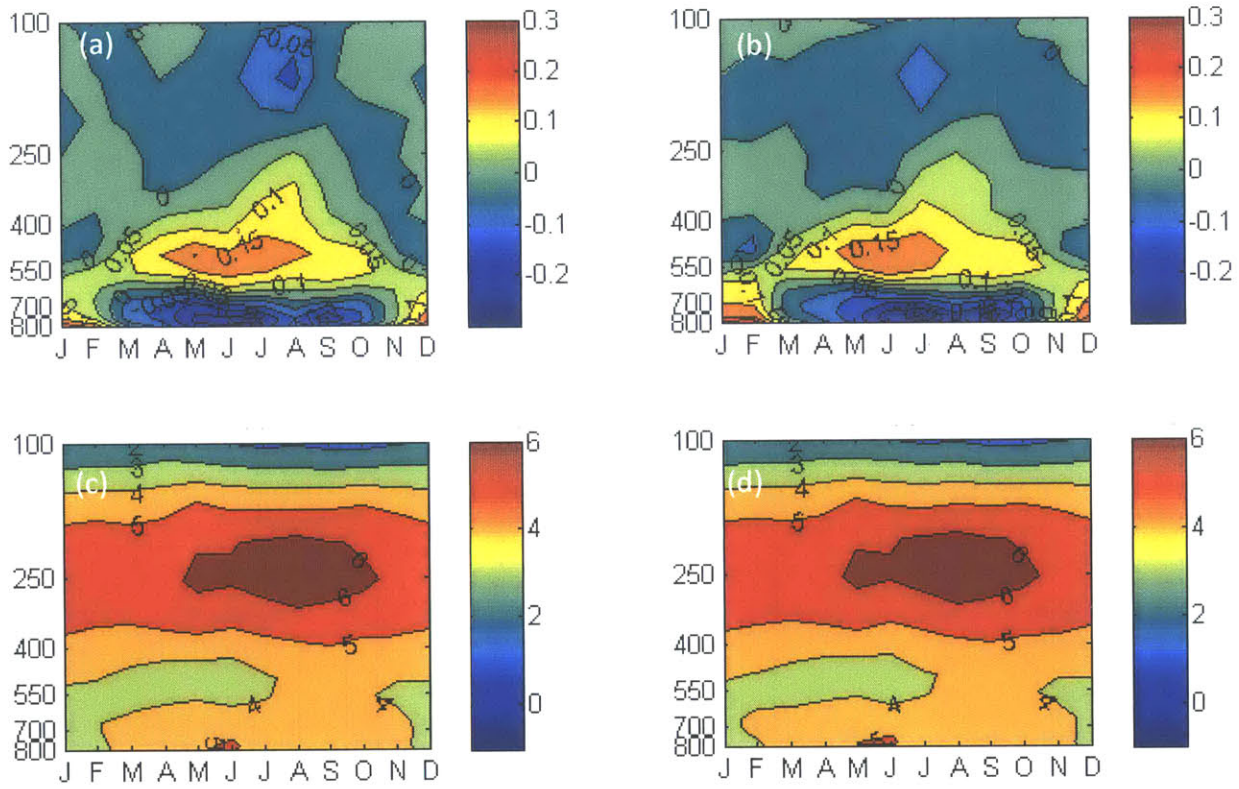


**Figure 6.9:** Monthly 21-years (1990-2010) averages values of the vertical profile in pressure coordinates (mb) of virtual temperature (Kelvin) over the Upper Blue Nile basin for: (a) Difference between GHG simulation and Past simulation, (b) Difference between BC+GHG simulation and BC simulation, (c) Difference between BC simulation and Past simulation, and (d) Difference between BC+GHG simulation and GHG simulation.

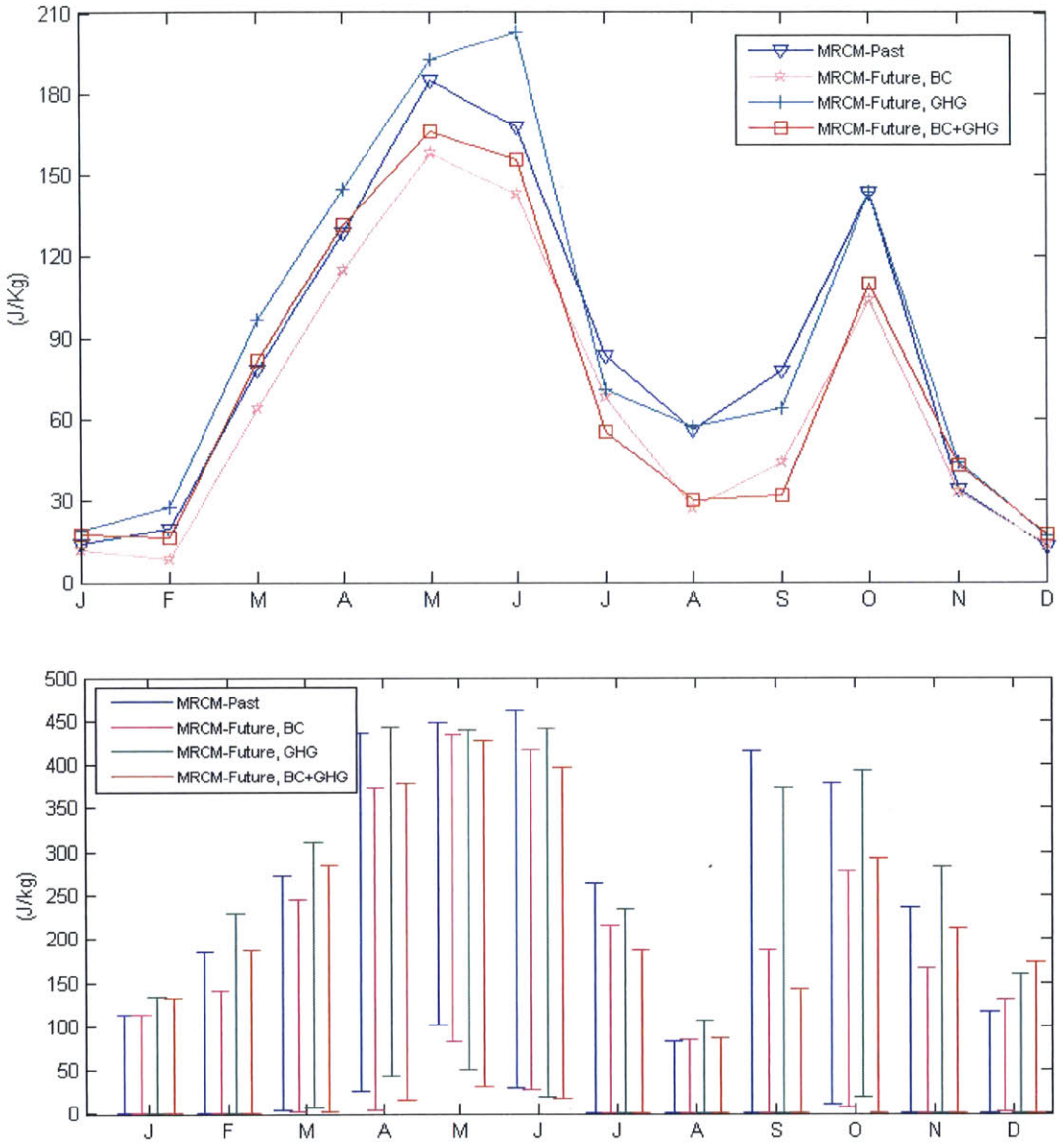


**Figure 6.10:** (a) Monthly 21-years averages values of Convective Available Potential Energy (CAPE), (b) 2.5% and 97.5% percentile range of values for CAPE for each month over the Upper Blue Nile basin for the four simulations.

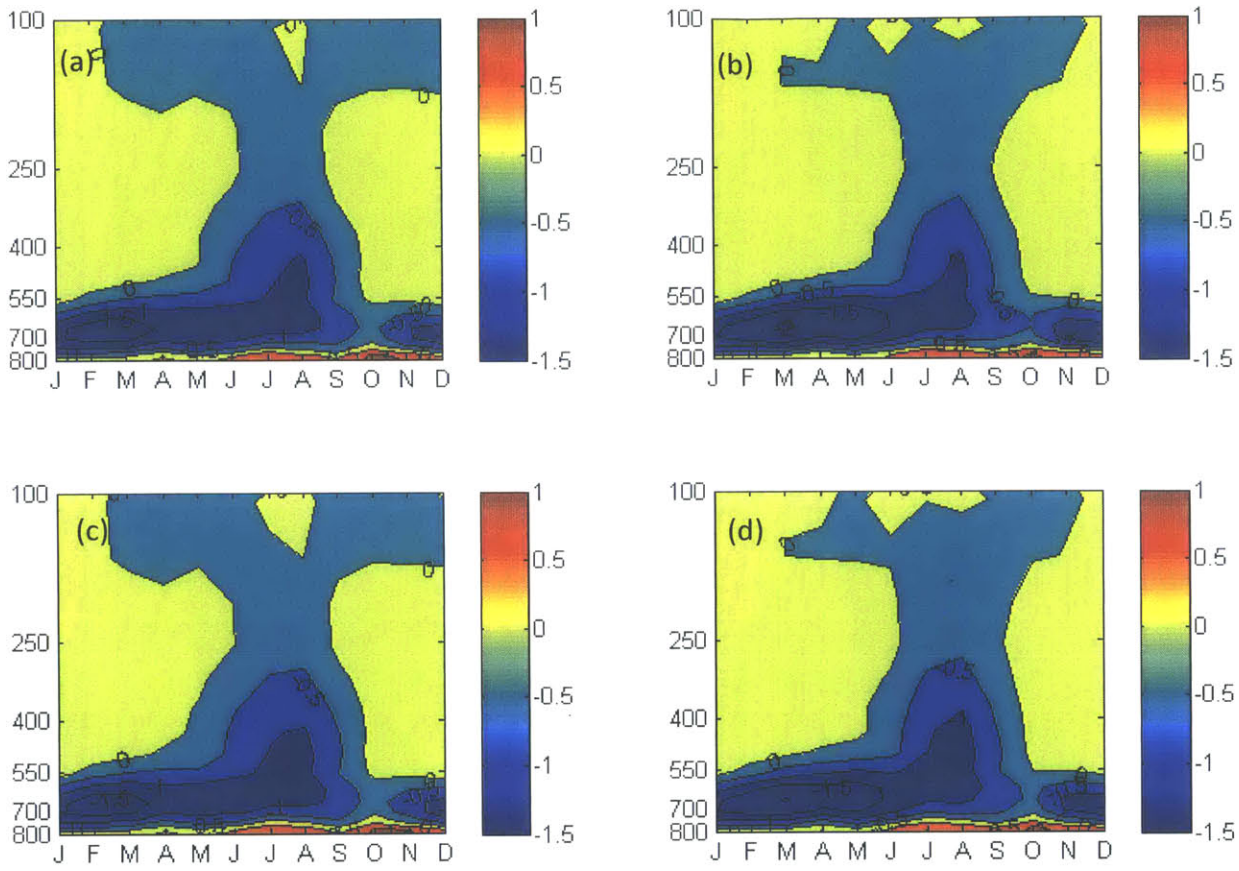


**Figure 6.11:** Monthly 21-years (1990-2010) averages values of the vertical profile in pressure coordinates (mb) of vertical velocity in pressure coordinates (x10 (Pa/s)) over the Upper Blue Nile basin for: (a) Past simulation, (b) BC simulation, (c) GHG simulation, and (d) BC+GHG simulation over the Upper Blue Nile basin.

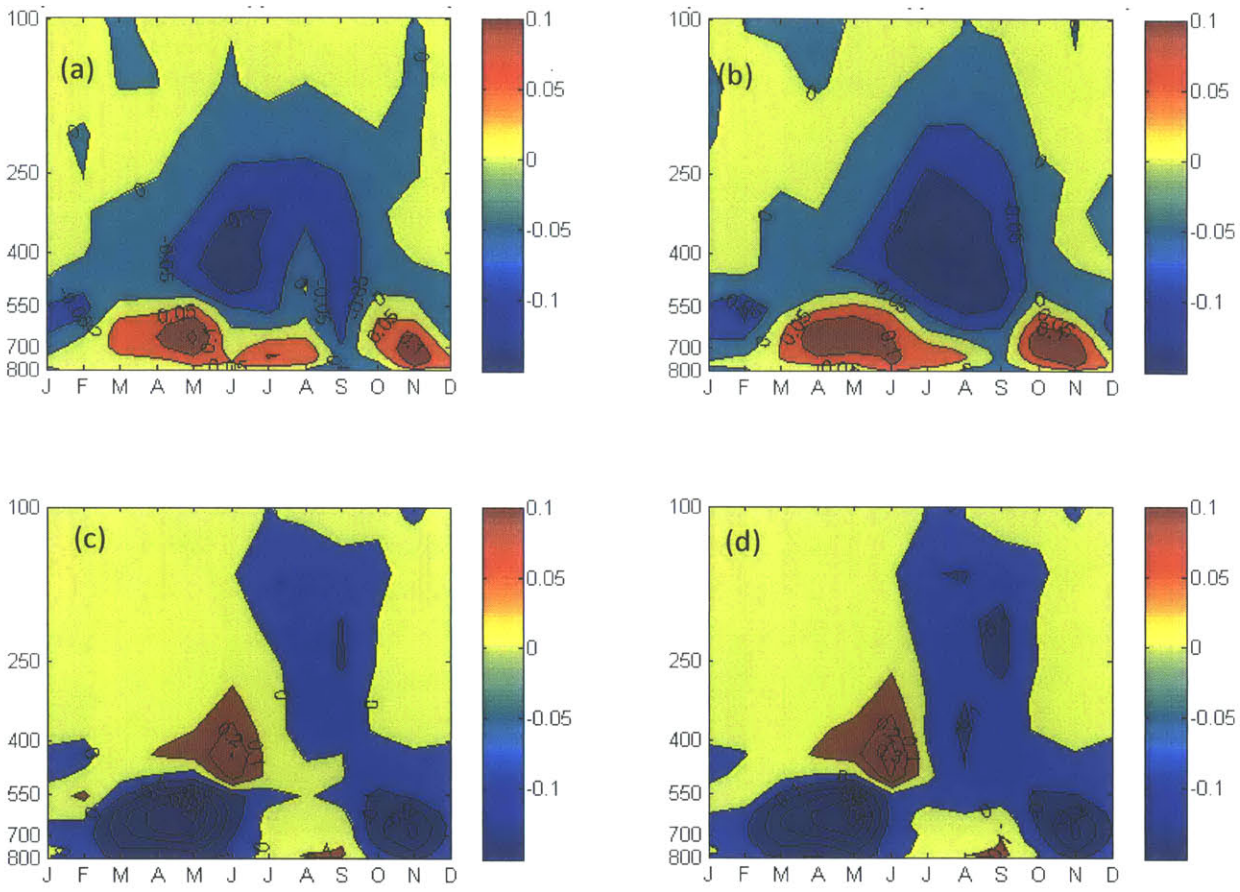


**Figure 6.12:** Monthly 21-years (1990-2010) averages values of the vertical profile in pressure coordinates (mb) of vertical velocity in pressure coordinates (x10 (Pa/s)) over the Upper Blue Nile basin for: (a) Difference between GHG simulation and Past simulation, (b) Difference between BC+GHG simulation and BC simulation, (c) Difference between BC simulation and Past simulation, and (d) Difference between BC+GHG simulation and GHG simulation.

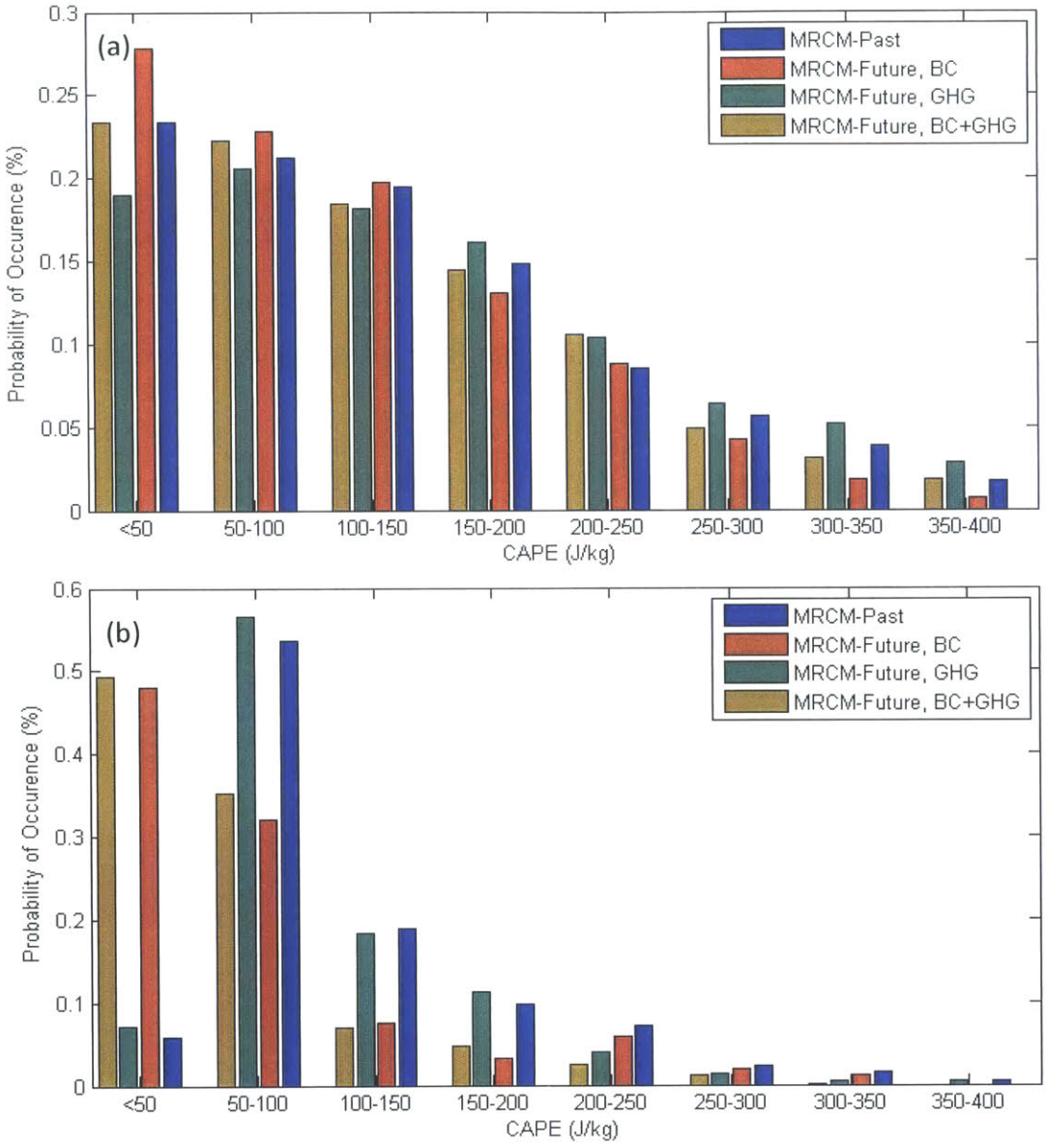


**Figure 6.13:** Convective Available Potential Energy (CAPE) histogram of the four simulations over the Upper Blue Nile basin for: a) March, April and May period and, b) for July, August and September.

Figures 6.14 and 6.15 show the spatial changes in the rainfall and 2 meters air temperature averaged from June to September for the different future simulations compared to the past simulation. The changes in the rainfall and 2 meters air temperature are different between the future simulations. For example, the BC simulation shows an increase of the rainfall over a small area close to the south eastern boundary of the Upper Blue Nile basin (Figure 6.14c). On the other hand, the GHG simulation shows an increase almost over all the northern part of the basin (Figure 6.14b). The BC+GHG simulations show the highest increase also close to the south eastern boundary and extend to include the central region of the basin (Figure 6.14d).

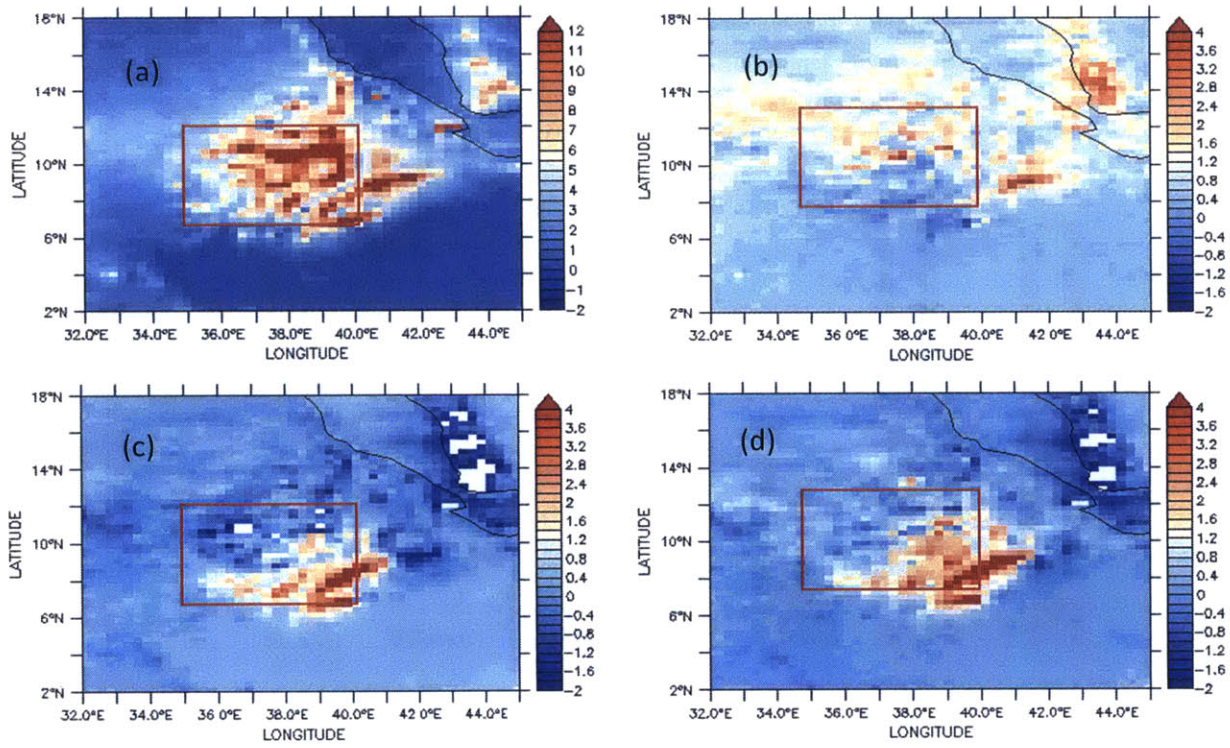


**Figure 6.14:** Monthly average of the rainfall from June to September for : (a) past simulation, (b) GHG simulation, (c) BC simulation, and (d) BC+GHG simulation. The red boxes encloses the Upper Blue Nile basin.

The changes in the 2 meters air temperature are shown in Figure 6.15. The 2 meters air temperature changes slightly using the GHG simulation (Figure 6.14b). On the other hand, the changes in the temperature are higher in the BC simulation (Figure 6.15c) and the BC+GHG simulation (Figure 6.15d) simulations. The 2 meters air temperature almost increases by 4°C in these simulations.

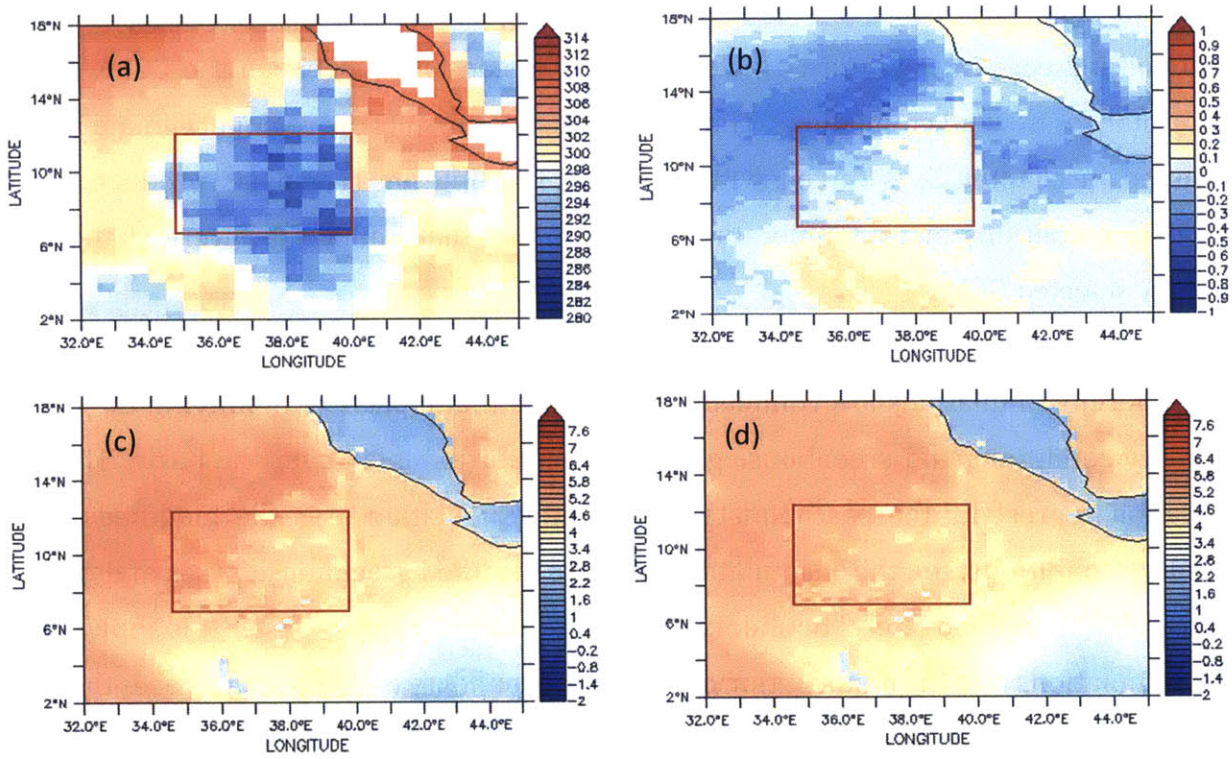


**Figure 6.15:** Monthly average of the 2 meters air temperature from June to September for : (a) past simulation, (b) difference between GHG simulation and past simulation, (c) difference between BC simulation and past simulation, and (d) difference between BC+GHG simulation and past simulation. The red boxes encloses the Upper Blue Nile basin.

## 6.5 Conclusions

In this chapter, changes in the long-term averages of rainfall are investigated. First, GCMs are analyzed to discern the common future changes in key factors that affect rainfall over the Nile basin. GCMs agree that the SST over the Indian ocean, humidity and rainfall over the basin will increase in the future. However, there no consensus between the GCMs on the future changes of wind circulations. Thus, based on these results the regional climate model, discussed in chapter 5, is forced with modified ERA-Interim reanalysis product lateral boundary conditions of air temperature and humidity that mimic the future changes by carefully selected GCMs.

Four different simulations are conducted to examine the impacts of modifying the lateral boundary conditions and greenhouse gases on the future rainfall over the basin. The first simulation represents the past climate, the second simulation uses the modified lateral boundary conditions, the third simulation uses the modified greenhouse gases and the last one uses both modified lateral boundary conditions and greenhouse gases. It is shown from these simulations that the modification of the lateral boundary conditions increases the large scale rainfall over the basin because of the increase in humidity and moisture fluxes. In addition, the modification of the lateral boundary conditions increases the temperature aloft, which stabilize the atmosphere and reduce the convective rainfall. On the other hand, the increase of greenhouse gas concentrations increases the air temperature in the middle atmospheric layers, which increases the convective available potential energy (CAPE) and hence the convection and convective rainfall over the basin and has the larger effect on the rainfall.

# Chapter 7: Sensitivity of the changes in the flow to changes in rainfall for the Upper Blue Nile basin

In chapter 6, it is shown that 1% increase of the rainfall translates into approximately 2% increase in the corresponding runoff. In this chapter, an analysis of the runoff elasticity to rainfall is investigated for the Upper Blue Nile basin based on observations of rainfall and streamflow. Then, the accuracy of the MIT-Regional climate model (MRCM) and the GCMs in simulating the runoff elasticity to rainfall are also investigated. It is important that the model has the right runoff elasticity to avoid introducing artificial biases in the simulated runoff. For example, if the model does not have the right elasticity, it can amplify or diminish the signal of climate change on the simulated future runoff and provides misleading estimates of the future changes in the runoff.

## 7. 1 Runoff Elasticity using observations of stream flow and rainfall data

The runoff elasticity to rainfall (Ɛ (R)) is defined as the proportional change in the runoff (R) to change in rainfall (P) as shown in the following equation:

$$\text{Ɛ (R)} = \frac{dR}{dP} \text{ x } \frac{P}{R} \qquad (7.1)$$

Several studies investigated the runoff elasticity to rainfall (Sankarasubramanian and Vogel, 2001; Sankarasubramanian and Vogel, 2003; Nieman and Eltahir, 2005; Yang and Yang, 2011; Tang and Lettenmaier, 2012; Wang and Alimohammadi, 2012). Although these studies agree on the definition of the runoff elasticity to rainfall as shown in equation 7.1, the approach to calculate it varies depending on the model used to simulate the relation between the runoff and rainfall. The relation between the runoff and rainfall had different forms including linear and nonlinear models. The linear models included simple linear regression between the rainfall and runoff (Tang and Lettenmaier, 2012; Wang and Alimohammadi, 2012), while the nonlinear relation took several forms including nonlinear regression or

using nonlinear relations between the rainfall and runoff (e.g. Budyko Curves) (Sankarasubramanian and Vogel, 2001, Yang and Yang, 2011). Sankarasubramanian and Vogel, 2003 used non-paramteric approach to estimate the runoff elasticity as follows:

$$\varepsilon\,(\mathrm{R}) = median\{(R_t - \bar{R})/((P_t - \bar{P})x(R_t/\bar{R})\} \quad (7.2)$$

Where, $\bar{R}$ = the long-term mean of the runoff, $\bar{P}$= the long-term mean of the rainfall, $R_t$= runoff value at time step (t), and $P_t$= rainfall value at time step (t).

Nieman and Eltahir, 2005 used a physically based model to simulate the relations between the different hydrological variables (e.g. rainfall, runoff, evapotranspiration and soil moisture). Then, temporal variations of the soil moisture and rainfall are fitted to certain probability density functions (PDF). Thus, as the long-term mean of the runoff, $E(\bar{R})$, depends on soil moisture and rainfall, it can estimated using the following equation:

$$E(\bar{R}) = \int_{\bar{s}=0}^{1}\int_{P=0}^{\infty}\bar{R}\; f_{\overline{P|S}}\, d\bar{s}\, d\bar{P} \quad (7.3)$$

Where, $f_{\overline{P|S}}$ is the joint distribution of $\bar{s}$ and $\bar{P}$, and $\bar{R}$can be replaced by the mathematical formulation that relates the runoff with the rainfall and soil moisture. Then the runoff elasticity is found numerically based on equation 7.3.

For the calculation of the runoff elasticity to rainfall for Upper Blue Nile basin, we use a combination of the shown approaches based on the available observed data over the basin. The observations include stream flow and rainfall gauges data for the period (1965-2010) that are used in chapter 4. In this analysis, we first fit a quadratic relation (i.e. R=g(P)) between the annual rainfall (P) over the basin and the annual runoff (R) as shown in Figure 7.1a. Then, we follow Nieman and Eltahir, 2005 approach by fitting the time series of the rainfall to a PDF ($f_p$). The gamma distribution fits well with the observed distribution of the rainfall as shown in Figure 7.2. Thus the long-term mean of the rainfall ($\bar{P}$) can be estimated as follows:

$$\bar{P} = \int_0^{\infty} f_p dP \qquad (7.4)$$

Then the long-term mean of the runoff ($\bar{R}$) can be calculated as:

$$\bar{R} = \int_0^{\infty} g(P).f_p dP \quad (7.5)$$

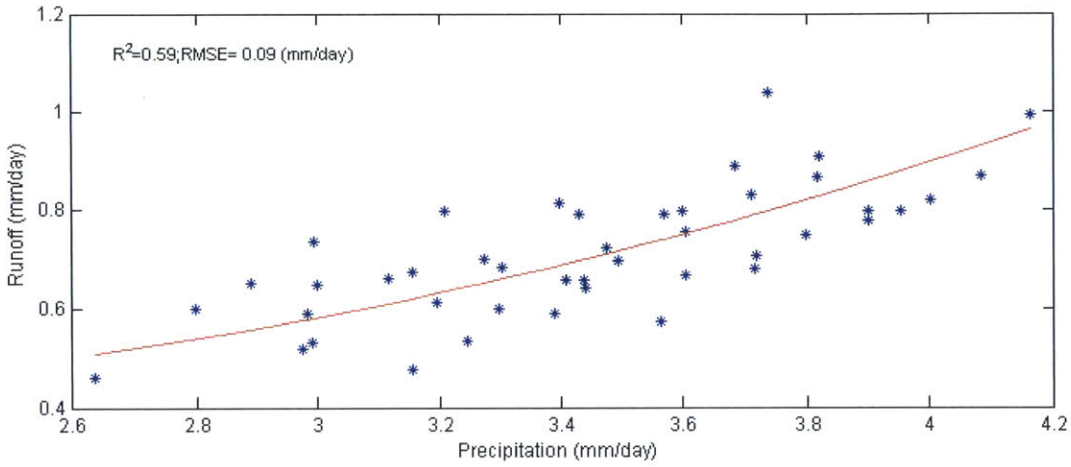


**Figure 7.1:** Relation between the annual observed runoff and rainfall over the Upper Blue Nile basin.

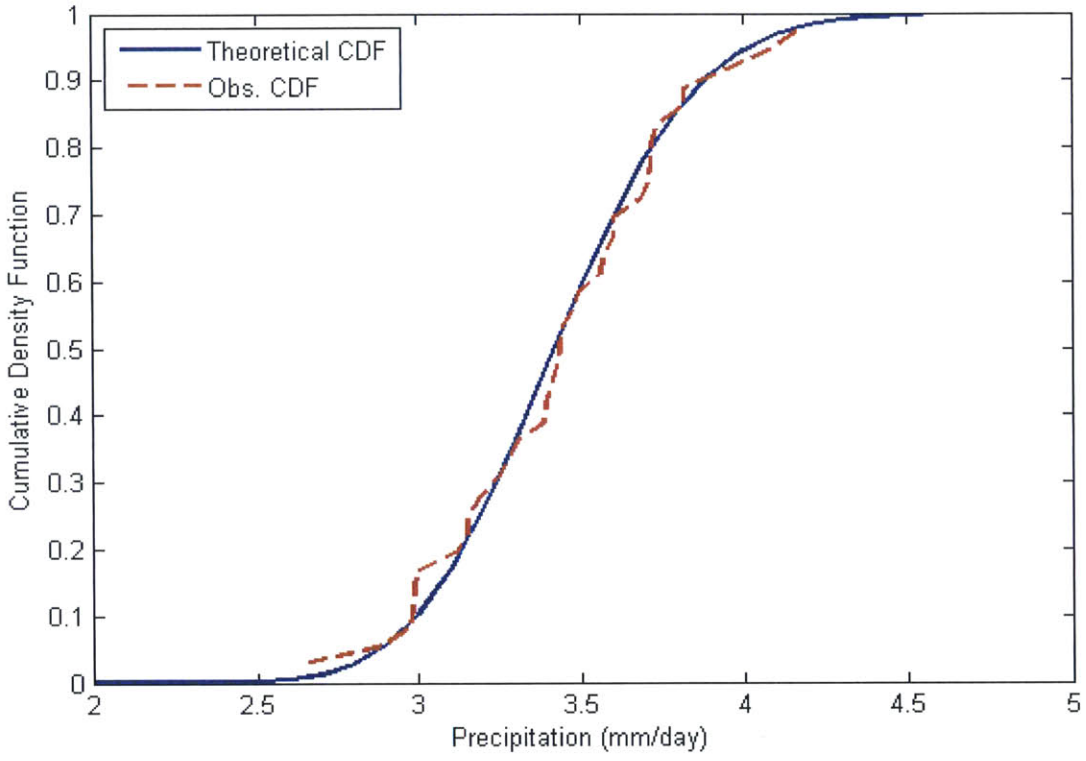


**Figure 7.2:** Observed Cumulative distribution function of the observed rainfall over the Upper Blue Nile basin compared with the fitted (theoretical) gamma distribution.

Finally, the runoff elasticity to rainfall is calculated numerically as following:

1) After fitting the original rainfall time series to a gamma distribution, which has a long-term mean $\bar{P}_1$ and the corresponding long-term mean runoff $\bar{R}_1$ is estimated using equation 7.5, the time series of the rainfall is multiplied by a small increment (e.g. 1.1) and the new long-term mean of the rainfall is $\bar{P}_2$
2) A new PDF ($f_p$) is fitted for the new rainfall time series and the corresponding runoff is estimated using the new PDF and using equation 7.5 to get the new corresponding long-term runoff $\bar{R}_2$.
3) The runoff elasticity to rainfall is estimated numerically using the following equation:

$$\varepsilon\,(\mathrm{R}) = \frac{\bar{R}_2 - \bar{R}_1}{\bar{P}_2 - \bar{P}_1}\; x\; \frac{\bar{P}_1}{\bar{R}_1} \qquad (7.6)$$

4) In addition, the elasticity of the evapotransiration to rainfall can be estimated using the soil water balance equation (R=P-ET-$\Delta S$), where the change in storage ($\Delta S$) can be neglected on annual time scale and using equation 7.6 as follows:

$$\varepsilon\,(\mathrm{ET}) = 1 - \left(\frac{\bar{R}_2 - \bar{R}_1}{\bar{P}_2 - \bar{P}_1}\; x\; \frac{\bar{P}_1}{\overline{ET_1}}\right) \quad (7.7)$$

Figure 7.3a shows the sensitivities of the runoff elasticity to rainfall. In order to produce this figure, we follow the work of Nieman and Eltahir, 2005, in which we use the same relation estimated in Figure 7.3a between the rainfall and runoff. Then, we change the long-term averages of the rainfall from 2.5 to 4 mm/day as shown in Figure 7.3 and follow the above steps to calculate the sensitivities numerically.

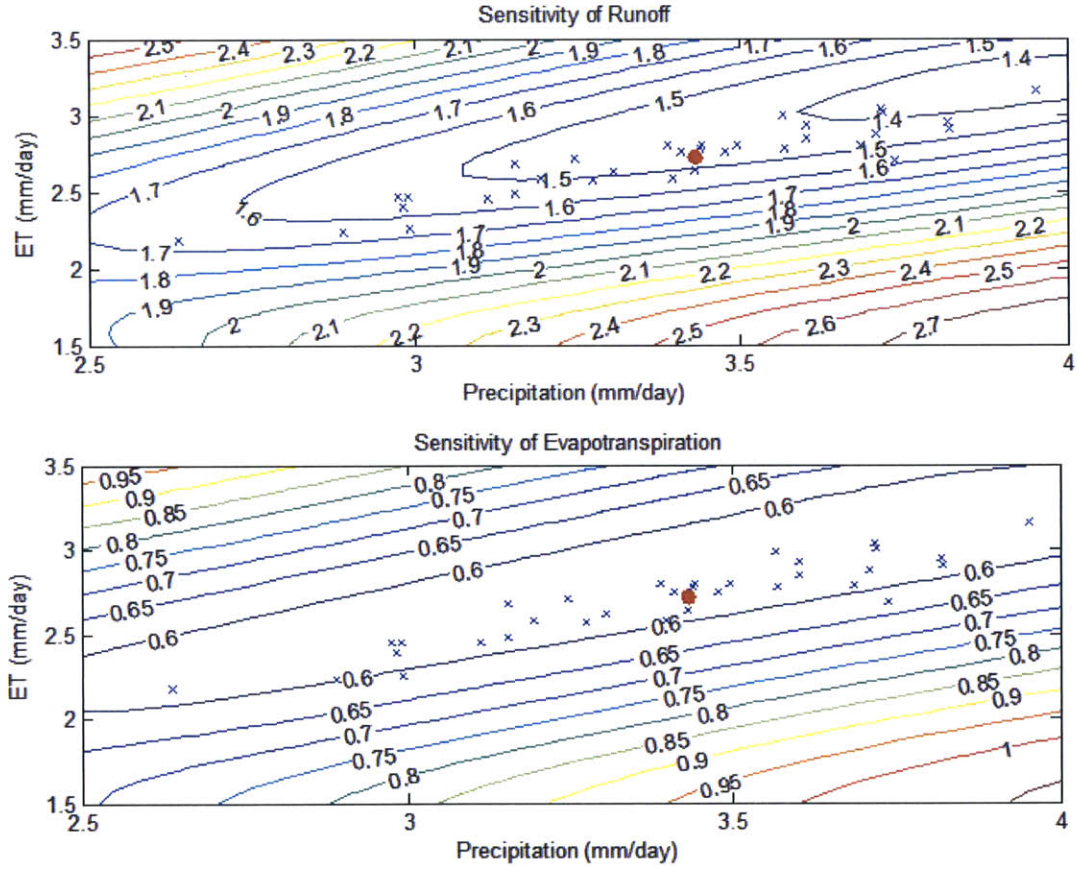


**Figure 7.3:** Sensitivities of the runoff and evaporation elasticity (contour lines) to changes in the rainfall. The blue crosses are for the different annual averages from (1965-2010) and the red dot is the climatology of the same period.

## 7. 2 Runoff Elasticity of MIT-Regional Climate model (MRCM) and GCMs

In the previous section it is shown that the runoff elasticity to rainfall for the Upper Blue Nile basin based on observations of stream flow and rainfall stations is approximately 1.5% (i.e. 1% change in the rainfall will induce 1.5% change in the runoff). In this section, we will investigate if the future changes in the runoff simulated by the four simulations, discussed in chapter 6, by MIT-Regional climate Model (MRCM) and the 18 GCMs, used in chapter 4, have the same elasticity to changes in rainfall.

**Table 7.1:** Summary of the annual averages of the rainfall and runoff over the Upper Blue Nile basin for the past period (1900-2000) and the future period (2000-2100) and the estimated runoff elasticity for the different GCMs.

| GCM | Average annual rainfall (mm/day) for (1900-2000) | Average annual rainfall (mm/day) for (2000-2100) | Average annual runoff (mm/day) for (1900-2000) | Average annual runoff (mm/day) for (2000-2100) | Runoff Elasticity |
|---|---|---|---|---|---|
| **BCC-CSM1-1M** | 2.54 | 2.9 | 0.75 | 0.94 | 1.8 |
| **BCC-CSM1-1** | 2.93 | 3.12 | 1.07 | 1.18 | 1.6 |
| **CCSM4** | 2.66 | 2.92 | 0.42 | 0.5 | 1.9 |
| **CMCC-CMS** | 2.86 | 2.87 | 0.56 | 0.52 | -20.4 |
| **CMCC-CM** | 2.47 | 2.54 | 0.53 | 0.52 | -0.7 |
| **GFDL-CM3** | 3.4 | 3.85 | 0.675 | 0.79 | 1.3 |
| **GFDL-ESM2G** | 3.55 | 3.51 | 1.14 | 1.04 | 7.8 |
| **GFDL-ESM2M** | 3.35 | 3.57 | 0.96 | 1.03 | 1.1 |
| **MPI-ESM-MR** | 3.22 | 3.34 | 0.55 | 0.61 | 2.9 |
| **MRI-CGCM3** | 2.62 | 2.84 | 0.38 | 0.48 | 3.1 |
| **NOR-ESM1-M** | 5.44 | 5.72 | 1.78 | 2.1 | 3.5 |
| **NOR-ESM1-ME** | 3.53 | 3.77 | 0.66 | 0.82 | 3.6 |
| **CESM1-BGC** | 2.33 | 2.6 | 0.22 | 0.26 | 1.6 |
| **CMCC-CESM** | 2.46 | 2.52 | 0.54 | 0.43 | -8.6 |
| **CESM1-CAM5** | 3.14 | 3.32 | 0.59 | 0.66 | 2.1 |
| **CNRM-CM5** | 4.64 | 4.72 | 1.98 | 2.02 | 1.2 |
| **ACCESS1** | 3.86 | 3.91 | 0.71 | 0.76 | 5.4 |
| **FGOALS** | 3.07 | 3.78 | 1.12 | 1.62 | 1.9 |

The runoff elasticity of the 18 GCMs, used in chapter 4, for the Upper Blue Nile basin are shown in Table 7.1. The runoff elasticity is estimated for the GCMs using the following equation:

$$\varepsilon\,(R) = \frac{\bar{R}_{(2000-2100)} - \bar{R}_{(1900-2000)}}{\bar{P}_{(2000-2100)} - \bar{P}_{(1900-2000)}} \; x \; \frac{\bar{P}_{(1900-2000)}}{\bar{R}_{(1900-2000)}} \qquad (7.7)$$

Most of the GCMs show reasonable values for the runoff elasticity to rainfall compared to the observed value (~ 1.5). For example, 8 out of the 18 GCMs show values within 50% of the observed runoff elasticity to rainfall. However, three out of the 18 GCMs show a negative runoff elasticity to rainfall (i.e. CMCC-CMS, CMCC-CM and CMCC-CESM). These GCMs have very low increase for the future rainfall of 0.01, 0.07 and 0.06 mm/day for the CMCC-CMS, CMCC-CM and CMCC-CESM respectively, while the evaporation increased in the future by 0.05, 0.08 and 0.17 mm/day for the CMCC-CMS, CMCC-CM and CMCC-CESM respectively, hence, the final runoff has decreased. Thus, the runoff elasticity to rainfall for these GCMs are negative. It is also important to note that the two GCMs (BCC-CSM1-1M and CCSM4), which are used to modify the lateral boundary conditions and SSTs for the MRCM simulations in chapter 6, have runoff elasticity to rainfall of 1.8 and 1.9 that are very close to the observed value of 1.5. Furthermore, the percent average change of the rainfall over the Upper Blue Nile basin from the 18 GCMs is ~6%, while the percent average change of the runoff is ~12%. Thus, the average runoff elasticity to rainfall for the 18 GCMs is around 2, which is also close to the observed value of 1.5.

Finally, the runoff elasticity to rainfall based on the regional climate model (MRCM) simulations is also investigated. The models show an average runoff elasticity to rainfall around 2, which is also close to the observed value of (~1.5) as shown in Table 7.2.

**Table 7.2:** Summary of average rainfall and runoff over the Upper Blue Nile basin using the different simulations discussed in chapter 6 and the estimated runoff elasticity to rainfall for each simulation.

| Simulation | Percent change in the future rainfall | Percent change in the future runoff | Runoff Elasticity |
|---|---|---|---|
| **BC Simulation** | 3.4 | 6.5 | 1.9 |
| **GHG Simulation** | 11.8 | 25 | 2.1 |
| **BC+GHG Simulation** | 8 | 17 | 2.1 |

## 7. 3 Conclusions

This chapter investigates the runoff elasticity to rainfall for the Upper Blue Nile basin. First, the runoff elasticity to rainfall is investigated using observation of stream flow and rainfall gauges data. It is estimated that the runoff elasticity to rainfall is approximately 1.5 (i.e. 1% change in the rainfall will induce 1.5% change in the runoff). Then, the runoff elasticity to rainfall is estimated for the 18 GCMs used in chapter 4 to verify if they have similar runoff elasticity to rainfall. Most of these GCMs have runoff elasticity that are close to the observed values. The average runoff elasticity of the 18 GCMs was approximately 2 (i.e. 1% change in the rainfall will induce 2% change in the runoff). Finally, the runoff elasticity to rainfall for the future simulations using MRCM are also verified and the model also has a runoff elasticity of approximately 2.

# Chapter 8: Summary of Results, Major Contributions and Future Work

## 8.1 Summary of Results

The goal of this thesis is to predict the impact of climate change on the flow in the Nile river. This goal was achieved by identifying the future changes in the long-term mean and inter-annnual variability of the flow in the river. In addition, this work investigated the different mechanisms behind these changes in the future as follows.

Chapter 2 investigated the interannual variability in the flow of the Nile river and the teleconnection between ENSO and the Nile flow. It is shown that the flows of the Nile river are low during El Nino event and high during La Nina events. Analyses of observation and reanalysis data showed that warming of Sea Surface Temperature (SST) over the central Pacific ocean induces warming around the equator over the Indian Ocean. This warming forces a gill-type circulation, which enhances the low level westerly air flow that reduces the convergence of air over the Upper Blue Nile basin and hence reduces the rainfall and streamflow.

Chapter 3 evaluated different CMIP3 and CMIP5 GCMs and reanalysis product to identify which GCMs and reanalysis product should be used for climate studies over the Nile basin. In addition, the effect of the spatial resolution on the simulation of the hydrological cycle is investigated. It is shown that the high resolution models are better in simulation the hydrology of the Upper Blue Nile basin.

Chapter 4 identified the future changes of the interannual variability in the flow of the Nile river and the mechanism behind these changes. It is shown that the interannual variability in the flow will increase in the future (i.e. the standard deviation and coefficient of variation

will increase by 50% and 35% respectively for the future period (2000-2100) compared to the past period (1900-2000)) and this increase was explained because of the increase of the frequency of El Nino and La Nina events in the future and the observed teleconnection between Nile flow and ENSO. Furthermore, implication of the increased interannual variability in the flow on the current water storage capacity in the basin is examined and it is shown that in the future more dams will be needed in the basin to overcome the increase in the variability of the flow.

Chapter 5 presented the development of new parametrizations for large scale rainfall and cloud cover to use within the MIT-regional climate model (MRCM). The new parametrizations improved the simulation of the clouds by reducing the cloud coverage, which improves the simulated outgoing longwave radiation and planetary albedo that become closer to observations. These improvements in the cloud coverage simulation are reflected in the simulation of the energy budget at the surface as the downward shortwave radiation reaching the surface increases because of the reduction of cloud coverage and increasing the net radiation at the surface, which become closer to observations. These improvements makes the model more credible to use for investigating the impacts of climate change on the Nile basin.

Chapter 6 investigated the future changes in the long-term averages of the flow of the Nile basin and the mechanisms behind these changes. First, GCMs are analyzed to discern the common changes between them for the future rainfall, SST, humidity and wind circulation. It is shown that they agree on the increase of future SST, humidity and rainfall. However, there is not a consensus between them on the change in wind circulation. Thus, the modified regional climate model, presented in chapter 5, is forced with modified lateral boundary conditions and greenhouse gases to mimic the future conditions. It is also shown that the modified lateral boundary conditions increases the large scale rainfall by increasing the humidity. Furthermore, the modification of the lateral boundary conditions reduces the convective rainfall, as the air temperature are warmer aloft compared to the surface, which tend to stabilize the atmosphere and reduce the convection. On the other hand, the greenhouse gases increases the convective rainfall by altering the vertical profile of air

temperature, which increase the convective available potential energy (CAPE), hence the vertical upward velocity and rainfall.

## 8.2 Major Contributions

The objective of this thesis is to better understand the impact of climate change on the future Nile flows. In order to achieve this objective, this thesis provides four major contributions:

- First, this study describes a physical explanation of the teleconnection between and ENSO and the Nile. During El Nino event, the SST over the Indian ocean warms following the warming the Pacific ocean. This warming forces a Gill-type circulation, which enhances the low level westerly air flow that reduces the convergence of air over the Upper Blue Nile basin and hence reduces the rainfall and streamflow. This mechanism is important in predicting the future flow in the Nile river, not only for the long-range predictions as in this study, but also for the medium-range forecast (i.e. few months).

- Second, identifying and explaining the future changes in the long-term mean and interannual variability in the flow of the Nile river. It is shown that the long-term mean and the standard deviation of the Nile flow will increase by 15% and 50% respectively for the future period (2000-2100) compared to the past period (1900-2000). The changes in the standard deviation of the Nile flow are mainly related to the increased frequency of El Nino and La Nina events in the future, which will increase the variability in the Nile flow through the teleconnection between the Nile and ENSO. Furthermore, the increase of the long-term mean of the flow is attributed primarily to the regional increase of the greenhouse gas concentrations which destabilizes the atmosphere, warming the lower and middle atmospheric layers and hence increases convection and convective rainfall.

- Third, this study provides guidelines for planning of the water resources of the Nile basin by identifying a future need for more water storage and hence dams to manage the projected increase of the interannual variability in the flow of Nile river. It is shown that the existing dams (~150 km3 of water storage capacity) in the basin are able to ensure water supply equivalent the past mean flow (i.e. mean of 1900-2000, 80km3/year) for 40 years. However, in order to ensure water supply equivalent to the future flow (i.e. mean of 2000-2100, 92 km3/year) for the same 40 years duration, an additional 100 km3 storage capacity should be added in the basin.

- Finally, this study contributed to the development of a regional climate model that can be used in future studies to understand the different processes that shape the hydrology and climate of the Nile basin as discussed in the next section. The performance of the newly developed version of the model is tested using several different observations including radiation data from satellites for the top of atmosphere and surface, stream flow data, rainfall observations from satellites and rain gauges. The new version of the model is not only able to accurately simulate the hydrological cycle over the basin but also the radiation at the top of the atmosphere and the surface, surface temperature, and cloud coverage.

## 8.3 Future work

This thesis shows opportunities for three major areas of research that may benefit from the presented work:

- First, the work done to predict the impact of climate change on the Nile flow can be used as a framework for other regions in the world that have a teleconnection with ENSO. This framework will provide predictions and explanations of the future

changes in the interannual variability and long-term mean of the rainfall over these regions.

- Second, this work highlights the importance of understanding the mechanisms of the future changes of rainfall. For example, it is shown the increases of humidity and temperature have different impacts on the rainfall compared to the greenhouse gases, which mainly affect the convective rainfall. It worth exploring these mechanisms over other regions, which increases our understanding of the future changes in the rainfall.

- Third, the presence of a calibrated regional climate model over the Nile basin provides a lot of opportunities to study the climate and hydrology of the Nile. For example, the impact of changing the land cover due to irrigation or urban expansions in the basin and how this might impact the hydrology of the basin. The model may be also used to study the water recycling in the basin, and how water recycling can change in the future or due changes in swampy area in the basin and how these changes might affect the Nile flow.

- Finally, this study showed that the need to increase the water storage capacity in the basin to overcome the projected increase in interannual variability in the basin. Thus, detailed studies will be required to investigate the best locations of the new dams and operation rules of the new dams with the existing dams in the basin to maximize the benefit for all the countries in the basin.

## Bibliography


Abdo, K.S., Fiseha, B.M., Rientjes, T.H.M., Gieske, A.S.M. and Haile, A.T., 2009. Assessment of climate change impacts on the hydrology of Gilgel Abay catchment in Lake Tana basin, Ethiopia. *Hydrological Processes,23*(26), pp.3661-3669.

Abtew, W., Melesse, A.M. and Dessalegne, T., 2009. El Niño southern oscillation link to the Blue Nile River Basin hydrology. *Hydrological Processes, 23*(26), pp.3653-3660.

Ahmed, K.F., Wang, G., Silander, J., Wilson, A.M., Allen, J.M., Horton, R. and Anyah, R., 2013. Statistical downscaling and bias correction of climate model outputs for climate change impact assessment in the US northeast. *Global and Planetary Change, 100*, pp.320-332.

Amarasekera, K.N., Lee, R.F., Williams, E.R. and Eltahir, E.A., 1997. ENSO and the natural variability in the flow of tropical rivers. *Journal of Hydrology,200*(1), pp.24-39.

Bartlein, P., 2000. Absolute minimum temperature minus average of the coldest monthly mean temperature Worldwide Airfield Summaries [Available online at: http://www.sage.wisc.edu/download/IBIS].

Beltrando, G. and Camberlin, P., 1993. Interannual variability of rainfall in the Eastern Horn of Africa and indicators of atmospheric circulation. *International Journal of Climatology, 13*(5), pp.533-546.

Berrisford, P., Kållberg, P., Kobayashi, S., Dee, D., Uppala, S., Simmons, A.J., Poli, P. and Sato, H., 2011. Atmospheric conservation properties in ERA-Interim. *Quarterly Journal of the Royal Meteorological Society,137*(659), pp.1381-1399.

Beyene, T., Lettenmaier, D.P. and Kabat, P., 2010. Hydrologic impacts of climate change on the Nile River Basin: implications of the 2007 IPCC scenarios. *Climatic change, 100*(3-4), pp.433-461.

Black, E., Slingo, J. and Sperber, K.R., 2003. An observational study of the relationship between excessively strong short rains in coastal East Africa and Indian Ocean SST. *Monthly Weather Review, 131*(1), pp.74-94.

Boé, J., Terray, L., Martin, E. and Habets, F., 2009. Projected changes in components of the hydrological cycle in French river basins during the 21st century. *Water Resources Research, 45*(8).

Bony, S., Colman, R., Kattsov, V.M., Allan, R.P., Bretherton, C.S., Dufresne, J.L., Hall, A., Hallegatte, S., Holland, M.M., Ingram, W. and Randall, D.A., 2006. How well do we understand and evaluate climate change feedback processes?. Journal of Climate, 19(15), pp.3445-3482.

Booij, M.J., Tollenaar, D., van Beek, E. and Kwadijk, J.C., 2011. Simulating impacts of climate change on river discharges in the Nile basin. *Physics and Chemistry of the Earth, Parts A/B/C, 36*(13), pp.696-709.

Cai, W., Borlace, S., Lengaigne, M., Van Rensch, P., Collins, M., Vecchi, G., Timmermann, A., Santoso, A., McPhaden, M.J., Wu, L. and England, M.H., 2014. Increasing frequency of extreme El Niño events due to greenhouse warming. *Nature Climate Change, 4*(2), pp.111-116.

Cai, W., Wang, G., Santoso, A., McPhaden, M.J., Wu, L., Jin, F.F., Timmermann, A., Collins, M., Vecchi, G., Lengaigne, M. and England, M.H., 2015. Increased frequency of extreme La Niña events under greenhouse warming. *Nature Climate Change, 5*(2), pp.132-137.

Calanca, P. and Ohmura, A., 1994. Atmospheric moisture flux convergence and accumulation on the Greenland Ice Sheet. *IAHS Publications-Series of Proceedings and Reports-Intern Assoc Hydrological Sciences, 223*, pp.77-84.

Camberlin, P., 1995. June-september rainfall in north-eastern Africa and atmospheric signals over the tropics: A zonal perspective. *International Journal of Climatology, 15*(7), pp.773-783.

Camberlin, P., 1997. Rainfall anomalies in the source region of the Nile and their connection with the Indian summer monsoon. *Journal of Climate, 10*(6), pp.1380-1392.

Christensen, J.H., B. Hewitson, A. Busuioc, A. Chen, X. Gao, I. Held, R. Jones, R.K. Kolli, W.-T. Kwon, R. Laprise, V. Magaña Rueda, L. Mearns, C.G. Menéndez, J. Räisänen, A. Rinke, A. Sarr and P. Whetton, 2007: Regional Climate Projections. In: Climate Change 2007: The Physical Science Basis. Contribution of Working Group I to the Fourth Assessment Report of the Intergovernmental Panel on Climate Change [Solomon, S., D. Qin, M. Manning, Z. Chen, M. Marquis, K.B. Averyt, M. Tignor and H.L. Miller (eds.)]. Cambridge University Press, Cambridge, United Kingdom and New York, NY, USA.

Christensen, J.H., K. Krishna Kumar, E. Aldrian, S.-I. An, I.F.A. Cavalcanti, M. de Castro, W. Dong, P. Goswami, A. Hall, J.K. Kanyanga, A. Kitoh, J. Kossin, N.-C. Lau, J. Renwick, D.B. Stephenson, S.-P. Xie and T. Zhou, 2013: Climate Phenomena and their Relevance for Future Regional Climate Change. In: Climate Change 2013: The Physical Science Basis. Contribution of Working Group I to the Fifth Assessment Report of the Intergovernmental Panel on Climate Change [Stocker, T.F., D. Qin, G.-K. Plattner, M. Tignor, S.K. Allen, J. Boschung, A. Nauels, Y. Xia, V. Bex and P.M. Midgley (eds.)]. Cambridge University Press, Cambridge, United Kingdom and New York, NY, USA, pp. 1217–1308, doi: 10.1017/CBO9781107415324.028.

Cole, J.E., Dunbar, R.B., McClanahan, T.R. and Muthiga, N.A., 2000. Tropical Pacific forcing of decadal SST variability in the western Indian Ocean over the past two centuries. *Science, 287*(5453), pp.617-619.

Collins, M., An, S.I., Cai, W., Ganachaud, A., Guilyardi, E., Jin, F.F., Jochum, M., Lengaigne, M., Power, S., Timmermann, A. and Vecchi, G., 2010. The impact of global warming on the tropical Pacific Ocean and El Niño. Nature Geoscience, 3(6), pp.391-397.

Conway, D. and Hulme, M., 1992. Recent fluctuations in rainfall and runoff over the Nile Basin and implications for assessing future climate change. *Climatic Research Unit, School of Environmental Sciences, University of East Anglia, Norwich, UK.*

Conway, D., 1996. The impacts of climate variability and future climate change in the Nile Basin on water resources in Egypt. *International Journal of Water Resources Development, 12*(3), pp.277-296.

Dee, D.P., Uppala, S.M., Simmons, A.J., Berrisford, P., Poli, P., Kobayashi, S., Andrae, U., Balmaseda, M.A., Balsamo, G., Bauer, P. and Bechtold, P., 2011. The ERA-Interim reanalysis: Configuration and performance of the data assimilation system. *Quarterly Journal of the Royal Meteorological Society, 137*(656), pp.553-597.

Demory, M.E., Vidale, P.L., Roberts, M.J., Berrisford, P., Strachan, J., Schiemann, R. and Mizielinski, M.S., 2014. The role of horizontal resolution in simulating drivers of the global hydrological cycle. Climate Dynamics,42(7-8), pp.2201-2225.

Eldaw, A.K., Salas, J.D. and Garcia, L.A., 2003. Long-range forecasting of the Nile River flows using climatic forcing. *Journal of Applied Meteorology,42*(7), pp.890-904.

Elsanabary, M.H., Gan, T.Y. and Mwale, D., 2014. Application of wavelet empirical orthogonal function analysis to investigate the nonstationary character of Ethiopian rainfall and its teleconnection to nonstationary global sea surface temperature variations for 1900–1998. *International Journal of Climatology, 34*(6), pp.1798-1813.

Elshamy, M.E., Seierstad, I.A. and Sorteberg, A., 2009. Impacts of climate change on Blue Nile flows using bias-corrected GCM scenarios. *Hydrology and Earth System Sciences, 13*(5), pp.551-565.

Eltahir, E.A., 1996. El Niño and the natural variability in the flow of the Nile River. *Water Resources Research, 32*(1), pp.131-137.

Eltahir, E.A.B. and Bras, R.L., 1993. Estimation of the fractional coverage of rainfall in climate models. *Journal of Climate*, *6*(4), pp.639-644.

FAO (Food and Agriculture Organization of the United Nations), New Dimensions in Water Security: Water, Society and Ecosystem Services in the 21st century. Rome; Food and Agriculture Organization of the United Nations (2000).

Fieux, M., Andrié, C., Delecluse, P., Ilahude, A.G., Kartavtseff, A., Mantisi, F., Molcard, R. and Swallow, J.C., 1994. Measurements within the Pacific-Indian oceans throughflow region. Deep Sea Research Part I: Oceanographic Research Papers, 41(7), pp.1091-1130.

Forster, P., V. Ramaswamy, P. Artaxo, T. Berntsen, R. Betts, D.W. Fahey, J. Haywood, J. Lean, D.C. Lowe, G. Myhre, J. Nganga, R. Prinn, G. Raga, M. Schulz and R. Van Dorland, 2007: Changes in Atmospheric Constituents and in Radiative Forcing. In: Climate Change 2007: The Physical Science Basis. Contribution of Working Group I to the Fourth Assessment Report of the Intergovernmental Panel on Climate Change [Solomon, S., D. Qin, M. Manning, Z. Chen, M. Marquis, K.B. Averyt, M.Tignor and H.L. Miller (eds.)]. Cambridge University Press, Cambridge, United Kingdom and New York, NY, USA.

G Baecher, G.B., Anderson, R., Britton, B., Brooks, K. and Gaudet, J., 2000. The Nile Basin: environmental transboundary opportunities and constraints analysis. *International Resources Group, for USAID, Washington DC.*

Gebre, S.L. and Ludwig, F., 2015. Hydrological Response to Climate Change of the Upper Blue Nile River Basin: Based on IPCC Fifth Assessment Report (AR5). *Journal of Climatology & Weather Forecasting, 2015.*

Giannini, A., Saravanan, R. and Chang, P., 2003. Oceanic forcing of Sahel rainfall on interannual to interdecadal time scales. *Science*, *302*(5647), pp.1027-1030.

Gianotti, R.L. and Eltahir, E.A., 2014. Regional climate modeling over the Maritime Continent. Part I: New parameterization for convective cloud fraction. *Journal of Climate*, *27*(4), pp.1488-1503.

Gianotti, R.L. and Eltahir, E.A., 2014. Regional climate modeling over the Maritime Continent. Part II: New parameterization for autoconversion of convective rainfall. *Journal of Climate, 27*(4), pp.1504-1523.

Gleckler, P.J., Taylor, K.E. and Doutriaux, C., 2008. Performance metrics for climate models. *Journal of Geophysical Research: Atmospheres, 113*(D6).

Global Soil Data Task, International Geosphere-Biosphere Programme, Data and Information System. 2000. Global soil data products CD-ROM, International Geosphere-Biosphere Programme, Data and Information System (IGDP-DIS), Potsdam, Germany.

Hastenrath, S., Polzin, D. and Mutai, C., 2011. Circulation mechanisms of Kenya rainfall anomalies. *Journal of Climate, 24*(2), pp.404-412.

Holtslag, A.A.M. and Boville, B.A., 1993. Local versus nonlocal boundary-layer diffusion in a global climate model. *Journal of Climate, 6*(10), pp.1825-1842.

Huffman, G.J., Bolvin, D.T., Nelkin, E.J., Wolff, D.B., Adler, R.F., Gu, G., Hong, Y., Bowman, K.P. and Stocker, E.F., 2007. The TRMM multisatellite rainfall analysis (TMPA): Quasi-global, multiyear, combined-sensor rainfall estimates at fine scales. *Journal of Hydrometeorology, 8*(1), pp.38-55.

Hurst, H.E., 1951. {Long-term storage capacity of reservoirs}. *Trans. Amer. Soc. Civil Eng., 116*, pp.770-808.

Hurst, H.E., Black, R.P. and Simaika, Y.M., 1965. Long-term storage. An experimental study, Constable, London (1965).

Intergovernmental Panel on Climate Change, (2001). "Climate change (2001): The scientific basis. Contribution of Working Group I to the Third Assessment Report of the Intergovernmental Panel on Climate Change (IPCC)". University Press for the IPCC, Cambridge.

IPCC (2007). The physical science basis. Contribution of working group I to the fourth assessment report of the intergovernmental panel on climate change. In: Solomon S, Qin D, Manning M, Chen Z, Marquis M, Averyt KB, Tignor M, Miller HL (eds) Climate change 2007. Cambridge University Press, Cambridge, United Kingdom and New York, NY, USA

Jobson JD (1991). Applied multivariate data analysis. Volume I: regression and experimental design. Springer, New York, pp 182–185

Johns, T.C., Durman, C.F., Banks, H.T., Roberts, M.J., McLaren, A.J., Ridley, J.K., Senior, C.A., Williams, K.D., Jones, A., Rickard, G.J. and Cusack, S., 2006. The new Hadley Centre climate model (HadGEM1): evaluation of coupled simulations. *Journal of Climate*, *19*(7), pp.1327-1353.

Johns, T.C., Durman, C.F., Banks, H.T., Roberts, M.J., McLaren, A.J., Ridley, J.K., Senior, C.A., Williams, K.D., Jones, A., Rickard, G.J. and Cusack, S., 2006. The new Hadley Centre climate model (HadGEM1): evaluation of coupled simulations. *Journal of Climate*, *19*(7), pp.1327-1353.

Ju, J. and Slingo, J., 1995. The Asian summer monsoon and ENSO.*Quarterly Journal of the Royal Meteorological Society*, *121*(525), pp.1133-1168.

Kalnay, E., Kanamitsu, M., Kistler, R., Collins, W., Deaven, D., Gandin, L., Iredell, M., Saha, S., White, G., Woollen, J. and Zhu, Y., 1996. The NCEP/NCAR 40-year reanalysis project. *Bulletin of the American meteorological Society*, *77*(3), pp.437-471.

Karam, H.N. and Bras, R.L., 2008. Climatological basin-scale Amazonian evapotranspiration estimated through a water budget analysis. *Journal of Hydrometeorology*, *9*(5), pp.1048-1060.

Karam, H.N. and Bras, R.L., 2008. Estimates of net atmospheric moisture flux convergence over the Amazon Basin: a comparison of reanalysis products. *Journal of Hydrometeorology*, *9*(5), pp.1035-1047.

Kawamura, R., 1998. A possible mechanism of the Asian summer monsoon-ENSO coupling. *Journal of the Meteorological Society of Japan, 76*(6), pp.1009-1027.

Kim, S.T., Cai, W., Jin, F.F., Santoso, A., Wu, L., Guilyardi, E. and An, S.I., 2014. Response of El Niño sea surface temperature variability to greenhouse warming. *Nature Climate Change, 4*(9), pp.786-790.

Kim, U., Kaluarachchi, J.J. and Smakhtin, V.U., 2008. *Climate change impacts on hydrology and water resources of the Upper Blue Nile River Basin, Ethiopia* (Vol. 126). Iwmi.

Knyazikhin, Y., Martonchik, J.V., Myneni, R.B., Diner, D.J. and Running, S.W., 1998. Synergistic algorithm for estimating vegetation canopy leaf area index and fraction of absorbed photosynthetically active radiation from MODIS and MISR data. *Journal of Geophysical Research, 103*(D24), pp.32257-32275.

Kubar, T.L., Hartmann, D.L. and Wood, R., 2009. Understanding the importance of microphysics and macrophysics for warm rain in marine low clouds. Part I: Satellite observations. *Journal of the Atmospheric Sciences,66*(10), pp.2953-2972.

Lenters, J.D., Coe, M.T. and Foley, J.A., 2000. Surface water balance of the continental United States, 1963–1995: Regional evaluation of a terrestrial biosphere model and the NCEP/NCAR reanalysis. *Journal of Geophysical Research: Atmospheres, 105*(D17), pp.22393-22425.

Maurer, E.P., O'Donnell, G.M., Lettenmaier, D.P. and Roads, J.O., 2001. Evaluation of the land surface water budget in NCEP/NCAR and NCEP/DOE reanalyses using an off-line hydrologic model. *Journal of Geophysical Research: Atmospheres, 106*(D16), pp.17841-17862.

Meehl, G.A., Covey, C., Taylor, K.E., Delworth, T., Stouffer, R.J., Latif, M., McAvaney, B. and Mitchell, J.F., 2007. The WCRP CMIP3 multimodel dataset: A new era in climate change research. *Bulletin of the American Meteorological Society, 88*(9), pp.1383-1394.

Melesse, A.M., Abtew, W., Setegn, S.G. and Dessalegne, T., 2011. Hydrological variability and climate of the Upper Blue Nile River basin. In *Nile River Basin* (pp. 3-37). Springer Netherlands.

Mitchell, T.D. and Jones, P.D., 2005. An improved method of constructing a database of monthly climate observations and associated high-resolution grids. *International journal of climatology*, *25*(6), pp.693-712.

Mutai, C.C. and Ward, M.N., 2000. East African rainfall and the tropical circulation/convection on intraseasonal to interannual timescales. *Journal of Climate*, *13*(22), pp.3915-3939.

Myneni, R.B., Hoffman, S., Knyazikhin, Y., Privette, J.L., Glassy, J., Tian, Y., Wang, Y., Song, X., Zhang, Y., Smith, G.R. and Lotsch, A., 2002. Global products of vegetation leaf area and fraction absorbed PAR from year one of MODIS data. *Remote sensing of environment*, *83*(1), pp.214-231.

New, M., Hulme, M. and Jones, P., 1999. Representing twentieth-century space-time climate variability. Part I: Development of a 1961-90 mean monthly terrestrial climatology. *Journal of Climate*, *12*(3), pp.829-856.

Nicholson, S.E., 1997. An analysis of the ENSO signal in the tropical Atlantic and western Indian Oceans. *International Journal of Climatology*,*17*(4), pp.345-375.

Niemann, J.D. and Eltahir, E.A., 2004. Prediction of regional water balance components based on climate, soil, and vegetation parameters, with application to the Illinois River Basin. Water resources research, 40(3).

Niemann, J.D. and Eltahir, E.A., 2005. Sensitivity of regional hydrology to climate changes, with application to the Illinois River basin. Water Resources Research, 41(7).

Nohara, D., Kitoh, A., Hosaka, M. and Oki, T., 2006. Impact of climate change on river discharge projected by multimodel ensemble. *Journal of Hydrometeorology*, *7*(5), pp.1076-1089.

Oki, T., Musiake, K., Matsuyama, H. and Masuda, K., 1995. Global atmospheric water balance and runoff from large river basins. *Hydrological Processes*, *9*(5-6), pp.655-678.

Pal, J.S., Eltahir, E.A. and Small, E.E., 2000. Simulation of regional-scale water and energy budgets- Representation of subgrid cloud and rainfall processes within RegCM. *Journal of Geophysical Research*, *105*(D24), pp.29579-29594.

Pal, J.S., Giorgi, F., Bi, X., Elguindi, N., Solmon, F., Rauscher, S.A., Gao, X., Francisco, R., Zakey, A., Winter, J. and Ashfaq, M., 2007. Regional climate modeling for the developing world: the ICTP RegCM3 and RegCNET.*Bulletin of the American Meteorological Society*, *88*(9), pp.1395-1409.

Peixoto, J.P. and Oort, A.H., 1992. Physics of Climate, American Institute of Physics. *New York*, p.520.

Perkins, S.E., Pitman, A.J., Holbrook, N.J. and McAneney, J., 2007. Evaluation of the AR4 climate models' simulated daily maximum temperature, minimum temperature, and rainfall over Australia using probability density functions. *Journal of climate*, *20*(17), pp.4356-4376.

Pohl, B. and Camberlin, P., 2006. Influence of the Madden–Julian oscillation on East African rainfall. I: Intraseasonal variability and regional dependency.*Quarterly Journal of the Royal Meteorological Society*, *132*(621), pp.2521-2539.

Räisänen, J., 2007. How reliable are climate models?. *Tellus A*, *59*(1), pp.2-29.

Ramankutty, N. and Foley, J.A., 1999. Estimating historical changes in global land cover: Croplands from 1700 to 1992. *Global biogeochemical cycles*, *13*(4), pp.997-1027.

Randall, D.A., Wood, R.A., Bony, S., Colman, R., Fichefet, T., Fyfe, J., Kattsov, V., Pitman, A., Shukla, J., Srinivasan, J. and Stouffer, R.J., 2007. Climate models and their evaluation. In *Climate Change 2007: The physical science basis. Contribution of Working Group I to the Fourth Assessment Report of the IPCC (FAR)* (pp. 589-662). Cambridge University Press.

Rangno, A.L. and Hobbs, P.V., 2005. Microstructures and rainfall development in cumulus and small cumulonimbus clouds over the warm pool of the tropical Pacific Ocean. *Quarterly Journal of the Royal Meteorological Society, 131*(606), pp.639-673.

Rangno, A.L. and Hobbs, P.V., 2005. Microstructures and rainfall development in cumulus and small cumulonimbus clouds over the warm pool of the tropical Pacific Ocean. *Quarterly Journal of the Royal Meteorological Society, 131*(606), pp.639-673.

Rasmusson, E.M., 1967. Atmospheric water vapor transport and the water balance of North America: Part I. Characteristics of the water vapor flux field. *Monthly Weather Review, 95*(7), pp.403-426.

Rasmusson, E.M., 1968. Atmospheric water vapor transport and the water balance of North America: II. Large-scale water balance investigations.*Monthly Weather Review, 96*(10), pp.720-734.

Rasmusson, E.M., 1971. A study of the hydrology of eastern North America using atmospheric vapor flux data. *Monthly Weather Review, 99*(2), pp.119-135.

Rayner, N.A., Parker, D.E., Horton, E.B., Folland, C.K., Alexander, L.V., Rowell, D.P., Kent, E.C. and Kaplan, A., 2003. Global analyses of sea surface temperature, sea ice, and night marine air temperature since the late nineteenth century. *Journal of Geophysical Research: Atmospheres,108*(D14).

Reid, J.S., Hobbs, P.V., Rangno, A.L. and Hegg, D.A., 1999. Relationships between cloud droplet effective radius, liquid water content, and droplet concentration for warm clouds in Brazil embedded in biomass smoke.*Journal of Geophysical Research, 104*(D6), pp.6145-6153.

Ringer, M.A., Martin, G.M., Greeves, C.Z., Hinton, T.J., James, P.M., Pope, V.D., Scaife, A.A., Stratton, R.A., Inness, P.M., Slingo, J.M. and Yang, G.Y., 2006. The physical properties of the atmosphere in the new Hadley Centre Global Environmental Model (HadGEM1). Part II: Aspects of variability and regional climate. *Journal of climate*, *19*(7), pp.1302-1326.

Ringer, M.A., Martin, G.M., Greeves, C.Z., Hinton, T.J., James, P.M., Pope, V.D., Scaife, A.A., Stratton, R.A., Inness, P.M., Slingo, J.M. and Yang, G.Y., 2006. The physical properties of the atmosphere in the new Hadley Centre Global Environmental Model (HadGEM1). Part II: Aspects of variability and regional climate. *Journal of climate*, *19*(7), pp.1302-1326.

Roads, J. and Betts, A., 2000. NCEP-NCAR and ECMWF reanalysis surface water and energy budgets for the Mississippi River basin. *Journal of Hydrometeorology*, *1*(1), pp.88-94.

Romps, D.M., Seeley, J.T., Vollaro, D. and Molinari, J., 2014. Projected increase in lightning strikes in the United States due to global warming.*Science*, *346*(6211), pp.851-854.

Roxy, M. and Tanimoto, Y., 2007. Role of SST over the Indian Ocean in influencing the intraseasonal variability of the Indian summer monsoon. Journal of Meteorological Society of Japan, 85(3).

Ruprecht, E. and Kahl, T., 2003. Investigation of the atmospheric water budget of the BALTEX area using NCEP/NCAR reanalysis data. *Tellus A*,*55*(5), pp.426-437.

Samba, G. and Nganga, D., 2011. Rainfall variability in Congo-Brazzaville: 1932–2007. *International Journal of Climatology*, *32*(6), pp.854-873.

Sankarasubramanian, A. and Vogel, R.M., 2003. Hydroclimatology of the continental United States. *Geophysical Research Letters*, *30*(7).

Sankarasubramanian, A., Vogel, R.M. and Limbrunner, J.F., 2001. Climate elasticity of streamflow in the United States. *Water Resources Research*,*37*(6), pp.1771-1781.

Schaller, N., Mahlstein, I., Cermak, J. and Knutti, R., 2011. Analyzing rainfall projections: A comparison of different approaches to climate model evaluation. *Journal of Geophysical Research: Atmospheres,116*(D10).

Seneviratne, S.I., Viterbo, P., Lüthi, D. and Schär, C., 2004. Inferring changes in terrestrial water storage using ERA-40 reanalysis data: The Mississippi River basin. *Journal of climate, 17*(11), pp.2039-2057.

Shumway, R.H. and Stoffer, D.S., 2010. *Time series analysis and its applications: with R examples*. Springer Science & Business Media.

Shukla, J. and Wallace, J.M., 1983. Numerical simulation of the atmospheric response to equatorial Pacific sea surface temperature anomalies. *Journal of the Atmospheric Sciences, 40*(7), pp.1613-1630.

Siam, M.S. and Eltahir, E.A.B., 2015. Explaining and forecasting interannual variability in the flow of the Nile River. *Hydrology and Earth System Sciences, 19*(3), pp.1181-1192.

Siam, M.S., Demory, M.E. and Eltahir, E.A., 2013. Hydrological cycles over the Congo and Upper Blue Nile Basins: Evaluation of general circulation model simulations and reanalysis products. *Journal of Climate, 26*(22), pp.8881-8894.

Siam, M.S., Wang, G., Demory, M.E. and Eltahir, E.A., 2014. Role of the Indian Ocean sea surface temperature in shaping the natural variability in the flow of Nile River. *Climate dynamics, 43*(3-4), pp.1011-1023.

Soden, B.J. and Held, I.M., 2006. An assessment of climate feedbacks in coupled ocean-atmosphere models. *Journal of Climate, 19*(14), pp.3354-3360.

Soman, M.K. and Slingo, J., 1997. Sensitivity of the asian summer monsoon to aspects of sea-surface-temperature anomalies in the tropical pacific ocean. *Quarterly Journal of the Royal Meteorological Society, 123*(538), pp.309-336.

Stackhouse Jr, P.W., Gupta, S.K., Cox, S.J., Zhang, T., Mikovitz, J.C. and Hinkelman, L.M., 2011. The NASA/GEWEX surface radiation budget release 3.0: 24.5-year dataset. *GEWEX News*, *21*(1), pp.10-12.

Strzepek, K.M., 1996. Economic and social adaptations to climate change impacts on water resources: A case study of Egypt. *International Journal of Water Resources Development*, *12*(2), pp.229-244.

Tang, Q. and Lettenmaier, D.P., 2012. 21st century runoff sensitivities of major global river basins. *Geophysical Research Letters*, *39*(6).

Taye, M.T., Ntegeka, V., Ogiramoi, N.P. and Willems, P., 2011. Assessment of climate change impact on hydrological extremes in two source regions of the Nile River Basin. *Hydrology and Earth System Sciences*, *15*(1), pp.209-222.

Taylor, K.E., Stouffer, R.J. and Meehl, G.A., 2012. An overview of CMIP5 and the experiment design. *Bulletin of the American Meteorological Society*,*93*(4), pp.485-498.

Taylor, K.E., Williamson, D. and Zwiers, F., 2000. *The sea surface temperature and sea-ice concentration boundary conditions for AMIP II simulations.* Program for Climate Model Diagnosis and Intercomparison, Lawrence Livermore National Laboratory, University of California.

Tomczak, M. and Godfrey, J.S., 1995. Regional oceanography: an introduction. Pregamon, London

Trenberth, K.E., 1997. The definition of el nino. *Bulletin of the American Meteorological Society*, *78*(12), pp.2771-2777.

Trenberth, K.E., Smith, L., Qian, T., Dai, A. and Fasullo, J., 2007. Estimates of the global water budget and its annual cycle using observational and model data. *Journal of Hydrometeorology*, *8*(4), pp.758-769.

United Nations, Department of Economic and Social Affairs, Population Division. World Population Prospects: The 2012 Revision, Highlights and Advance Tables. Working Paper No. ESA/P/WP.228 (2013).

United States Geological Survey. 1996, *Global 30-arc second elevation dataset (GTOPO30)*, [Available online at: http://eros.usgs.gov/#/Find_Data/Products_and_Data_Available/gtopo30_info].

Uppala SM et al (2005) The ERA-40 re-analysis. Q J R Meteorol Soc 131:2961–3012

Uppala, S.M., Kållberg, P.W., Simmons, A.J., Andrae, U., Bechtold, V.D., Fiorino, M., Gibson, J.K., Haseler, J., Hernandez, A., Kelly, G.A. and Li, X., 2005. The ERA-40 re-analysis. *Quarterly Journal of the Royal Meteorological Society*, *131*(612), pp.2961-3012.

Vizy, E.K. and Cook, K.H., 2003. Connections between the summer east African and Indian rainfall regimes. *Journal of Geophysical Research: Atmospheres*, *108*(D16).

Vörösmarty, C.J., Fekete, B. and Tucker, B.A., 1998. River discharge database, Version 1.1 (RivDIS v1. 0 supplement). *Institute for the Study of Earth, Oceans, and Space, University of New Hampshire, Durham, NH.*

Wang, D. and Alimohammadi, N., 2012. Responses of annual runoff, evaporation, and storage change to climate variability at the watershed scale. *Water Resources Research*, *48*(5).

Wang, G. and Eltahir, E.A., 1999. Use of ENSO information in medium-and long-range forecasting of the Nile floods. *Journal of Climate*, *12*(6), pp.1726-1737.

Williamson, D.L., Kiehl, J.T. and Hack, J.J., 1995. Climate sensitivity of the NCAR Community Climate Model (CCM2) to horizontal resolution. *Climate Dynamics*, *11*(7), pp.377-397.

Winter, J.M., Pal, J.S. and Eltahir, E.A., 2009. Coupling of Integrated Biosphere Simulator to Regional Climate Model Version 3. *Journal of climate*, *22*(10), pp.2743-275

Yamana, T., thesis, Massachusetts Institute of Technology (2015).

Yang, H. and Yang, D., 2011. Derivation of climate elasticity of runoff to assess the effects of climate change on annual runoff. *Water Resources Research*, *47*(7).

Yang, J., Liu, Q., Xie, S.P., Liu, Z. and Wu, L., 2007. Impact of the Indian Ocean SST basin mode on the Asian summer monsoon. *Geophysical Research Letters*, *34*(2).

Yang, W., Tan, B., Huang, D., Rautiainen, M., Shabanov, N.V., Wang, Y., Privette, J.L., Huemmrich, K.F., Fensholt, R., Sandholt, I. and Weiss, M., 2006. MODIS leaf area index products: From validation to algorithm improvement. *Geoscience and Remote Sensing, IEEE Transactions on*,*44*(7), pp.1885-1898.

Yates, D.N. and Strzepek, K.M., 1998. An assessment of integrated climate change impacts on the agricultural economy of Egypt. *Climatic Change*,*38*(3), pp.261-287.

Yeh, P.J.F., Irizarry, M. and Eltahir, E.A., 1998. Hydroclimatology of Illinois: A comparison of monthly evaporation estimates based on atmospheric water balance and soil water balance. *Journal of geophysical research*, *103*(D16), pp.19823-19837.

Zeng, X., Zhao, M. and Dickinson, R.E., 1998. Intercomparison of bulk aerodynamic algorithms for the computation of sea surface fluxes using TOGA COARE and TAO data. *Journal of Climate*, *11*(10), pp.2628-2644.

Zhang, K., Kimball, J.S., Nemani, R.R. and Running, S.W., 2010. A continuous satellite-derived global record of land surface evapotranspiration from 1983 to 2006. *Water Resources Research*, *46*(9).

# Appendix A: ENSO and Future Changes in the Frequency of El Nino and La Nina Events

El Nino Southern Oscillation (ENSO) refers to an interannual phenomenon that occurs over the tropical Pacific Ocean due to interactions between the ocean and atmosphere. The warm phase of ENSO (i.e. El Nino event) is characterized by an increase of the sea surface temperature (SST) and lower atmospheric pressure over the Eastern Pacific ocean. On the other hand, the cold phase of ENSO (i.e. La Nina event) is characterized by a decrease of the sea surface temperature (SST) and higher atmospheric pressure over the central Eastern Pacific Ocean. In this appendix, future changes in the frequency of El Nino and La Nina events are discussed based on the work of Cai et al., 2014 and Cai et al., 2015. In these two papers, it is shown that the frequency of extreme ENino and La Nina events will increase in the future. This appendix is divided to three main parts. First, a description of the atmospheric and oceanic conditions during neutral events (i.e. absence of El Nino or La Nina events) over the tropical Pacific. Second, a description of the mechanism of the future changes of El Nino events. Third, a description of the mechanism of the future changes of La Nina events.

## Neutral Atmospheric and Oceanic Conditions over the tropical Pacific

During neutral events, the westward trade winds, drived by the strong SSTs gradients across the equator, are strong over the tropical Pacific Ocean, which affect the surface ocean currents below it and tend to increase the sea levels over the Western Pacific relative to the Eastern Pacific. This increases the upwelling of water over the Eastern Pacific and allow the thermocline (i.e. transtion layer between the warm mixed layer at the surface and the deep cold water layer) to be close to the surface over the Eastern Pacific, which cool the surface as shown in Figure A.1. The formation of warm pool over the Western Pacific and reduction of surface pressure enhances the convergence of air and rainfall over this region and induces divergence of air over the Eastern Pacific forming the Walker circulation. This mechansim is also known as Bjerknes feedback, which is a postive feedback beween the easterly trade winds, zonal SSTs gradient and convection activity over the Western Pacific Ocean and any increase in any of this compenents is reflected positively to the other components of this mechanism (Collins et al., 2010; Christensen et al., 2013).

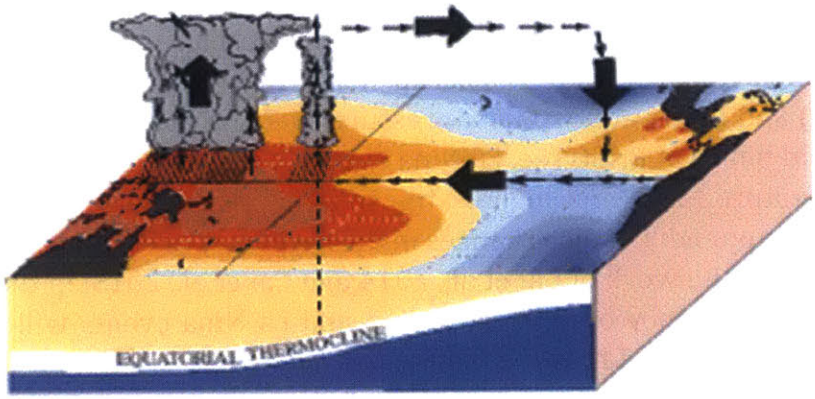


**Figure A.1:** Schematic of Ocean and atmosphere circulations during neutral events. Figure adapted from IPCC-AR5 report, WG1-Chapter14.

### El Nino and future changes in the frequency of El Nino events

During El Nino event, the strong easterly winds weaken and anomouls westerly winds are formed over the eastern Pacific as a result of the weaking of the eas-west and meridional SST gradients (Figures A.2b and A.2d) because of the warming over the eastern Pacific (Figures A.2a and A.2b). These westerly winds bring warm water from the west to the central Pacific, pushes the thermocline down and further increase the SST over the Eastern Pacific. The warm SSTs over the central Pacific modulate the Walker circulation by reducing the surface pressure and enhancing convection and rainfall over this region.

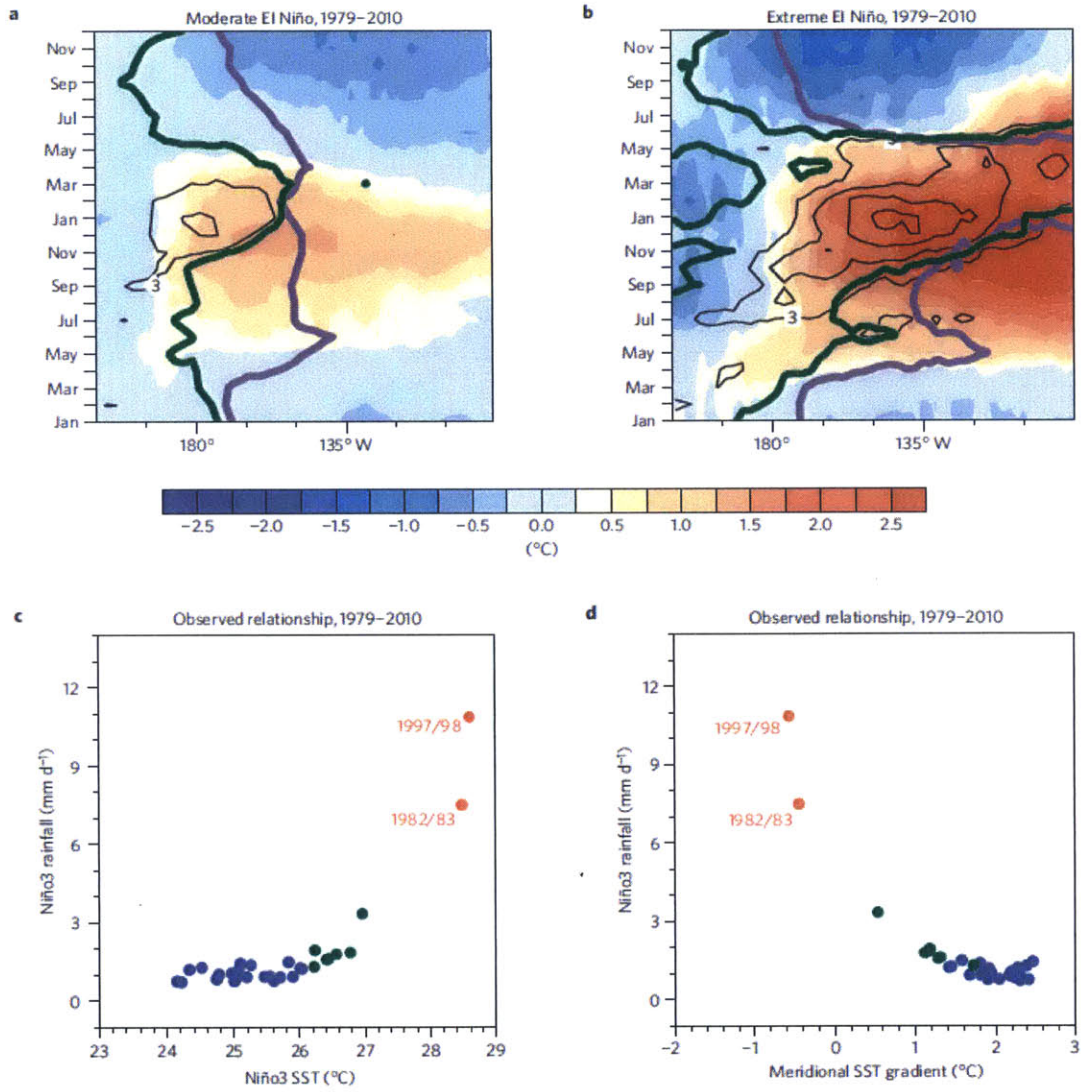


**Figure A.2:** Evolution and nonlinear characteristics of observed extreme El Niño events. (**a**, **b**) Time–longitude diagram for composite moderate and extreme El Niño events, respectively, of equatorial SST anomalies (colour scale) and rainfall anomalies (contour, at intervals of 3mm per day), 28 _C isotherm (purple curve) and total rainfall 5mm per day isopleth (green curve). (**c**, **d**) Relationship of eastern equatorial Pacific (Niño3 area: 5°S–5° N, 150° W–90° W) DJF total rainfall with DJF Niño3 SST and meridional SST gradients in the Niño3 longitude range. The meridional SST gradient is defined as the average SST over the off-equatorial region (5° N–10° N, 150° W–90° W) minus the average over the equatorial region (2.5° S–2.5° N, 150°W–90° W). Extreme El Niño (defined as events for which austral summer rainfall is greater than 5mm per day), moderate El Niño (defined as events with SST anomalies greater than 0.5 standard deviation of that over the period since 1979 that are not extreme El Niño events), and La Niña and neutral events, are indicated by red, green and blue dots respectively. During extreme El Niño, the meridional SST gradient diminishes, or reverses, shifting the ITCZ to the eastern equatorial Pacific. Figure adapted from Cai et al., 2014.

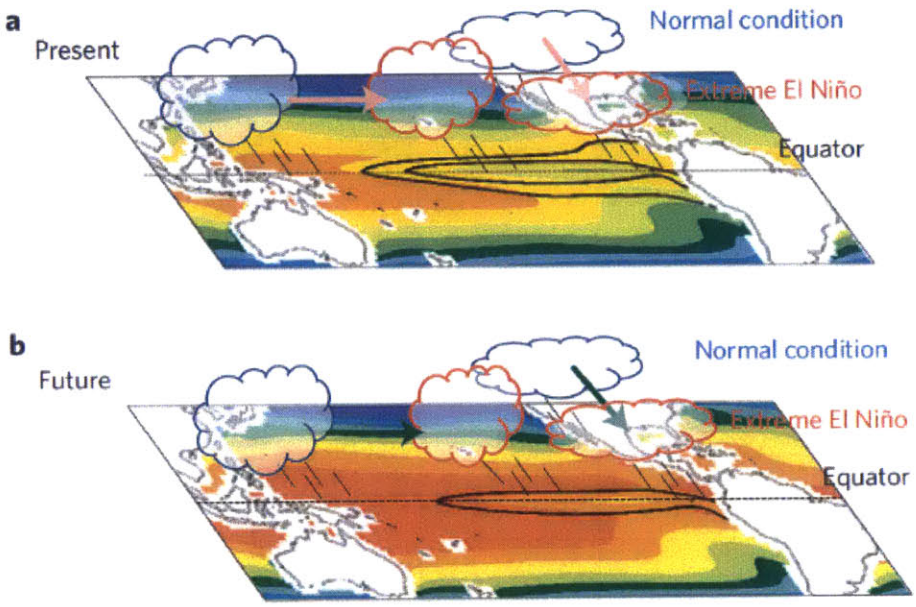


**Figure A.3:** Schematic depicting the mechanism for increased occurrences of extreme El Niño under greenhouse warming (a, b). In both present-day climate (a) and future climate (b), convection zones in the western Pacific and the ITCZ latitudes shift from their normal positions (indicated by blue clouds) to the eastern equatorial Pacific during an extreme El Niño event (indicated by red clouds). Color shading indicates mean SSTs and black contours indicate SST anomalies. Under greenhouse-gas-induced warming conditions, warming occurs everywhere but at a faster rate in the eastern equatorial Pacific, diminishing the zonal and meridional SST gradients. Strong SST gradients are a barrier to a shift in convection zones. Therefore, in the future climate, shifts in convection zones can be facilitated by weaker changes in SST and thus SST gradients (indicated by one black contour and by green arrows), as compared with the present-day climate in which stronger changes are required (indicated by two black contours and red arrows). Figure adapted from Cai et al., 2014.

In the future, warming will occur everywhere, however, the warming of the equatorial eastern Pacific will be faster. These changes in the SST will reduce the zonal and meridional gradients, which facilitate the movement of the Intertropical convergence zone (ITCZ) from off the equator to the equator over the eastern Pacific and forming El Nino conditions as shown in Figure A.3. The increased frequency of low meridional SST gradient events in the

future (Figure A.4a) will facilitate the occurrence of extreme El Nino events, even with lower SST anomalies over eastern Pacific as shown in Figure A.4b. Hence, the future frequency of extreme El Nino conditions will increase (Figure A.5).

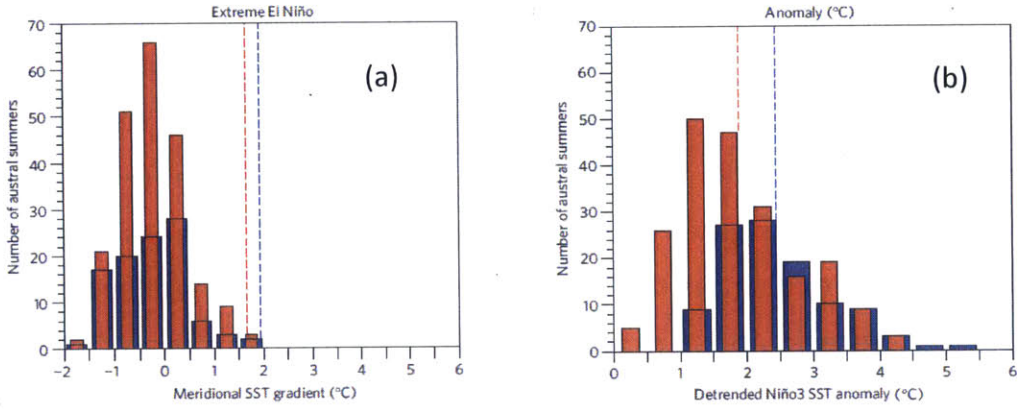


**Figure A.4:** Multi-model statistics associated with the increase in the frequency of extreme El Niño events. (**a**) Multi-model histograms of the meridional SST gradient in the eastern equatorial Pacific for extreme El Niño. The meridional SST gradient is defined as the average SST over the east off-equatorial region (5° N–10° N, 150° E–90° W) minus the average over the eastern equatorial region (2.5° S–2.5° N, 155° E–120° W). (**c**) Multi-model histogram of SST anomalies for extreme El Niño events. The blue and red bars and lines are for the past and future period respectively. Figure adapted from Cai et al., 2014.

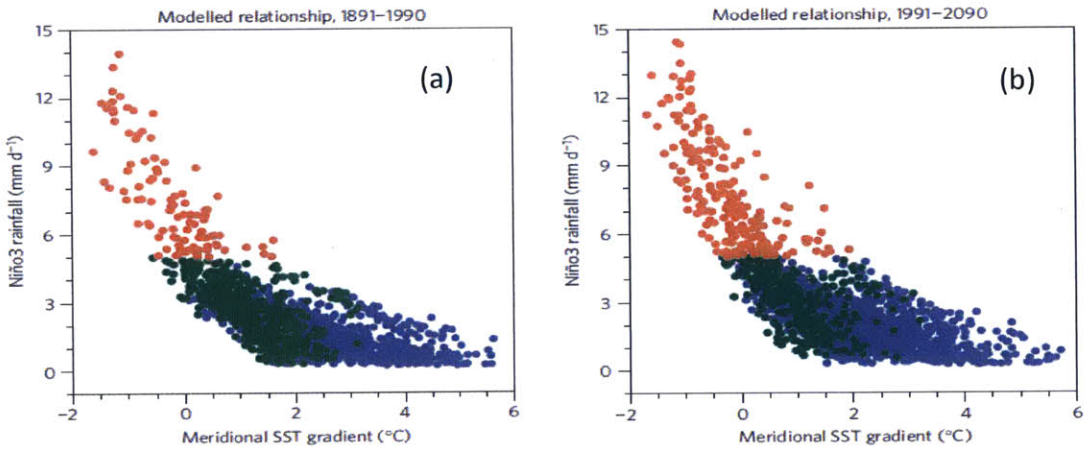


**Figure A.5:** Evolution and nonlinear characteristics of model extreme El Niño events, and changes in occurrences under greenhouse warming. (c, d) Relationship between eastern equatorial Pacific (Niño3 area: 5° S–5° N, 150° W–90° W) austral summer total rainfall and austral summer meridional SST gradient for the control and climate change periods, respectively. Red, green and blue dots indicate extreme El Niño (defined as events for which austral summer rainfall is greater than 5mm per day), moderate El Niño (defined as events with SST anomalies greater than 0.5 standard deviation of the control period that are not extreme El Niño events), and La Niña and neutral events, that is, all non-El Niño years, respectively. Figure adapted from Cai et al., 2014.

## La Nina and future changes in the frequency of La Nina events

The extreme La Nina events are usually initiated after extreme El Nino events. For example, extreme La Nina events in 1998-1999 and 1987-1988 were after 1997-1998 and 1986-1987 El Nino events respectively. After extreme El Nino events, heat is discharged, thermocline over the equatorial Pacific shoals and initiate the onset of cold SST in the central equatorial Pacific. The cooling increases the east-west zonal temperature gradient (Figures A.6b and A.6c), which enhances the easterly winds(Figure A.6b) and induces further shallowing of the thermocline that further enhances the east-west zonal temperature gradient through the Bjerknes positive feedback. Another mechanism that also decreases the SST over central Pacific is through Ekman pumping of deep cold water to the surface because of the ocean vertical temperature gradient initiated by shallowing of the thermocline.

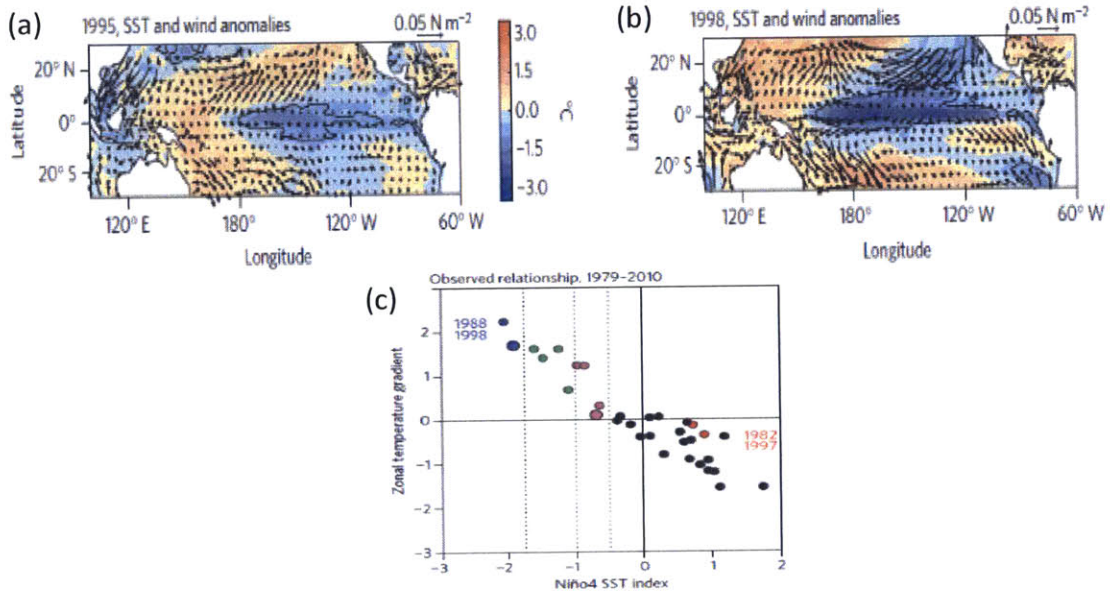


**Figure A.6:** Identification of observed extreme La Niña events. (a, b) December–February average SST anomalies (shading, ⍰0.75°C contour highlighted by a black curve) and surface wind stress anomalies associated with a weak (a) and extreme (b) La Niña. (c) Relationship between Niño4 and a time series of the Maritime continent region (5° S–5° N, 00° E–125° E)–central Pacific (Niño4, 5° S–5° N, 160° E–150° W) surface temperature gradient, with a correlation coefficient of $r$=-0.93.. Extreme El Niño events are indicated by red dots. Green dots indicate moderate La Niña, and purple dots weak La Niña (big purple 1995), defined as when Niño4 is greater than 0.5 standard deviation but less than 1.0 standard deviation in amplitude. Black dots indicate all other years. Figure adapted from Cai et al., 2015.

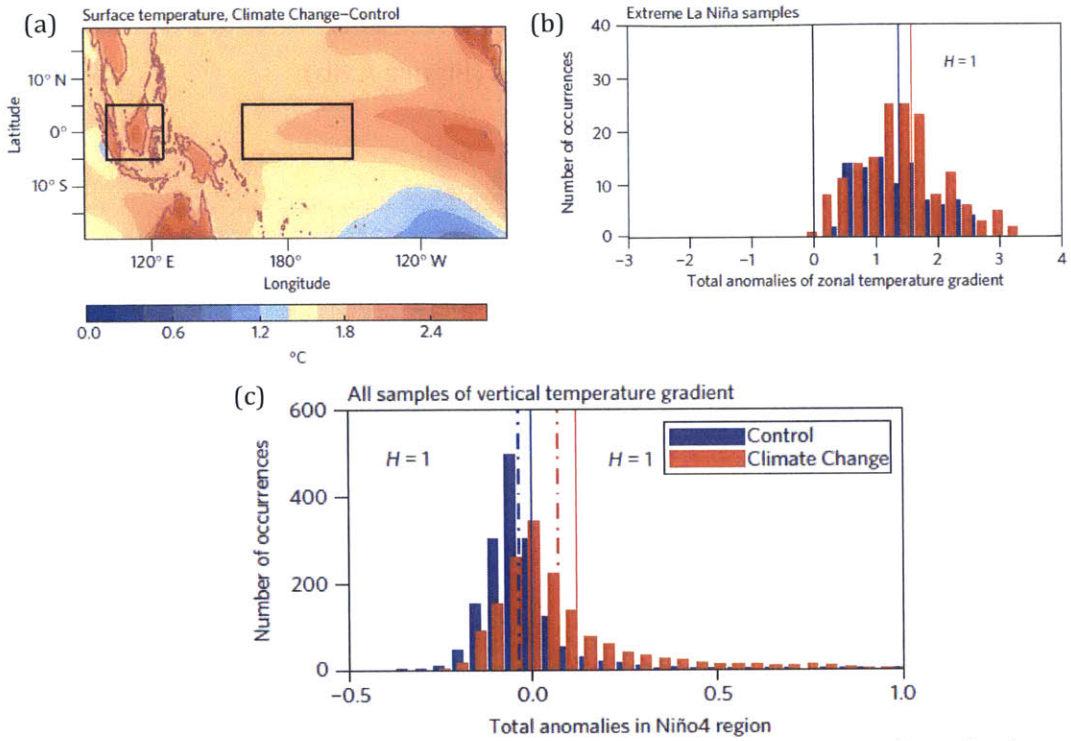


**Figure A.7:** Multi-model statistics in August–December associated with the increase in frequency of extreme La Niña events. (a) Multi-model ensemble average of surface temperature changes (in °C) between the average over the Climate Change and the Control periods. (b) Multi-model ensemble histogram of the Maritime–central Pacific surface temperature gradient (referenced to the mean of the Control period) for extreme La Niña samples. Values are separated into 0.25 bins centered at the tick point for the Control (blue) and Climate Change (red) periods. (c) Multi-model ensemble histogram of the upper ocean vertical temperature gradient in the Niño4 region, defined as the average of temperature in the top 50m minus temperature at 60 m, showing an increase in the gradient for all samples. Values are separated into 0.05 bins centered at the tick point for the Control (blue) and Climate Change (red) periods. The multi-model medians for the Control (solid blue line) and the Climate Change (solid red line) periods are indicated. The shift histograms in b and c are statistically significant above the 95% confidence level (as indicated by $H$=1) according to a two-sided Student $t$-test. Figure adapted from Cai et al., 2015.

In the future, the frequent occurrence extreme El Nino events initiate frequent extreme La Nina events after the release of heat associated with them. Furthermore, the increase of temperature over the maritime continent is faster than the central equatorial Pacific (A.7a), which enhances the SST east-west temperature gradient (Figure A.7b) and enhances easterly winds, which further increases because of Bjerknes feedback. In addition, the warming of the ocean surface compared to the deep water enhances the vertical ocean temperature gradient

(Figure A.7c) and Ekman pumping, which enhances the cooling of the surface. Hence, the future frequency of extreme La Nina events increases (Figure A.8b).

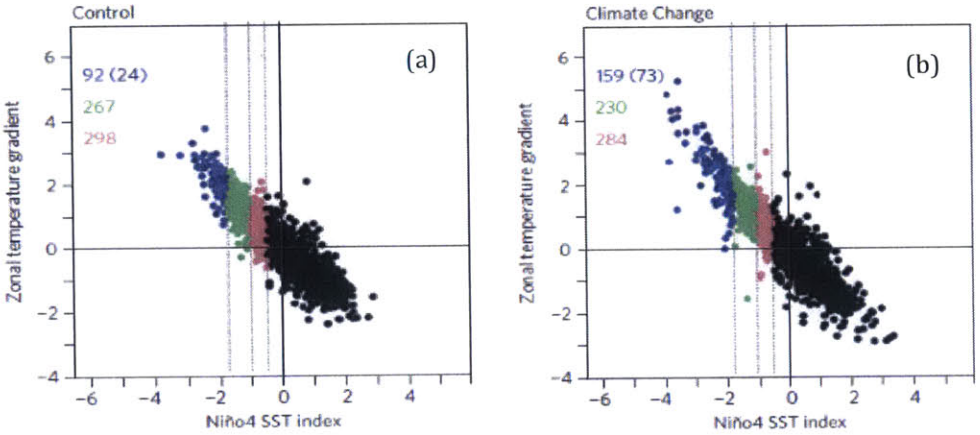


**Figure A.8:** Identification of model extreme La Niña events using 21 selected models. An extreme La Niña is defined as Niño4 amplitude greater than 1.75 s.d. (**a**, **b**) Relationship of Niño4 with surface temperature gradients between the Maritime continent region (5°S–5°N, 100°E–125°E) and the central Pacific (5°S–5°N, 160°E–150°W), for the Control (**a**) and Climate Change (**b**) period. Blue, green and purple dots indicate extreme (with |Niño4|>1.75 s.d.), moderate (1.0 s.d.<|Niño4|<1.75 s.d.) and weak (0.5 s.d.<|Niño4|<1.0 s.d.) La Niña. Black dots are all the years that do nott fall into these criteria. The number of different types of La Niña event is indicated, with dark blue dots and the dark blue number in brackets indicating extreme La Niña events that follow an extreme El Niño. Figure adapted from Cai et al., 2015.

# Appendix B: Correction Factors of the Bias Correction Approach used in Chapter 4

In this appendix a summary of the bias correction factors used with the different GCMs to correct the biases of their simulated runoff with observations is presented. These factors should be multiplied by the annual runoff (mm/day) simulated by the GCMs over the Eastern Nile basin to get the equivalent flow at Dongola ($km^3$/year) that have the same cumulative probability.

**Table B.1:** Summary of Bias Correction factors for the different GCMs.

| Cumulative Probability | BCC-CSM1-1M | BCC-CSM1-1 | CCSM4 | CMCC-CMS | CMCC-CM | CNRM-CM5 | GFDL-CM3 | GFDL-ESM2G | GFDL-ESM2M |
|---|---|---|---|---|---|---|---|---|---|
| 1 | 118.5 | 111.3 | 165.8 | 225.8 | 271.7 | 71.6 | 193.0 | 104.3 | 123.4 |
| 2 | 118.5 | 111.3 | 165.8 | 225.8 | 271.7 | 71.6 | 193.0 | 104.3 | 123.4 |
| 3 | 118.5 | 111.3 | 165.8 | 225.8 | 271.7 | 71.6 | 193.0 | 104.3 | 123.4 |
| 4 | 118.5 | 111.3 | 165.8 | 225.8 | 271.7 | 71.6 | 193.0 | 104.3 | 123.4 |
| 5 | 118.5 | 111.3 | 165.8 | 225.8 | 271.7 | 71.6 | 193.0 | 104.3 | 123.4 |
| 6 | 117.8 | 106.1 | 176.2 | 252.1 | 286.2 | 80.1 | 205.0 | 109.3 | 139.1 |
| 7 | 117.8 | 106.1 | 176.2 | 252.1 | 286.2 | 80.1 | 205.0 | 109.3 | 139.1 |
| 8 | 117.8 | 106.1 | 176.2 | 252.1 | 286.2 | 80.1 | 205.0 | 109.3 | 139.1 |
| 9 | 117.8 | 106.1 | 176.2 | 252.1 | 286.2 | 80.1 | 205.0 | 109.3 | 139.1 |
| 10 | 117.8 | 106.1 | 176.2 | 252.1 | 286.2 | 80.1 | 205.0 | 109.3 | 139.1 |
| 11 | 132.4 | 110.6 | 186.1 | 273.3 | 317.5 | 88.8 | 226.2 | 118.2 | 149.0 |
| 12 | 132.4 | 110.6 | 186.1 | 273.3 | 317.5 | 88.8 | 226.2 | 118.2 | 149.0 |
| 13 | 132.4 | 110.6 | 186.1 | 273.3 | 317.5 | 88.8 | 226.2 | 118.2 | 149.0 |
| 14 | 132.4 | 110.6 | 186.1 | 273.3 | 317.5 | 88.8 | 226.2 | 118.2 | 149.0 |
| 15 | 132.4 | 110.6 | 186.1 | 273.3 | 317.5 | 88.8 | 226.2 | 118.2 | 149.0 |
| 16 | 133.8 | 105.3 | 185.9 | 275.7 | 319.3 | 90.7 | 228.8 | 118.2 | 145.8 |
| 17 | 133.8 | 105.3 | 185.9 | 275.7 | 319.3 | 90.7 | 228.8 | 118.2 | 145.8 |
| 18 | 133.8 | 105.3 | 185.9 | 275.7 | 319.3 | 90.7 | 228.8 | 118.2 | 145.8 |
| 19 | 133.8 | 105.3 | 185.9 | 275.7 | 319.3 | 90.7 | 228.8 | 118.2 | 145.8 |
| 20 | 133.8 | 105.3 | 185.9 | 275.7 | 319.3 | 90.7 | 228.8 | 118.2 | 145.8 |
| 21 | 135.1 | 107.7 | 185.5 | 281.4 | 319.8 | 92.3 | 231.1 | 121.0 | 146.0 |
| 22 | 135.1 | 107.7 | 185.5 | 281.4 | 319.8 | 92.3 | 231.1 | 121.0 | 146.0 |
| 23 | 135.1 | 107.7 | 185.5 | 281.4 | 319.8 | 92.3 | 231.1 | 121.0 | 146.0 |
| 24 | 135.1 | 107.7 | 185.5 | 281.4 | 319.8 | 92.3 | 231.1 | 121.0 | 146.0 |
| 26 | 135.1 | 107.7 | 185.5 | 281.4 | 319.8 | 92.3 | 231.1 | 121.0 | 146.0 |
| 27 | 132.8 | 104.9 | 184.1 | 276.9 | 322.1 | 91.7 | 226.8 | 120.8 | 142.2 |
| 28 | 132.8 | 104.9 | 184.1 | 276.9 | 322.1 | 91.7 | 226.8 | 120.8 | 142.2 |
| 29 | 132.8 | 104.9 | 184.1 | 276.9 | 322.1 | 91.7 | 226.8 | 120.8 | 142.2 |
| 30 | 132.8 | 104.9 | 184.1 | 276.9 | 322.1 | 91.7 | 226.8 | 120.8 | 142.2 |

**Table 1 (Continued):** Summary of Bias Correction factors for the different GCMs.

| Cumulative Probability | BCC-CSM1-1M | BCC-CSM1-1 | CCSM4 | CMCC-CMS | CMCC-CM | CNRM-CM5 | GFDL-CM3 | GFDL-ESM2G | GFDL-ESM2M |
|---|---|---|---|---|---|---|---|---|---|
| 31 | 132.8 | 101.9 | 184.6 | 281.9 | 322.9 | 92.3 | 226.9 | 121.5 | 143.1 |
| 32 | 132.8 | 101.9 | 184.6 | 281.9 | 322.9 | 92.3 | 226.9 | 121.5 | 143.1 |
| 33 | 132.8 | 101.9 | 184.6 | 281.9 | 322.9 | 92.3 | 226.9 | 121.5 | 143.1 |
| 34 | 132.8 | 101.9 | 184.6 | 281.9 | 322.9 | 92.3 | 226.9 | 121.5 | 143.1 |
| 35 | 132.8 | 101.9 | 184.6 | 281.9 | 322.9 | 92.3 | 226.9 | 121.5 | 143.1 |
| 36 | 131.4 | 100.3 | 182.3 | 281.5 | 320.4 | 92.3 | 221.7 | 120.6 | 141.2 |
| 37 | 131.4 | 100.3 | 182.3 | 281.5 | 320.4 | 92.3 | 221.7 | 120.6 | 141.2 |
| 38 | 131.4 | 100.3 | 182.3 | 281.5 | 320.4 | 92.3 | 221.7 | 120.6 | 141.2 |
| 39 | 131.4 | 100.3 | 182.3 | 281.5 | 320.4 | 92.3 | 221.7 | 120.6 | 141.2 |
| 40 | 131.4 | 100.3 | 182.3 | 281.5 | 320.4 | 92.3 | 221.7 | 120.6 | 141.2 |
| 41 | 132.7 | 101.0 | 182.1 | 279.7 | 326.9 | 93.4 | 225.8 | 122.5 | 140.7 |
| 42 | 132.7 | 101.0 | 182.1 | 279.7 | 326.9 | 93.4 | 225.8 | 122.5 | 140.7 |
| 43 | 132.7 | 101.0 | 182.1 | 279.7 | 326.9 | 93.4 | 225.8 | 122.5 | 140.7 |
| 44 | 132.7 | 101.0 | 182.1 | 279.7 | 326.9 | 93.4 | 225.8 | 122.5 | 140.7 |
| 45 | 132.7 | 101.0 | 182.1 | 279.7 | 326.9 | 93.4 | 225.8 | 122.5 | 140.7 |
| 46 | 133.2 | 101.4 | 184.0 | 278.4 | 327.5 | 94.5 | 229.0 | 124.0 | 140.6 |
| 47 | 133.2 | 101.4 | 184.0 | 278.4 | 327.5 | 94.5 | 229.0 | 124.0 | 140.6 |
| 48 | 133.2 | 101.4 | 184.0 | 278.4 | 327.5 | 94.5 | 229.0 | 124.0 | 140.6 |
| 49 | 133.2 | 101.4 | 184.0 | 278.4 | 327.5 | 94.5 | 229.0 | 124.0 | 140.6 |
| 50 | 133.2 | 101.4 | 184.0 | 278.4 | 327.5 | 94.5 | 229.0 | 124.0 | 140.6 |
| 51 | 131.7 | 100.5 | 180.6 | 274.9 | 327.6 | 94.4 | 225.1 | 122.6 | 139.9 |
| 52 | 131.7 | 100.5 | 180.6 | 274.9 | 327.6 | 94.4 | 225.1 | 122.6 | 139.9 |
| 53 | 131.7 | 100.5 | 180.6 | 274.9 | 327.6 | 94.4 | 225.1 | 122.6 | 139.9 |
| 54 | 131.7 | 100.5 | 180.6 | 274.9 | 327.6 | 94.4 | 225.1 | 122.6 | 139.9 |
| 55 | 131.7 | 100.5 | 180.6 | 274.9 | 327.6 | 94.4 | 225.1 | 122.6 | 139.9 |
| 56 | 133.1 | 101.7 | 181.1 | 275.0 | 324.9 | 95.3 | 224.2 | 122.5 | 140.5 |
| 57 | 133.1 | 101.7 | 181.1 | 275.0 | 324.9 | 95.3 | 224.2 | 122.5 | 140.5 |
| 58 | 133.1 | 101.7 | 181.1 | 275.0 | 324.9 | 95.3 | 224.2 | 122.5 | 140.5 |
| 59 | 133.1 | 101.7 | 181.1 | 275.0 | 324.9 | 95.3 | 224.2 | 122.5 | 140.5 |
| 60 | 133.1 | 101.7 | 181.1 | 275.0 | 324.9 | 95.3 | 224.2 | 122.5 | 140.5 |
| 61 | 131.8 | 99.9 | 180.4 | 276.7 | 326.1 | 96.8 | 225.4 | 122.8 | 138.3 |
| 62 | 131.8 | 99.9 | 180.4 | 276.7 | 326.1 | 96.8 | 225.4 | 122.8 | 138.3 |
| 63 | 131.8 | 99.9 | 180.4 | 276.7 | 326.1 | 96.8 | 225.4 | 122.8 | 138.3 |
| 64 | 131.8 | 99.9 | 180.4 | 276.7 | 326.1 | 96.8 | 225.4 | 122.8 | 138.3 |
| 65 | 131.8 | 99.9 | 180.4 | 276.7 | 326.1 | 96.8 | 225.4 | 122.8 | 138.3 |
| 66 | 128.8 | 99.0 | 175.5 | 277.2 | 323.8 | 97.3 | 223.8 | 120.0 | 131.1 |
| 67 | 128.8 | 99.0 | 175.5 | 277.2 | 323.8 | 97.3 | 223.8 | 120.0 | 131.1 |
| 68 | 128.8 | 99.0 | 175.5 | 277.2 | 323.8 | 97.3 | 223.8 | 120.0 | 131.1 |
| 69 | 128.8 | 99.0 | 175.5 | 277.2 | 323.8 | 97.3 | 223.8 | 120.0 | 131.1 |
| 70 | 128.8 | 99.0 | 175.5 | 277.2 | 323.8 | 97.3 | 223.8 | 120.0 | 131.1 |
| 71 | 128.5 | 98.0 | 172.0 | 267.7 | 320.4 | 98.1 | 220.8 | 119.3 | 126.9 |
| 72 | 128.5 | 98.0 | 172.0 | 267.7 | 320.4 | 98.1 | 220.8 | 119.3 | 126.9 |
| 73 | 128.5 | 98.0 | 172.0 | 267.7 | 320.4 | 98.1 | 220.8 | 119.3 | 126.9 |
| 74 | 128.5 | 98.0 | 172.0 | 267.7 | 320.4 | 98.1 | 220.8 | 119.3 | 126.9 |
| 75 | 128.5 | 98.0 | 172.0 | 267.7 | 320.4 | 98.1 | 220.8 | 119.3 | 126.9 |

**Table 1 (Continued):** Summary of Bias Correction factors for the different GCMs.

| Cumulative Probability | BCC-CSM1-1M | BCC-CSM1-1 | CCSM4 | CMCC-CMS | CMCC-CM | CNRM-CM5 | GFDL-CM3 | GFDL-ESM2G | GFDL-ESM2M |
|---|---|---|---|---|---|---|---|---|---|
| 76 | 129.8 | 98.9 | 173.6 | 271.8 | 327.7 | 100.9 | 224.4 | 122.6 | 130.2 |
| 77 | 129.8 | 98.9 | 173.6 | 271.8 | 327.7 | 100.9 | 224.4 | 122.6 | 130.2 |
| 78 | 129.8 | 98.9 | 173.6 | 271.8 | 327.7 | 100.9 | 224.4 | 122.6 | 130.2 |
| 79 | 129.8 | 98.9 | 173.6 | 271.8 | 327.7 | 100.9 | 224.4 | 122.6 | 130.2 |
| 80 | 129.8 | 98.9 | 173.6 | 271.8 | 327.7 | 100.9 | 224.4 | 122.6 | 130.2 |
| 81 | 130.8 | 99.8 | 176.3 | 279.1 | 334.0 | 103.1 | 225.8 | 119.0 | 130.6 |
| 82 | 130.8 | 99.8 | 176.3 | 279.1 | 334.0 | 103.1 | 225.8 | 119.0 | 130.6 |
| 83 | 130.8 | 99.8 | 176.3 | 279.1 | 334.0 | 103.1 | 225.8 | 119.0 | 130.6 |
| 84 | 130.8 | 99.8 | 176.3 | 279.1 | 334.0 | 103.1 | 225.8 | 119.0 | 130.6 |
| 85 | 130.8 | 99.8 | 176.3 | 279.1 | 334.0 | 103.1 | 225.8 | 119.0 | 130.6 |
| 86 | 131.2 | 98.9 | 179.5 | 282.6 | 334.5 | 103.9 | 218.3 | 114.8 | 131.1 |
| 87 | 131.2 | 98.9 | 179.5 | 282.6 | 334.5 | 103.9 | 218.3 | 114.8 | 131.1 |
| 88 | 131.2 | 98.9 | 179.5 | 282.6 | 334.5 | 103.9 | 218.3 | 114.8 | 131.1 |
| 89 | 131.2 | 98.9 | 179.5 | 282.6 | 334.5 | 103.9 | 218.3 | 114.8 | 131.1 |
| 90 | 131.2 | 98.9 | 179.5 | 282.6 | 334.5 | 103.9 | 218.3 | 114.8 | 131.1 |
| 91 | 133.4 | 96.2 | 182.7 | 280.8 | 332.4 | 106.3 | 209.1 | 107.3 | 131.5 |
| 92 | 133.4 | 96.2 | 182.7 | 280.8 | 332.4 | 106.3 | 209.1 | 107.3 | 131.5 |
| 93 | 133.4 | 96.2 | 182.7 | 280.8 | 332.4 | 106.3 | 209.1 | 107.3 | 131.5 |
| 94 | 133.4 | 96.2 | 182.7 | 280.8 | 332.4 | 106.3 | 209.1 | 107.3 | 131.5 |
| 95 | 133.4 | 96.2 | 182.7 | 280.8 | 332.4 | 106.3 | 209.1 | 107.3 | 131.5 |
| 96 | 133.4 | 94.8 | 186.3 | 268.3 | 319.3 | 107.5 | 192.7 | 103.2 | 118.9 |
| 97 | 133.4 | 94.8 | 186.3 | 268.3 | 319.3 | 107.5 | 192.7 | 103.2 | 118.9 |
| 98 | 133.4 | 94.8 | 186.3 | 268.3 | 319.3 | 107.5 | 192.7 | 103.2 | 118.9 |
| 99 | 133.4 | 98.9 | 186.3 | 271.8 | 327.7 | 107.5 | 224.4 | 103.2 | 130.2 |
| 100 | 133.4 | 98.9 | 186.3 | 271.8 | 327.7 | 107.5 | 224.4 | 103.2 | 130.2 |

**Table B.2:** Summary of Bias Correction factors for the different GCMs.

| Cumulative Probability | MPI-ESM-MR | MRI-CGCM3 | NOR-ESM1-ME | NOR-ESM1-M | CMCC-CESM | CESM1-BGC | CESM1-CAM5 | ACCESS1 | FGOALS |
|---|---|---|---|---|---|---|---|---|---|
| 1 | 41.3 | 116.4 | 187.8 | 201.6 | 59.9 | 194.8 | 102.9 | 255.3 | 83.2 |
| 2 | 42.4 | 116.4 | 187.8 | 201.6 | 59.9 | 194.8 | 102.9 | 255.3 | 83.2 |
| 3 | 46.6 | 116.4 | 187.8 | 201.6 | 59.9 | 194.8 | 102.9 | 255.3 | 83.2 |
| 4 | 50.9 | 116.4 | 187.8 | 201.6 | 59.9 | 194.8 | 102.9 | 255.3 | 83.2 |
| 5 | 53.6 | 116.4 | 187.8 | 201.6 | 59.9 | 194.8 | 102.9 | 255.3 | 83.2 |
| 6 | 53.7 | 89.1 | 182.1 | 193.7 | 64.8 | 206.4 | 113.7 | 234.8 | 90.0 |
| 7 | 54.5 | 89.1 | 182.1 | 193.7 | 64.8 | 206.4 | 113.7 | 234.8 | 90.0 |
| 8 | 57.8 | 89.1 | 182.1 | 193.7 | 64.8 | 206.4 | 113.7 | 234.8 | 90.0 |
| 9 | 57.9 | 89.1 | 182.1 | 193.7 | 64.8 | 206.4 | 113.7 | 234.8 | 90.0 |
| 10 | 59.0 | 89.1 | 182.1 | 193.7 | 64.8 | 206.4 | 113.7 | 234.8 | 90.0 |
| 11 | 63.5 | 74.6 | 190.7 | 208.3 | 66.2 | 217.6 | 121.5 | 224.8 | 98.0 |
| 12 | 63.9 | 74.6 | 190.7 | 208.3 | 66.2 | 217.6 | 121.5 | 224.8 | 98.0 |
| 13 | 64.1 | 74.6 | 190.7 | 208.3 | 66.2 | 217.6 | 121.5 | 224.8 | 98.0 |
| 14 | 65.6 | 74.6 | 190.7 | 208.3 | 66.2 | 217.6 | 121.5 | 224.8 | 98.0 |
| 15 | 65.8 | 74.6 | 190.7 | 208.3 | 66.2 | 217.6 | 121.5 | 224.8 | 98.0 |
| 16 | 66.8 | 70.2 | 187.0 | 207.5 | 64.5 | 213.9 | 121.9 | 201.7 | 98.3 |
| 17 | 66.9 | 70.2 | 187.0 | 207.5 | 64.5 | 213.9 | 121.9 | 201.7 | 98.3 |
| 18 | 67.8 | 70.2 | 187.0 | 207.5 | 64.5 | 213.9 | 121.9 | 201.7 | 98.3 |
| 19 | 68.0 | 70.2 | 187.0 | 207.5 | 64.5 | 213.9 | 121.9 | 201.7 | 98.3 |
| 20 | 68.0 | 70.2 | 187.0 | 207.5 | 64.5 | 213.9 | 121.9 | 201.7 | 98.3 |
| 21 | 69.4 | 68.3 | 176.8 | 205.0 | 64.2 | 207.0 | 121.6 | 202.3 | 99.4 |
| 22 | 70.4 | 68.3 | 176.8 | 205.0 | 64.2 | 207.0 | 121.6 | 202.3 | 99.4 |
| 23 | 70.5 | 68.3 | 176.8 | 205.0 | 64.2 | 207.0 | 121.6 | 202.3 | 99.4 |
| 24 | 70.5 | 68.3 | 176.8 | 205.0 | 64.2 | 207.0 | 121.6 | 202.3 | 99.4 |
| 25 | 70.6 | 68.3 | 176.8 | 205.0 | 64.2 | 207.0 | 121.6 | 202.3 | 99.4 |
| 26 | 70.7 | 67.8 | 173.3 | 192.3 | 63.7 | 202.5 | 121.6 | 200.5 | 98.7 |
| 27 | 71.1 | 67.8 | 173.3 | 192.3 | 63.7 | 202.5 | 121.6 | 200.5 | 98.7 |
| 28 | 71.1 | 67.8 | 173.3 | 192.3 | 63.7 | 202.5 | 121.6 | 200.5 | 98.7 |
| 29 | 72.4 | 67.8 | 173.3 | 192.3 | 63.7 | 202.5 | 121.6 | 200.5 | 98.7 |
| 30 | 72.9 | 67.8 | 173.3 | 192.3 | 63.7 | 202.5 | 121.6 | 200.5 | 98.7 |
| 31 | 73.2 | 66.0 | 173.7 | 186.8 | 64.6 | 203.5 | 122.1 | 197.5 | 99.2 |
| 32 | 73.7 | 66.0 | 173.7 | 186.8 | 64.6 | 203.5 | 122.1 | 197.5 | 99.2 |
| 33 | 74.0 | 66.0 | 173.7 | 186.8 | 64.6 | 203.5 | 122.1 | 197.5 | 99.2 |
| 34 | 74.5 | 66.0 | 173.7 | 186.8 | 64.6 | 203.5 | 122.1 | 197.5 | 99.2 |
| 35 | 74.6 | 66.0 | 173.7 | 186.8 | 64.6 | 203.5 | 122.1 | 197.5 | 99.2 |
| 36 | 74.7 | 63.8 | 168.8 | 181.2 | 63.8 | 193.7 | 118.7 | 190.4 | 98.0 |
| 37 | 74.7 | 63.8 | 168.8 | 181.2 | 63.8 | 193.7 | 118.7 | 190.4 | 98.0 |
| 38 | 74.9 | 63.8 | 168.8 | 181.2 | 63.8 | 193.7 | 118.7 | 190.4 | 98.0 |
| 39 | 75.6 | 63.8 | 168.8 | 181.2 | 63.8 | 193.7 | 118.7 | 190.4 | 98.0 |
| 40 | 76.7 | 63.8 | 168.8 | 181.2 | 63.8 | 193.7 | 118.7 | 190.4 | 98.0 |
| 41 | 76.8 | 61.6 | 167.5 | 176.0 | 63.0 | 194.9 | 119.7 | 186.7 | 98.0 |
| 42 | 77.2 | 61.6 | 167.5 | 176.0 | 63.0 | 194.9 | 119.7 | 186.7 | 98.0 |
| 43 | 77.6 | 61.6 | 167.5 | 176.0 | 63.0 | 194.9 | 119.7 | 186.7 | 98.0 |
| 44 | 77.6 | 61.6 | 167.5 | 176.0 | 63.0 | 194.9 | 119.7 | 186.7 | 98.0 |
| 45 | 77.9 | 61.6 | 167.5 | 176.0 | 63.0 | 194.9 | 102.9 | 186.7 | 98.0 |

**Table B.2 (Continued):** Summary of Bias Correction factors for the different GCMs.

| Cumulative Probability | MPI-ESM-MR | MRI-CGCM3 | NOR-ESM1-ME | NOR-ESM1-M | CMCC-CESM | CESM1-BGC | CESM1-CAM5 | ACCESS1 | FGOALS |
|---|---|---|---|---|---|---|---|---|---|
| 46 | 78.3 | 58.5 | 166.5 | 172.5 | 63.1 | 194.6 | 119.7 | 180.6 | 98.6 |
| 47 | 79.3 | 58.5 | 166.5 | 172.5 | 63.1 | 194.6 | 120.8 | 180.6 | 98.6 |
| 48 | 79.5 | 58.5 | 166.5 | 172.5 | 63.1 | 194.6 | 120.8 | 180.6 | 98.6 |
| 49 | 79.9 | 58.5 | 166.5 | 172.5 | 63.1 | 194.6 | 120.8 | 180.6 | 98.6 |
| 50 | 80.0 | 58.5 | 166.5 | 172.5 | 63.1 | 194.6 | 120.8 | 180.6 | 98.6 |
| 51 | 80.2 | 56.0 | 163.5 | 169.5 | 62.7 | 192.3 | 120.8 | 175.3 | 97.9 |
| 52 | 80.5 | 56.0 | 163.5 | 169.5 | 62.7 | 192.3 | 120.4 | 175.3 | 97.9 |
| 53 | 80.6 | 56.0 | 163.5 | 169.5 | 62.7 | 192.3 | 120.4 | 175.3 | 97.9 |
| 54 | 81.0 | 56.0 | 163.5 | 169.5 | 62.7 | 192.3 | 120.4 | 175.3 | 97.9 |
| 55 | 81.4 | 56.0 | 163.5 | 169.5 | 62.7 | 192.3 | 120.4 | 175.3 | 97.9 |
| 56 | 81.5 | 52.1 | 161.1 | 162.7 | 62.3 | 190.9 | 120.4 | 173.2 | 98.8 |
| 57 | 82.3 | 52.1 | 161.1 | 162.7 | 62.3 | 190.9 | 120.0 | 173.2 | 98.8 |
| 58 | 83.0 | 52.1 | 161.1 | 162.7 | 62.3 | 190.9 | 120.0 | 173.2 | 98.8 |
| 59 | 83.2 | 52.1 | 161.1 | 162.7 | 62.3 | 190.9 | 120.0 | 173.2 | 98.8 |
| 60 | 83.2 | 52.1 | 161.1 | 162.7 | 62.3 | 190.9 | 120.0 | 173.2 | 98.8 |
| 61 | 83.4 | 51.0 | 157.3 | 160.8 | 62.6 | 189.0 | 120.0 | 172.5 | 98.6 |
| 62 | 84.7 | 51.0 | 157.3 | 160.8 | 62.6 | 189.0 | 121.3 | 172.5 | 98.6 |
| 63 | 85.0 | 51.0 | 157.3 | 160.8 | 62.6 | 189.0 | 121.3 | 172.5 | 98.6 |
| 64 | 85.2 | 51.0 | 157.3 | 160.8 | 62.6 | 189.0 | 121.3 | 172.5 | 98.6 |
| 65 | 85.3 | 51.0 | 157.3 | 160.8 | 62.6 | 189.0 | 121.3 | 172.5 | 98.6 |
| 66 | 85.5 | 49.4 | 154.7 | 157.3 | 61.0 | 183.7 | 121.3 | 168.6 | 98.2 |
| 67 | 85.5 | 49.4 | 154.7 | 157.3 | 61.0 | 183.7 | 119.8 | 168.6 | 98.2 |
| 68 | 85.9 | 49.4 | 154.7 | 157.3 | 61.0 | 183.7 | 119.8 | 168.6 | 98.2 |
| 69 | 86.1 | 49.4 | 154.7 | 157.3 | 61.0 | 183.7 | 119.8 | 168.6 | 98.2 |
| 70 | 87.0 | 49.4 | 154.7 | 157.3 | 61.0 | 183.7 | 119.8 | 168.6 | 98.2 |
| 71 | 87.2 | 46.8 | 152.5 | 155.1 | 60.3 | 181.0 | 119.8 | 167.9 | 98.5 |
| 72 | 87.6 | 46.8 | 152.5 | 155.1 | 60.3 | 181.0 | 120.5 | 167.9 | 98.5 |
| 73 | 88.1 | 46.8 | 152.5 | 155.1 | 60.3 | 181.0 | 120.5 | 167.9 | 98.5 |
| 74 | 88.1 | 46.8 | 152.5 | 155.1 | 60.3 | 181.0 | 120.5 | 167.9 | 98.5 |
| 75 | 88.2 | 46.8 | 152.5 | 155.1 | 60.3 | 181.0 | 120.5 | 167.9 | 98.5 |
| 76 | 90.9 | 47.0 | 156.0 | 154.7 | 58.7 | 185.6 | 120.5 | 169.5 | 100.2 |
| 77 | 91.3 | 47.0 | 156.0 | 154.7 | 58.7 | 185.6 | 123.5 | 169.5 | 100.2 |
| 78 | 92.0 | 47.0 | 156.0 | 154.7 | 58.7 | 185.6 | 123.5 | 169.5 | 100.2 |
| 79 | 92.1 | 47.0 | 156.0 | 154.7 | 58.7 | 185.6 | 123.5 | 169.5 | 100.2 |
| 80 | 93.8 | 47.0 | 156.0 | 154.7 | 58.7 | 185.6 | 123.5 | 169.5 | 100.2 |
| 81 | 95.1 | 46.7 | 156.2 | 154.4 | 59.6 | 185.7 | 123.5 | 171.9 | 101.0 |
| 82 | 96.2 | 46.7 | 156.2 | 154.4 | 59.6 | 185.7 | 124.0 | 171.9 | 101.0 |
| 83 | 96.6 | 46.7 | 156.2 | 154.4 | 59.6 | 185.7 | 124.0 | 171.9 | 101.0 |
| 84 | 96.7 | 46.7 | 156.2 | 154.4 | 59.6 | 185.7 | 124.0 | 171.9 | 101.0 |
| 85 | 97.2 | 46.7 | 156.2 | 154.4 | 59.6 | 185.7 | 124.0 | 171.9 | 101.0 |
| 86 | 97.5 | 44.1 | 152.6 | 150.0 | 59.1 | 180.7 | 124.0 | 171.2 | 100.4 |
| 87 | 99.2 | 44.1 | 152.6 | 150.0 | 59.1 | 180.7 | 122.9 | 171.2 | 100.4 |
| 88 | 99.9 | 44.1 | 152.6 | 150.0 | 59.1 | 180.7 | 122.9 | 171.2 | 100.4 |
| 89 | 100.2 | 44.1 | 152.6 | 150.0 | 59.1 | 180.7 | 122.9 | 171.2 | 100.4 |
| 90 | 102.1 | 44.1 | 152.6 | 150.0 | 59.1 | 180.7 | 122.9 | 171.2 | 100.4 |

**Table B.2 (Continued):** Summary of Bias Correction factors for the different GCMs.

| Cumulative Probability | MPI-ESM-MR | MRI-CGCM3 | NOR-ESM1-ME | NOR-ESM1-M | CMCC-CESM | CESM1-BGC | CESM1-CAM5 | ACCESS1 | FGOALS |
|---|---|---|---|---|---|---|---|---|---|
| 91 | 103.6 | 42.3 | 142.2 | 143.5 | 57.4 | 173.8 | 123.7 | 160.7 | 101.8 |
| 92 | 103.9 | 42.3 | 142.2 | 143.5 | 57.4 | 173.8 | 123.7 | 160.7 | 101.8 |
| 93 | 105.1 | 42.3 | 142.2 | 143.5 | 57.4 | 173.8 | 123.7 | 160.7 | 101.8 |
| 94 | 105.3 | 42.3 | 142.2 | 143.5 | 57.4 | 173.8 | 123.7 | 160.7 | 101.8 |
| 95 | 105.4 | 42.3 | 142.2 | 143.5 | 57.4 | 173.8 | 123.7 | 160.7 | 101.8 |
| 96 | 107.0 | 32.6 | 125.9 | 118.7 | 50.7 | 168.8 | 124.3 | 148.0 | 101.8 |
| 97 | 107.3 | 32.6 | 125.9 | 118.7 | 50.7 | 168.8 | 124.3 | 148.0 | 99.9 |
| 98 | 108.5 | 32.6 | 125.9 | 118.7 | 50.7 | 168.8 | 124.3 | 148.0 | 99.9 |
| 99 | 115.1 | 32.6 | 142.2 | 143.5 | 50.1 | 168.8 | 123.7 | 148.0 | 99.9 |
| 100 | 117.2 | 32.6 | 142.2 | 143.5 | 50.7 | 168.8 | 123.7 | 148.0 | 99.9 |

# Appendix C: Analysis of GCMs

In this appendix, detailed analysis of the changes in SST, humidity, rainfall and wind circulation for each of the GCMs used in chapter 4 and 6 is presented. In each of the following figures, the climatological averages of July and August of the different variables are calculated for the period (1970-2000), while the changes are calculated for the period (2070-2100) compared to (1970-2000). Climatological average for the period (1970-2000) for July and August for the Sea Surface Temperature ($^{o}$C) overlaid by the wind (m/s) at 800 mb is shown in panel (a), rainfall (mm/day) is shown in panel (c), and vertical profiles of specific humidity (g/kg) with wind (m/s) averaged between 5$^{o}$N to 15$^{o}$N is shown in panel (e). Average of the changes for the period (2070-2100) compared to the period (1970-2000) for July and August for the Sea Surface Temperature ($^{o}$C) overlaid by the wind (m/s) at 800 mb is shown in panel (b), (d) rainfall (mm/day) is shown in panel (d), and vertical profiles of specific humidity (g/kg) with wind (m/s) averaged between 5$^{o}$N to 15$^{o}$N is shown in panel (f).

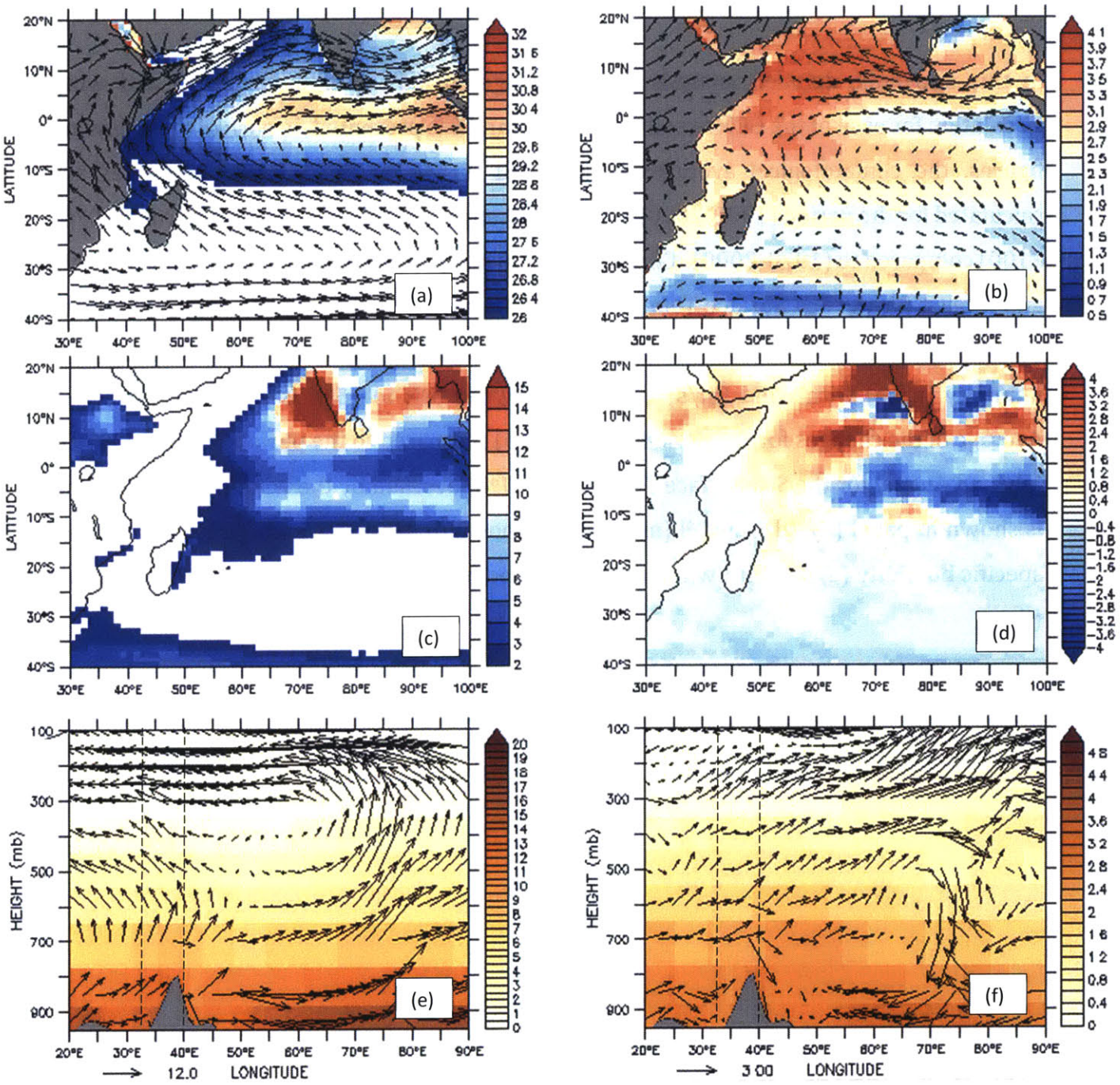


**Figure B.1:** BCC-CSM1-1M

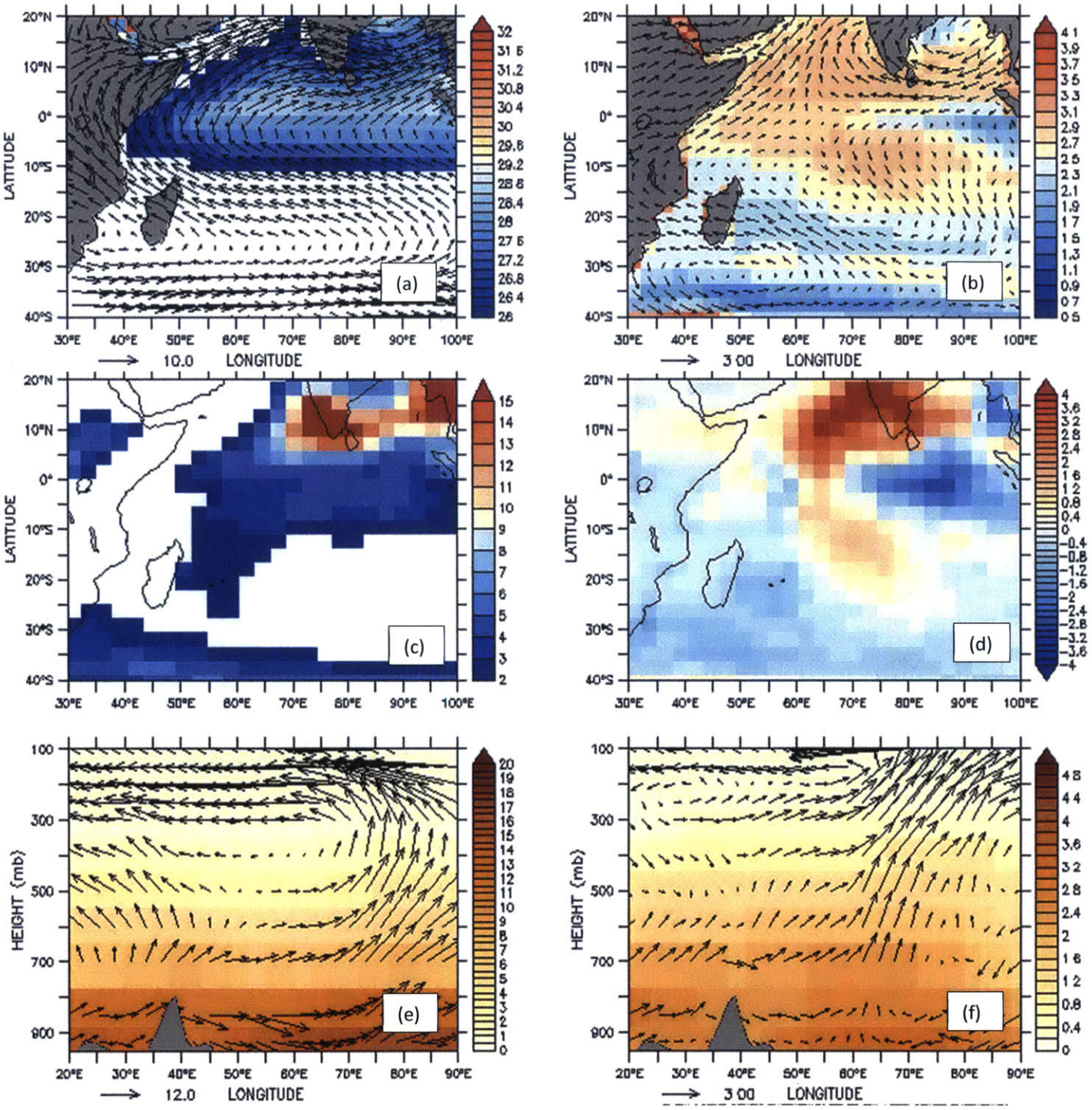


**Figure B.2:** BCC-CSM1-1

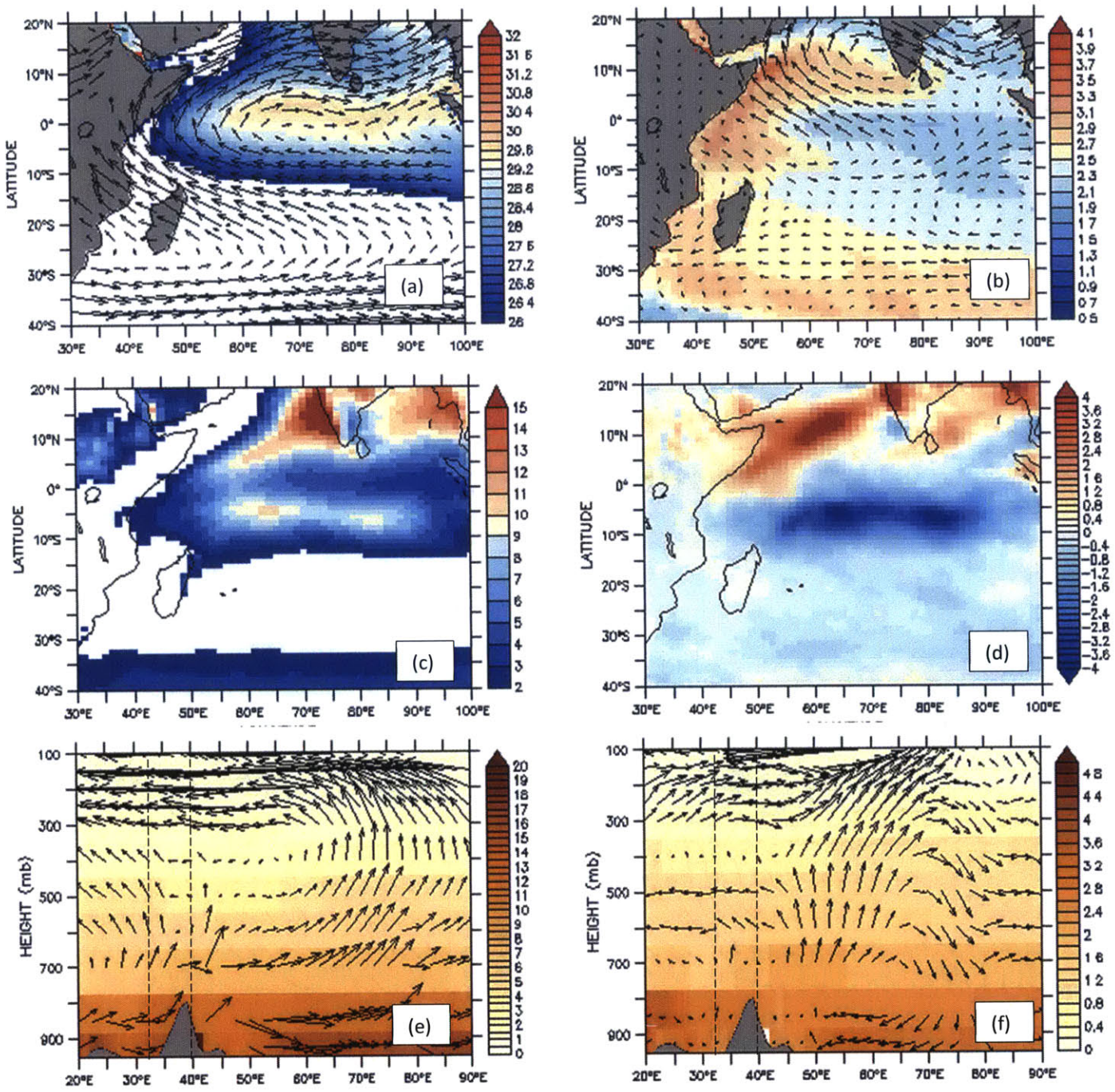


**Figure B.3:** CCSM4

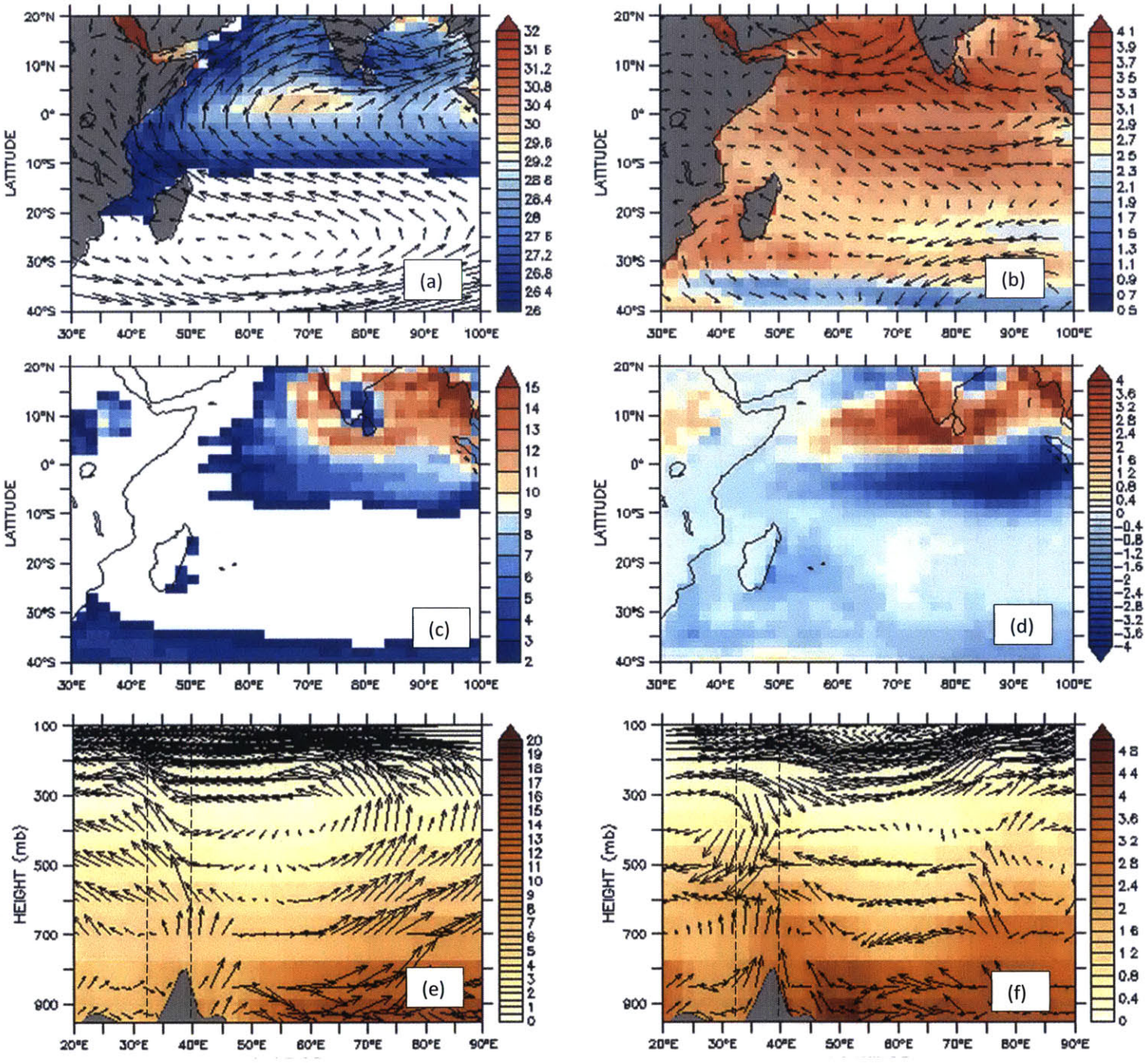


**Figure B.4:** CMCC-CMS

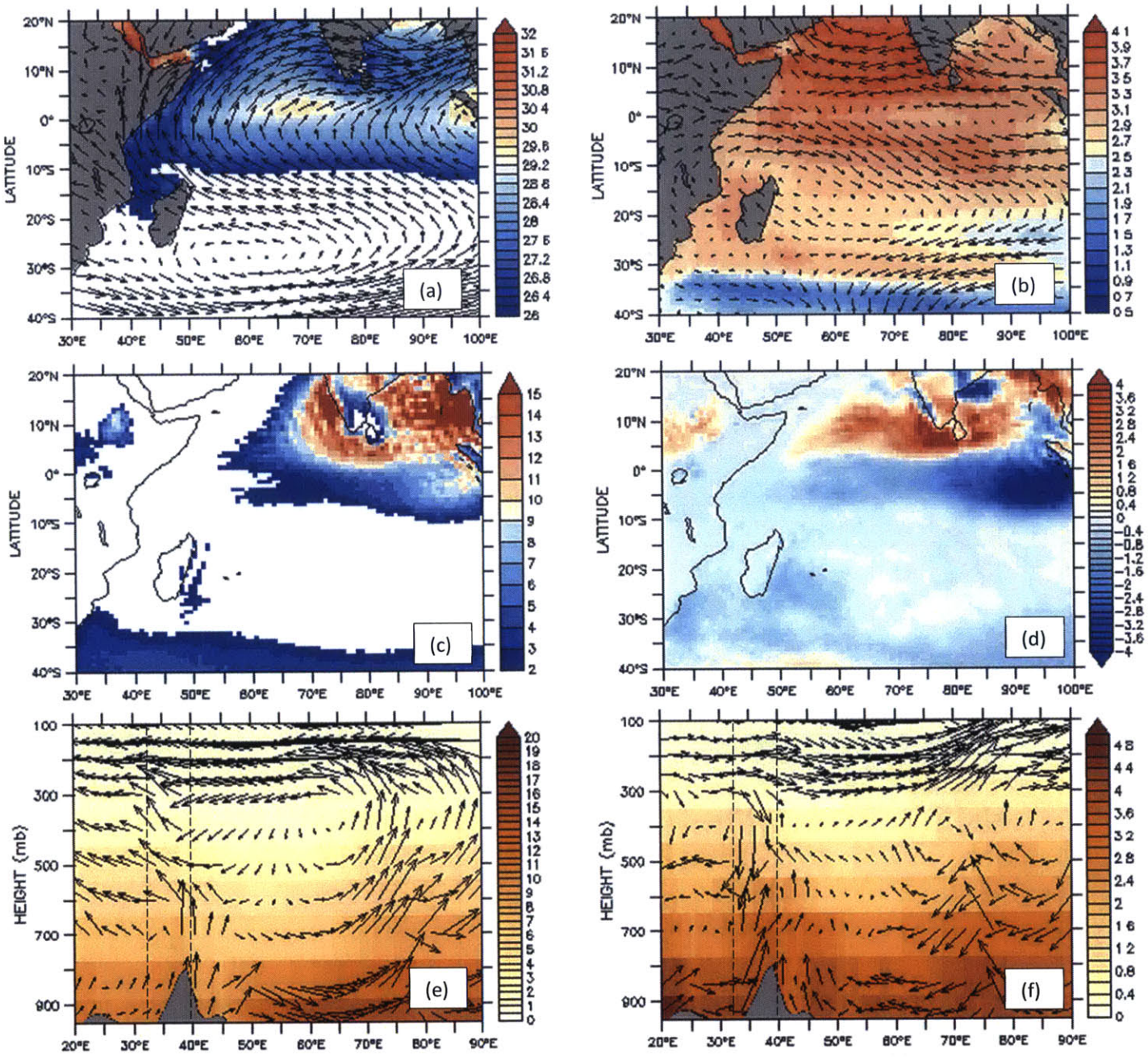


**Figure B.5:** CMCC-CM

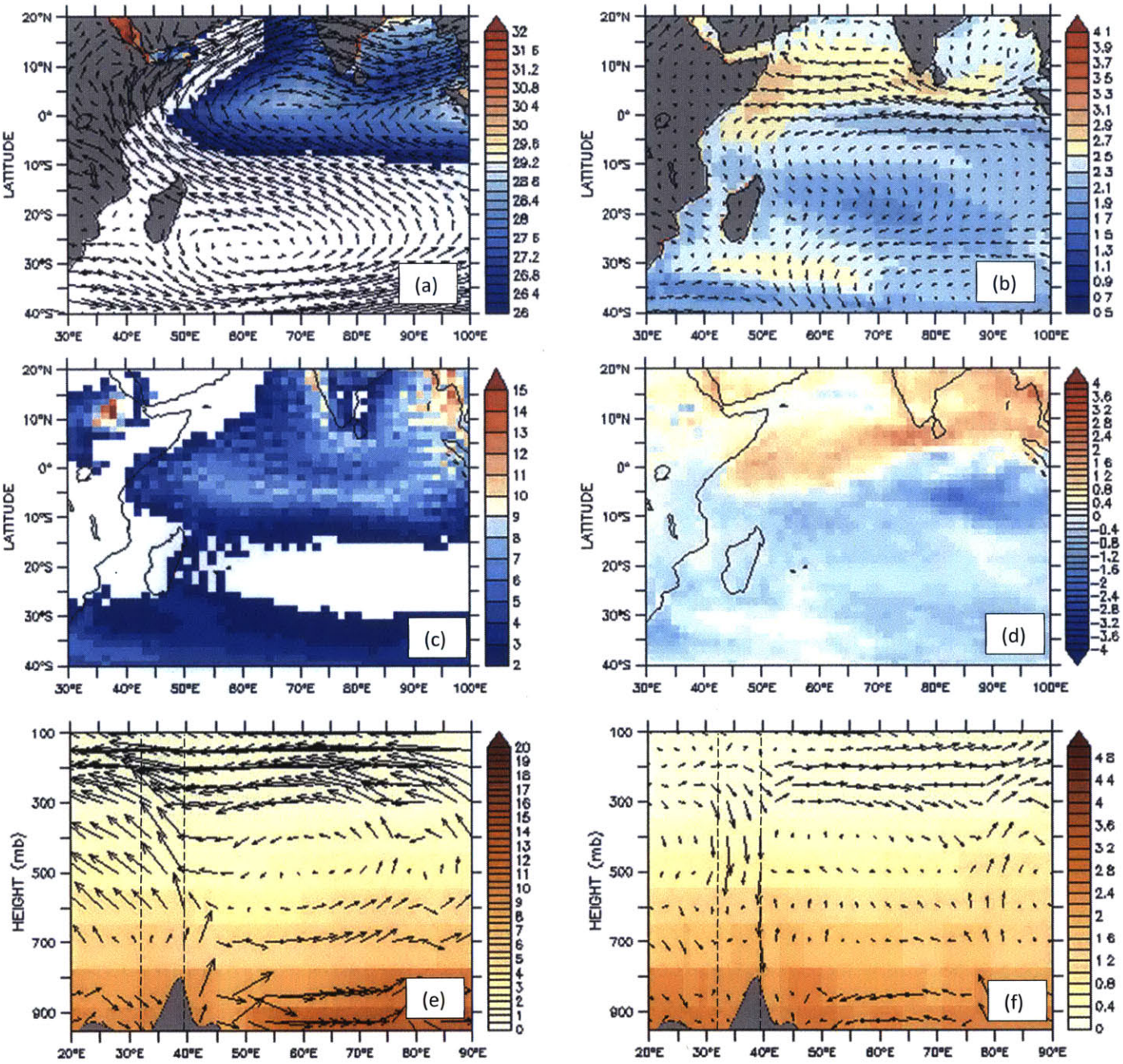


**Figure B.6:** CNRM-CM5

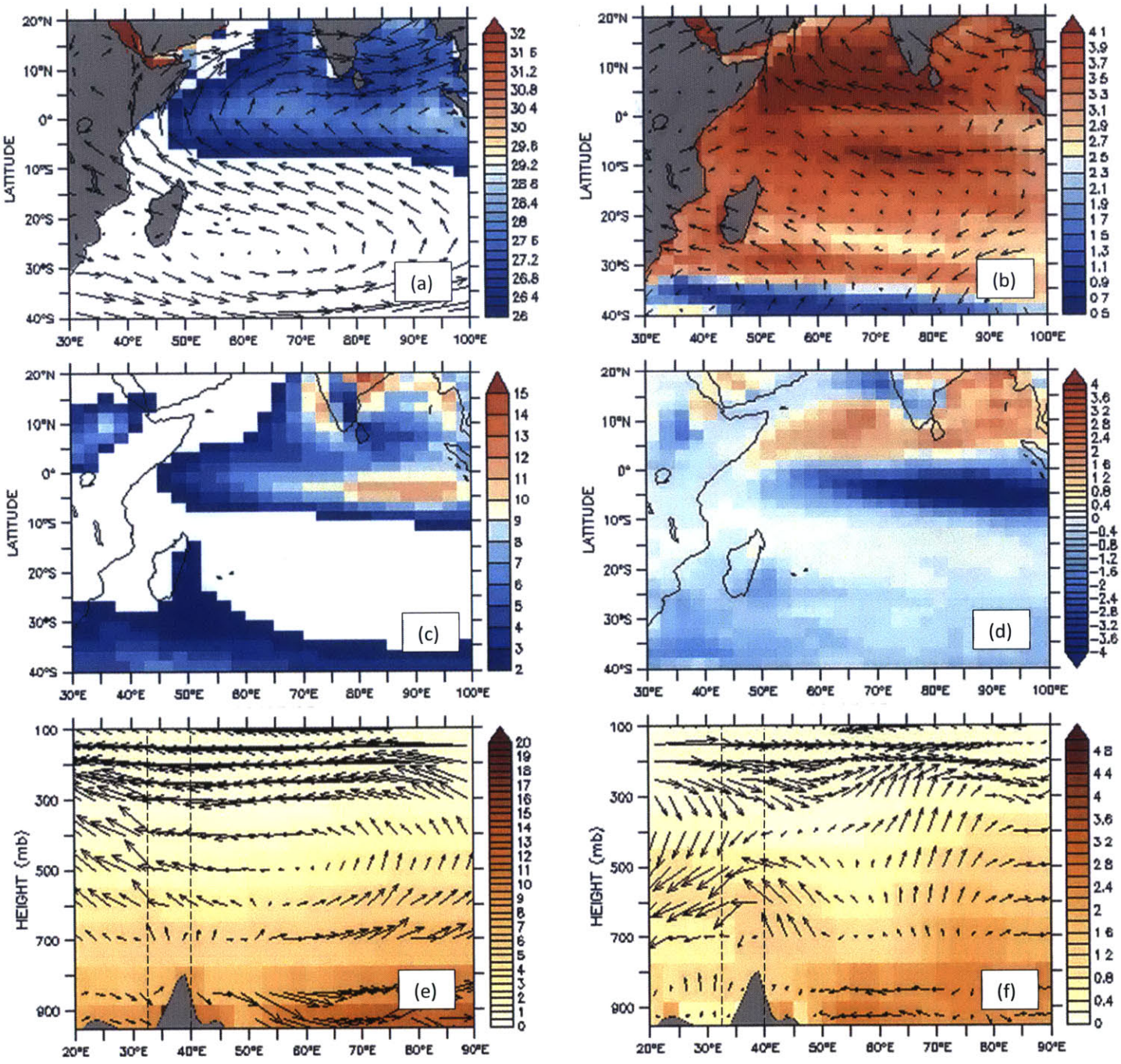


**Figure B.7:** GFDL-CM3

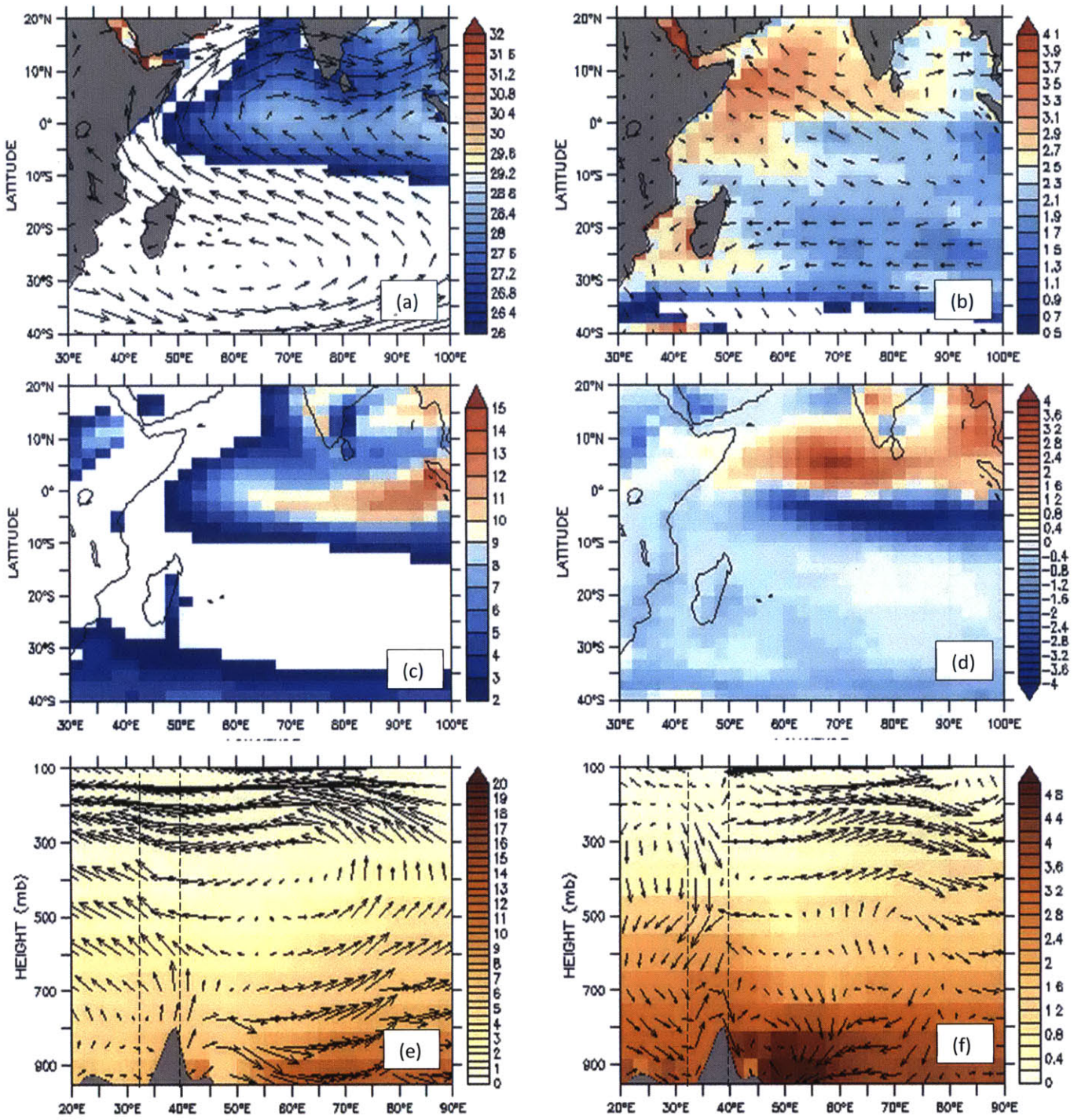


**Figure B.8:** GFDL-ESM2M

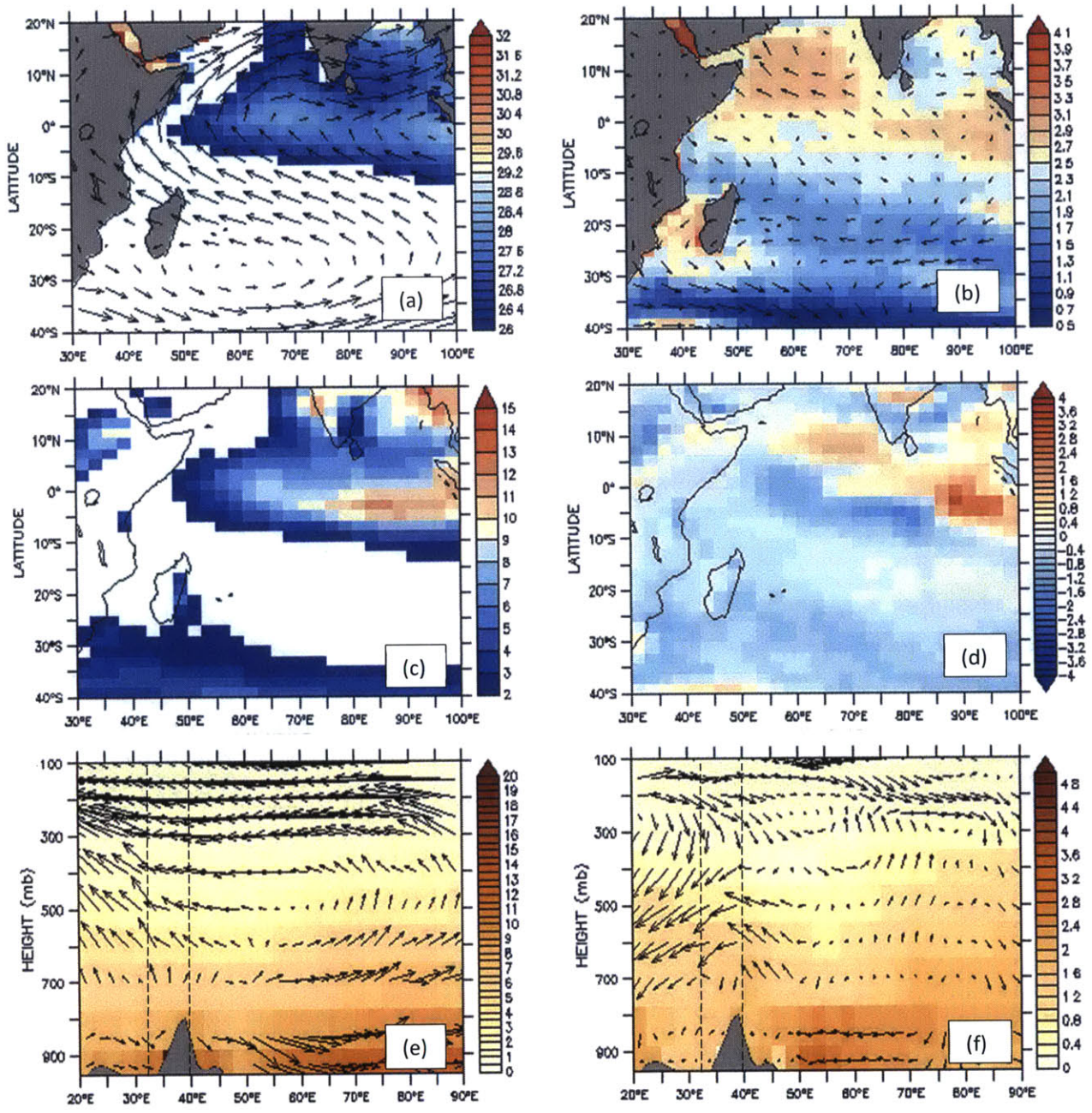


**Figure B.9:** GFDL-ESM2G

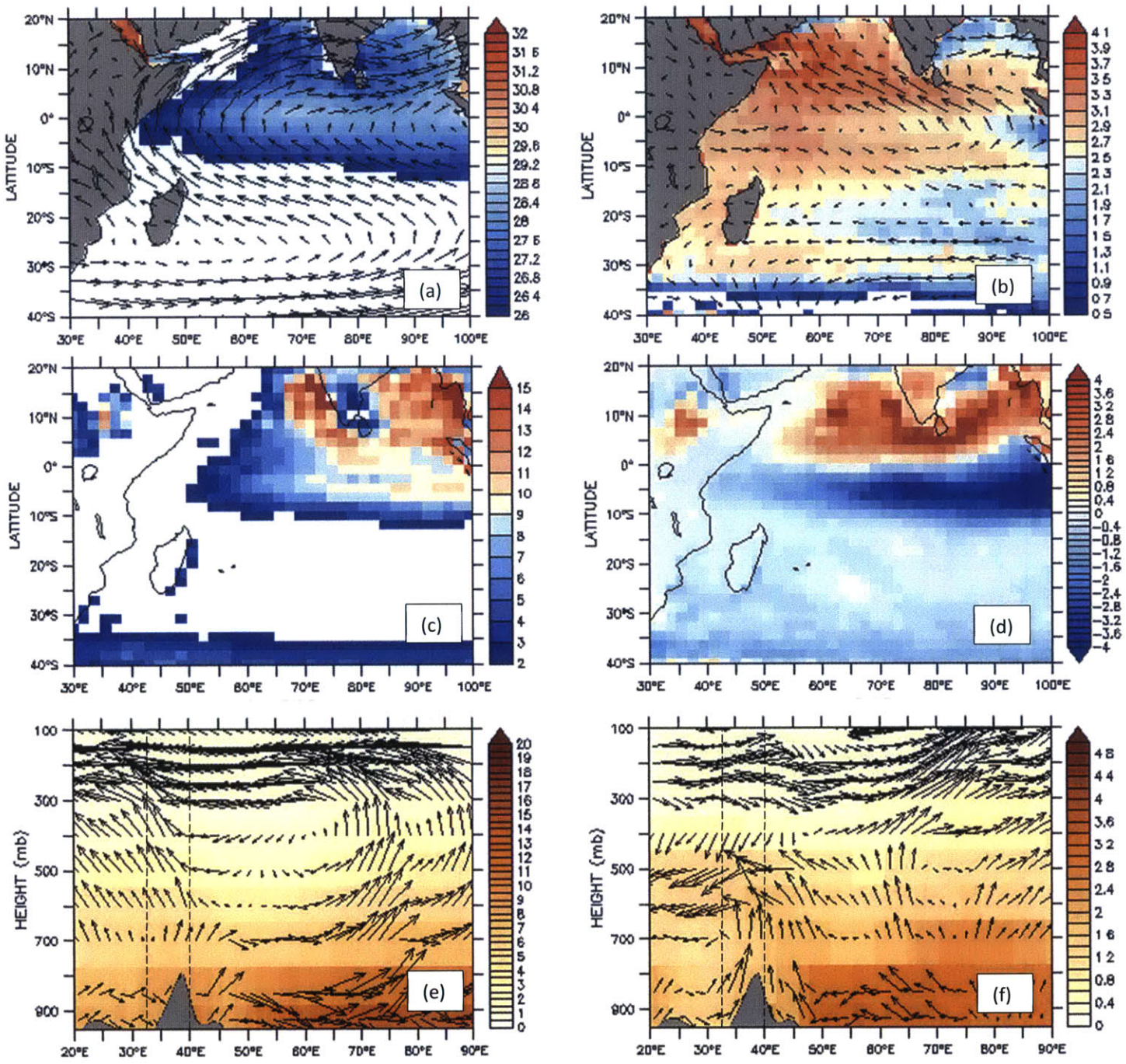


**Figure B.10:** MPI-ESM-MR

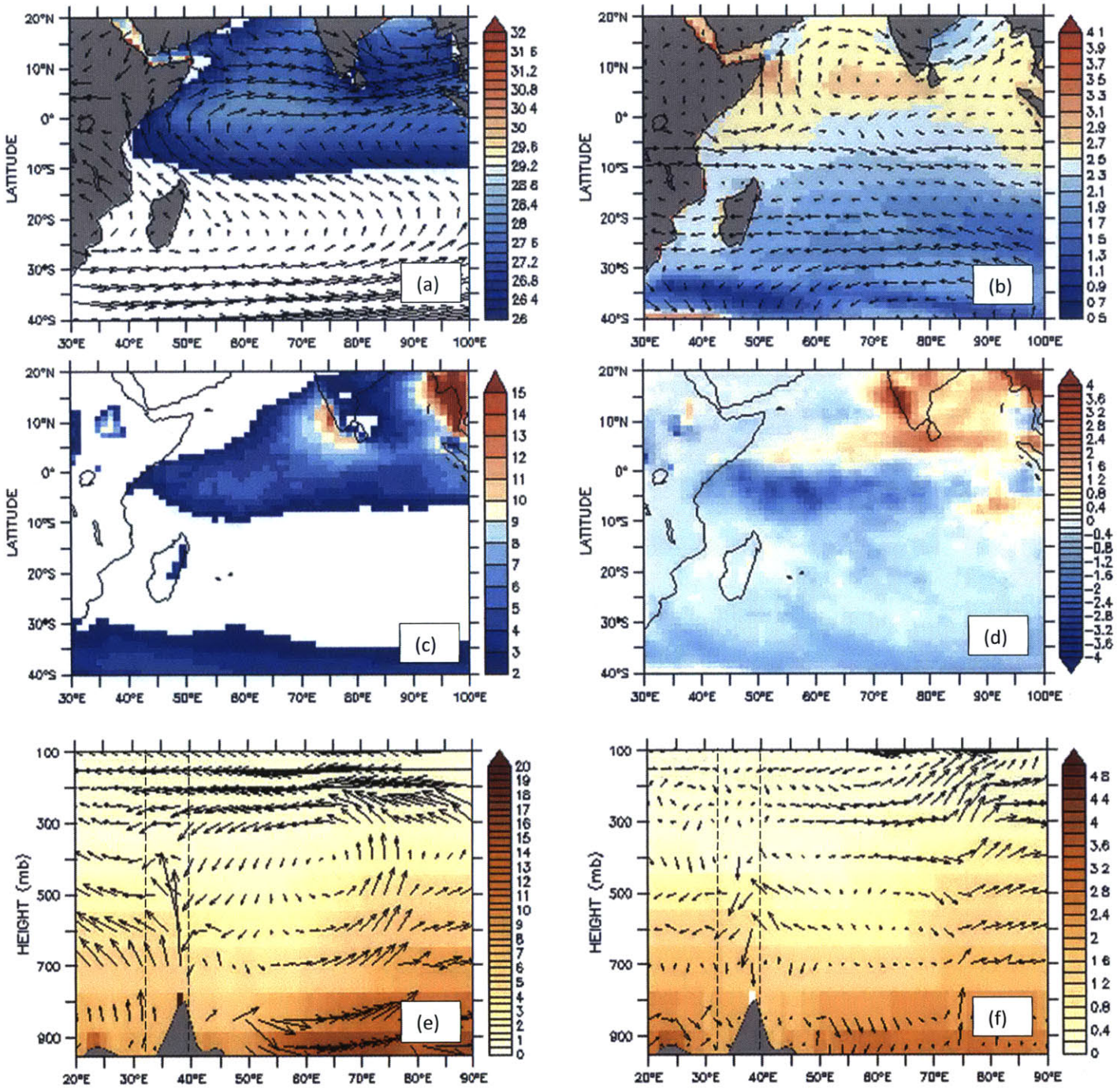


**Figure B.11:** MRI-CGCM3

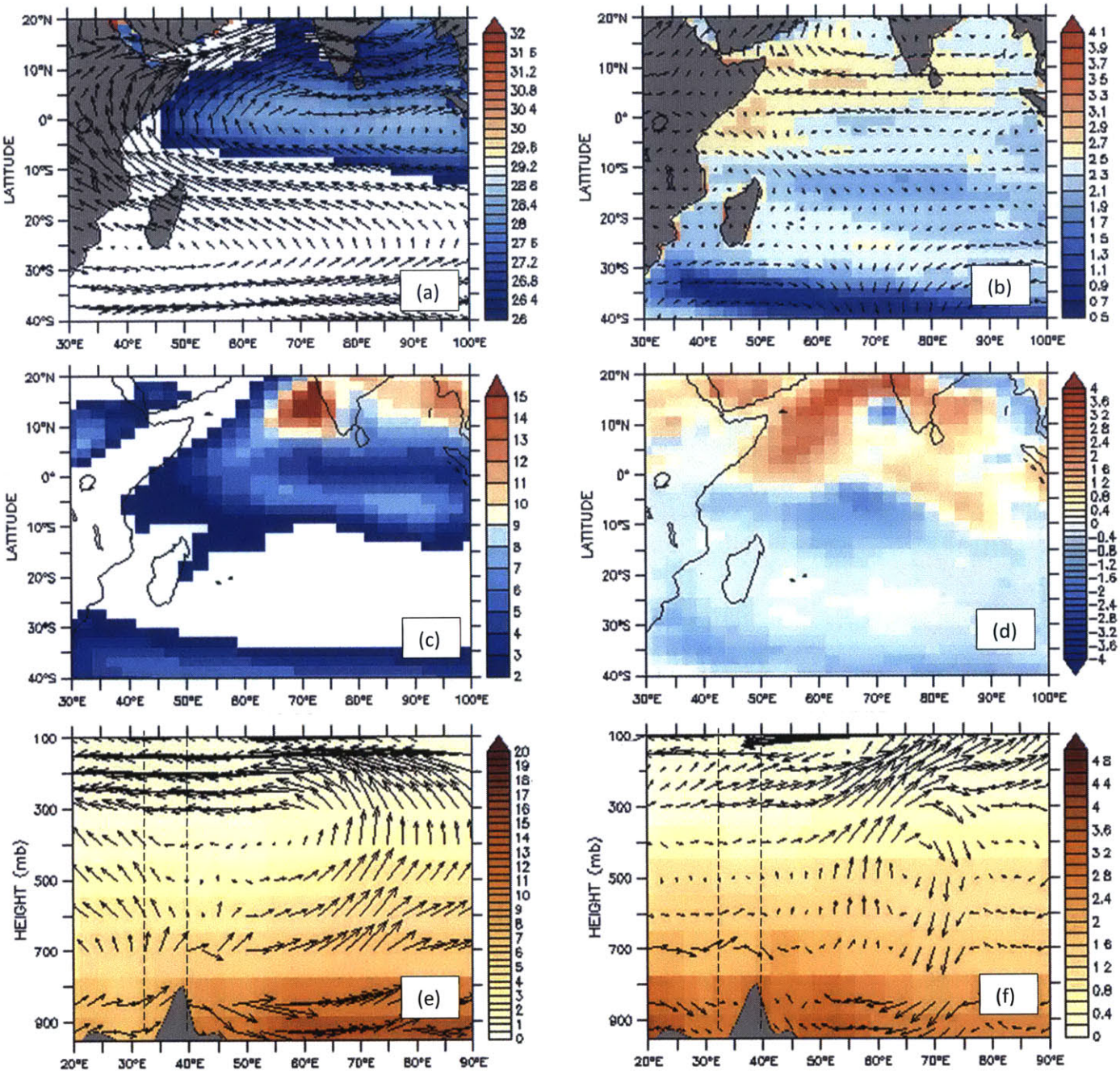


**Figure B.12:** NOR-ESM1-M

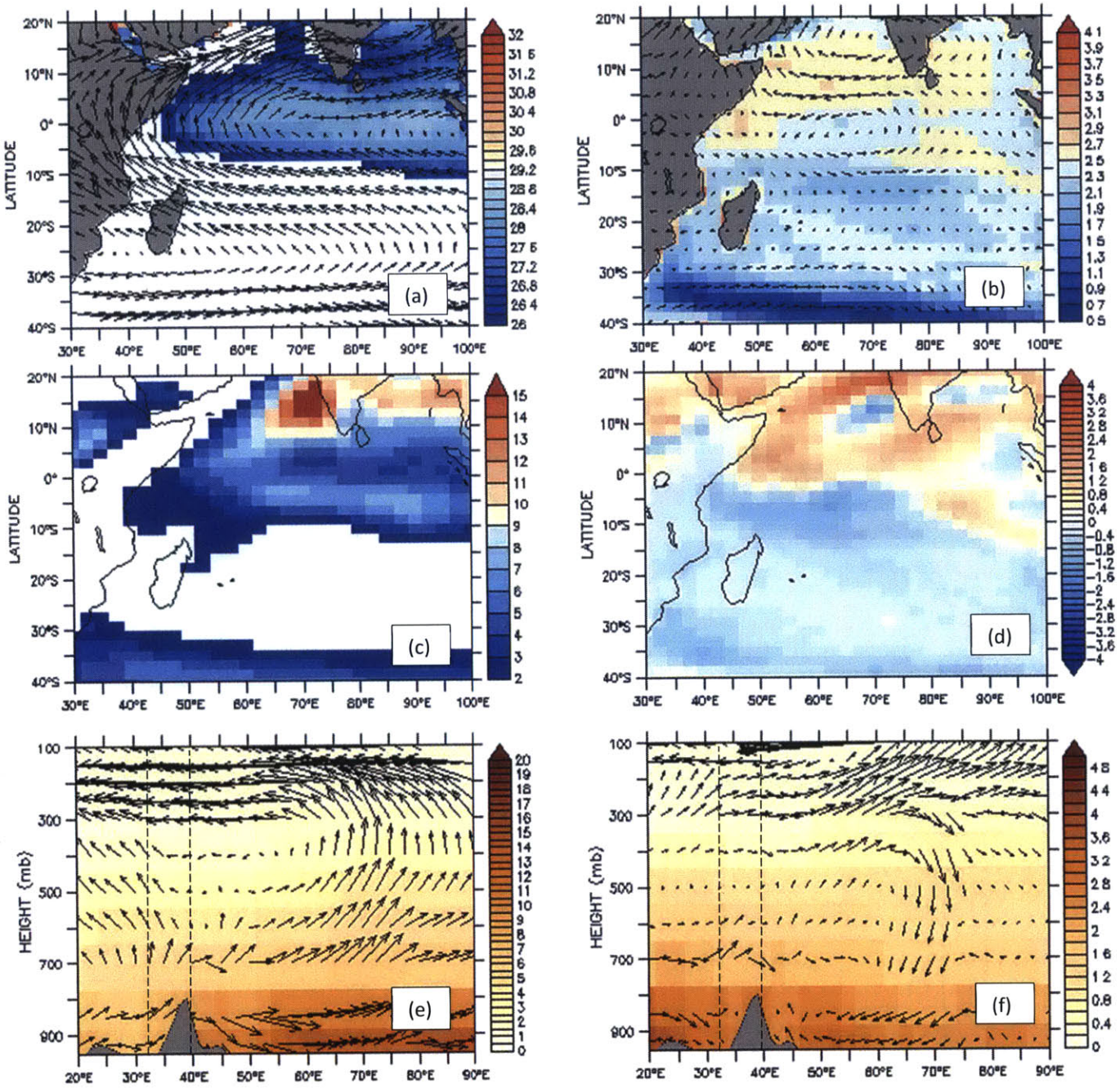


**Figure B.13:** NOR-ESM1-ME

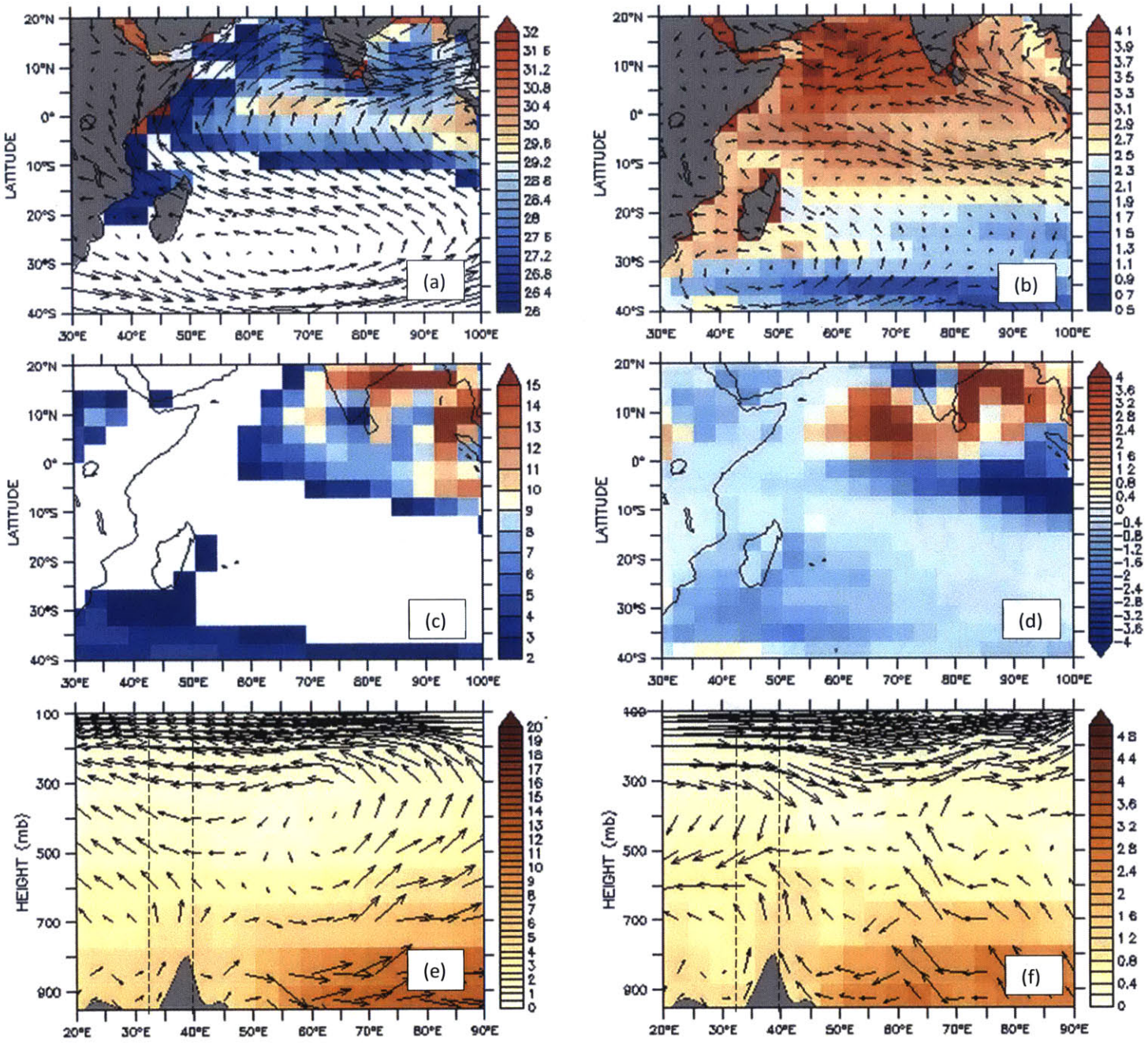


**Figure B.14:** CMCC-CESM

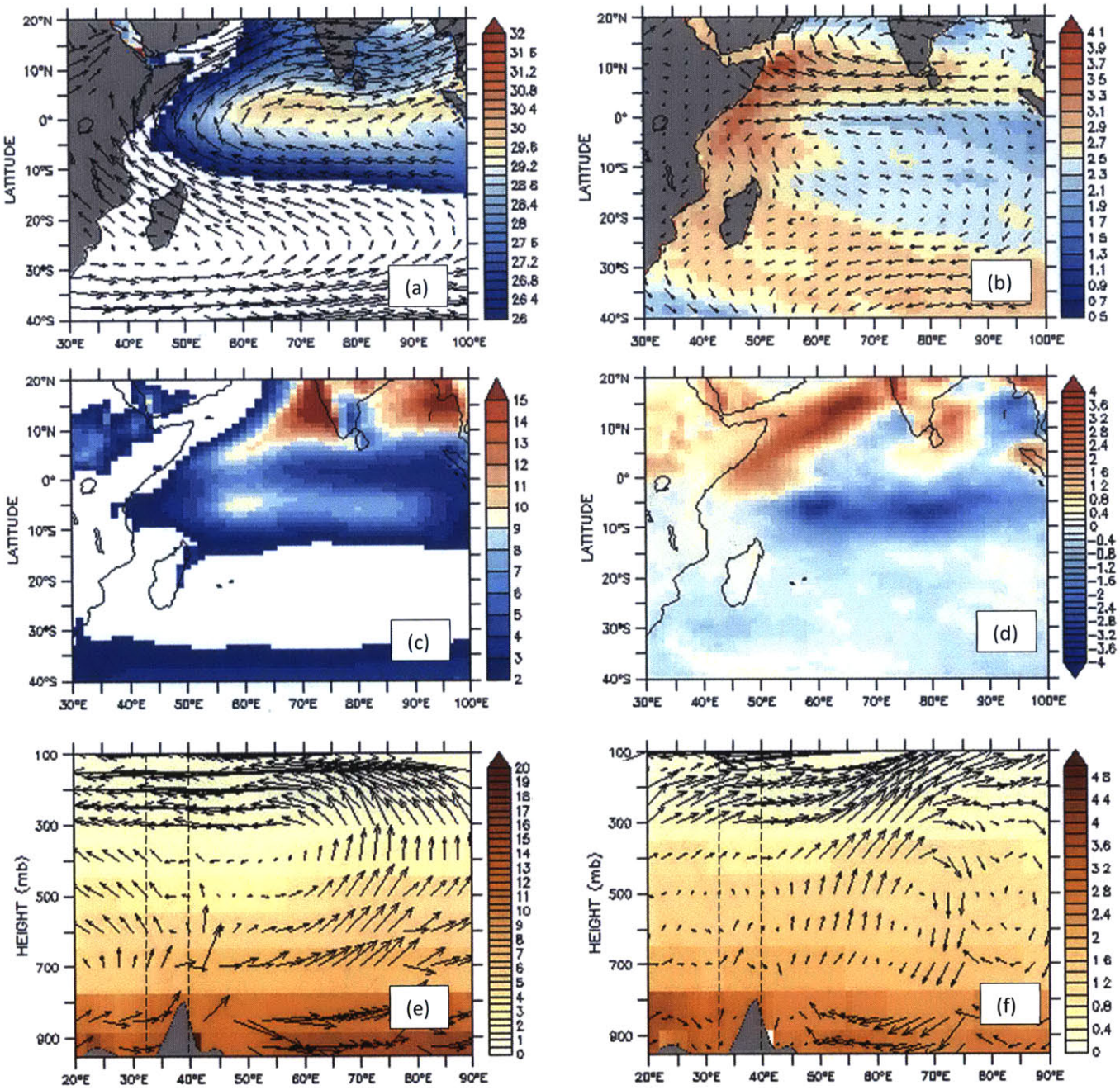


**Figure B.15:** CESM1-BGC

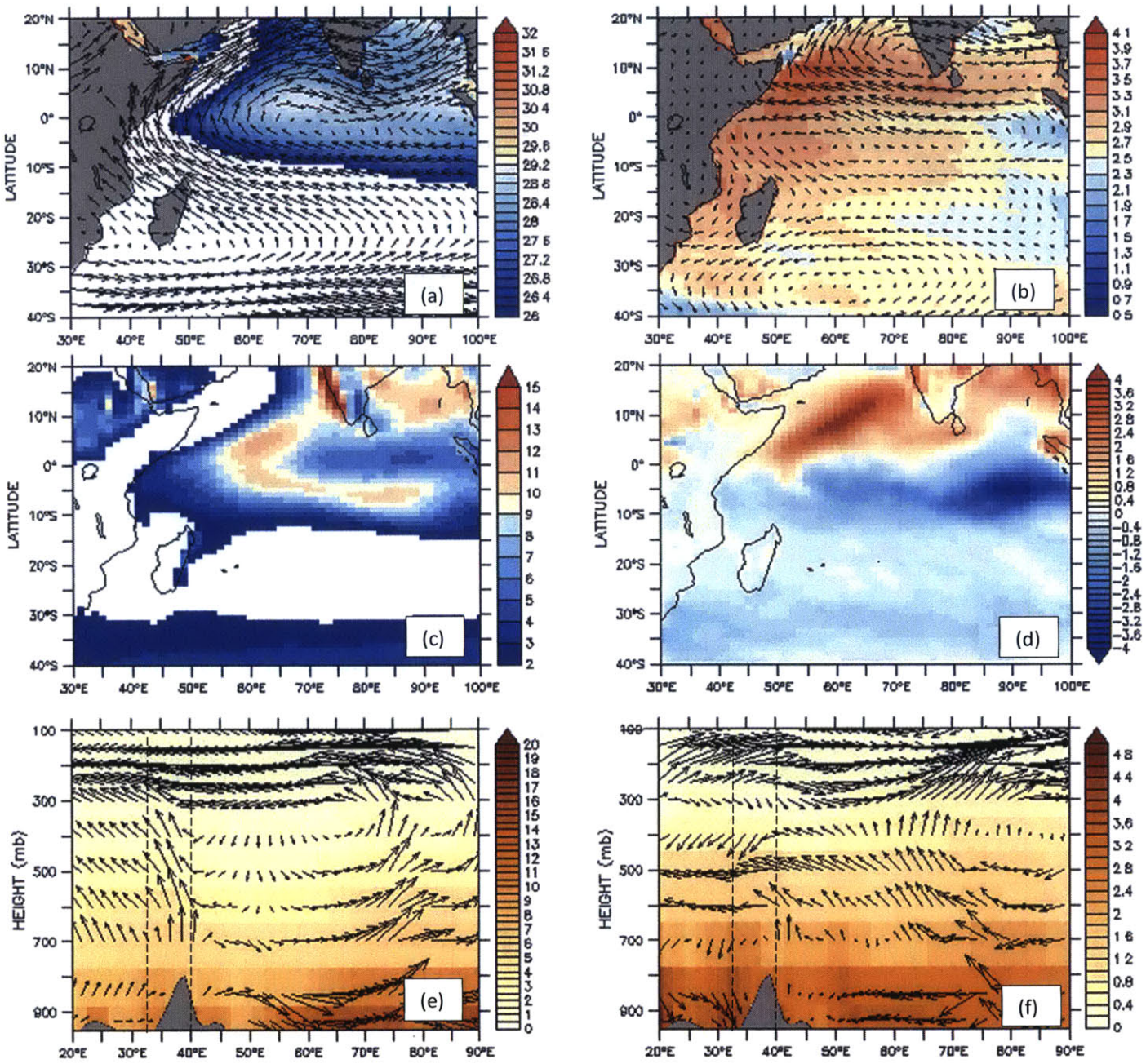


**Figure B.16:** CESM1-CAM5

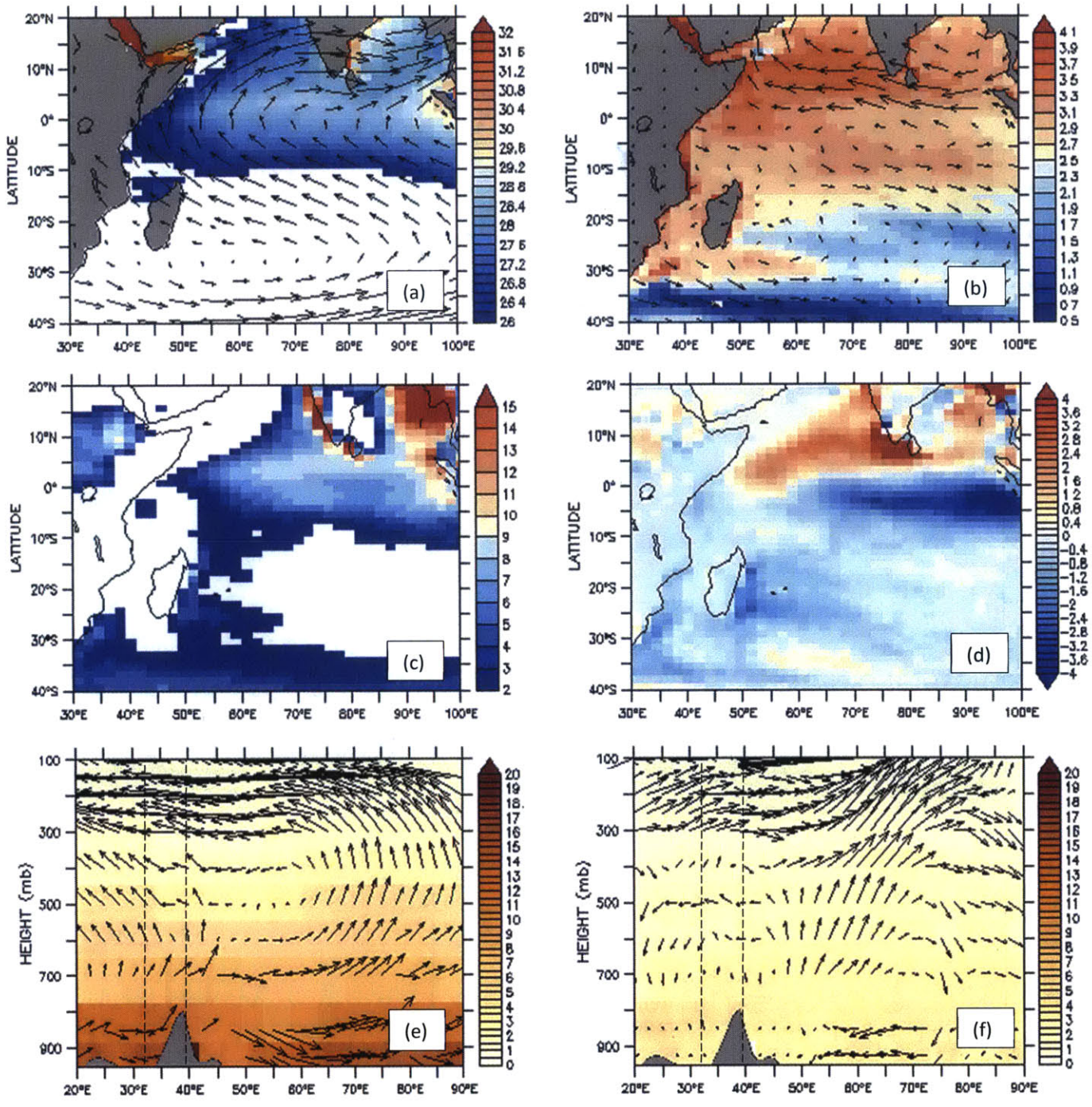


**Figure B.17:** ACCESS1.0

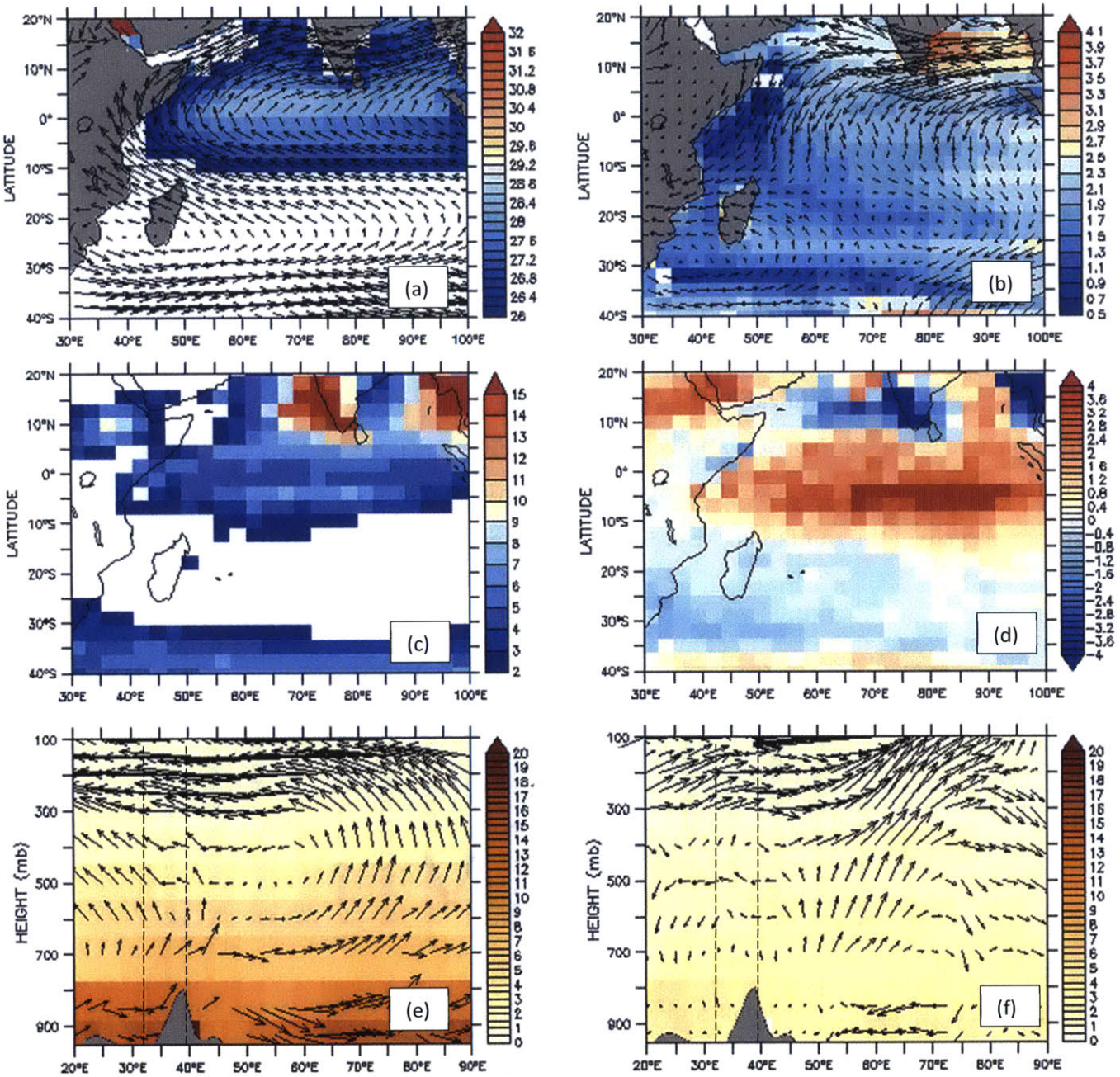


**Figure B.18:** FGOALS

# Appendix D: Analysis of the effect of the resolution on simulation of the hydrological cycle over the Eastern Nile basin using CMIP5 GCMs.

In chapter 3, the effect of the resolution on the simulation of the hydrological cycle using CMIP3 and CMIP5 GCMs is investigated for the Upper Blue Nile basin. Here, we present the same analysis, however, using the 18 GCMs used to predict the changes in the future flows of the Nile in Chapter 4 (Table 4.1) and for the Eastern Nile basin. The conclusions from the analysis presented in Chapter 3 on the effect of the model resolution on the simulation of the hydrological cycle are still valid. The GCMs show an overestimation of the rainfall and runoff over basin compared to observations as shown in Figure D.1. In addition, the increase of the spatial resolution improves the simulation of the hydrological cycle over the basin and the seasonal cycle of the rainfall is closer to observations as shown in Figure D.2.

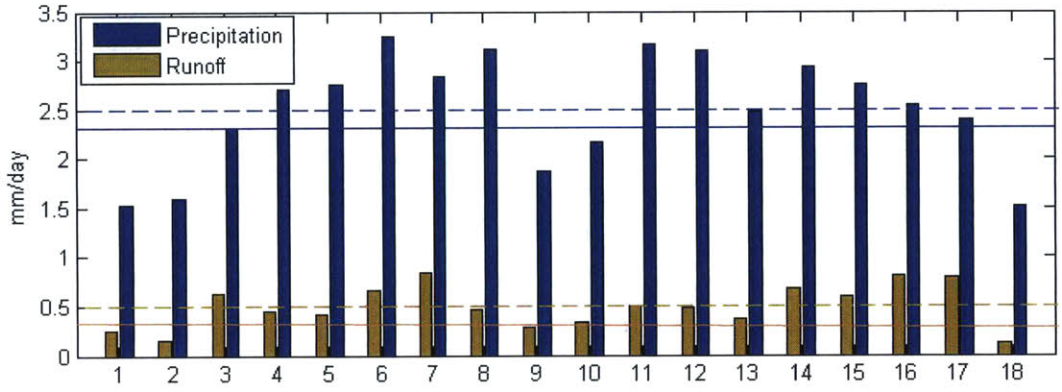


**Figure D.1:** Analysis of rainfall and runoff for 30 years (1970-2000) for 18 GCMs of the CMIP5 project over the Eastern Nile basin. The long-term mean of the rainfall is from TRMM V7 3B43 rainfall (blue solid line) and the observed stream flow based on the work of Conway and Hulme (1993) (brown solid line). The blue and brown dashed lines are for the multi-model ensemble average using the 18 GCMs for rainfall and runoff respectively. The model numbers are listed in Table 4.1.

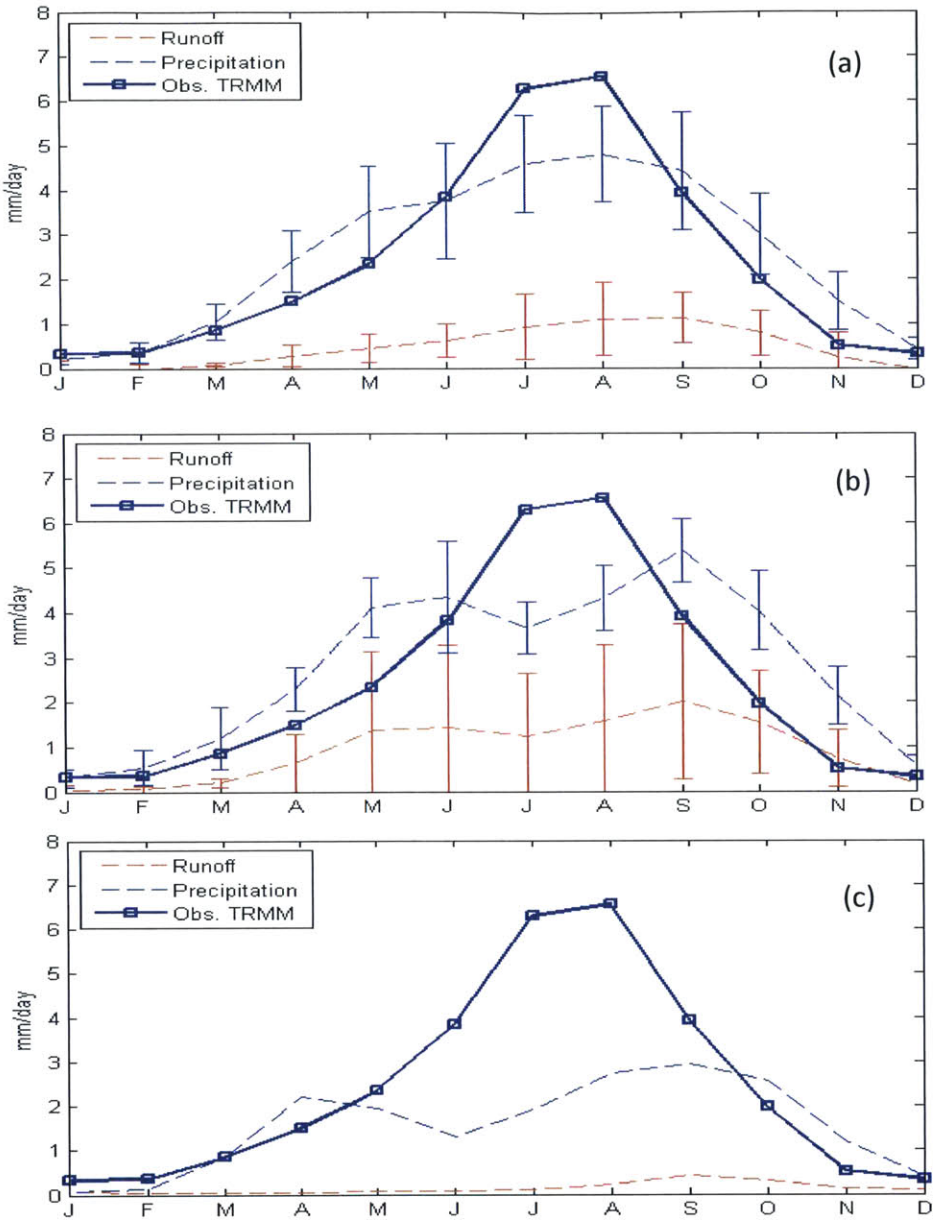


**Figure D.2:** Average seasonal cycle of rainfall and runoff for 30 years (1970-2000) for 18 GCMs of the CMPI5 project over the Eastern Nile basin. The figures are sorted according to the spatial resolution of the GCMs: (a) is for the highest resolution GCMs of approximately (1.8°x1.8°), (b) is for medium resolution models of approximately (2.8°x1.8°) and (c) for low resolution of approximately (4°x3°), only one model (CMCC-CESM). The error bars indicates a variation around the ensemble mean of the models of equivalent resolution by one standard deviation. The solid line with circles and stars are for the long-term averages of observations of rainfall using TRMM V7 3B43, while the dashed lines are for rainfall and runoff of the GCMs.